Targeted Interrogation of Blood-Brain Barrier Biology

By

Emma Hollmann Neal

Dissertation

Submitted to the Faculty of the

Graduate School of Vanderbilt University

in partial fulfillment of the requirements

for the degree of

DOCTOR OF PHILOSOPHY

in

Chemical Engineering

May 8, 2020

Nashville, Tennessee

Approved:

Ethan Lippmann, Ph.D.

John Wilson, Ph.D.

Matthew Lang, Ph.D.

Vivian Gama, Ph.D.

For my mother, who deserves the world but will have to settle for this dissertation.

ACKNOWLEDGEMENTS

As my time in the Department of Chemical Engineering at Vanderbilt quickly draws to a close, I can firmly say that the past nearly five years have been some of the most challenging, yet also most rewarding, of my life. I owe my success during this time to countless individuals who have gifted me their time, expertise, and understanding, and while I shall do my best to articulate how much this help has meant to me, I truly believe that no words are adequate to express the gratitude I feel. This is going to get emotional.

I want to express my sincerest thanks to my committee members Dr. John Wilson, Dr. Matthew Lang, and Dr. Vivian Gama. Your collective expertise and guidance have been invaluable to improving my work. I will forever appreciate the manner in which you cautioned, but never suppressed, my ambition towards my projects. I am a better scientist for it. On a lighter note, I appreciate the collective patience of my committee towards my tendency to speak far too quickly and include exorbitant amounts of information in my presentations to you. I am aware of this habit, and I promise I will continue to work on it.

I would like to thank the many collaborators with which I have had the privilege to work during my graduate tenure. Dr. Shannon Faley, the lab of Dr. Aaron Bowman, Natalya Ortolano, Megan Rasmussen and many others were vital to my success in the first years of my Ph.D. and provided invaluable assistance with microscopy as well as molecular biology techniques. Dr. Joshua Bauer, Dr. Paige Vinson, and David Baughman of the High Throughput Screening Facility were instrumental in bringing our CRISPR screen to fruition. I would like to thank the Vanderbilt Institute for Clinical and Translation Research for providing financial support for my RNA sequencing experiments. I sincerely appreciate individuals at the Vanderbilt Flow Cytometry Shared Resource, Vanderbilt Technologies for Advanced Genomics (VANTAGE), Vanderbilt

Antibody and Protein Resource (VAPR), Vanderbilt Cell Imaging Shared Resource (CISR) for all of the technical expertise and guidance they have provided, as well as Jean-Philippe Cartailler and Lawrence Hsu of Creative Data Solutions for their immense help in processing our extensive sequencing data. Thank you to Natasha O'Brown for your indispensable work generating zebrafish knockouts and for your continual sass towards Ethan. Additionally, I am grateful to have been supported by a National Science Foundation Graduate Research Fellowship as well as a P.E.O. Scholar Award during my graduate tenure. Finally, I want to thank Felisha Baquera, the saving grace of my Ph.D. Thank you for all of the emails answered that fell outside of your job description and for your endless encouragement to finish this degree. You are a light in this department, and none of us thank you enough for the work that you do.

To my fellow lab mates present and past, you all have become a second family to me during my graduate tenure. Jonah Rosch, Allison Bosworth, Kylie Balotin, Nicholas Marinelli, Yajuan Shi, Ketaki Katdare, Everett Allchin, Alexander Sorets, Lexi Yates, Madison Stiefbold, Daniel Balikov, Hyosung Kim, and Brian O'Grady are some of the best individuals I have ever had the pleasure to meet. You all have celebrated with me on the best days, comforted me on the worst, and shared many, many donuts and cups of coffee with me on the days in between. My only regret is that I did not meet you all sooner. Though, to be honest, I'm pretty sure you all would have beaten me out for a spot in our lab if we had actually met earlier. Maybe it's best we met when we did. Regardless, you all inspire me daily, and I am immensely proud of the supportive, collaborative environment we have built. I cannot wait to see the heights which you all reach in the years to come. I will be cheering you on each step of the way.

Many thanks are owed to my undergraduate students Amanda Weaver, Dalton Gullett, Kameron Hagerla, and Riley Knight for bringing me an immense amount of joy, countless laughs,

and maybe a tad bit of frustration during the past few years. Watching each of you grow into passionate researchers who truly care about our science and believe in our mission is one of the most meaningful experiences of my life. You all evolved from being my mentees to being some of my closest friends, and I thank you for sharing this time with me.

To my parents, Carl and Sandra Hollmann, thank you for your never-ending support in my academic pursuits and for generally shaping who I am as a person. Dad, your tireless work ethic and humility never cease to inspire me, and I have done my absolute best to embody them in my own career. Mom, your courage, resilience, and compassion are beyond measure, and I aspire to be even a tenth of the person you are. This work was for you, and I would do it a hundred times over if it meant I could help you more. Thank you to my sisters, Anna and Sara, and brothers-in-law, Jason and James, for being my fire-breathing, larger than life role models. You all have given me large shoes to fill, and I don't think I will ever fully grow out of trying to be more like each of you. Thank you to my extended family for your support and understanding these past few years as I've pursued my degree and had to miss more than a few family events. To Annie Epley, Lexi Clark, and Sonia Chakrabarty—you three have been a constant in my life since middle school (and earlier), and your encouragement these past years has meant so much to me. Thank you for forgiving me for all the gatherings I could not attend and messages I failed to answer.

To my adviser, Dr. Ethan Lippmann, I've spent a considerable amount of time contemplating what I wish to say to you, and no words are sufficient. Before I started graduate school, I genuinely thought that I was making the biggest professional mistake of my life. Now, I realize that missing the experience of working with you these past few years would truly have been the biggest mistake I could have made. Thank you for the countless hours you have invested in my professional development and for the abundance of patience you've had with me as I've discovered

new ways to fail at science daily. More importantly, thank you for your boundless excitement towards our science, your willingness to jump headfirst into the unknown, the countless laughs we have shared in our many meetings, the memories from our globe-trotting conference adventures, and for the frequent, well placed reminders that it's not all about me. I believe we have built something truly special with this research group, and it has been an honor and privilege to be your first student. I hope that I made you proud.

Finally, and most importantly, I want to thank my husband, Matthew, for the countless ways in which you made this Ph.D. possible. I will never be able to adequately thank you for all of the sacrifices you have made so that I could pursue this goal. Your selflessness and patience as we've lived life in thirty-hour increments for the past few years is nearly beyond comprehension. Thank you for being my biggest advocate, my strongest supporter, and my best friend. This Ph.D. simply would not exist without you. I am forever thankful that you are my person.

TABLE OF CONTENTS

Page

LIST OF TABLES

Table Page

LIST OF FIGURES

Figure Page

Chapter 1

INTRODUCTION

1.1 The blood-brain barrier in human health and disease

More than 3 million adult Americans are diagnosed annually with neurological disorders, including Parkinson's, Alzheimer's, and Huntington's diseases [1], and an estimated $789 billion (2014 dollars) is spent annually by Americans as a result of only 9 of these diseases. This cost is likely to increase dramatically as the population is expected to nearly double from 43.1 million in 2011 to 83.7 million by 2050 [2]. Despite the increasing personal and societal burdens caused by these diseases, the pathophysiology of these diseases remains a mystery in many cases. Blood-brain barrier (BBB) dysfunction has been associated with many neurological diseases [3–5]. Therefore, understanding of the biology and pathophysiology of the BBB will provide insight into potentially druggable targets to help treat neurological disease.

The BBB, composed of brain microvascular endothelial cells (BMECs), tightly regulates material exchange between the blood stream and central nervous system (CNS) parenchyma. Such microenvironment regulation is critical to maintain synaptic transmission and circuit organization [6]. BMECs are characterized by specialized tight junction proteins, including claudin-5 and occludin, that limit paracellular diffusion of proteins, hydrophilic small molecules, and ions [7,8]. Limited paracellular flux across the BBB results in a characteristically high transendothelial electrical resistance (TEER) [9]. In contrast, non-BBB endothelium exhibits less restrictive flux of ions and molecules [10–12]. Transport across the BBB is regulated by multiple import transporters [13], such as GLUT-1 [14,15], and efflux transporters [16], including P-glycoprotein [17,18], breast cancer resistance protein (BCRP) [19], and multidrug resistance related protein

(MRP) family transporters [19]. Collectively, these transporters work to exclude potential neurotoxins from the CNS parenchyma, which has a limited ability for self-repair, while ensuring proper nutrient supply to the brain [20] (Figure 1.1). Finally, the BBB lacks fenestrae [8] and experiences exceedingly low levels of bulk transcytosis and pinocytosis to restrict non-specific macromolecule access to the brain [4,6].

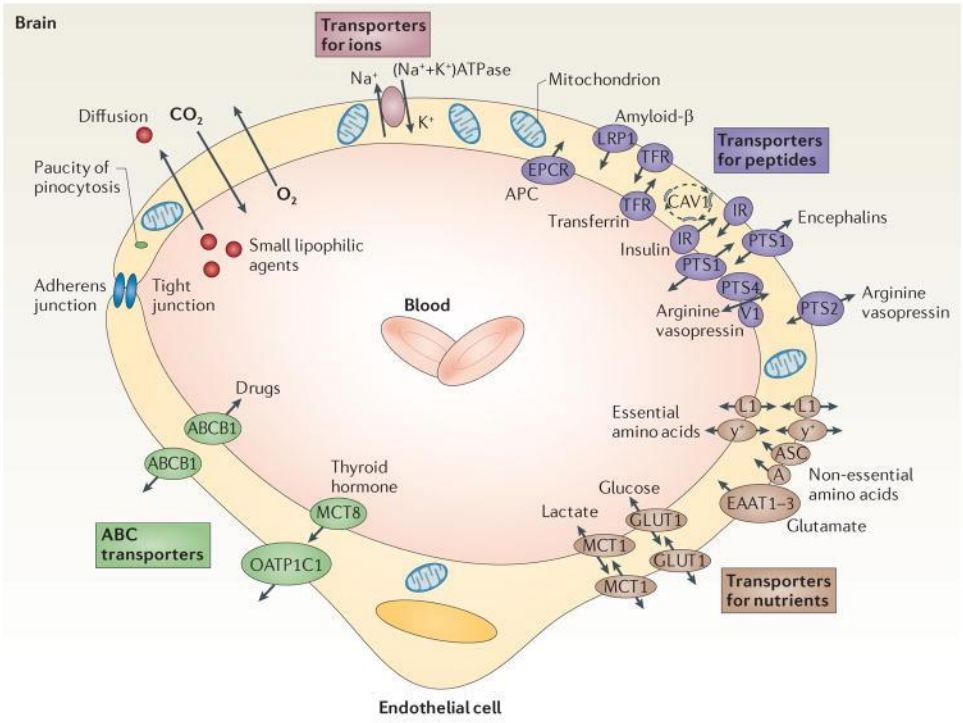

Figure 1.1 Transporter expression at the blood-brain barrier. Brain microvascular endothelial cells express a host of molecular transporters tasked with providing nutrients to the CNS parenchyma, clearing waste, effluxing potential neurotoxins, and preventing nonspecific transport by transcellular and paracellular routes. Image adopted from Zlokovic, 2011, with permission from Springer Nature [4].

The specialized nature of the BBB as compared to peripheral endothelium is evident from the beginning of development. Development of brain vasculature is initiated when mesoderm-derived angioblasts migrate and cover the neural tube to form the perineural vascular plexus [21].

Vascular sprouts then invade surrounding neuroectoderm, guided by vascular endothelial growth factor (VEGF) concentration gradients [22]. This VEGF-mediated guidance is not CNS specific, though, and is critical for proper vascular development throughout the body [23]. In contrast, Wnt/β-catenin signaling has been shown to be essential for CNS, but not non-CNS, angiogenesis [15,24]. Neural progenitors in the developing forebrain and ventral region of the neural tube express Wnt7a and Wnt7b. Binding of these ligands to Frizzled (Fzd) receptors on the developing vasculature leads to inhibition of β-catenin degradation and activation of β-catenin target genes, including *SLC2A1* [24]. Further evidence of the CNS-specific role of Wnt signaling in angiogenesis is found in the downstream activation of *DR6* and *TROY* which further mediate vessel sprouting [25]. Finally, while Wnt/β-catenin signaling acts in a non-cell autonomous fashion to control CNS angiogenesis, cell autonomous control of CNS vessel sprouting is exerted by orphan G protein-coupled receptor (GPR124) [26]. Deletion of *Gpr124* in mice resulted in embryonic lethality secondary to profound cerebral hemorrhage. Further investigation of this signaling cascade identified *Gpr124* and *RECK* as integral components for transducing Wnt7a/Wnt7b signaling for CNS angiogenesis [27]. Thus, both cell-autonomous and non-cell autonomous events contribute to the unique development of CNS vasculature.

Development of BBB endothelial cells does not occur in a vacuum. Rather, interactions between brain microvascular endothelial cells, astrocytes, pericytes, microglia, and neurons are essential for the development and maintenance of BBB properties, and together these cell types form the neurovascular unit (NVU) [8]. Astrocytic secretion of Sonic hedgehog (Shh) promotes the formation and maintenance of robust tight junctions, and deficits in this pathway result in increased paracellular leakage [28]. Conversely, pericytes suppress transcytosis to reduce vascular permeability and reduce immune cell infiltration by suppressing expression of *Angpt2*, *Plvap*,

Icam1, and *Alcam*, among others, in BMECs [29]. Microglia interactions with the BBB are receiving increased attention due to their role in neuroinflammation [30], and increased understanding of these interactions is likely to prove vital to the design and/or identification for effective therapies for neuroinflammation.

Advances in transcriptional profiling techniques, especially RNA sequencing at both the bulk and single cell levels, has provided significant insight into the molecular heterogeneity of the BBB both regionally and along the vasculature tree [31] (Figure 1.2). Certain features of the BBB, such as extensive tight junctions formed by claudin-5 and occludin, appear to be conserved across these domains while expression of certain transporters and cell adhesion molecules appear to depend strongly on positional identity [32]. For instance, recent work by Yousef, *et al*., identified clustering of VCAM1 expression to arterial and venous endothelial cells within the aged mouse hippocampus without appreciable expression in capillaries [33]. However, the molecular profiles of these two clusters were markedly distinct. Arterial VCAM1+ populations displayed further expression of genes associated with migration and proliferation. Venous VCAM1+ populations were characterized by expression of cytokine receptors associated with inflammation [33]. The degree to which changes in transcriptional activity as a function of location are regulated by interactions with other members of the NVU is not yet fully understood. Understanding these distinct molecular profiles, the resulting changes in BMEC behavior, and the role of NVU interactions in mediating these identities is imperative for the future design of BBB-targeting therapeutics.

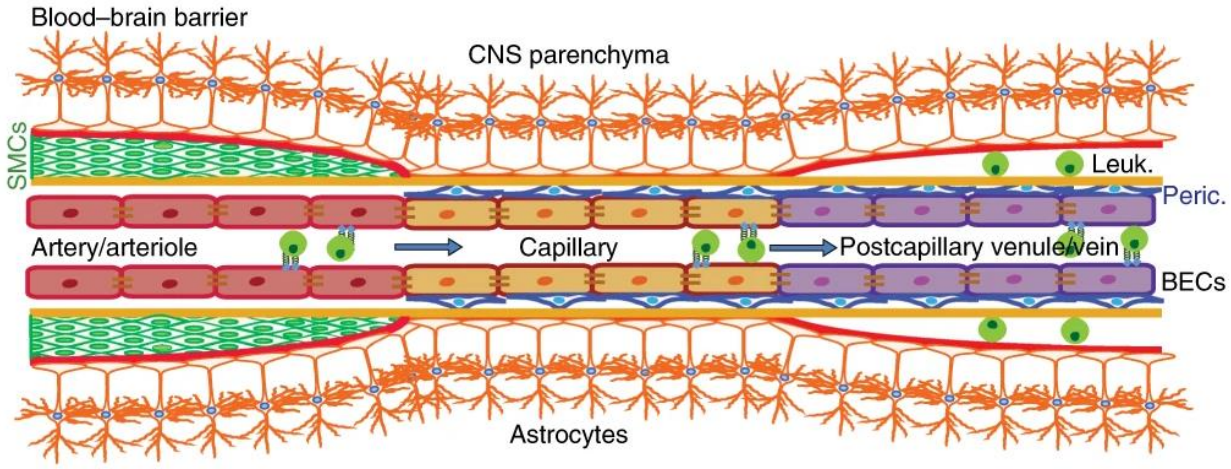

Figure 1.2 The blood-brain barrier along the vascular tree. Oxygenated blood flows from arteries/arterioles, which are supported by smooth muscle cells, to highly specialized capillaries, and finally through postcapillary venules/veins. Postcapillary venules/veins have a larger perivascular space than other portions of the vascular tree and are the site of immune cell extravasation on the rare incidence it occurs. Capillaries and venules/veins are supported by pericytes, and astrocytes ensheath endothelial and mural cells across the entire tree. Adopted from Yousef, et al., with permission from Springer Nature [33].

Dysfunction of the BBB is associated with many neurodegenerative diseases, including multiple sclerosis [34], traumatic brain injury [35–38], Huntington's Disease [39], ischemic stroke [40], and natural neurovascular aging [41]. In diseases that do not disrupt the BBB, delivery of therapeutics is hindered as many pharmaceuticals are unable to freely diffuse through the barrier due to molecular size, hydrophilicity, and/or are substrates for efflux transporters [42,43]. BBB dysfunction often manifests as increased transcellular and paracellular permeability, seen in ischemic stroke [44], and as diminished efflux transporter activity and/or expression, as is seen in Alzheimer's Disease and Parkinson's Disease [45–47] (Figure 1.3). Such dysregulation results in altered brain concentrations of ions and macromolecules, including albumin and neurotransmitters, thereby leading to altered synaptic and axonal transmission as well as further exacerbation of inflammation[6].

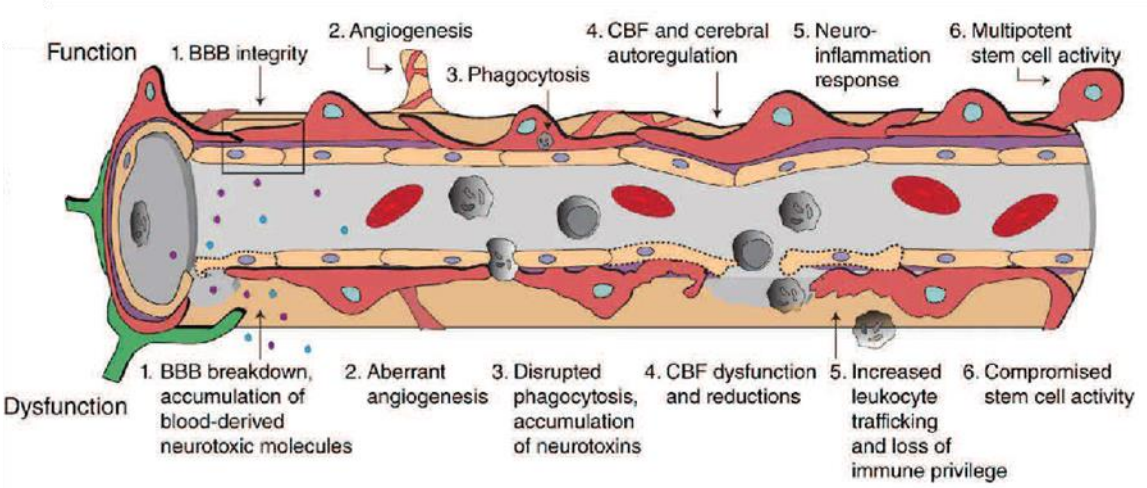

Figure 1.3 Consequences of blood-brain barrier breakdown. Blood-brain barrier breakdown may result in the non-specific leakage of blood-borne ions, molecules, and cells into the CNS parenchyma. The collective result of this breakdown is the interruption of correct neuronal function. Adopted from Sweeney, et al., with permission from Springer Nature [48]**.**

1.2 Approaches to modeling the blood-brain barrier

In vivo approaches have been employed to understand the development and regulation of the BBB, including the transport and toxicity of pharmaceuticals across the barrier. However, these approaches are time intensive, expensive, and characteristically low throughput [49]. The BBB comprises 1/1000th of total brain volume, necessitating isolations from multiple animals in order to have enough BMECs to either culture or perform direct analyses upon (e.g.- RNA sequencing) [50]. *In vivo* platforms utilized in pharmaceutical screens require a prohibitive number of animals to test compound libraries, plus perform downstream characterizations. Therefore, in *vitro* BBB models are a preferred tool to interrogate BBB biology and study potential BBB-penetrating therapeutics.

Traditional *in vitro* BBB models include BMECs isolated from animal sources as well as immortalized or primary human BMECs [49,51]. Animal BMEC sources include mice [52], rats

[53,54], cows [55], and pigs [56,57]. BMECs from any of the aforementioned sources also have the additional advantage of being amenable to culture with other cells of the neurovascular unit, namely astrocytes, pericytes, and neurons, that aid in recapitulating the *in vivo* environment to realize a more accurate BBB phenotype (e.g.- highly-organized tight junctions and low levels of transcytosis) [58–61]. However, the non-human cell sources contain intrinsic species' differences in transporter sequences and structures, transporter activities, and transporter expression levels [62]. Findings in these non-human cell-based models may not adequately translate into suitable applications in humans. Therefore, a BBB model constructed only of human cells is the ideal tool to investigate BBB function with the highest possibility of translational success.

Original fully-human BBB models employed either immortalized BMEC lines [63] or BMECs isolated from primary tissue [64]. Immortalized BMECs provide an easily scalable and relatively limitless supply of BMECs for *in vitro* modeling. These immortalized BMECs display active efflux transporter activity but exhibit TEER levels well below physiologically relevant values, thus rendering any biological findings as less than ideal for complete understanding of paracellular transport across the barrier. In contrast, primary human BMECs possess moderate barrier properties, but their tedious and low-yield isolation hinders their use in applications necessitating large quantities of cells. Thus, an ideal BBB model would consist of easily scalable human cells which accurately recapitulate the *in vivo* neurovascular environment.

Owing to their ability to extensively self-renew and differentiate into all somatic cell types found in the human body, human induced pluripotent stem cells (iPSCs) offer an unprecedented opportunity to interrogate BBB regulation and dysfunction. Human iPSCs have been successfully differentiated into endothelial cells displaying characteristic *in vivo* BBB properties, including expression of tight junction proteins, nutrient transporters, and active efflux transporters [65].

However, this model suffered from TEER values significantly below those recorded in animals. The inclusion of retinoic acid (RA), secreted by radial glial cells in the developing CNS and thought to impart BBB characteristics on immature BMECs *in vivo* [66], during the differentiation process significantly improved the passive barrier properties of the BMECs, and co-culture of these cells with other cell types of the neurovascular unit produced near *in vivo* TEER values [67]. While this model overcomes some limitations of the first-generation differentiation procedure, the RA-enhanced BBB model still requires a lengthy differentiation scheme with chemically undefined, costly medium, both issues which preclude the widespread adoption of this model. Therefore, advances in differentiation techniques that decrease the time and cost of model generation while further promoting *in vivo* properties will advance the adoption of an iPSC-derived BBB model.

1.3 Current limitations in understanding blood-brain barrier regulation

While many advances have been made in understanding BBB development and regulation, many questions remain unanswered concerning the genomic underpinnings of the highly restrictive nature of the BBB [68,69]. Furthermore, despite the increasingly widespread use of stem cell-based *in vitro* BBB models, much of the exploratory work relating to the BBB has been limited to transcriptome profiling of isolated animal and human BMECs [70–72]. This approach has recently resulted in discovering genes critical to BBB functionality, specifically *Gpr124*, a gene encoding for a G-protein-coupled-receptor required for proper CNS angiogenesis and BBB integrity via interactions in Wnt signaling [27,73–75], and *Mfsd2a*, encoding for a protein found to be critical in regulating permeability across the BBB [72,76]. Though these breakthroughs have contributed greatly to understanding BBB biology, these two genes constitute a small fraction of

what is likely a plethora of yet to be identified genes critical for maintaining a healthy BBB phenotype. The limitation still exists that transcriptome profiling approaches from isolated primary cells are intrinsically low throughput and subject to variability resulting from isolation techniques [69]. Thus, a high-throughput platform for screening for BBB functional genomics is critical.

1.4 CRISPR/Cas9 use in functional genomic screens

Forward genetic screens, characterized by their "phenotype-to-genotype" approach, have traditionally consisted of the use of chemical DNA mutagens and RNA interference (RNAi) reagents to modify phenotypes and allow for the subsequent selection of causal genotypes [77,78]. However, incomplete gene knockdown/knockout, costly and labor-intensive identification of causal genotypes, and confounding off-target effects have limited their utility in mammalian genome-wide functional screens [79,80]. Programmable nucleases, including zinc finger proteins (ZFNs) [81,82], transcription activator-like effectors (TALEs) [83], and, most recently, Cas9 [84–87], have emerged as ideal strategies for genetic manipulation [88].

Cas9 has gained considerable attention due to its programmable versatility and scalability [89]. Originally derived from the microbial adaptive immune system CRISPR (clustered regularly interspaced short palindromic repeat)[90], Cas9 may be directed to any genomic locus through the complexing of the nuclease to a single-guide RNA (sgRNA). The sgRNA imparts specificity on the nuclease activity by identifying target sequences through Watson-Crick base pairing of a 20-base pair sequence at the 5' end of the sgRNA [91]. Thus, multiple genomic loci may be targeted in a single experiment through the addition of multiple sgRNA [84]. CRISPR/Cas9 is advantageous over RNAi in genetic screens as off-target effects are reduced by the specificity

imparted by the sgRNA sequence, and gene knockdown is irreversible rather than dependent on trans-gene expression levels [77].

Genome scale CRISPR-Cas9 screens have, thus far, been used primarily to identify mechanisms for drug resistance or identify gene essentiality through live-dead readouts [91,92]. Limited progress has been made in applying this system to genome-wide screens in systems where relevant phenotypes are considerably more subtle than a simple live-dead readout. For example, in the case of BBB screens, genes responsible for regulating endocytosis and transcytosis may not cause visual phenotypic changes while still representing an extremely important finding. Advancements in this area, particularly as related to neurovascular health, stand to significantly enhance our understanding of these complex systems and identify novel therapeutic targets to ameliorate many as-yet untreatable neurodegenerative diseases.

1.5 Organization of dissertation

This dissertation consists of 8 chapters.

Chapter 2 details the use of defined medium to expedite the differentiation of induced pluripotent stem cells (iPSCs) to brain microvascular endothelial cells (BMECs). BMECs generated using this protocol expressed hallmark tight junction proteins, possessed active efflux transporter activity, and responded to inductive cues from astrocytes and pericytes.

Chapter 3 transitions BMECs differentiated using methods detailed in Chapter 2 from two-dimensional culture to a three-dimensional, biomimetic macrovessel with blood-brain barrier properties. This study highlights the role of perfusion in maintaining BMEC barrier properties and serves as an important first step towards more representative *in vitro* models of brain vasculature.

Chapter 4 addresses the use of serum as a source of significant variability in the outcome of iPSC differentiations to BMECs and details the development of serum-free and fully-defined differentiation protocols to produce BMECs from iPSCs. BMECs produced using this method recapitulated many key *in vivo* features of the blood-brain barrier. Furthermore, the study underscored the role of undefined media components as a potential confounding factor in the interpretation of experimental results.

Chapter 5 explores the influence of basal media composition upon the barrier fidelity of iPSC-derived BMECs. These BMECs possessed markedly different passive and active barrier properties as a result of their extracellular environment. Despite these functional changes, no striking alterations in the transcriptional landscapes of the BMECs were observed as a function of basal media composition, suggesting functional changes were the result of downstream signaling pathways.

Chapter 6 describes the use of transcriptional profiling of iPSC-derived BMECs to identify genes which contribute to the highly specialized but poorly understood blood-brain barrier phenotype. Though previously unidentified at the BBB, *IQGAP2* was identified as a potential novel regulator of barrier phenotype, and its expression was validated *in vivo*. These results indicate the potential predictive power of our *in vitro* model for uncovering novel mechanisms of barrier regulation with *in vivo* relevance.

Chapter 7 utilizes high-throughput CRISPR screening and high content imaging to identify potential regulators of blood-brain barrier paracellular permeability.

Chapter 8 provides conclusions for the work presented within this presentation as well as future directions for continued efforts in this area.

Chapter 2

ACCELERATED DIFFERENTIATION OF HUMAN INDUCED PLURIPOTENT STEM CELLS TO BLOOD-BRAIN BARRIER ENDOTHELIAL CELLS

Adopted from: Hollmann EK, Bailey AK, Potharazu AV, Neely MD, Bowman AB, Lippmann ES. Accelerated differentiation of human induced pluripotent stem cells to blood–brain barrier endothelial cells. Fluids Barriers CNS. 2017;14:9 *with permission from the BioMed Central.*

2.1 Summary

Due to their ability to limitlessly proliferate and specialize into almost any cell type, human induced pluripotent stem cells (iPSCs) offer an unprecedented opportunity to generate human brain microvascular endothelial cells (BMECs), which compose the blood-brain barrier (BBB), for research purposes. Unfortunately, the time, expense, and expertise required to differentiate iPSCs to purified BMECs precludes their widespread use. Here, we report the use of a defined medium that accelerates the differentiation of iPSCs to BMECs while achieving comparable performance to BMECs produced by established methods. iPSCs were seeded at defined densities and differentiated to BMECs using defined medium termed E6. Resultant purified BMEC phenotypes were assessed through transendothelial electrical resistance (TEER), fluorescein permeability, and P-glycoprotein and MRP family efflux transporter activity. Expression of endothelial markers and their signature tight junction proteins were confirmed using immunocytochemistry. The influence of co-culture with astrocytes and pericytes on purified BMECs was assessed via TEER measurements. The robustness of the differentiation method was confirmed across independent iPSC lines. The use of E6 medium, coupled with updated culture methods, reduced the differentiation time of iPSCs to BMECs from thirteen to eight days. E6-derived BMECs expressed GLUT-1, claudin-5, occludin, PECAM-1, and VE-cadherin and consistently achieved TEER values exceeding 2,500 $\Omega \times cm^2$ across multiple iPSC lines, with a maximum TEER value of 4,678

± 49 Ω×cm^2 and fluorescein permeability below 1.95×10^{-7} cm/s. E6-derived BMECs maintained TEER above 1,000 Ω×cm^2 for a minimum of 8 days and showed no statistical difference in efflux transporter activity compared to BMECs differentiated by conventional means. The method was also found to support long-term stability of BMECs harboring biallelic *PARK2* mutations associated with Parkinson's Disease (PD). Finally, BMECs differentiated using E6 medium responded to inductive cues from astrocytes and pericytes and achieved a maximum TEER value of 6,635 ± 315 Ω×cm^2, which to our knowledge is the highest reported *in vitro* TEER value to date. Given the accelerated differentiation, equivalent performance, and reduced cost to produce BMECs, our updated methods should make iPSC-derived *in vitro* BBB models more accessible for a wide variety of applications.

2.2 Introduction

The blood-brain barrier (BBB) is composed of brain microvascular endothelial cells (BMECs), which strictly regulate molecular transport between the bloodstream and the brain to ensure proper function of neuronal circuits, synaptic transmission, and other essential processes that depend upon a tightly controlled neurovascular environment [93]. BMECs are characterized by specialized tight junctions [7,8] that limit paracellular flux of biologics, hydrophilic small molecules, and ions, which results in a characteristically high transendothelial electrical resistance (TEER) across the barrier not observed in other capillary beds in the body [9,94]. For import and export of molecules, BMECs express multiple transporters, such as GLUT-1 [95], and active efflux transporters [95], including P-glycoprotein and multidrug resistance related protein (MRP) family transporters [16], that confer protection. BBB disruption is implicated in many chronic neurodegenerative diseases, such as multiple sclerosis [34], traumatic brain injury [35], ischemic

stroke [36–38,40], and in natural aging of the neurovascular unit [41]. Moreover, the BBB often hinders delivery of therapeutics to diseased tissue when the barrier remains intact [43]. The time, expense, difficulty, and limited throughput of all *in vivo* research often precludes widespread use of such techniques, necessitating *in vitro* platforms to investigate certain biological phenomena. Therefore, *in vitro* BBB models are often employed to study BBB mechanisms, neurovascular cell-cell interactions, and to perform screens for BBB-permeant therapeutics.

In vitro BBB models have most often been constructed using primary BMECs isolated from rat, bovine, and porcine sources [16–21]. Such models extended to BMECs in co-culture with astrocytes, pericytes, and neurons, cell types known to enhance the BBB phenotype and thereby more accurately recapitulate the *in vivo* neurovascular environment [96,97]. These models can be used to study BBB development, regulation, and disease, as well as assay potential drug candidates for permeability [98,99]. However, due to species' differences in transporter sequences/structures, activities, and expression levels [62], a robust fully-human BBB model is preferred to investigate BBB function and disease in a human context and to perform drug screens that yield the most promising pharmacological compounds for clinical applications.

Human *in vitro* BBB models have most often utilized either BMECs isolated from primary tissue [64] or immortalized BMEC cell lines [63]. Primary BMECs demonstrate moderate barrier properties, but difficult isolation procedures and low yields hinder their widespread use. Immortalized BMECs provide a readily scalable source of cells for *in vitro* models, but these cells do not recapitulate the impermeable character of the BBB. Due to their ability to limitlessly proliferate and specialize into any cell type, human induced pluripotent stem cells (iPSCs) offer an unprecedented opportunity to provide human BMECs for research purposes. iPSCs were recently shown to be capable of differentiating to endothelial cells with BBB properties [65].

Though the first-generation differentiation procedure yielded BMECs with passive barrier properties that remained below measurements in animals [9], the addition of retinoic acid (RA) during the differentiation process substantially improved the BBB phenotype, and RA-treated BMECs exhibited TEER reaching near *in vivo* levels after co-culture with other cell types of the neurovascular unit [67]. Unfortunately, full differentiation from the iPSC state to purified BMECs is a protracted multi-week process and uses complex, expensive maintenance and differentiation medium. The time and cost associated with iPSC culture and this differentiation method are detrimental to widespread use of these BMECs, and an expedited and less costly differentiation process yielding cells of equal performance with significantly less associated expense would alleviate some of these hurdles.

iPSC maintenance and differentiation procedures are rapidly evolving towards fully defined compositions [100–103]. In this study, we sought to adopt these procedures in an effort to streamline the BBB differentiation process. We transitioned to recently-described E8 medium for iPSC maintenance [101], as utilized by others for BBB differentiation [104], with no discernable issues. A derivative of E8 medium composition, collectively termed E6 medium (Dulbecco's modified Eagle's medium [DMEM]/F-12, ascorbic acid, sodium bicarbonate, selenium, human transferrin, and human insulin) has recently been used for efficient conversion of iPSCs to neuroectoderm [102], and we decided to explore its use in place of unconditioned medium (UM) in the BBB differentiation process. Intriguingly, we discovered that E6 medium, compared to UM, shortens the differentiation timeline without compromising BMEC performance as measured by TEER, sodium fluorescein permeability, and efflux transporter activity [65,67]. The E6 differentiation procedure was reproducible across several iPSC lines, and upon co-culture with iPSC-derived astrocytes and primary human brain pericytes, BMECs achieved maximum TEER

of 6,635 ± 315 Ω×cm2, which to our knowledge is the highest value ever recorded in any BBB model, and stability of the barrier above 1,000 Ω×cm2 was observed for 22 days. Overall, we have shortened the differentiation procedure to 8 days with no discernable loss of BBB character. Given that defined medias can be prepared in-house at greatly reduced costs, we suggest that the methods described herein will better enable widespread use of iPSC-derived BMECs.

2.3 Materials and methods

2.3.1 E4 medium preparation

E4 basal medium was prepared in 48 L batches and used to prepare E8 and E6 medium as described below. 48 L of DMEM/F12 with HEPES (Thermo Fisher Scientific, catalog number 11330057) was added to a large carboy along with 3.072 g L-Ascorbic acid 2-phosphate sesquimagnesium salt hydrate (Sigma-Aldrich), 931 μL of sodium selenite solution (0.7 mg/mL in PBS; Sigma-Aldrich), and 26.064 g sodium bicarbonate (Sigma-Aldrich). The solution was mixed for 20 min followed by alternating pH and osmolarity tests and adjustments. Osmolarity of the solution was adjusted to 340 ± 5 mOsm/kg using sodium chloride (Fisher Scientific) and tested using a Precision Systems Micro-OSMETTE Model 5004 osmometer. pH of the solution was adjusted to 7.4 ± 0.05 using 5M sodium hydroxide and measured using a Thermo Scientific Orion Star A211 benchtop pH meter. The solution was mixed for 10 minutes between each pH and osmolarity adjustment. Final E4 medium was frozen in 500 mL aliquots. Final concentrations in E4 basal medium were 64 mg/L L-Ascorbic acid 2-phosphate sesquimagnesium salt hydrate, 14 μg/L of sodium selenite, and 1743 mg/L sodium bicarbonate (20.75 mM) [101]. Detailed protocols for media preparation are available upon request.

2.3.2 E8 medium preparation

E8 medium was prepared by adding 100 μL of human insulin solution (Sigma-Aldrich), 500 μL of 10 mg/mL of human holo-transferrin (R&D Systems), 500 μL of 100 μg/mL human basic fibroblast growth factor (bFGF; Peprotech), and 500 μL of 2 μg/mL TGFβ1 (Peprotech) to 500 mL of E4. The final concentrations are 2.14 mg/L insulin, 100 μg/L bFGF, 2 μg/L TGFβ1, and 10.7 mg/L holo-transferrin [101]. Media was sterile filtered and stored at 4°C for a maximum of two weeks.

2.3.3 E6 medium preparation

E6 medium was prepared by adding 100 μL of human insulin solution and 500 μL of 10 mg/mL of human holo-transferrin to 500 mL of E4. The final concentrations are 2.14 mg/L insulin and 10.7 mg/L holo-transferrin [102]. The medium was sterile filtered and stored at 4°C for a maximum of two months.

2.3.4 Unconditioned medium (UM) preparation

Unconditioned medium (UM) was prepared as previously described [65]. UM consisted of DMEM/F12 (Thermo Fisher Scientific), 20% Knockout Serum Replacer (Thermo Fisher Scientific), 1× MEM non-essential amino acids (Thermo Fisher Scientific), 1 mM Glutamax (Thermo Fisher Scientific), and 0.1 mM β-mercaptoethanol (Sigma-Aldrich). UM was sterile filtered and stored at 4°C for a maximum of two weeks.

2.3.5 Endothelial cell (EC) medium preparation

Endothelial cell (EC) medium consisted of human Endothelial Serum-Free Medium (Thermo Fisher Scientific) supplemented with 1% platelet-poor plasma-derived bovine serum (Fisher Scientific) [105]. EC medium was supplemented with 20 ng/mL bFGF and 10 μM all-trans

retinoic acid (Sigma-Aldrich) during the EC phase prior to subculture and during the first 24 h of subculture, then removed to promote induction of the barrier phenotype [67]. EC medium was sterile filtered and stored at 4°C for a maximum of two weeks.

2.3.6 Maintenance of iPSCs

Cell lines used were IMR90-4 iPSCs [106], CD12 iPSCs [107], CC3 iPSCs [108], and SM14 iPSCs [109,110]. IMR90-4 and CC3 lines are female. CD12 and SM14 lines are male. All cell lines were thawed directly into E8 medium containing 10 μM Y-27632 (Tocris). 24 h after thaw, cells were changed to E8 medium without Y-27632. E8 medium was changed every day thereafter. All iPSCs were maintained on Matrigel (Corning). Once 70% confluent, iPSCs were passaged by washing cells once with Versene solution (Thermo Fisher Scientific), incubating cells with Versene solution for 5 minutes at 37°C, collecting the cells in fresh E8 medium, and distributing the cells at desired ratios to Matrigel-coated plates.

2.3.7 iPSC differentiation to BMECs

iPSCs were washed once with DPBS (Thermo Fisher Scientific) and incubated with Accutase (Stem Cell Technologies) for 3 min to yield a single cell suspension. Cells were collected via centrifugation, resuspended in E8, and counted using either a hemocytometer or Countess II (Thermo Fisher Scientific). Trypan blue was not used to measure cell viability when using a hemocytometer but was used when measuring cell density using the Countess II. Cells were seeded at densities ranging from 10,000–15,600 cells per square centimeter in E8 containing 10 μM Y-27632 (Day -1). Approximately 24 h after seeding, media was changed to UM or E6 medium (Day 0) to induce differentiation. Media was changed every 24 h. Cells were differentiated in UM for 6 days or in E6 medium for 4 days. Next, cells were treated with EC medium containing 20 ng/mL

bFGF and 10 μM retinoic acid for 48 h. Following treatment, EC medium was removed, and cells were washed once with DPBS and incubated with Accutase for 20 to 25 min [111]. Cells were collected via centrifugation and subsequently purified by selective adhesion onto a collagen-fibronectin matrix. In brief, tissue culture polystyrene plates and Transwell filters (polyethylene terephthalate, 0.4 μm pore size, 1.1 cm^2 surface area in 12-well format) were coated with a solution of 400 μg/mL collagen IV (Sigma-Aldrich) and 100 μg/mL fibronectin (Sigma-Aldrich) for a minimum of 1 h for plates and a minimum of 4 h up to overnight for Transwell filters. Cells were subcultured onto plates and filters at a ratio of 1 well of a 6-well plate of differentiated cells to 3 wells of a 12-well plate, 6 wells of a 24-well plate, or 3 Transwell filters. To assess barrier properties, TEER was measured 24 h after subculture using an EVOM2 voltohmeter with STX3 chopstick electrodes (World Precision Instruments). Following TEER measurement, cells were changed to EC medium containing no bFGF and no RA to induce barrier phenotype. No further media changes occurred after this point. TEER was measured approximately every 24 h thereafter. Experiments were terminated when average TEER fell below 1,000 $\Omega \times cm^2$. All reported TEER values are corrected for the resistance due to an empty Transwell filter.

2.3.8 Immunocytochemistry

Cells were washed twice with DPBS and fixed for either 20 min in 4% paraformaldehyde (Sigma-Aldrich) or 10 min in 100% ice-cold methanol. Cells were washed 3 times with DPBS and blocked for a minimum of 1 h in PBS or TBS containing 5% donkey serum and 0.3% Triton X-100 (PBS-DT and TBS-DT, respectively). Cells were incubated with primary antibody diluted in PBS or TBS containing 5% donkey serum (PBSD and TBSD, respectively) or in PBS-DT or TBS-DT overnight at 4°C. Following primary antibody incubation (Table A.2.1), cells were rinsed once with PBS or TBS and washed five times with PBS or TBS for a minimum of five minutes per

wash. Cells were incubated in secondary antibody (Table A.2.2) diluted in the same buffer as primary antibody for a minimum of 1 h. Following secondary antibody incubation, cells were incubated with 4′,6-Diamidino-2-pheny-lindoldihydrochloride (DAPI; Thermo Fisher Scientific) for 10 min to label nuclei. Cells were rinsed once and washed five times with PBS/TBS and then visualized using a Zeiss AxioObserver Z1 microscope or a Leica DMi8 microscope. An average of three images were taken for each stain and the entire field was visually assessed to ensure that the presented images are representative of the entire dish.

2.3.9 Efflux transporter activity assay: substrate accumulation

iPSC-derived BMECs were purified into 24-well plates and subjected to EC medium lacking bFGF and RA for 24 h prior to efflux assays. For inhibition experiments, BMECs were incubated with 10 μM PSC833 (Sigma-Aldrich) or 10 μM MK-571 (Sigma-Aldrich) for 1 h at 37°C. Following this incubation, BMECs were incubated with 10 μM rhodamine 123 (Sigma-Aldrich; 488 nm excitation and 540 nm emission) or 10 μM 2',7'-dichlorodihydrofluorescein diacetate (H_2DCFDA, ThermoFisher, 492 nm excitation and 527 nm emission), with or without their respective inhibitors, for 1 h at 37°C. Cells were washed three times with DPBS and subsequently lysed using DPBS with 5% Triton X-100 to measure dye accumulation in the cells. Fluorescence was measured on a BioTek Synergy H1 multi-mode microplate reader. For each condition, one well of cells was not lysed. These conserved wells were fixed for 10 min in 100% ice-cold methanol and incubated with DAPI for 10 min. Cells were washed three times with DPBS and imaged. 6 images per condition were taken, and nuclei count per culture area was found using CellProfiler analysis software [112]. Fluorescence is reported on a per-cell basis, normalized to control fluorescence from cells treated with fluorescent substrate but no inhibitor.

2.3.10 Efflux transporter activity assay: aplical-to-basolateral flux

iPSC-derived BMECs were purified onto Transwell filters and subjected to EC medium lacking bFGF and RA for 24 h prior to assays. For inhibition experiments, BMECs were incubated with 10 μM PSC833 or 10 μM MK-571 for 1 h at 37°C. Inhibitor was only included in the apical chamber. Following this incubation, 10 μM rhodamine 123 or 10 μM H_2DCFDA was added to the apical chamber, with or without respective inhibitors, for 1 h at 37°C. 200 μL of media was then removed from the basolateral chamber and fluorescence was measured on a BioTek Synergy H1 multi-mode microplate reader.

2.3.11 Sodium fluorescein permeability

iPSC-derived BMECs were purified onto Transwell filters and subjected to EC medium lacking bFGF and RA for 24 h prior to permeability measurements. Medium was aspirated from the apical and basolateral chambers of each filter and replaced with fresh medium of the same composition to allow for monolayer equilibration. After 1 h, medium from the apical chamber was aspirated and replaced with 0.5 mL of sodium fluorescein (10 μM, Sigma-Aldrich) diluted in fresh medium. Every 30 min, 200 μL of medium was removed from the basolateral chamber and replaced with 200 μL of fresh medium. The same experiment was conducted on an empty filter. After 2 h, fluorescence was measured on a BioTek Synergy H1 multi-mode microplate reader. The rate of accumulation, corrected for media removal and flux across the empty filter, was used to calculate Pe values.

2.3.12 Primary human pericyte culture

Primary human brain vascular pericytes were purchased from ScienCell Research Laboratories. Pericytes were cultured on plates coated with 0.1% gelatin (Sigma-Aldrich) and maintained in DMEM (Corning) supplemented with 10% fetal bovine serum (Thermo Fisher

Scientific). Medium was changed every three days, and cells were passaged for maintenance when approximately 80% confluent. Pericytes (passage 15) were subcultured onto Matrigel-coated 12-well plates for co-culture experiments when approximately 40% confluent at a ratio of 1 well of a 6-well plate to 3 wells of a 12-well plate. Once co-cultured with iPSC-derived glia, pericytes were maintained in E6 medium with 10 ng/mL CNTF and 10 ng/mL EGF. Pericyte co-culture with BMECs (with or without astrocytes and glial progenitors) was initiated 24 h after BMEC seeding onto Transwell filters. At this time, pericytes were changed to EC medium lacking bFGF and RA. Medium was not changed for the duration of the experiment.

2.3.13 iPSC differentiation to astrocytes

IMR90-4 iPSCs were washed with 2 mL DPBS and incubated with Accutase for 3 min at 37°C. Cells were collected via centrifugation, resuspended in E8 medium, and counted using a hemocytometer. Cells were seeded at $2\times10_5$ cells/cm_2 onto Matrigel-coated plates in E8 medium containing 10 μM Y-27632. 24 h after seeding, media was changed to E6 medium containing 10 μM SB431542 (Tocris) and 1 μM dorsomorphin dihydrochloride (Tocris). The medium was changed every 24 h for 6 days. On day 6 of differentiation, strips of cells were mechanically picked from the culture using a P200 pipette and transferred to a Matrigel-coated plate with E6 medium containing 10 ng/mL ciliary neurotrophic factor (CNTF; Peprotech), 10 ng/mL epidermal growth factor (EGF; Peprotech), and 10 μM Y-27632. 72 h after picking, media was changed to E6 medium containing 10 ng/mL CNTF and 10 ng/mL EGF but no Y-27632. The medium was changed every three days for 30 days. On day 30, cells were incubated with Accutase for 3 min, collected via centrifugation, and seeded at a ratio of 1 well of a 6-well plate to 1 full 6-well plate. Cells were maintained in E6 medium containing 10 ng/mL CNTF and 10 ng/mL EGF with media changes every 48 h. Cells were passaged when approximately 80% confluent. Cells were cultured

through a second passage and frozen in liquid nitrogen in E6 medium containing 10% DMSO (Sigma-Aldrich). Frozen iPSC-derived astrocytes were thawed and cultured for two passages before being seeded for co-culture. Astrocytes were seeded for co-culture at a ratio of 1 well of a 6-well plate to 6 wells of a 12-well plate. Cells were maintained in E6 medium containing 10 ng/mL CNTF and 10 ng/mL EGF when in co-culture with pericytes but were switched to EC medium lacking bFGF and RA upon co-culture with BMECs.

2.3.14 Initiation of co-culture

To initiate co-culture with astrocytes and pericytes, BMECs were subcultured onto Transwell filters as described above. 24 h after subculture, TEER was measured. Transwell filters were then transferred to wells containing astrocytes, pericytes, or astrocytes and pericytes, and medium was changed to EC medium lacking bFGF and RA. BMECs in monoculture served as a control for the experiment. TEER was measured approximately every 24 h. Medium was not changed throughout the duration of the experiment.

2.3.15 Statistical analysis

Data were expressed as mean ± standard deviation. Two-way ANOVA analysis and Student's unpaired t test were used to determine statistical significance for efflux transporter activity assays and TEER values.

2.4 Results and discussion

Previous protocols to differentiate iPSCs to BMECs relied on seeding iPSCs at defined densities, expanding the cells in mTeSR media for 3 days [100], and differentiating the cells for 6 days in UM to immature BMECs [65,67,111,113]. BMECs were expanded in EC medium supplemented with basic fibroblast growth factor (bFGF) and RA and purified onto

collagen/fibronectin matrices. Barrier phenotype was then induced by changing to EC medium lacking both bFGF and RA. Peak barrier phenotypes were observed 24 h after this medium change, and it was at this time point that most assays to measure barrier fidelity were conducted. In total, these methods required a minimum of 13 days from time of iPSC seeding to achieving functional, purified BMECs. We sought to improve these established methods in several ways. First, in place of mTeSR, we utilized E8 medium for maintenance [101], as described by others [104]. Next, we removed the 3 day expansion phase prior to differentiation and instead seeded IMR90-4 iPSCs overnight as single cells at densities ranging from 10,000-15,600 cells per square centimeter in E8 medium supplemented with Y-27632 before initiating differentiation the following day, a technique that has been utilized in other differentiation protocols [102]. Finally, we explored the use of E6 medium in place of UM during the differentiation process (Figure 2.1).

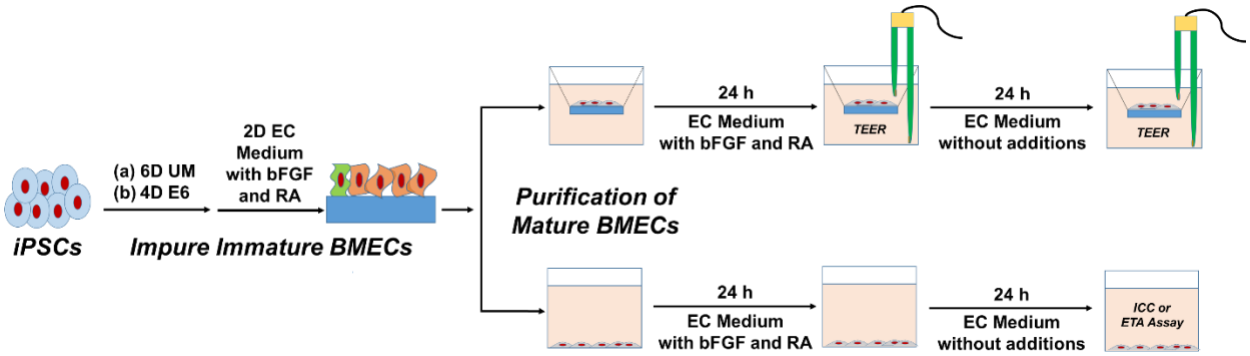

Figure 2.1 Differentiation of iPSCs to BMECs. iPSCs were seeded at defined densities and differentiated for either 6 days in unconditioned medium (UM) or for 4 days in defined E6 medium. Impure immature BMECs were subsequently treated for 2 days with endothelial cell (EC) medium supplemented with bFGF and retinoic acid (RA). Mature BMECs were purified onto Transwell filters or plates for 24 h in EC medium supplemented with bFGF and RA. 24 h after purification, barrier was induced by treating cells with EC medium lacking bFGF and RA.

With E6 medium, we were surprised to observe large patches of PECAM-1+ endothelial cells after only 4 days of differentiation, which contrasts the time point when endothelium is first

observed during UM differentiation (Figure 2.2a) [65]. After 48 h in EC medium containing bFGF and RA, expression of PECAM-1, GLUT-1, VE-cadherin, and occludin were observed, indicating acquisition of a BBB phenotype (Figure 2.2b). Cells were then purified onto Transwell filters or polystyrene culture plates using updated passaging techniques described by Wilson et al [111]. Barrier phenotype was evaluated every 24 h by TEER, while immunocytochemistry was used to evaluate expression of endothelial and BBB markers 48 h after barrier induction. Immunocytochemical analysis of E6-derived BMECs showed robust expression of GLUT-1, claudin-5, occludin, VE-cadherin, and PECAM-1 (Figure 2.2c), similar to UM-derived BMECs [65,67]. E6-derived BMECs exhibited a maximum barrier of 4,678 ± 49 $\Omega \times cm^2$, and a minimum barrier stability of 1,000 $\Omega \times cm^2$ was observed over 12 days for three independent biological replicates (Figure 2.3a). For comparison, UM-derived BMECs exhibited maximum TEER of 3,980 ± 151 $\Omega \times cm^2$ 24 h after barrier induction, a value comparable to previously published results [67], and maintained stability for a similar timeframe as E6-derived BMECs (Figure 2.3b).

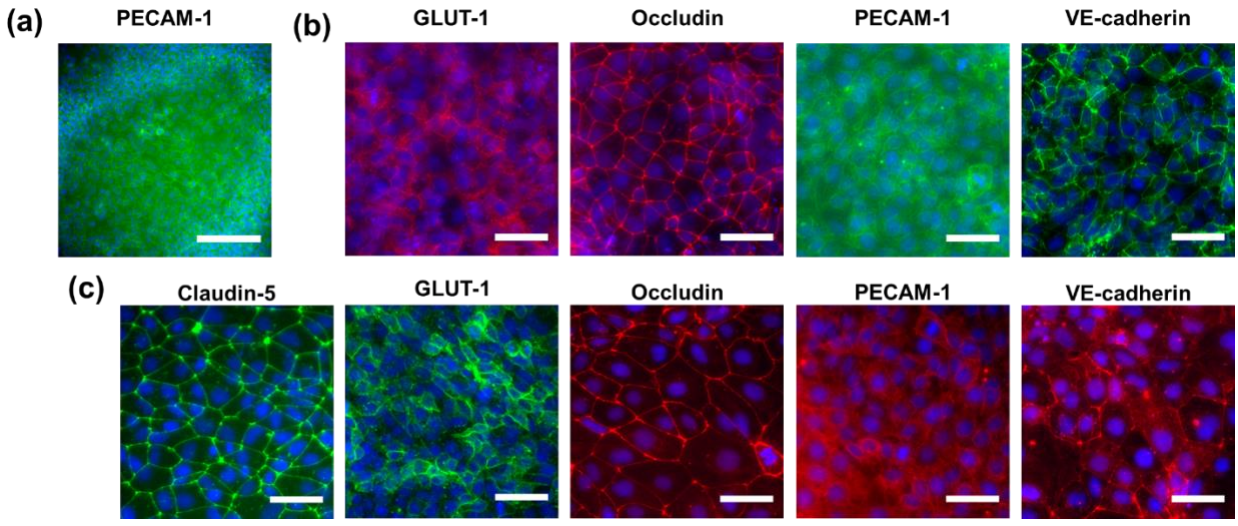

Figure 2.2 Immunocytochemical analysis of BBB markers before and after purification. (a) Immunocytochemical detection of PECAM-1 after 4 D E6 medium. Scale bar is 200 μm. (b) Immunocytochemical detection of GLUT-1, occludin, PECAM-1, and VE-cadherin after 4 D E6 medium and 2 D EC medium supplemented with bFGF and RA. All scale bars are 50 μm. (c)

Immunocytochemical detection of claudin-5, GLUT-1, occludin, PECAM-1, and VE-cadherin following purification and induction of barrier phenotype. All scale bars are 50 μm.

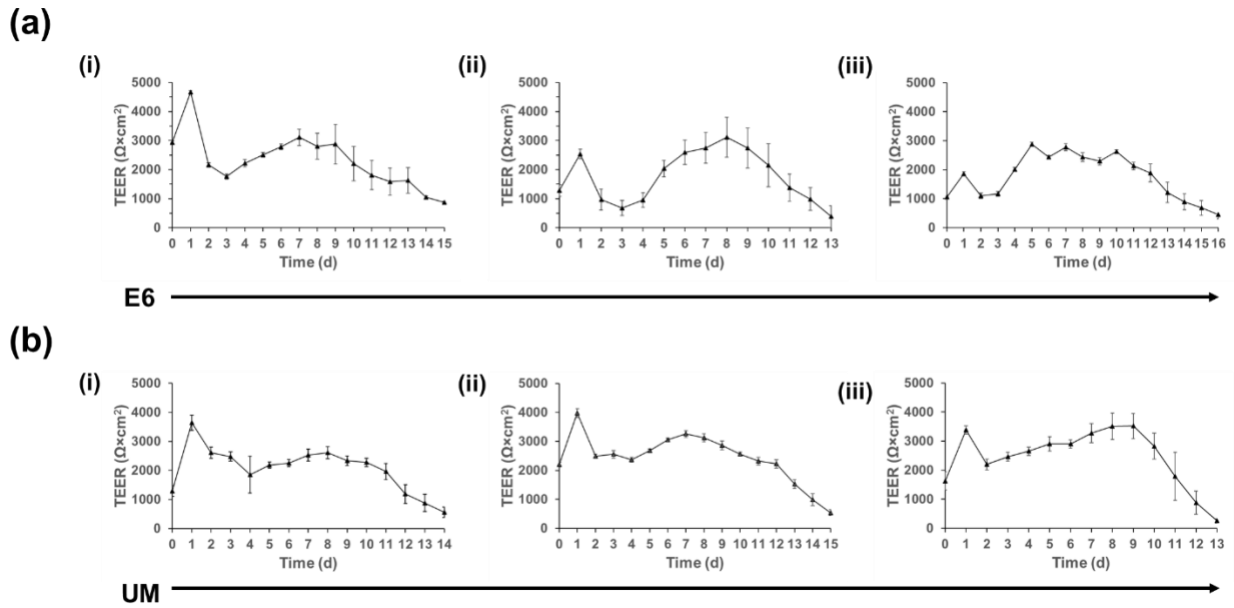

Figure 2.3 BMECs differentiated using UM and E6 medium demonstrate equivalent maximum TEER and stability. For each medium, three filters were seeded with BMECs, and TEER was measured in three different positions for each filter. Each plot is the result of one biological replicate (n=1) with each daily TEER measurement the result of a technical n=9. Values are reported as mean ± standard deviation of these collective measurements. (a) BMECs differentiated using E6 medium demonstrated maximum TEER values of at least 2,500 Ω×cm2 for a minimum of 11 days in three biological replicates (i-iii). TEER was measured approximately every 24 h for the duration of the experiment. (b) BMECs differentiated using UM demonstrated maximum TEER values of at least 2,500 Ω×cm2 for a minimum of 12 days in three biological replicates (i-iii). TEER was measured approximately every 24 h for the duration of the experiment.

E6-derived BMECs were next evaluated for efflux transporter activity (ETA) and compared to UM-derived BMECs. Purified BMECs were incubated with rhodamine 123, a fluorescent substrate for P-glycoprotein, in the presence and absence of P-glycoprotein inhibitor PSC833. Fluorescence accumulation increased in the presence of PSC833 for both E6-derived BMECs (154 ± 5%) and UM-derived BMECs (151 ± 14%), which indicates inhibition of P-

glycoprotein (Figure 2.4). Purified BMECs were also incubated with H_2DCFDA, a fluorescent MRP family substrate, in the presence and absence of MK-571, an MRP family inhibitor. Fluorescence accumulation increased in the presence of MK-571 for both E6-derived BMECs (267 ± 19%) and UM-derived BMECs (249 ± 31%), which indicates inhibition of MRP efflux transporters (Figure 2.4). Differences in efflux transporter activity for the two sets of BMECs were statistically insignificant for both P-glycoprotein and the MRP family, suggesting that the change in differentiation medium did not have an effect on the efflux transporter activity of BMECs. Overall, these results indicate that using E6 medium to differentiate iPSCs to BMECs, in conjunction with updated seeding methods, reduces differentiation time and yields equivalent functionality as compared to established UM-based differentiation protocols.

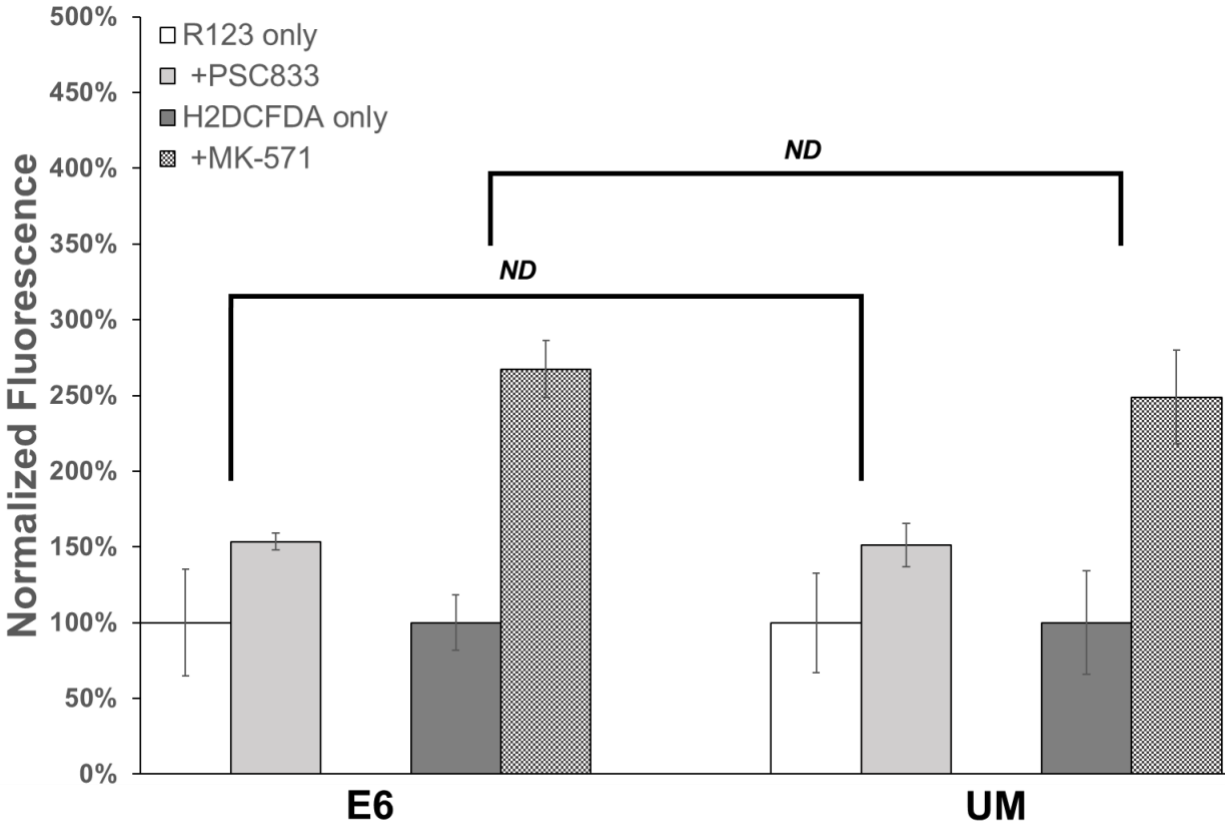

Figure 2.4 E6-derived BMECs and UM-derived BMECs demonstrate equivalent efflux transporter activity. E6-derived BMECs and UM-derived BMECs were incubated with rhodamine 123 (R123) or H2DCFDA in the presence and absence of efflux transporter inhibitors, PSC833 and MK-571, respectively. Fluorescence accumulation within cells incubated with fluorescent substrate in the presence of the desired inhibitor was normalized to fluorescence accumulation in cells incubated with substrate but with no inhibitor. Each condition was performed using triplicate wells, and cell count per condition was calculated as an average from 6 images taken from 1 additional well for each condition. All fluorescence values are normalized on per-cell basis and reported as normalized mean fluorescence ± standard deviation. Two-way ANOVA analysis indicates no statistical difference ($p > 0.05$) in fluorescence accumulation between E6-derived BMECs and UM-derived BMECs. All substrate and inhibitor conditions were repeated in an additional independent differentiation per medium to confirm reported trends.

After demonstrating the successful use of E6 medium to differentiate IMR90-4 iPSCs to BMECs, we sought to confirm the utility of this medium in other iPSC lines. Control iPSC lines CD12 and CC3 as well as iPSC line SM14, from a preclinical PD patient carrying compound heterozygous loss-of-function mutations in *PARK2* associated with familial early-onset PD [108–

110], were differentiated to BMECs using E6 medium (Figure 2.1). TEER measurements were used to assess barrier fidelity in three independent biological replicates for each line, and TEER exceeding 1,000 $\Omega \times cm^2$ was measured for a minimum of 8 days, with 5 out of 6 lines exhibiting stability above 1,000 $\Omega \times cm^2$ for at least 11 days (Figure 2.5a-CD12, 2.5b-CC3, 2.5c-SM14). This barrier stability was comparable to results achieved in IMR90-4-derived BMECs differentiated in both E6 and UM. Notably, CD12-derived BMECs achieved TEER in excess of 4,000 $\Omega \times cm^2$ 10 days after purification, a maximum value that was also comparable to IMR90-4-derived BMECs.

Next, we sought to validate efflux transporter activity in these lines by conducting directional flux inhibition measurements. When treated with PSC833 and MK-571, CC3- and CD12-derived BMECs exhibited increased transport of corresponding substrate across the monolayer (Figure 2.5d). SM14-derived BMECs, however, showed increased substrate transport across the barrier upon treatment with MK-571 but not PSC833, possibly indicating diminished P-glycoprotein function or polarization. Paracellular permeability of fluorescein (P_e) was less than 1.95×10^{-7} cm/s for all lines, further confirming the passive barrier properties observed by TEER (Figure 2.5e). These P_e measurements align with previously published values of BMECs derived using UM [104,111].

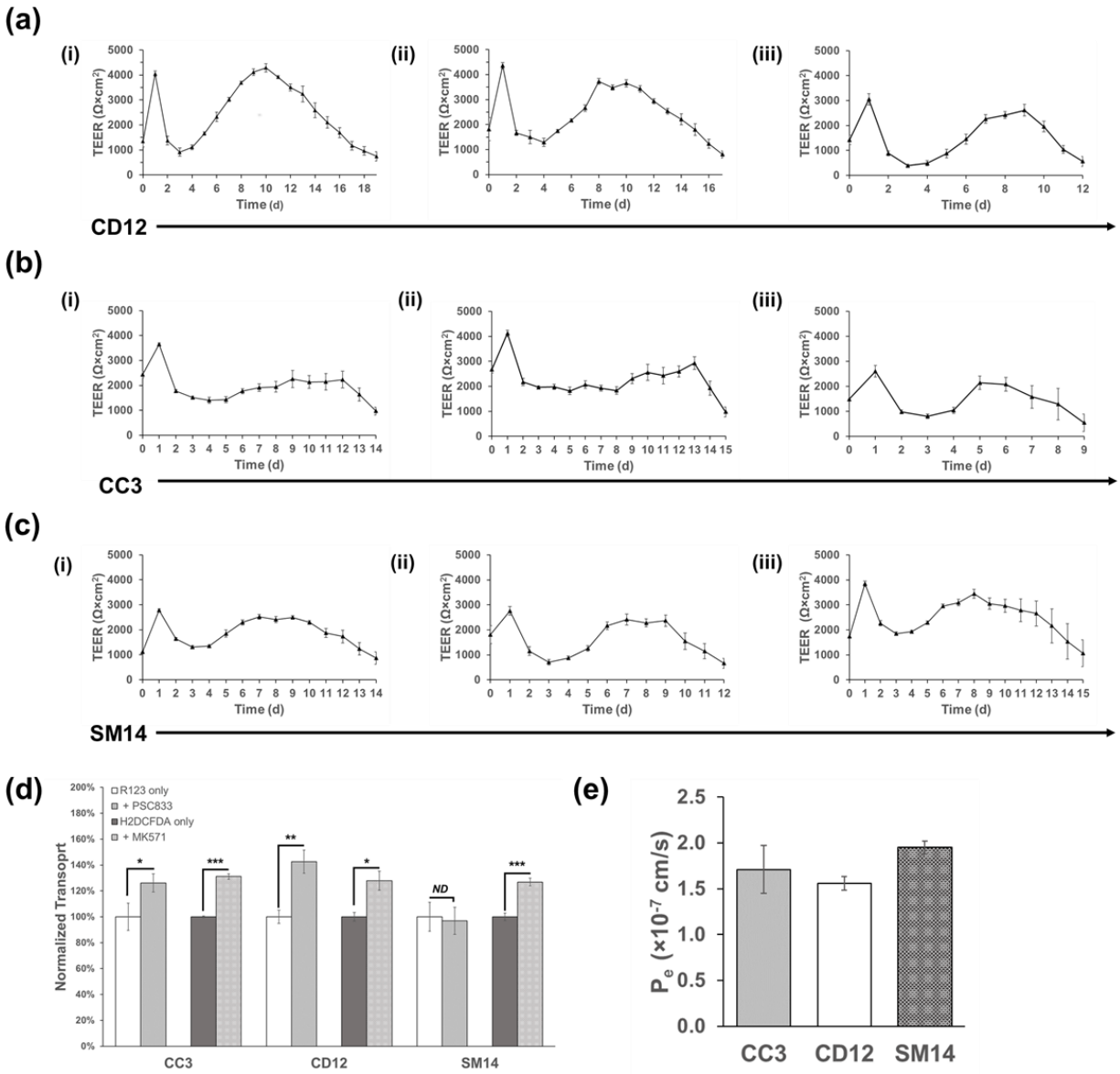

Figure 2.5 BMEC differentiation using E6 medium translates to additional iPSC lines. iPSC lines CD12, CC3, and SM14 were differentiated to BMECs with E6 medium as described in Figure 1, and TEER was measured approximately every 24 h. For each differentiation, three filters were seeded with BMECs, and each filter was measured at three locations on the filter. Each plot is the result of one biological replicate (n=1) with each daily TEER measurement the result of a technical n=9. All values are mean ± standard deviation of these nine total measurements per condition. (a) CD12-derived BMECs achieved maximum TEER values exceeding 4,000 Ω×cm2 and maintained TEER above 1,000 Ω×cm2 for a minimum of 11 days in 3 independent biological replicates. (b) CC3-derived BMECs achieved maximum TEER values exceeding 3,500 Ω×cm2 and maintained TEER above 1,000 Ω×cm2 for a minimum of 8 days in 3 independent biological replicates. (c) SM14-derived BMECs achieved maximum TEER values exceeding 2,500 Ω×cm2 and maintained TEER above 1,000 Ω×cm2 for a minimum of 11 days in 3 independent biological replicates. (d) Apical-to-basolateral flux of rhodamine 123 (R123) and H2DCFDA was measured across BMECs in the presence or absence of PSC833 and MK-571, respectively. Fluorescence was normalized to

cells not treated with inhibitor and reported as normalized mean fluorescence ± standard deviation. Each condition was performed using triplicate filters and statistics were calculated using a technical n of 3. Statistical significance was determined using the Student's unpaired t test (*, $p<0.1$; **, $p<0.05$; ***, $p<0.01$). Data from one biological experiment are shown, and an additional biological replicate was performed for each line to verify the observed trends. (e) The permeability of sodium fluorescein was measured across BMECs. Each experiment was performed using triplicate filters and data are presented as mean ± standard deviation. Biological duplicates were used to verify each measurement. The effective permeability (Pe) was calculated at less than 1.95×10-7 cm/s for all lines.

iPSC-derived BMECs have previously been shown to gain an elevated barrier phenotype when co-cultured with astrocytes and pericytes [67]. In order to evaluate if BMECs differentiated in E6 medium responded to such cues in a similar manner, iPSCs were differentiated to a mix of astrocytes and glial progenitors [102]. Co-culture of this cell population (49% ± 8% $GFAP^+$, see Additional File 1, Figure S1) with CD12-derived BMECs was initiated 24 h after subculture onto Transwell filters, and co-culture was maintained in EC medium lacking bFGF and RA. Co-cultured cells were seeded in the bottom of the well plates; therefore, no direct contact occurred between BMECs and co-cultured cell types. As such, all observed differences are the result of soluble factors released in the system. Compared to BMECs in monoculture, BMECs in co-culture with glia reached both a higher absolute maximum TEER (5,378 ± 479 $\Omega\times cm^2$ versus 4,227 ± 370 $\Omega\times cm^2$, $p < 10^{-4}$) and maintained TEER above 1,000 $\Omega\times cm^2$ in excess of 22 days (Figure 2.6a). BMECs were also co-cultured with primary human brain pericytes (Figure A. 2.1) and achieved a maximum TEER of 5,937 ± 157 $\Omega\times cm^2$ ($p < 10^{-6}$ versus monoculture) with a stable barrier phenotype above 1,000 $\Omega\times cm^2$ for longer than 22 days (Figure 2.6a). BMECs co-cultured with both astrocytes and pericytes (35% ± 13% astrocytes, 63% ± 13% pericytes, Figure S1), achieved the highest maximum TEER of 6,635 ± 315 $\Omega\times cm^2$ ($p < 10^{-9}$ versus monoculture, $p < 10^{-4}$ versus astrocyte co-culture, $p < 10^{-3}$ versus pericyte co-culture) and maintained TEER exceeding 1,000

Ω×cm2 in excess of 22 days. These inductive effects were further verified through co-culture of CC3-derived BMECs with astrocytes and pericytes. A similar statistically significant increase in TEER was observed in co-cultured BMECs versus control BMECs, further validating the responsive nature of E6-derived BMECs to soluble cues from astrocytes and pericytes (Figure 2.6b). Co-cultured and control BMECs grown on Transwell filters were stained for claudin-5 and occludin, and no significant phenotypic change was evident between monocultured BMECs on filters, BMECs in co-culture with astrocytes and pericytes, or BMECs grown in well plates (Figure 2.2). Thus, the barrier-promoting effects of co-culture with astrocytes and pericytes exceeds effects of the two cell types alone, as expected from previous reports [67]. We note that media was not changed after day 0 to ascertain stability without any external stimulation, and we suspect that partial media exchanges could extend stability further. At present, we are also unsure why the TEER drops precipitously after day 1 and rebounds over the course of a week. We hypothesize this effect may be due to complete removal of bFGF, which is worthy of future exploration.

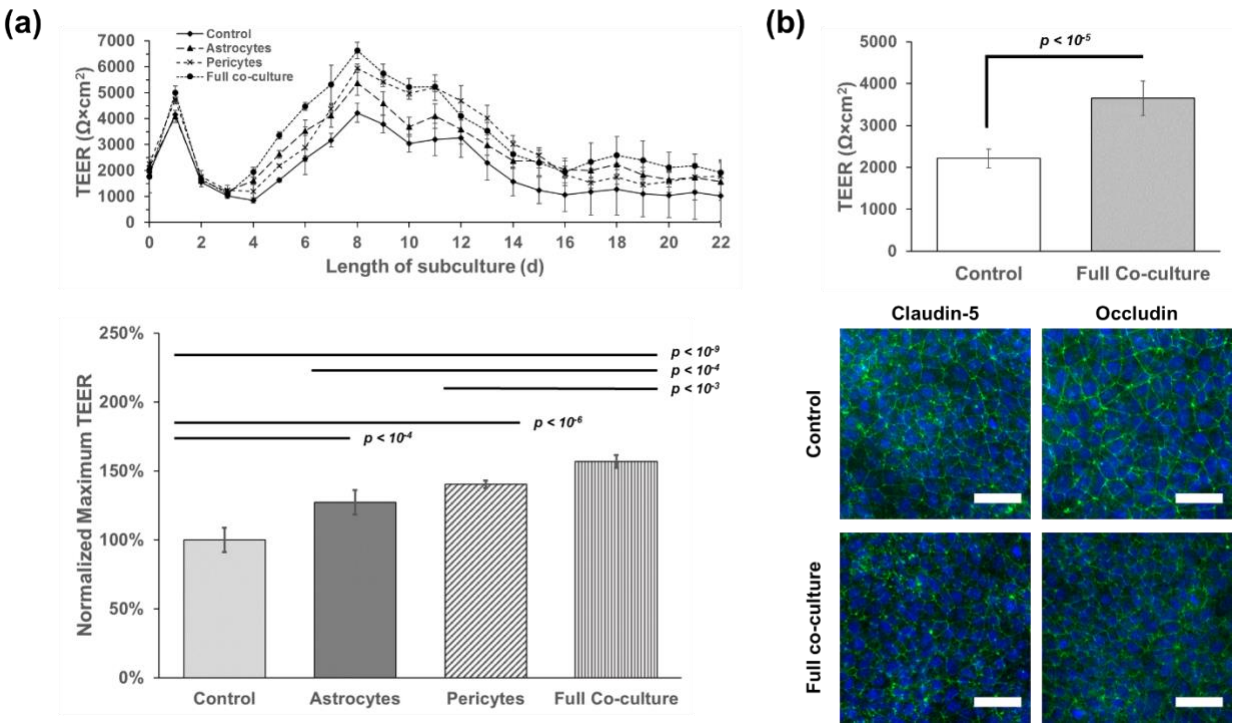

Figure 2.6 E6-derived BMECs respond to inductive cues from astrocytes and pericytes. (a) Co-culture of CD12-derived BMECs with astrocytes, pericytes, and a mixture of astrocytes and pericytes achieved maximum TEER values exceeding 4,000 Ω×cm2 and maintained TEER above 1,000 Ω×cm2 for a minimum of 22 days under all co-culture conditions. Each condition was conducted on triplicate filters with all BMECs purified from a single differentiation. Each filter was measured at three different locations on the filter each day. Values are mean ± standard deviation from these collective nine technical replicates per condition per day. Maximum TEER values achieved on day 8 of subculture were normalized to the TEER of the monoculture control. Statistical significance was calculated using Student's unpaired t test. (b) CC3-derived BMECs were co-cultured with a mixture of astrocytes and pericytes, achieving a significant increase in TEER 24 h after barrier induction ($p<10^{-5}$, Student's unpaired t-test). Each condition was conducted on triplicate filters with all BMECs purified from a single differentiation. Each filter was measured at three different locations on the filter each day. Values are mean ± standard deviation from these collective nine technical replicates per condition per day. BMECs were subsequently stained for occludin and claudin-5 in both control and co-culture conditions. Scale bars are 50 μm.

Protocols to differentiate iPSCs to BMECs for *in vitro* BBB modeling have not necessarily achieved widespread adoption, potentially due in part to the time required to produce purified BMECs and the cost associated with such differentiation and purification. The purpose of this study was to decrease both the time and cost required for such differentiation while still achieving

BMECs of comparable performance to established differentiation methods. These advancements will potentially allow iPSC-derived BMECs to be more readily accessible to researchers, thereby providing high-fidelity human *in vitro* BBB models for a wide range of applications.

In this study, existing BMEC differentiation protocols were modified to exclude the iPSC expansion phase prior to initiation of differentiation [65,67,111]. By controlling initial iPSC seeding density [111], maximum TEER values of purified BMECs from such differentiations remained consistently in excess of 2,500 $\Omega \times cm^2$, and barrier fidelity, as indicated by TEER above 1,000 $\Omega \times cm^2$, was maintained for a minimum of 8 days, as was similarly achieved in a recent microfluidics-based model using UM-derived BMECs [114]. E8 medium was also used for iPSC maintenance in place of mTeSR, as described by others [104]. Given that we routinely use E6 medium (a derivative of E8 medium that lacks growth factors promoting pluripotency) for neural differentiations [102], we further explored its use for differentiating iPSCs to BMECs. Upon differentiation in E6 medium, immunocytochemical analysis unexpectedly showed PECAM-1$^+$ cells at 4 days of differentiation rather than 6 days. We note that changes in culture methods and differentiation medium have previously been shown to alter differentiation times to lineages such as neuroectoderm [102,115,116] and midbrain dopaminergic neurons [115,117], with all methods ultimately resulting in cells expressing the same characteristic markers. Therefore, it is unsurprising that changes made in differentiation medium resulted in altered differentiation timelines. After establishing this accelerated differentiation timeline from iPSCs to BMECs using E6 medium, BMECs were evaluated for BBB phenotype by TEER measurement and efflux transporter activity. BMECs differentiated in E6 medium maintained a stable barrier above 1,000 $\Omega \times cm^2$ for 8 days, longer than previously published reports using similar Transwell-based methods [67,111] , while achieving similar maximum TEER values to UM-derived BMECs. BMECs

differentiated using E6 medium and UM also had no statistical difference in efflux transporter activity for P-glycoprotein and MRP family members. BMEC differentiation using E6 medium was further validated in iPSC lines CD12, CC3, and SM14. CD12- and CC3-derived BMECs demonstrated equivalent maximum TEER and long-term stability as IMR90-4-derived BMECs differentiated in both E6 medium and UM. Notably, CD12-derived BMECs achieved TEER greater than 4,000 $\Omega \times cm^2$ on days 9 and 10 of subculture, a value equivalent to the maximum TEER achieved after initial induction of BMEC phenotype. Finally, SM14 iPSCs, which harbor biallelic loss-of-function *PARK2* mutations associated with familial early onset PD, yielded BMECs with maximum TEER and long-term stability equivalent to BMECs derived from control lines, similar fluorescein permeability, and equivalent MRP family efflux transporter activity. Interestingly, SM14-derived BMECs did not show active P-glycoprotein in the apical-to-basolateral transport assays. Studies on advanced PD patients have demonstrated increased brain uptake of P-glycoprotein substrates [45]. Our data may indicate that patients with familial PD mutations are predisposed to loss of P-glycoprotein function. However, our results are very preliminary and would need to be rigorously confirmed across multiple iPSC lines from different patients harboring the same mutation. As this manuscript is centered on the utility of E6 medium for *in vitro* differentiation, we have not pursued these studies herein. Even so, this exciting result indicates researchers can probe mechanisms of BBB regulation in the context of genetic disease or evaluate molecular transport and toxicology over extended experimental time points. Our methods can ostensibly be extended to other iPSC disease lines of interest, provided that the genetic mutation does not impact barrier stability.

To further explore the utility of the model, we investigated the effect of co-culturing BMECs with iPSC-derived astrocytes and primary human brain pericytes. Astrocytes and

pericytes are known to aid in induction of BBB phenotype in the developing neurovascular environment [8]. Though co-culture of BMECs with astrocytes and co-culture of BMECs with pericytes individually were both found to increase barrier function as indicated by TEER, co-culture with astrocytes and pericytes concurrently enhanced the TEER above that achieved through co-culture with either cell type alone. This effect has been noted in other *in vitro* BBB models, though the reported maximum TEER value from co-culture in this study exceeds previously published *in vitro* TEER values by more than 700 $\Omega \times cm^2$ [67]. Excitingly, this achievement approaches *in vivo* TEER predictions of 8,000 $\Omega \times cm^2$ put forth by Smith and Rapoport [118]. In addition, medium was not changed following barrier induction to minimize external influences on barrier stability. Due to prospective increased metabolic burden in the co-culture system as evidenced by a qualitative decrease in number of co-cultured cells between the start and end of the experiment, we suspect that gradual media changes following barrier induction may further improve the stability of the model by supporting neurovascular health. Owing to the extended barrier phenotype observed, researchers may now conduct long-term experiments without concern that barrier degradation may confound results.

2.5 Conclusion

The differentiation of iPSCs to BMECs using defined E6 medium shortened differentiation time and produced BMECs of equivalent performance as BMECs differentiated according to previously published protocols using UM. Stability of the model system has also been greatly improved, with monocultured BMECs exhibiting enhanced stability for greater than 8 days and co-cultured BMECs exhibiting stability of more than three weeks. We routinely produce E6 and E8 medium in-house in large batches (see Methods), thus substantially reducing the cost of

maintenance and differentiation to allow increased throughput of experiments. Thus, the overall improvements described in this manuscript will enable iPSC-derived BMECs to become more accessible to researchers and more broadly enable studies ranging from disease pathogenesis to analyses of repeated drug dosing.

2.6 Appendix

Table A. 2.1 Primary antibodies used in immunocytochemistry experiments

Target Antigen	Antibody Species	Vendor	Clone or product number	Dilution
PECAM-1	Rabbit	Thermo Fisher Scientific	RB-10333-P	1:25
Claudin-5	Mouse	Thermo Fisher Scientific	4C3C2	1:50
Occludin	Mouse	Thermo Fisher Scientific	OC-3F10	1:100
VE-Cadherin	Goat	R&D Systems	AF938	1:100
GLUT-1	Mouse	Thermo Fisher Scientific	SPM498	1:50
Glial fibrillary acidic protein (GFAP)	Rabbit	Dako	Z0334	1:500
Platelet-derived growth factor β (PDGFRβ)	Rabbit	Santa Cruz Biotechnology	sc-432	1:100
NG2	Mouse	Santa Cruz Biotechnology	sc-53389	1:50
SMA	Mouse	Santa Cruz Biotechnology	sc-130616	1:100

Table A. 2.2 Secondary antibodies used in immunocytochemistry experiments

Species Reactivity	Host	Conjugate	Vendor	Dilution
Rabbit	Donkey	Alexa Fluor 488	Thermo Fisher Scientific	1:200
Rabbit	Donkey	Texas Red	Thermo Fisher Scientific	1:200
Mouse	Donkey	Alexa Fluor 488	Thermo Fisher Scientific	1:200
Mouse	Donkey	Texas Red	Thermo Fisher Scientific	1:200
Goat	Donkey	Alexa Fluor 488	Thermo Fisher Scientific	1:200
Goat	Donkey	Texas Red	Thermo Fisher Scientific	1:200

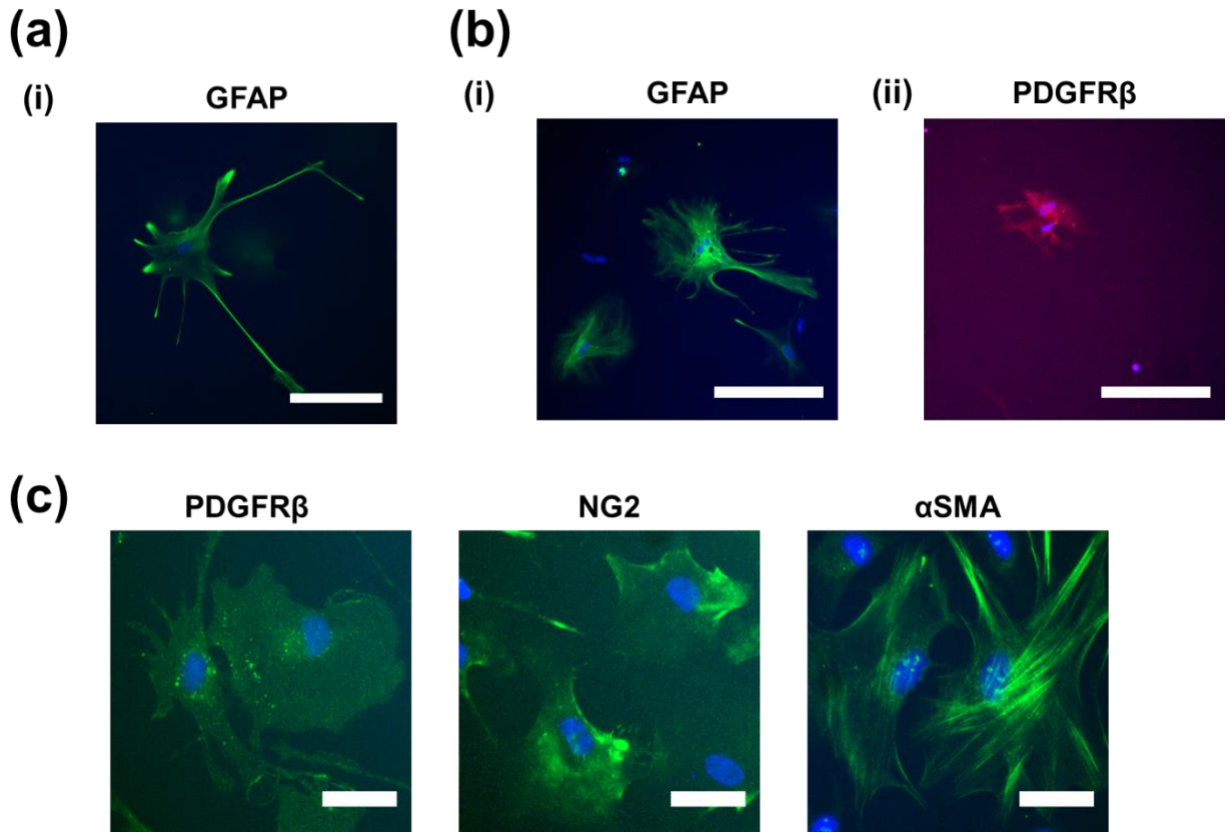

Figure A. 2.1 Characterization of astrocytes and pericytes in coculture with iPSC-derived BMECs. (a) IMR90-4 iPSC-derived astrocytes were fixed upon termination of the coculture experiment, and the impure populations were stained for (i) GFAP. (b) IMR90-4 iPSC-derived impure astrocytes and primary brain pericytes were fixed upon termination of the coculture experiment. Astrocytes were stained for (i) GFAP, and pericytes were stained for (ii) PDGFRβ. Percentage of GFAP+ and PDGFRβ+ cells in (a) and (b) was determined by normalizing GFAP+ and PDGFRβ+ positive cells to total nuclei count in 6 frames per stain imaged, and scale bars 200 μm. (c) Primary brain pericytes, absent co-culture with BMECs, were stained for PDGFRβ, NG2, and αSMA at passage 15 to verify identity. Scale bars are 50 μm.

Chapter 3

IPSC-DERIVED BRAIN ENDOTHELIUM EXHIBITS STABLE, LONG-TERM BARRIER FUNCTION IN PERFUSED HYDROGEL SCAFFOLDS

Adopted from: Faley SL*, Neal EH*, Wang JX, Bosworth AM, Weber CM, Balotin KM, et al. iPSC-Derived Brain Endothelium Exhibits Stable, Long-Term Barrier Function in Perfused Hydrogel Scaffolds. Stem Cell Rep. 2019;12:474–87 *with permission from Elsevier Publishing.*

3.1 Summary

There is a profound need for functional, biomimetic in vitro tissue constructs of the human blood-brain barrier (BBB) and neurovascular unit (NVU) to model diseases and identify therapeutic interventions. Here, we show that induced pluripotent stem cell (iPSC)-derived human brain microvascular endothelial cells (BMECs) exhibit robust barrier functionality when cultured in 3D channels within gelatin hydrogels. We determined that BMECs cultured in 3D under perfusion conditions were 10-100 times less permeable to sodium fluorescein, 3 kDa dextran, and albumin relative to HUVEC and human dermal microvascular endothelial cell controls, and the BMECs maintained barrier function for up to 21 days. Analysis of cell-cell junctions revealed expression patterns supporting barrier formation. Finally, efflux transporter activity was maintained over 3 weeks of perfused culture. Taken together, this work lays the foundation for development of a representative 3D in vitro model of the human NVU constructed from iPSCs.

3.2 Introduction

The neurovascular unit (NVU), comprised of brain microvascular endothelial cells (BMECs) that form the blood-brain barrier (BBB), pericytes, neurons, and glial cells, tightly regulates transport of substances between the bloodstream and the brain. Abnormal BBB and NVU function is associated with a broad spectrum of neurological pathologies [119], and increasing

evidence suggests a number of non-neural disorders, such as diabetes [120], are associated with compromised BBB integrity and/or functionality, often giving rise to secondary complications and cumulative neurological insults that increase the risk of additional neurodegenerative and cerebrovascular disease. Animal models (*in vitro* and *in vivo*) have historically been the gold-standard platform for investigating the complexities of human neurovascular disease. However, the difficulties in translating information gleaned from animal models to successful clinical intervention, which are exemplified by the lack of therapeutics that can effectively treat neurodegenerative diseases, highlight the need to develop a functional *in vitro* tissue model of the human NVU that will improve mechanistic understanding of disease progression and accelerate the development of new treatment strategies.

Recent advances in biomaterials patterning and microfluidic device fabrication have enabled a shift from standard 2D monolayer cell culture to 3D approaches that either seed cells on the surface of porous scaffolds or embed cells within hydrogel matrices. This shift has highlighted the fact that 3D culture techniques generally result in cell behavior that more closely mimics *in vivo* phenotypes [121–123]. Approaches that rely on cell-laden hydrogels are particularly attractive, as hydrogels mimic many aspects of the natural extracellular matrix (ECM) including stiffness, enzymatic degradability, and (with appropriate material choice or RGD modification) binding sites [124]. Cell-laden hydrogels cast with thicknesses in the few hundred-micron range have allowed researchers to observe cell behavior in a more biomimetic, 3D environment. Additionally, cell-laden hydrogels can be patterned so that channels supporting fluid flow exist within the gel. Initial work in this area leveraged photolithographic and soft templating techniques [125–127], and more recently many researchers have moved towards using 3D printing approaches to pattern either the gel itself or a sacrificial template that is first embedded within the gel and

subsequently removed to form a channel [128–130]. While these approaches are still generally limited to forming channels with diameters on the 100 micron or larger scale, this advance enables new investigations into phenomena occurring within and around arteriole and larger-sized vessels. These platforms allow variation of multiple critical parameters, such as flow, shear, pressure, and soluble biochemical concentration in a 3D geometry that mimics a natural vessel.

Accordingly, several reports have implemented advanced fabrication methods to develop more complex *in vitro* BBB and NVU models. Thin-film, synthetic PEG hydrogels supporting self-assembled NVU constructs have been used for high-throughput toxicity screening [131,132]. Meanwhile, microfluidic approaches have enabled the observation and measurement of NVU function in a highly-controlled, perfused environment; these range from the commercially available, sym-bbb [133] to highly complex, organ-on-a-chip platforms that provide powerful methods for gaining critical insights into population-specific responses to environmental perturbations with multiple readout mechanisms [134,135]. While there are some recent reports that have incorporated hydrogel matrices into microfluidic devices [136,137], most of these models rely on the use of solid substrates such as PDMS or glass [138]. Such BBB models are well-suited to high-throughput, massively parallel drug screening efforts. However, scaffolds should ideally be more biomimetic, such that the scale, biological matrix, cellular components, and organization better approximate physiological processes, including both direct and indirect cellular interactions. Of late, there have only been a few studies involving tissue-scale biological scaffolds with 3D cultures of endothelial cells [139,140].

Indeed, cell fidelity has often been a limiting factor for recreating the BBB portion of NVU models. Historically, BMECs have been isolated from primary animal sources [141], but as described above, species differences can limit the predictive power of such non-human models

[142]. However, BMECs from primary human sources are tedious to isolate, genetically heterogeneous between donors, can only be obtained in low yield, and often come from unhealthy tissue (e.g. brain tumor resections). Conversely, immortalized human BMECs can be obtained in high yields from a clonal source but suffer from poor passive barrier properties that do not appropriately mimic the *in vivo* BBB [143]. In recent years, the development of protocols to differentiate human induced pluripotent stem cells (iPSCs) into BMECs has circumvented many of these issues. iPSC-derived BMECs were initially characterized by expression of representative BBB markers, active efflux transporter activity, permeability to a panel of small molecules that correlate with *in vivo* uptake in rodents, and modest barrier properties as determined by transendothelial electrical resistance (TEER) measurements of ~800 Ωxcm^2 [144]. Subsequently, retinoic acid (RA) was shown to boost the passive barrier properties of iPSC-derived BMECs above 3000 Ωxcm^2 [145]. Since these initial publications, others have validated the fidelity of these cells and advancements have been made towards improving the differentiation procedure [146–149]. In addition, these iPSC-derived BMECs, co-cultured with astrocytes on opposite sides of a Transwell filter, have been incorporated into a microfluidic device which maintained BBB properties over 10 days [150]. However, studies of iPSC-derived BMEC performance in biomimetic 3D hydrogel scaffolds, which are a crucial step towards building representative *in vivo*-like NVU models that can be used for disease modeling and preclinical validation of drug efficacies, have been limited.

Ideally, a 3D NVU model constructed from iPSCs would be fully isogenic from a single pluripotent source, exhibit robust BBB function (including passive and active barrier properties), possess long-term stability, and be relatively simple to fabricate and implement. Herein, we describe a process to fabricate such a model, with a focus on establishing a functional iPSC-derived

BMEC layer within a continuously perfused channel. Using easily accessible materials (unmodified, enzymatically-crosslinked porcine gelatin) and a straightforward fabrication approach to assemble a platform that recirculates liquid through a single channel (Figure 3.1A-C), we demonstrate that iPSC-derived BMECs assembled in 3D establish a robust barrier that remains stable for up to three weeks under continuous perfusion. Furthermore, we found that BMECs in perfused channels retain efflux transporter activity, a key functional characteristic of BBB endothelium, for over two weeks in culture. Together, these results validate the performance of a 3D, continuously perfused biomimetic model of brain microvasculature with long-term functional barrier properties.

3.3 Materials and methods

3.3.1 Cell culture

IMR90-4 [151] and CC3 [152] iPSCs were maintained on growth factor-reduced Matrigel (VWR) in E8 medium (produced in-house as previously described) [147]. iPSCs were passaged every 3-4 days with Versene (Thermo Fisher) as previously described. Differentiation to BMECs was conducted as previously described. In brief, iPSCs were passaged to single cells with Accutase (Thermo Fisher) and seeded overnight on Matrigel at a density of 12,500-15,800 cells/cm2 in E8 medium containing 10 μM Y27632 (Tocris). The following day, cells were fed with E6 medium (produced in-house as previously described) [147], and media was changed every day thereafter. On day 4, cells were switched to human endothelial serum-free medium (hESFM; Thermo Fisher) containing 1% platelet-poor plasma-derived serum (PDS; Alfa Aesar), 20 ng/ml basic fibroblast growth factor (bFGF; Peprotech), collectively referred to as EC culture medium, and 10 μM all-trans retinoic acid (RA; Sigma). On day 6, cultures were collected with Accutase and either frozen

in 60% EC culture medium, 10% DMSO (Sigma), 30% fetal bovine serum (FBS; Thermo Fisher), and 10 μM Y27632 as previously described [153], or seeded directly into scaffolds. HUVECs and μVas (Angioproteomie) were cultured in DMEM/F12 medium (Thermo Fisher) supplemented with 5% FBS (Gibco), 10 mM L-glutamine (Corning), 50 μg/ml Ascorbic Acid (Thermo-Fisher), 0.75 U/ml Heparin (Thermo-Fisher), 15 ng/ml insulin growth factor 1 (IGF-1), 5 ng/ml vascular endothelial growth factor (VEGF), 5 ng/ml bFGF, and 5 ng/ml epidermal growth factor (EGF) (all from Peprotech).

3.3.2 Scaffold fabrication

External support frames for gelatin scaffolds were generated from thin slabs of PDMS cast in small Peel-A-Way embedding molds (Fisher Scientific) transected by two intersecting needles (Gauge 23 and 16, BD Biosciences). After removing the central section and bonding to a thin PDMS film base, a barbed luer fitting (Cole Parmer) was attached to the inlet to facilitate easy integration with the fluidic apparatus. Tubing (1/16th inch O.D., VWR) threaded through the barbed inlet served as the channel mold (Figure 3.1A). PDMS frames (5 x 5 x 2 mm) were washed and sterilized in 70% ethanol with sonication. Sterile solution of 10% (w/v) porcine gelatin (300 bloom, Sigma) combined 10:1 (v/v) with 10% (w/v) microbial transglutaminase (mTG, Modernist Pantry) was poured into the assembled frames and allowed to polymerize in a 37 °C incubator for four hours. The channel was formed by removal of tubing and was coated with 0.4 mg/ml collagen IV (Sigma) and 0.1 mg/ml fibronectin (Sigma) and conditioned in complete medium overnight before seeding channels with 3x106 cells/ml of either iPSC-derived BMECs, RFP-expressing HUVECs, or μVas. The approximate volume of the channel (~800 μm x 5 mm) is 2.5 μl.

3.3.3 Cell seeding

IMR90-4-derived BMECs were reconstituted from frozen stock, whereas CC3-derived BMECs, HUVECs, and μVas were seeded from live cultures. For quality control, TEER was measured across BMECs seeded concurrently in Transwell filters and was consistent with previous publications. Cells were suspended at 3x106 cells/ml in their standard medium and pipetted through the inlet fitting to coat the bottom half of a channel. Cells were incubated for either 4 h or overnight at 37 °C to facilitate attachment. The process was then repeated to seed the top half of the channel. Cells were stained with 2 μM Calcein AM (Life Technologies) and imaged by confocal microscopy (LSM 710, Zeiss) to confirm a confluent cell layer throughout channel before connecting to perfusion (Figure 3.1C).

3.3.4 Scaffold culture and perfusion

On experiment day 0, hydrogels were placed in a Petri dish and either remained in static culture or were connected to a perfusion system (Figure 3.1B). Under both conditions, the hydrogels are submerged in ~40-45 ml of medium. Based on the design of the PDMS frame, the upper surface of each hydrogel is in direct contact with the medium. For perfusion, a custom peristaltic pump [154] circulated culture medium through the channel at 100 ul/min. For samples perfused at rates greater than 100 μl/min, the flow rate was increased to the indicated value following an initial 24-hour perfusion at 100 μl/min. As seen in Figure 3.1B, medium is extracted through the open tube not connected to the hydrogel, circulated through the hydrogel, and expelled back into the bulk reservoir. HUVECs were cultured in the same medium described above, whereas BMECs and μVas were both cultured in hESFM containing 1% PDS, 10 μM RA, and 10 μM Y27632. The media was unchanged throughout the course of each experiment. Components used to construct the perfusion system are described in Figure A. 3.5.

3.3.5 Permeability measurements

Permeability was measured by imaging diffusion of 2 µM sodium fluorescein (Sigma), 12.5 µg/ml 3 kDa AF680-conjugated dextran (Thermo Fisher), and 80 µg/ml Texas Red-conjugated albumin (Thermo Fisher) across cell monolayers. During the course of the imaging experiment, channels were perfused at a rate of 30 µl/min for 2 hours while obtaining fluorescence images every 30 seconds using the LSM 710 confocal microscope with pinhole set to 1 Airy unit. The resulting image intensity profiles were processed in FIJI [155] using a custom macro to automate extraction of fluorescence intensity values of the channel region, the diffusion region between channel and edge, and the edge of the gel. These values were then imported into a MATLAB (MathWorks) script to calculate K [cm s-1], the permeability of gelatin scaffold and cell layer combined, as detailed below and in Figure A. 3.6.

3.3.6 Efflux transporter activity assays

P-glycoprotein (Pgp) activity was assessed by measuring accumulation of fluorescent dye, Rhodamine 123, in samples pre-incubated with and without Pgp specific inhibitor, cyclosporin A. MRP activity was assessed by measuring fluorescence accumulation of fluorescent dye H2DCFDA, in samples pre-incubated with and without MRP specific inhibitor, MK-571. Specifically, non-inhibited controls were evaluated by perfusion (30 µl/min) with medium supplemented with 10 µM Rhodamine 123 (Thermo Fisher) or 10 µM H2DCFDA (Thermo Fisher) and 12.5 µg/ml 3 kDa dextran. Inhibited samples were pre-incubated in medium containing 10 µM cyclosporin A (Tocris) or 10 µM MK-571 (Tocris) for 1 hour, then similarly perfused with the medium supplemented with 12.5 µg/ml 3 kDa dextran and appropriate inhibitor/ dye cocktail (Pgp: 10 µM cyclosporin A and 10 µM Rhodamine 123; MRP: 10 µM MK-571 and 10 µM H2DCFDA). Confocal z-stacks were obtained at 0 and 60 min of perfusion. For each sample, the change in

intracellular fluorescence intensity was determined using FIJI by adding the cellular fluorescence from each z-stack, then subtracting the cumulative fluorescence intensity of the initial z-stack from the final z-stack ($\Delta I = I_{final} - I_{initial}$). The percent increase in fluorescence was calculated using the formula:

$$\frac{\Delta I_{inhibited} - \Delta I_{non-inhibited}}{\Delta I_{inhibited}} \times 100 \quad (1)$$

where $\Delta I_{inhibited}$ is the change in fluorescence calculated from channels exposed to cyclosporin A and $\Delta I_{non\text{-}inhibited}$ is the change in fluorescence calculated from channels not exposed to inhibitor.

3.3.7 FRAP measurements

In order to calculate the permeability of endothelial cell layers to sodium fluorescein, dextran, and albumin based upon time lapse images, the diffusivity of each molecule in gelatin was first determined through fluorescence recovery after photobleaching (FRAP) analysis. Excellent in-depth reviews of the principles and mathematical theory for determining diffusion coefficients based upon FRAP analysis have been previously described [156–158]. In summary, an intense laser beam of known dimension is used to irreversibly bleach fluorophores within the exposed sample region. The diffusion coefficient is related to the speed at which the fluorescence the bleached region recovers, dictated by the speed at which bleached compounds diffuse out of the region and are replaced by unbleached fluorophores. Hence, the diffusion coefficient is most strongly related to the size of the compounds. Potential sources of error include immobilized compounds (e.g. molecules that stick to a coverslip) and unbound fluorophore which could under- or over-estimates of diffusion coefficients. To account for this, we performed FRAP analysis in control samples using five different compounds ranging in molecular weight between ~300 to 66,000 Daltons. Using multiple compounds of varying molecular weight allowed us to verify

accuracy of the FRAP method as diffusivity should relate directly to molecular weight. Our results (Figure A. 3.6) indicated a strong linear relationship between diffusion coefficient and molecular weight, suggesting these potential sources error having minimal impact and, thus, no further steps to introduce correction for immobile molecules or unbound fluorophores were taken.

Uniform solutions of 10% (w/v) gelatin containing 10 μg/ml fluorescein (*MW = 332 g/mol*), 125 μg/ml Cascade Blue-Dextran (*MW = 3,000 g/mol*), 125 μg/ml Alexa-Fluor 680-Dextran (*MW = 3,000 g/mol*), 0.5 mg/ml Oregon Green-Dextran (*MW = 10,000 g/mol*), or 100 μg/ml Fluorescein-BSA (*MW = 66,000 g/mol*) were crosslinked with 1% (w/v) mTG. Approximately 200 μl of crosslinked gelatin solution containing individual fluorophores was sandwiched between two glass slides (Fisher Scientific) to form a thin gelatin layer approximately 60 μm in thickness. FRAP experiments were conducted using a Zeiss LSM 710 laser scanning confocal microscope and the bleaching module included in Zen Black (Zeiss) imaging software. For each trial, 10 pre-bleach images were obtained to calculate initial fluorescence intensity. Samples were then bleached, using the zoom-bleaching function to increase efficiency, with the appropriate laser (405 nm line of 30 mW Diode laser was used to bleach Cascade Blue Dextran, the 488 nm line of 35 mW Argon laser bleached Fluorescein, Oregon Green-Dextran, and Fluorescein-BSA, and 633 nm line of 5mW HeNe laser bleached Alexa-Fluor 680-Dextran) within a central designated bleach region (diameter = 60 pixels, or ~100 μm) until the bleached intensity reached 50% of the initial fluorescence intensity. Subsequent acquisition of time series images over the course of 100-500 seconds, depending on the dye, documented the fluorescence recovery. The pinhole aperture was held at maximum for all samples. Laser power was set to maximum to effectively bleach each dye through the entire thickness (*z*-axis) of the sample, such that fluorescence recovery depended most upon diffusion along the *x-y* dimension. To minimize the

effects of diffusion occurring during the process of photo-bleaching from skewing calculations based upon FRAP data, image resolution was set to 512x512 pixels per frame to reduce scan time (pixel dwell = 1.58 μs).

3.3.8 Calculating diffusivity from FRAP data

Diffusion coefficients for isotropic, nonreactive solutions were calculated from FRAP data based upon Fickian diffusion, most notably outlined by Axelrod and Soumpasis [156,158] and later optimized [157] to account for special consideration associated with photobleaching using laser-scanning confocal microscopy. Most recently, a simplified method for extracting the diffusion coefficients from confocal laser scanning FRAP data was described according to Equation 2, where D is the diffusion coefficient ($\mu m^2/s$), R_n is the nominal radius of the laser spot, R_e is the effective radius (1/2 diameter of bleached region), and $\boldsymbol{\tau}_{1/2}$ is the half-recovery time [159].

$$D = \frac{R_n^2 + R_e^2}{8\tau_{1/2}} \qquad (2)$$

Automated measurements performed by modified version of the freely available Frap-jython macro for ImageJ [155,160] provided the half-recovery time from individual FRAP data sets and identified the "FRAP frame" where fluorescence intensity within the bleached region reached a minimum. This frame was then used to measure the effective radius (R_e) from the plot profile function in ImageJ. The nominal radius (R_n) was the same for every sample at 50 μm. Calculated diffusion coefficients based upon FRAP experiments are shown in Figure A. 3.6.

3.3.9 Diffusion imaging analysis

Using Fiji, each dataset was first aligned (if necessary), before identifying the coordinates defining each region of interest corresponding to the areas comprising (1) channel interior, (2) gelatin background (farthest point from channel) and (3) gelatin next to the channel were entered

into a custom Fiji macro. The macro script used to obtain the intensity profiles corresponding to the aforementioned region of interest is included as Figure A. 3.7. Diffusivity was then calculated based on methods previously reported [127], first using Equation 3:

$$Bi = \frac{K\delta}{D_{gelatin}} = \lambda \cdot tan\lambda \quad (3)$$

Where Bi is the Biot number, K (cm/s) is the permeability, δ is the distance between the edge of the channel and the edge of the gel (cm), $D_{gelatin}$ (cm/s) is the diffusivity of the compound of interest (e.g. 3 kDa dextran) in gelatin, and λ is the slope of linear fit for the following relation describing the change in fluorescence intensity versus time:

$$\lambda = \ln(\Delta \frac{I_{edge} - I_{channel}}{I_{gel} - I_{channel}}) \cdot \frac{1}{\Delta t} \quad (4)$$

Where I_{edge} is the integrated fluorescence intensity profile corresponding to the edge of the gelatin scaffold (also referenced as gel background), $I_{channel}$ is the integrated fluorescence intensity profile of channel, and I_{gel} correspond to the fluorescence intensity of the gel next to the channel (the active area of dextran diffusion). The previous two equations are combined to yield a formula for determining permeability (K):

$$K = \frac{D_{gelatin} \cdot \lambda \cdot \tan\lambda}{\delta} \quad (5)$$

The intensity profiles extracted from imaging analysis were then imported into a MATLAB script to calculate the permeability of cell layers to generate a plot corresponding to Equation 4, which was used to determine λ. This value was then used in Equation 5, along with known values for $D_{gelatin}$ and distance (δ) to calculate the permeability (K) reflecting the combined permeability of the gelatin matrix and cell monolayer. The MATLAB script used for these calculations is included as Figure A. 3.8.

Control scaffolds comprised of channels without cells lining the channel were used to determine the permeability of the gelatin matrix alone (K_g). The permeability of the cell monolayer (K_c) was then determined using the following equation:

$$\frac{1}{k} = \frac{1}{k_C} + \frac{1}{k_G} \quad (6)$$

3.3.10 Shear calculations

Fluidic shear stress along the channel wall using the following equations:

$$V = \frac{Q}{A} \quad (7)$$

Where V is the mean fluid velocity (mm/s), Q is the pump flow rate, and A is the area of the channel. An average channel diameter (d) of 800 µm was used for all calculations. We then calculated wall shear rate (γ) using:

$$\gamma = 8 * \frac{V}{d} \quad (8)$$

Shear stress (τ) is then calculated by:

$$\tau = \gamma * \mu \quad (9)$$

where µ is viscosity. For all calculations, the media viscosity was approximated using the viscosity for 1X PBS, 0.01 Pa [161].

3.3.11 Immunocytochemistry

At indicated time points, gelatin constructs were washed 3 times in 1X PBS, then fixed in 4% paraformaldehyde for 10 min at room temperature (RT). Fixed constructs were washed 3 times in 1X PBS at RT, then incubated in 1X PBS supplemented with 5% donkey serum overnight at 4 °C. After washing with 1X PBS at RT, samples were incubated in 1X PBS containing 1 µg/ml claudin-5 antibody (Alexa-Fluor 488 conjugate; 4C3C2; Thermo Fisher), 1 µg/ml occludin antibody (Alexa-Fluor 594 conjugate; OC-3F10; Thermo Fisher), and/or 1 µg/ml VE-Cadherin

antibody (PA519612, Thermo Fisher) overnight at 4 °C. Samples were washed 3 times in 1X PBS before incubation with 1 mg/ml Alexa-Fluor 680 donkey anti-rabbit secondary antibody (Thermo Fisher) overnight at 4 °C to fluorescently label bound VE-cadherin antibodies. Unbound secondary antibody was removed by washing 5 times in 1X PBS at RT. For actin labeling, cells were incubated with Rhodamine Phalloidin (1:1000 dilution; Thermo Fisher) for 20 min at RT prior to imaging. For nuclei labeling, cells were incubated with 1 µg/ml Hoechst (BD Bioscience) for 10 min at RT prior to imaging.

3.3.12 qPCR analysis

Cells were detached from the channel surface by first washing 2 times in 1X PBS for 5 min, then incubating the entire gel in 5 ml 0.25% Trypsin-EDTA (Gibco) at 37 °C for 10 min. Gels were then washed twice with 5 ml Trypsin Neutralizing solution (Gibco), vigorously pipetting the solution through the channels to dislodge remaining cells. Each collection tube included cells collected from two channels (experimental replicates). The cell suspensions were pelleted by centrifugation at 1000 G for 5 min. The supernatant was discarded and the pellet was resuspended in 500 µl of room temperature TRIzol reagent (Thermo Fisher) for 10 min before storage at -80 °C. To extract RNA, samples were mixed with chloroform at a 1:5 v/v chloroform:TRIzol and centrifuged at 12,000×g for 15 min at 4°C. RNA was subsequently isolated from the resulting aqueous phase and reversed transcribed to cDNA via manufacturers' instructions using an RNeasy Mini Kit (Qiagen) and a High-Capacity cDNA Reverse Transcription Kit (Applied Biosystems), respectively. qPCR was performed on a BioRad CFX96 using a TaqMan Universal PCR Master Mix (Applied Biosystems), 15 ng cDNA per replicate per gene, and desired TaqMan Gene Expression Assays (Applied Biosystems) and manufacturers' specified thermocycler parameters. Gene expression was measured using N=3 biological replicates.

3.3.13 RNA sequencing and analysis

IMR90-4-derived BMECs were detached from channels and collected in TRIzol as described above. Total RNA was isolated using the Direct-zol RNA MiniPrep Plus Kit (Zymo Research) with DNase I treatment according to the manufacturer's instructions. Samples were submitted to Vanderbilt Technologies for Advanced Genomics (VANTAGE) for sequencing using an Illumina NovaSeq6000. Sequences were aligned to the human transcriptome (GRCh38) using HISAT2 [162] and a text file containing a list of known splice sites generated using the UCSC Table Browser [163] and hisat2_extract_splice_sites.py. Alignments were assembled using StringTie [164], and transcript levels (FPKM values) were extracted using Ballgown [165]. Pearson correlation coefficient was calculated by generating a scatter plot of FPKM values with each sample on a separate axis and performing a linear regression of the plotted data. The RNA-sequencing data referenced in this chapter were submitted to GEO under accession number GEO: GSE122588.

3.4 Results and discussion

We first optimized scaffold composition and determined that iPSC-derived BMECs performed best when seeded on gelatin hydrogels coated with collagen IV and fibronectin (Figure A. 3.1)**,** an approach determined to be effective in previously published protocols [145,147]. With our intention to incorporate glial and neural cells in future NVU models, we initially explored fabricating the scaffolds using alginate/gelatin composite hydrogels based upon previous reports in the literature characterizing 3D culture of neural and glia cells [166]. We evaluated the ability of IMR90-4-derived BMECs to adhere to the surface of tissue-culture plates coated with thin hydrogel films comprised of 10% gelatin or 10% gelatin/ 0.25% alginate composite hydrogels

both with and without subsequent adsorption of the collagen/fibronectin solution commonly used in iPSC-derived BMEC cultures [144]. As shown in Figure A. 3.1A, visual inspection of cells 24 hours after seeding revealed that iPSC-derived BMECs failed to attach and grow on hydrogels containing alginate, even with additional treatment with collagen/fibronectin. Although visually indistinguishable in terms of cell morphology and viability, TEER measurements of BMECs grown on gelatin hydrogels with and without additional collagen/fibronectin coating demonstrated that gelatin treated with these additional ECM proteins yielded enhanced barrier properties (Figure A. 3.1B). Thus, we elected to proceed with all experiments using scaffolds comprised of 10% gelatin and channel surfaces coated with collagen/fibronectin solution 24 hours prior to cell seeding. Visual comparison of IMR90-4-derived BMECs indicates that cell morphology remains unchanged in the transition from 2D to 3D culture formats (Figure 3.1D-E).

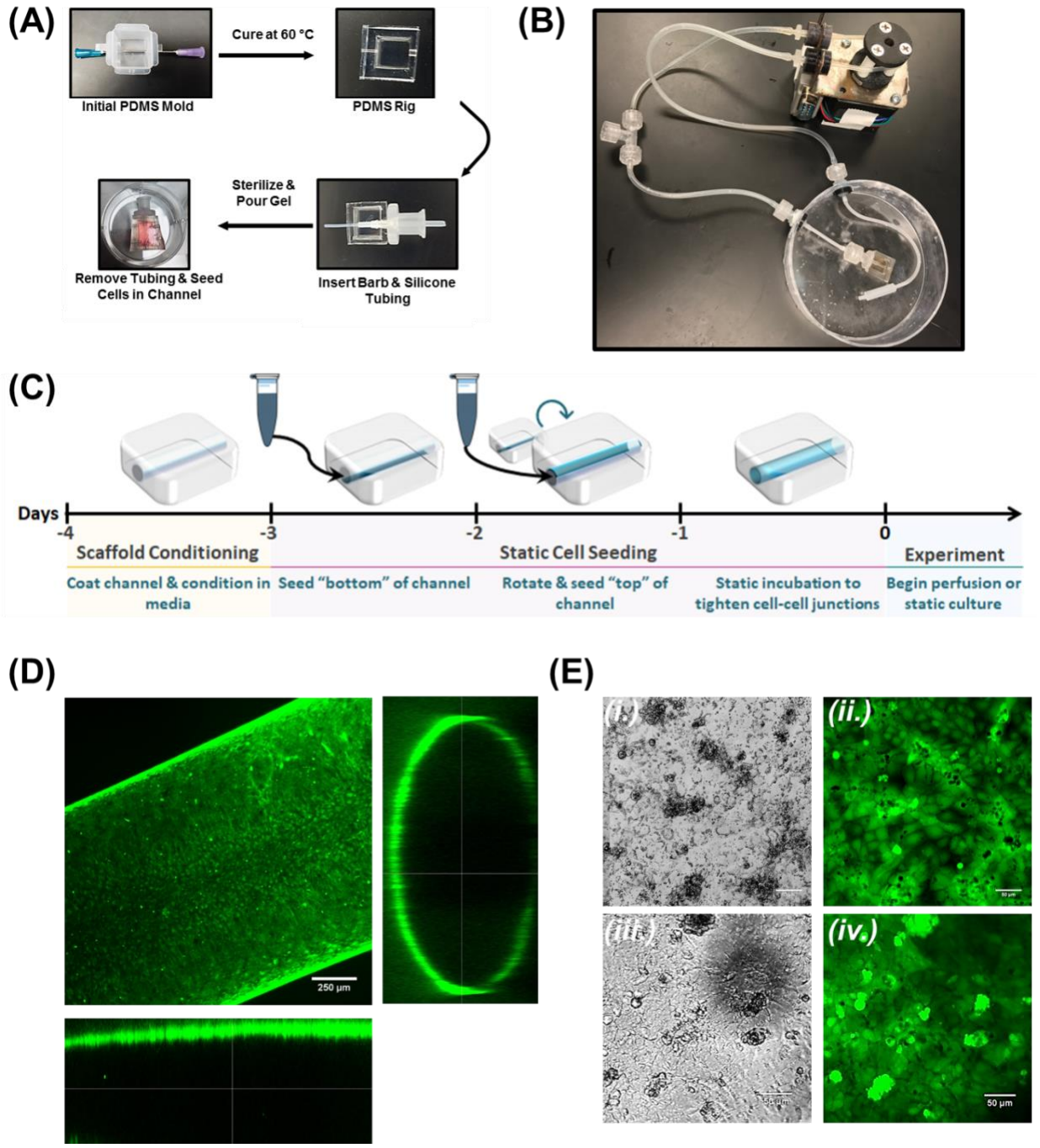

Figure 3.1 Cell-laden scaffold assembly and perfusion. (A) Fabrication of gelatin channel within supportive PDMS rig and (B) fully assembled perfusion platform. (C) Schematic for cell seeding and initiation of experiments. (D) BMECs stained with Calcein AM Ester following 7 days of culture on the channel surface as shown by orthogonal confocal image. Scale = 100 µm. (E) Morphology comparison between Calcein AM-stained BMECs cultured in 2D tissue culture plates (i. & ii.) and in gelatin channels (iii. & iv.). Scale = 50 µm.

To evaluate the ability of iPSC-derived BMECs to recapitulate passive barrier function in 3D culture over the course of at least 2 weeks, the diffusive permeability of sodium fluorescein (MW = 330 Da), 3 kDa MW dextran, and albumin (MW = 66 kDa) was measured and compared to HUVECs and human dermal microvascular endothelial cell (μVas) cells. The use of these tracers was intended to assess permeability to relatively small, medium, and large sized molecules. In each cellular cohort, we compared samples cultured under static conditions versus continuous perfusion (100 μl/min). Results from these experiments are summarized in Figures 3.2 and 3.3, with all raw data located in Figure A. 3.2.

We initially examined the permeability of 3 kDa dextran in static versus perfused channels on days 1, 7, and 14 of culture (Figure 3.2A-D). The permeability coefficients for 3 kDa dextran in IMR90-4-derived BMECs were measured at nearly 2 orders of magnitude lower than HUVECs on day 1 static (K_{BMEC}=1.2x10^{-7} cm/s, K_{HUVEC}=1.2x10^{-5} cm/s) and perfused (K_{BMEC}=1.9x10^{-7} cm/s, K_{HUVEC}=1.2x10^{-5} cm/s) samples and roughly five times lower than μVas ($K_{\mu Vas}$=5x10^{-7} cm/s) (e.g. the BMECs exhibit a >100-fold and 5-fold stronger passive barrier compared to HUVECs and μVas, respectively). These data indicate that the BMECs not only attach to the gelatin matrix, but also immediately form a robust barrier that is tighter than the non-BBB endothelial cells. In static culture, BMEC barrier function declined on day 7 (K_{BMEC}=4.6x10^{-7} cm/s) and 14 (K_{BMEC}=2.2x10^{-6} cm/s), although it remained ~10-fold better than HUVEC (K_{HUVEC}=7x10^{-6} cm/s and 2x10^{-5} cm/s, day 7 and 14 respectively) and μVas controls ($K_{\mu Vas}$=1.3x10^{-6} cm/s and 1.2x10^{-6} cm/s, day 7 and 14 respectively). In contrast, the barrier against 3 kDa dextran in BMECs that were continuously perfused for 2 weeks was comparable to initial values (K_{BMEC}=4.3x10^{-8} cm/s on day 14), suggesting that exposure to shear might further stabilize, and perhaps enhance, BMEC barrier integrity over time. A similar trend was observed in μVas

($K_{\mu Vas}$ =1.5x 10^{-6} cm/s on day 14), although the permeability coefficient for these cells remained more than 10 times greater than BMECs. We also separate data compiled from different IMR90-4 BMECs differentiations to show biological reproducibility (all data from Figures 3.2-3.3 are compiled from more than 5 independent differentiations). The permeability to 3 kDa dextran from two separate IMR90-4 BMECs differentiations (indicated as either D1 or D2) were measured at day 14 under both static and perfused conditions. All BMEC cohorts exhibit permeability coefficients over 10 times smaller than those for HUVEC/μVas controls. Furthermore, all BMECs under perfusion are significantly less permeable than their non-perfused counterparts, further highlighting reproducibility of the system.

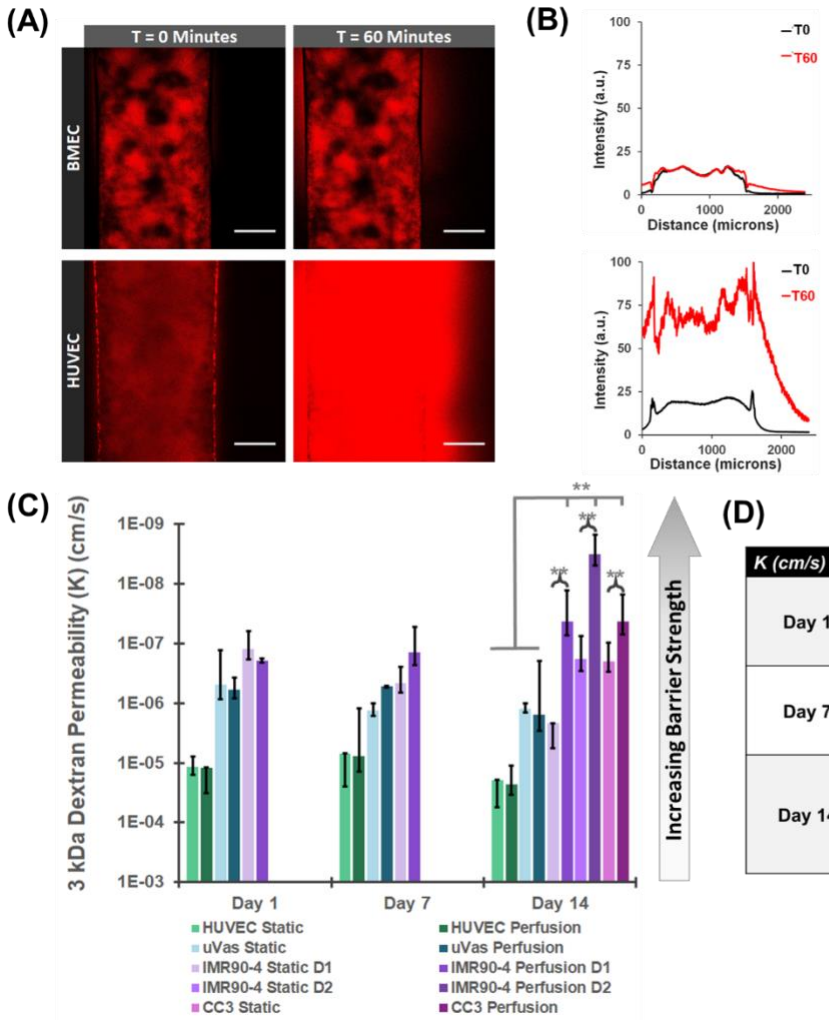

K (cm/s) (x10^{-7})		Static	Perfusion
Day 1	IMR90-4 BMEC	1.2 ± 0.6	1.9 ± 0.2
	HUVEC	118 ± 28	119 ± 130
	µVas	5 ± 3.6	6 ± 2.3
Day 7	IMR90-4 BMEC	4.5 ± 2	1.4 ± 0.8
	HUVEC	69.8 ± 10	76.2 ± 49
	µVas	31 ± 3	5.3 ± 1
Day 14	IMR90-4 BMEC	20.1 ± 26	0.4 ± 0.3
	CC3 BMEC	8.9 ± 1.7	2.6 ± 2.1
	HUVEC	195 ± 150	228 ± 48
	µVas	33 ± 0.9	15.6 ± 13.7

Figure 3.2 Quantitative comparison of cell monolayer permeability in perfused and non-perfused channels. (A) Confocal images of 3 kDa dextran (Red) diffusion in gelatin channels lined with either iPSC-derived BMECs or HUVECs. Images show samples cultured for 7 days under static conditions (Scale = 100 µm). (B) Intensity profiles across channels lined with BMECs (top) or HUVECs at 0 and 60 min of perfusion with 3 kDa dextran. (C) Graphical depiction of permeability to 3 kDa dextran on days 1, 7, and 14 of culture under either static culture or continuous perfusion at 100 µl/min. Average permeability coefficients are listed in (D). Data are compiled from at least 8 separate channel seedings, comprised of cells obtained from 5 independent differentiations. N ≥ 3 independent biological replicates for all data points. Error = ± 1 SD, (*) indicates $p < 0.05$, (**) indicates $p < 0.01$ based on one-way ANOVA. Individual values from each replicate (e.g. measurements from individual devices) are listed in Figure A. 3.2.

To further explore the influence of perfusion upon barrier strength in BMECs, we measured the diffusion coefficients of sodium fluorescein and albumin in addition to 3 kDa dextran after 14

days of perfused or static culture (Figure 3.3). In order to validate these results in a different iPSC line, we also measured permeability in CC3-derived BMECs [147] (Figures 3.2 and 3.3). Both IMR90-4- and CC3-derived BMECs subjected to perfusion for 14 days exhibited permeability to all compounds that was an order of magnitude lower than μVas controls. Additionally, IMR90-4-derived BMECs subjected to perfusion exhibited permeability that was significantly lower compared to non-perfused counterparts, confirming permeability trends across a spectrum of molecular weights. Exclusion of albumin suggests reduced vesicular transport, which is a hallmark of the BBB. To further probe this finding, we used qPCR to quantify *MFSD2A* and *CAV1* (caveolin-1) expression. *MFSD2A*, which is highly expressed in brain endothelium relative to lung and liver endothelium and known to suppress endocytosis/transcytosis [167], was not expressed at significantly different levels between BMECs and μVas (Figure A. 3.3). However, *CAV1*, an important component of vesicular transport that is suppressed in BMECs and activated under pathogenic conditions such as ischemia/reperfusion [168], exhibited ~8-fold higher expression in μVas relative to BMECs. Coupled with the permeability data demonstrating reduced albumin extravasation, these data suggest the BMECs suppress vesicular transport, although not necessarily through *MFSD2A* upregulation. Since these BMECs are maintained in isolation, it is possible that regulatory cues for *MFSD2A* provided by other cell types (e.g. pericytes) are not present. In future model iterations, inclusion of these cell types could further suppress vesicular transport.

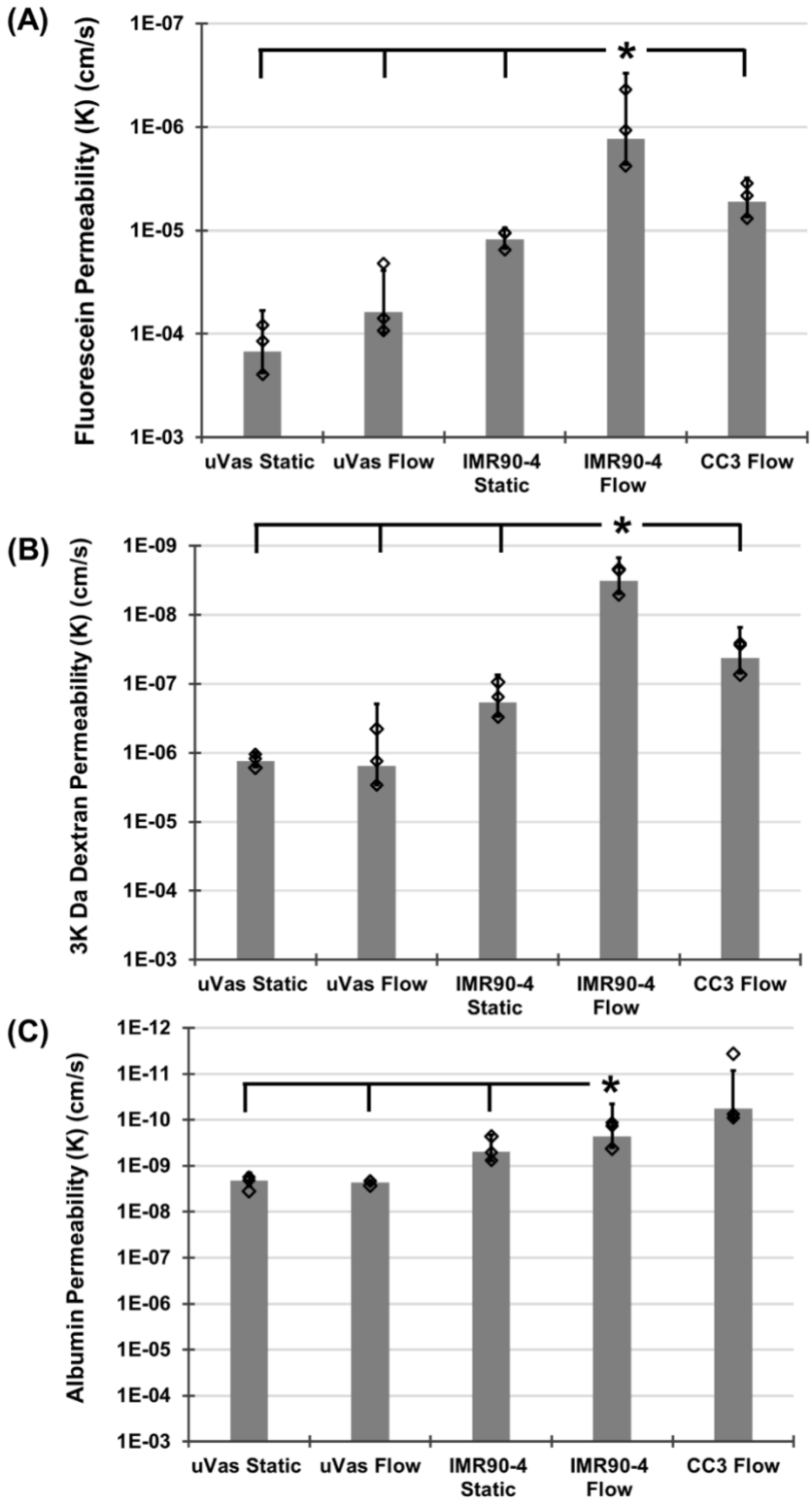

Figure 3.3 Permeability coefficients for molecules of varying molecular weights. Comparison of permeability for (A) sodium fluorescein, (B) 3 kDa dextran, and (C) albumin between μVas,

IMR90-4-derived BMECs, and CC3-derived BMECs that were maintained under either static conditions or continual perfusion for 14 days. (◊) indicate actual values of individual replicates. N ≥ 3 independent biological replicates for all data points. Error = ± 1 SD, (*) indicates $p < 0.05$ based on one-way ANOVA.

To further examine gene expression patterns, we used qPCR to quantify *OCLN* (occludin), and *SLC2A1* (GLUT-1) between IMR90-4-derived BMECs and μVas at day 14 under perfusion. *OCLN* and *SLC2A1* are recognized as being relatively specific to BBB compared to peripheral endothelium [169], and these genes were expressed at ~5-fold and ~11-fold higher levels, respectively, in BMECs (Figure A. 3.3). Next, we used RNA sequencing to compare global gene expression patterns in BMECs cultured for 1 day under static conditions and 14 days under constant perfusion (Figure A. 3.7). The Pearson correlation coefficient between these samples was 0.91, which indicates a strong positive association and provides evidence that the BMEC gene expression signatures are maintained under longitudinal perfusion.

Finally, to establish appropriate correlations between 2D and 3D barrier function, we performed a similar dextran diffusion assay using CC3-derived BMECs and HUVECs cultured in Transwell filters (Figure A. 3.4). Permeability values obtained from cells cultured in 2D were on the same order of magnitude as those obtained in 3D channels (10^{-7} cm/s for BMECs, 10^{-5} cm/s for HUVECs), thus validating the measurements made within the tissue construct. Interestingly, permeability values for both BMECs and HUVECs remained stable over time in 2D, unlike the steady increase in permeability observed in cells lining non-perfused channels, indicating a possible role for nutrient exchange in maintaining barrier integrity in the 3D construct. To further explore this potential impact of nutrient exchange, we examined the permeability in BMECs and μVas in 3D culture under stop-flow conditions, in which samples were subjected to perfusion from the medium reservoir, but for only 10 min per day; these experiments permitted nutrient exchange

with minimal exposure to shear stress (we note that the scaffolds are designed such that the upper surface of the hydrogel is in direct contact with the medium reservoir, which likely provides some additional material exchange to the cells). Results from these stop-flow experiments revealed permeability was similar to, and in some cases worse than, static conditions, suggesting that fluidic shear stress does maintain barrier integrity within the context of the 3D culture platform (Figure A. 3.4B). We note the possibility that the endothelial cells provide greater conditioning of the medium in the Transwell system relative to the hydrogel system due to volume differences (2 ml versus ~40 ml), and that shear stress-induced effects may compensate for these trophic factors in the perfusion versus static conditions. However, because the goal of this work is to solely establish the performance of the 3D BBB culture platform, these mechanisms were not explored further.

To validate that the observed permeability values corresponded to proper cell-cell junction formation, cells were evaluated for junctional and cytoskeletal markers including occludin, claudin-5, VE-cadherin, and F-actin. CC3-derived BMECs lining gelatin channels show robust expression of both occludin and claudin-5 localized to intercellular junctions (Figure 3.4A). F-actin expression (Figure 3.4B) similarly indicated strong intercellular localization in BMEC-lined channels. In addition, F-actin staining patterns demonstrate the lack of cellular elongation in cells exposed to fluidic shear, a property previously reported to be a unique characteristic of BMECs [150,170–172]. This is particularly evident when BMEC morphology is compared to HUVEC and μVas maintained under static (Figure 3.4C) and perfused (Figure 3.4D) conditions. HUVECs and μVas also strongly expressed VE-cadherin along cell boundaries, but claudin-5 expression was generally absent at cell boundaries and instead diffusely distributed within the cells. Claudin-5 is essential for TJ formation and regulation of BBB permeability, particularly to small compounds [173]. In contrast, claudin-5 is functionally insignificant in establishment of umbilical vein

(HUVEC) barrier [174]. When compared to the fluorescein permeability data (Figure 3.3), these overall data strongly suggest the formation of robust cell-cell junctions in BMECs in 3D culture.

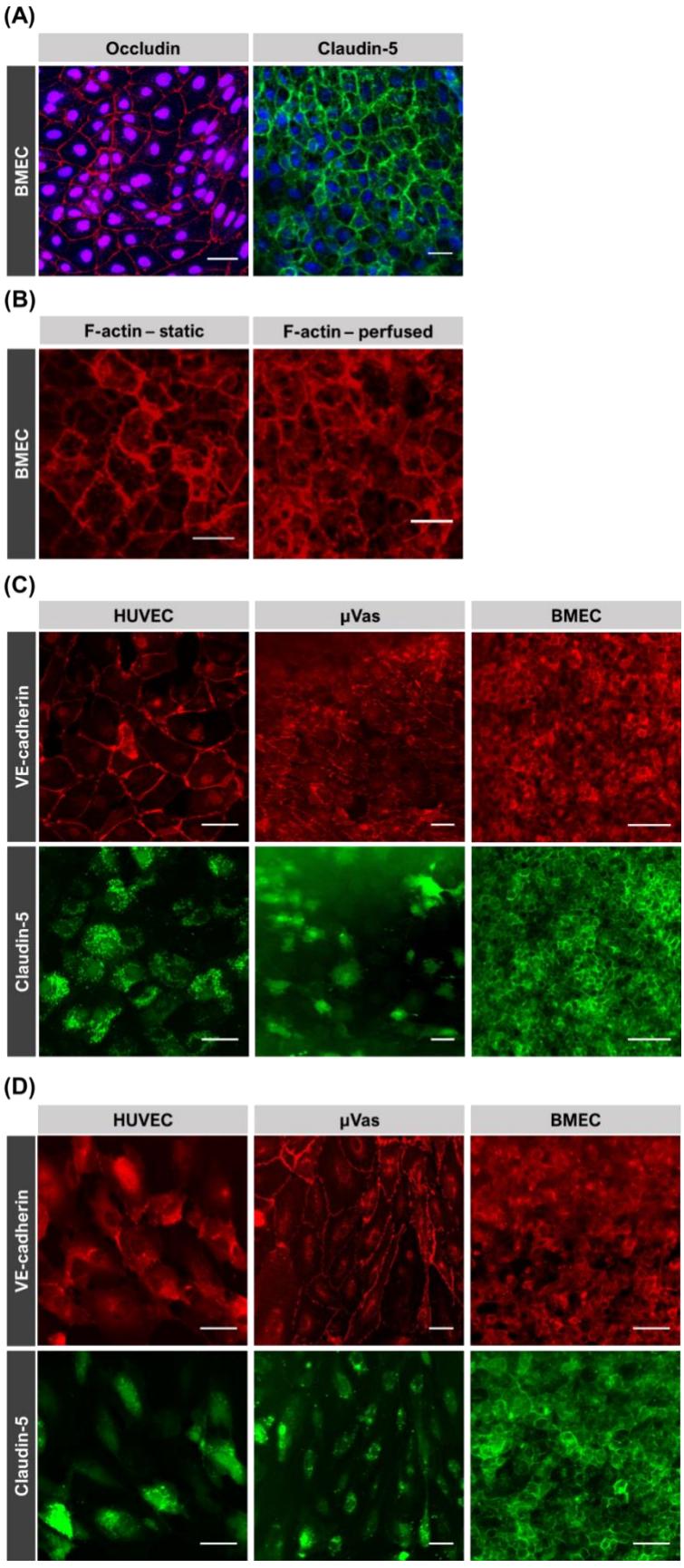
(A)
Occludin
Claudin-5
BMEC
(B)
F-actin – static
F-actin – perfused
BMEC
(C)
HUVEC
μVas
BMEC
VE-cadherin
Claudin-5
(D)
HUVEC
μVas
BMEC
VE-cadherin
Claudin-5

Figure 3.4 Immunofluorescent staining. (A) IMR90-4-derived BMECs labeled for occludin and claudin-5 at day 1 under static conditions. Nuclei are counterstained with Hoechst. (B) IMR90-4-derived BMECs labeled for F-actin at day 1 under static conditions and day 14 under perfused conditions. (C-D) HUVECs, μVas, and IMR90-4-derived BMECs labeled for VE-cadherin and claudin-5 at day 7 under static (panel C) and perfused (panel D) conditions. Each individual image reflects a summative z-projection of individual confocal images without additional processing to flatten images. For each fluorescence channel, the intensity scale is held constant across all samples. As a result, in some images there is a perceived decrease in fluorescence signal for points farthest from the objective that is reflective of channel curvature and slight variations in gelatin topology rather than inherent signal. Scale = 50 μm.

Based on the comparisons between perfusion, static, and stop-flow permeability experiments, we sought to further probe the effects of shear stress on barrier integrity. We found that permeability in channels perfused at 100 μl/min heterogeneously declined between two samples by day 21 (Figure 3.5A). One sample exhibited substantially worse permeability of 2.4×10^{-6} cm/s, while the other sample remained extremely tight at 5.8×10^{-8} cm/s. At this time, we observed signs of angiogenic sprouting at 21 days of perfusion (Figure 3.5C), which was not evident in previous time points in either static or perfused samples and could explain the decline in barrier function between samples.

Perfusion of the ~800 μm diameter channel at a rate of 100 μl/min generates a wall shear of approximately 32 mPa (0.3 dynes/cm^2), well below the physiological range of ~1-3 Pa (10-30 dyne/cm^2) estimated for brain microvasculature [175–178]. Compared to the permeability of BMECs perfused at 100 μl/min, perfusion at 300 μl/min and 1000 μl/min (wall shear of approximately 100 mPa {1 dyne/cm^2} and 320 mPa {3.2 dyne/cm^2}, respectively) for 14 days yielded an overall reduction in passive barrier function. As shown in Figure 3.5B, the permeability coefficient to 3 kDa dextran for BMECs perfused at 300 μl/min and 1000 μl/min was 2.9×10^{-7} cm/s and 4.8×10^{-7} cm/s, respectively, which is approximately 10 times more permeable than BMECs perfused at 100 μl/min. This increase in permeability also corresponded to an increase in

observed incidence of angiogenic sprouting observed on day 14 in channels perfused at higher flow rates and day 21 in channels perfused at 100 µl/min (Figure 3.5C). Importantly, these values are still 10-fold lower than BMECs maintained under static conditions, providing additional evidence that perfusion, even at sub-physiological levels of shear, stabilizes barrier function over time despite minor vascular sprouting.

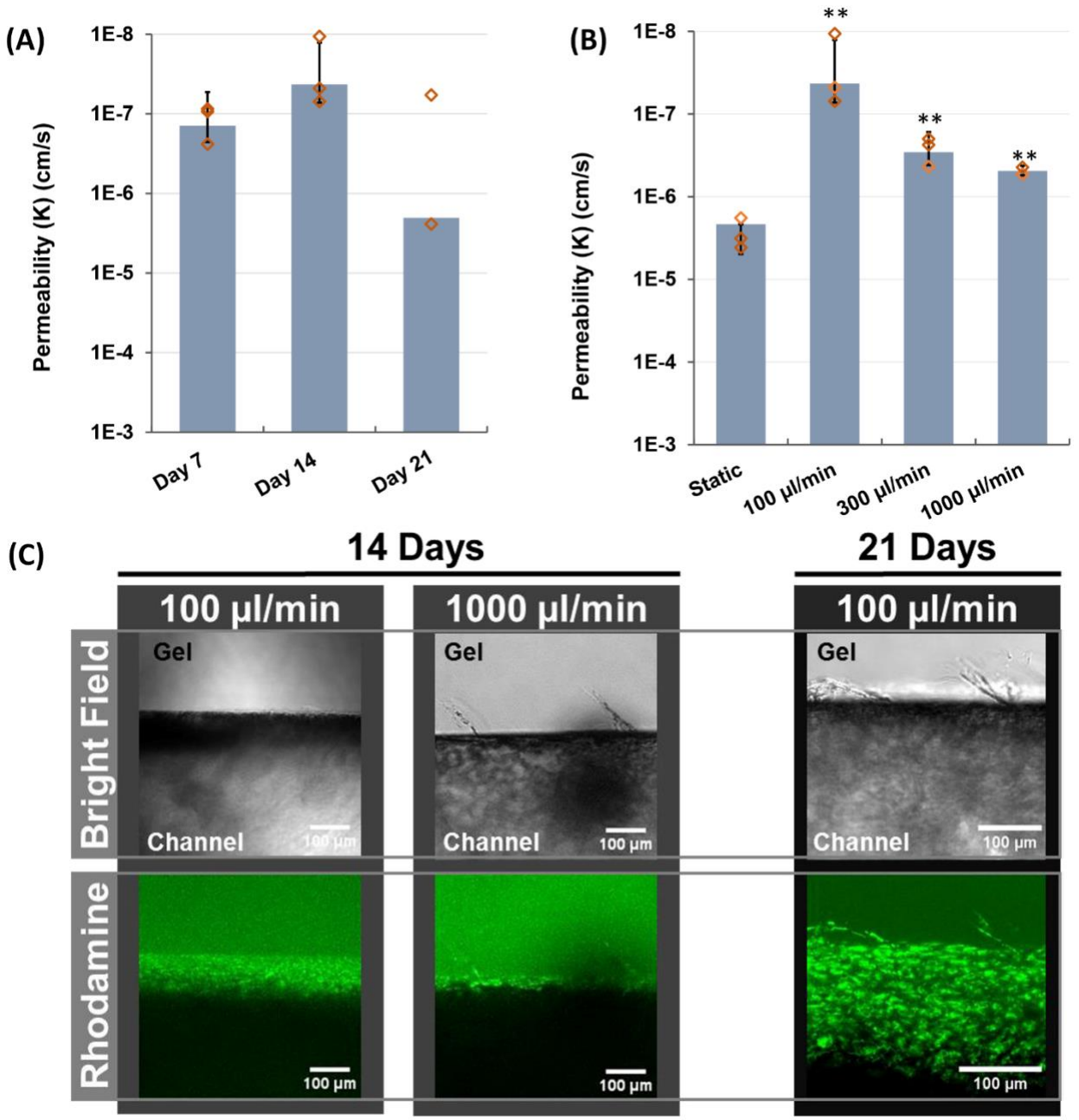

Figure 3.5 Relative impact of shear on BMEC permeability. (A) Permeability to 3 kDa dextran in IMR90-4-derived BMECs perfused at 100 µl/min over 21 days. N ≥ 3 independent biological replicates for all data sets, except N=2 independent biological replicates for the day 21 time point. (◊) indicate actual values of individual replicates. Error bars indicates ± 1 SD. (B) Permeability coefficients to 3 kDa dextran in BMECs perfused for 14 days at 100, 300, and 1000 µl/min, compared to the static control. (◊) indicate actual values of individual replicates. N=2 independent biological replicates for 1000 µl/min dataset, N ≥ 3 independent biological replicates for all other cohorts, (**) indicates $p<0.01$ as compared to static based upon one-way ANOVA and error bar indicates ± 1 SD. (C) Images showing cell sprouting in channels perfused for 14 days (left) at 100

and 1000 µl/min, and 21 days (right) at 100 µl/min. Top image is bright field, bottom image shows cells stained by Rhodamine 123. Scale = 100 µm.

As discussed previously, a hallmark of brain endothelium is the expression of active efflux transporter such as p-glycoprotein (Pgp), breast cancer resistance protein (BCRP), and MRPs. Accordingly, numerous reports have demonstrated that iPSC-derived BMECs possess active efflux activity determined by substrate inhibition assays [144,145,147]. Here, we sought to characterize this efflux activity in IMR90-4-derived BMECs under 3D perfusion culture. Intracellular accumulation of Rhodamine 123 (a Pgp substrate) was evaluated in the presence or absence of cyclosporin A (a Pgp inhibitor) in BMECs after 14 days of perfusion. Similarly, MRP-associated efflux activity was assessed by measuring intracellular accumulation of H2DCFDA in the presence or absence of inhibitor MK-571. As shown in Figure 3.6A-B, BMECs possess robust Pgp activity after 14 days in culture as determined by an increase in intracellular fluorescence of inhibited samples exceeding 80%, providing supporting evidence of the long-term functionality of iPSC-derived BMECs in this 3D culture format. Pgp activity was not influenced by perfusion rate (100, 300, or 1000 µl/min) and remained stable at 21 days of perfusion at 100 µl/min. Comparatively, µVas also exhibited increased uptake of Rhodamine and H2DCFDA in the presence of inhibitors (Figure 3.6C). However, uptake was significantly lower than for BMECs, likely indicating that BMECs have a higher efflux activity and/or expression of efflux transporters. Although peripheral endothelial cells are not commonly known for possessing efflux activity, Pgp expression has historically been observed in skin endothelial cells from papillary but not reticular dermis [179]. Thus, some baseline efflux activity may reflect the source of these control cells.

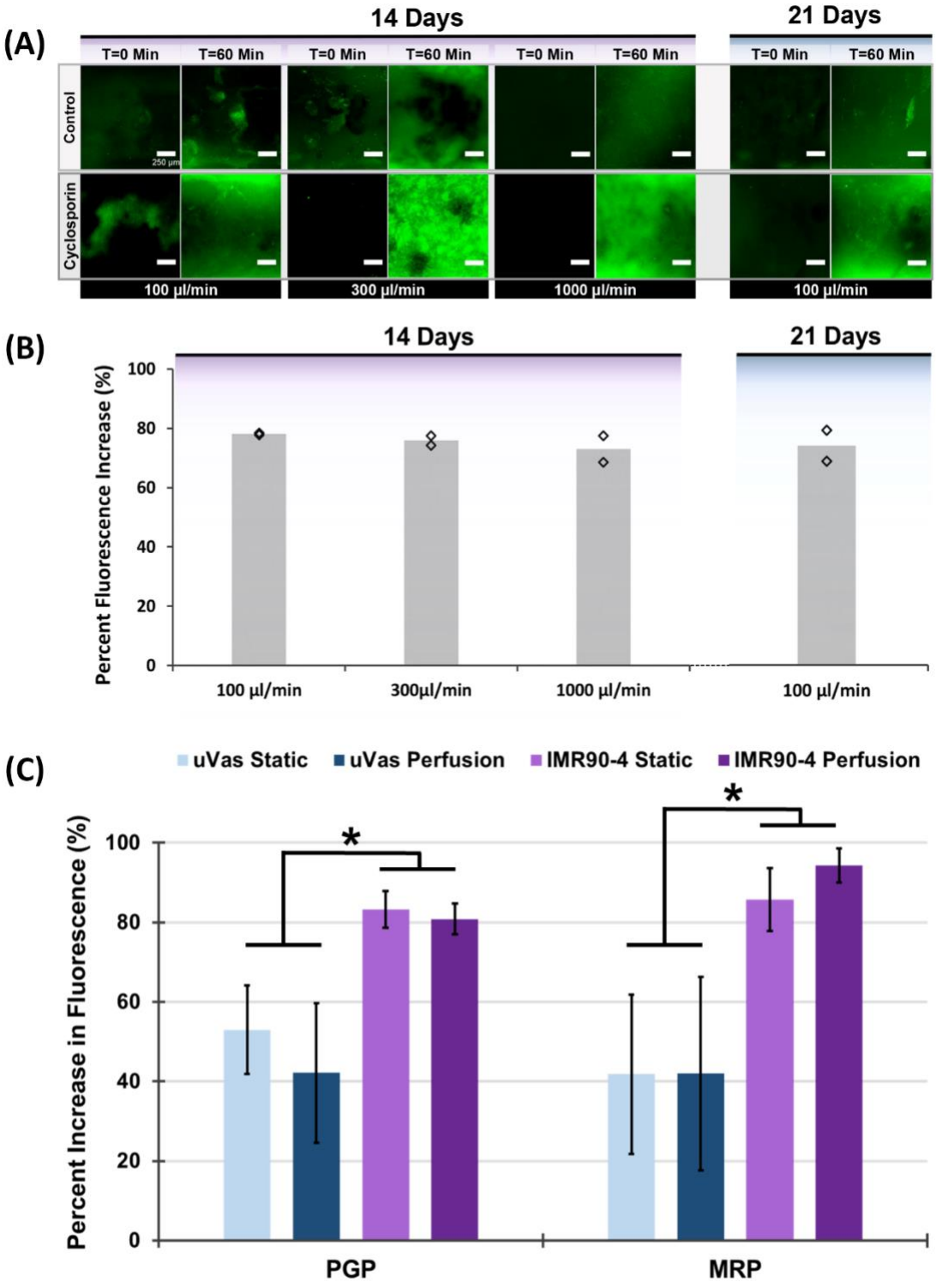

Figure 3.6 Assessment of efflux transporter activity reflects long-term BMEC functionality in perfused channels. (A) Confocal images (z-projections) of IMR90-4-derived BMECs after 14 and

21 days of perfusion at various flow rates that were imaged over the course of one hour of perfusion with medium containing Rhodamine 123 alone (control; top row) or following a 1-hour pre-incubation with cyclosporin A (bottom row). Each pair of control versus cyclosporin A comparisons were conducted using separate channel devices from the same seeding and perfusion cohort. Images reflect summative z-projections of confocal z-stacks without any further processing to flatten images, and all images are presented using the same intensity scale. (B) The increase in cellular Rhodamine 123 accumulation resulting from p-glycoprotein inhibition is quantified in terms of cellular fluorescence intensity relative to non-inhibited controls. $N \geq 2$ independent biological replicates for each data set. (◊) indicate actual values of individual replicates. (C) Comparison of Pgp and MRP activity in channels lined with either μVas or BMECs after 14 days of culture. $N \geq 3$ independent biological replicates for each data set. Error bars indicate ± 1 SD. (*) indicates $p < 0.05$ based on a one-way ANOVA.

In this study, we demonstrate the capability of iPSC-derived BMECs to form confluent 3D monolayers that sustain barrier integrity for up to 3 weeks under continuous perfusion, as measured by low passive diffusion to a cohort of molecular tracers, tight junction localization, and efflux transporter activity. Overall, two of the most significant findings in this work are the longevity of BMEC barrier function and relative barrier properties compared to the non-BBB controls, particularly with respect to permeability of low molecular weight compounds. We note that relative to μVas, iPSC-derived BMECs were significantly less permeable to fluorescein, which is an important small molecule tracer for qualifying BBB integrity. The absolute permeability of fluorescein is similar to results obtained from measurements in 2D Transwell platforms (10^{-6}-10^{-7} cm/s) [147], indicating consistency in BMEC performance and robustness of the paracellular barrier in 3D culture. Meanwhile, the exclusion of albumin and decreased *CAV1* expression suggest reduced vesicular transport in BMECs relative to non-BBB controls.

We further note that perfusion of BMEC-lined channels under low shear conditions has a stabilizing effect on barrier integrity over time compared to non-perfused controls, with similar performance in barrier function in BMECs derived from two separate iPSC lines. Our data indicate that perfusion helps maintain long-term barrier function through a combined effect of shear-

induced mechanical cues and continual medium circulation providing improved nutrient/waste exchange. Recently, iPSC-derived BMECs co-cultured with astrocytes in perfused microfluidic channels were reported to maintain *in vivo*-like TEER values for 12 days, where the authors concluded that shear forces were not essential for the establishment of strong intercellular junctions but did provide a clear stabilizing effect upon barrier integrity over time [150], which is consistent with our findings. Another group has reported that shear forces are non-requisite for tight junction formation in iPSC-derived BMEC monolayers, but that shear positively contributes to barrier health by providing necessary mechanical cues as well as reducing ROS-mediated degradation [170,180]. In our 3D system, increased shear forces above our initially tested values did not strengthen or stabilize barrier function. However, these measurements are complicated by the observation of increased angiogenic sprouting at earlier time points associated with higher flow rates, and the cytoskeletal restructuring of angiogenic sprouting is known to increase the permeability of brain endothelium [181]. It is likely that the increase in interstitial flow associated with higher perfusion rates resulted in increased sprouting in BMEC monolayers, a process normally inhibited by interactions with surrounding smooth muscle cells and astrocytes [182,183]. Thus, we hypothesize that incorporation of additional NVU cell types will further stabilize barrier function by preventing angiogenic sprouting, which will be examined in future studies.

Interestingly, despite robust barrier function and expression of junction-associated VE-cadherin, claudin-5, and occludin protein, our global expression data indicates low mRNA transcript abundances for both endothelial and BBB-associated genes. Transcript levels in iPSC-derived BMECs cultured for 1 day under static conditions were similar to iPSC-derived BMECs cultured in 2D well plates [184], suggesting consistency with other models. We note that transcriptional profiling has been performed on both mouse and human brain endothelial cells, and

for canonical BBB/endothelial genes (e.g. *OCLN*, *CLDN5*, *CDH5*, *PECAM1*, *SLC2A1*, *MFSD2A*, *ABCB1*), expression levels in mouse are consistently ~10-100-fold higher than human [185]. At present, it is unclear whether low transcript abundance in iPSC-derived BMEC models reflects *in vitro* culture conditions or a species difference, and more investigations are required in this area. We also note that despite overall similarity between day 1 static cultures and day 14 perfusion cultures, endothelial-specific genes become noticeably downregulated at the later time point. Thus, although perfusion and shear stress may help stabilize barrier function through upregulation of currently unknown signaling pathways, these factors potentially have a lower influence on maintenance of vascular identity. We hypothesize that inclusion of pericytes and future optimization of media composition will help promote maintenance of endothelial gene signatures at these later time points. These investigations and more in-depth analyses of transcript data are expected to identify more explicit differences between 2D and 3D cultures of iPSC-derived BMECs, similar to other studies [186], as well as possible human-specific BBB gene expression signatures.

3.5 Conclusion

Overall, we highlight the utility of our 3D model for exploring interactions between NVU cell types, modeling neurovascular disease, and assessing treatment strategies. Since we have used gelatin with a benign enzymatic crosslinking approach compatible with cell encapsulation [187], we expect to be able to establish co-cultures that represent endogenous organization of NVU cell types. Given advancements in the production of neurovascular cells from iPSCs, including diverse subtypes of neurons, astrocytes, oligodendrocytes, microglia, pericytes, and smooth muscle, a fully isogenic 3D model is a realistic possibility in the near future. Also, given prominent vascular

contributions to neurodegenerative diseases [119], future iterations of this biomimetic 3D NVU model could provide a useful platform for modeling disease phenotypes. Lastly, although this model is not expected to replace standard Transwell setups for screening prospective therapeutic compounds for BBB permeation, the performance of lead candidates could be further tested in these 3D NVU systems, where a more physiological microenvironment is expected to improve predictions of therapeutic efficacy.

3.6 Appendix

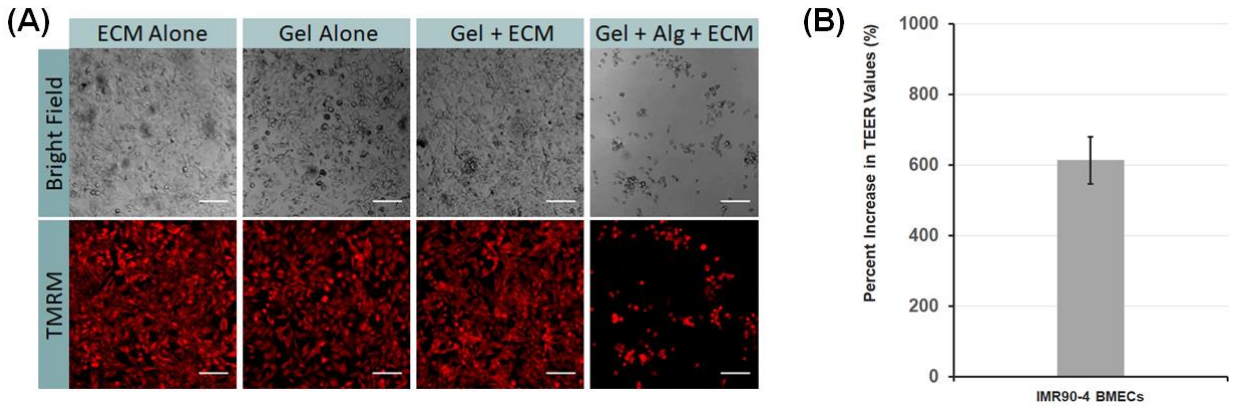

Figure A. 3.1 Effects of hydrogel composition upon EC attachment. **(A)** IMR90-4-derived BMECs were seeded in 6-well plates coated with collagen/fibronectin solution (ECM Alone) or thin hydrogels comprised of enzymatically crosslinked 10% gelatin (Gel Alone), 10% gelatin treated with collagen/fibronectin (Gel + ECM), or 10% gelatin/0.25% Sodium-alginate treated with collagen/fibronectin solution (Gel+Alg+ECM). Gelatin/alginate hydrogels were crosslinked with mTG suspended in a 30 mM $CaCl_2$ solution. Cells were labeled with 1 µM mitochondrial stain, tertramethylrhodamineester (TMRM, Thermo Fisher) to identify live cells in fluorescence images. Scale bar represent 100 µm. **(B)** Graph illustrating the percent increase in maximum TEER values obtained from IMR90-4-derived BMECs, initially differentiated at starting iPSC densities of 120,000 or 150,000 cells per well [147], cultured on 7.5% gelatin hydrogels treated with collagen/fibronectin solution relative to non-treated hydrogels. Results reflects data compiled from 3 independent seedings from the 120,000 cells/well condition (N=3 Transwell filters per seeding, or N=9 total) and 2 independent seedings from the 150,000 cells/well condition (N=3 Transwell filters per seeding, or N=6 total). Error bars indicate ± 1 SD.

(A)

Static Culture						
		Average	SD	*N1*	*N2*	*N3*
Day 1	IMR90-4 (D1)	1.22389E-07	5.9755E-08	1.6227E-07	5.4123E-08	1.5077E-07
	HUVEC	1.18354E-05	3.9553E-06	1.0857E-05	9.66E-06	1.499E-05
	uVas	4.95379E-07	3.6477E-07	2.7962E-07	2.9571E-07	9.1081E-07
Day 7	IMR90-4 (D1)	4.55303E-07	2.0771E-07	4.0714E-07	6.819E-07	2.7686E-07
	HUVEC	6.9814E-06	1.7915E-05	8.7731E-07	1.158E-06	1.8909E-05
	uVas	1.30489E-06	3.0378E-07	1.0538E-06	1.217E-06	1.6438E-06
Day 14	IMR90-4 (D2)	1.82649E-07	1.0749E-07	3.0547E-07	1.5376E-07	9.3933E-08
	IMR90-4 (D1)	2.15148E-06	3.6044E-06	1.8057E-07	4.1224E-06	3.1932E-06
	HUVEC	1.95006E-05	3.6499E-05	2.7554E-05	2.9059E-05	1.8894E-06
	uVas	1.23186E-06	2.1343E-07	1.2382E-06	1.017E-06	1.4438E-06
	CC3	1.98234E-07	1.019E-07	9.247E-08	2.9578E-07	2.0645E-07

(B)

Perfused Culture						
		Average	SD	*N1*	*N2*	*N3*
Day 1	IMR90-4 (D1)	1.94198E-07	1.8145E-08	2.0702E-07	1.8138E-07	1.8057E-07
	HUVEC	1.19041E-05	2.0004E-05	2.0793E-05	3.0155E-06	2.8306E-05
	uVas	5.95E-07	2.25E-07	5.30E-07	4.16E-07	7.56E-07
Day 7	IMR90-4 (D1)	1.40283E-07	8.6925E-08	9.3816E-08	2.4042E-07	8.6609E-08
	HUVEC	7.61697E-06	6.4097E-06	8.5993E-06	1.1918E-05	2.334E-06
	uVas	5.30E-07	1.04E-08	1.3171E-06	1.6912E-06	1.1606E-06
Day 14	IMR90-4 (D2)	3.21978E-09	1.733E-09	5.2198E-09	2.2743E-09	2.1652E-09
	IMR90-4 (D1)	4.27278E-08	3E-08	4.7624E-08	6.9907E-08	1.0653E-08
	HUVEC	2.28263E-05	1.1676E-05	1.8236E-05	2.2458E-05	2.7785E-05
	uVas	1.56426E-06	1.3679E-06	2.9212E-06	1.3171E-06	4.5456E-07
	CC3	4.24561E-08	2.7269E-08	2.5754E-08	2.7707E-08	7.3907E-08

Figure A. 3.2 Permeability measurement data. Calculated values for 3 kDa dextran in (A) static and (B) perfused channels lined with HUVEC, µVas, IMR90-4-derived BMECs, or CC3-derived BMECs. Two explicitly different IMR90-4-derived BMEC batches were used to directly compare biological variance (denoted as D1 and D2).

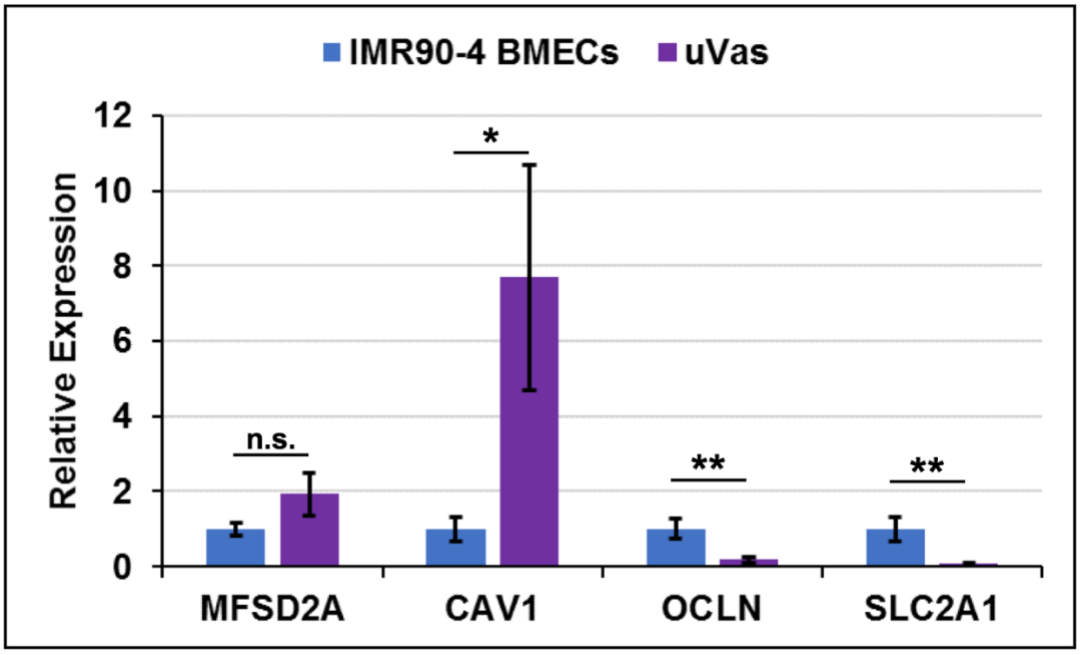

Figure A. 3.3 qPCR analysis of BBB related markers. Relative expression of MSFD2A, CAV1 (Caveolin-1), OCLN (Occludin), and SLC2A1 (GLUT-1) in IMR90-4-derived BMECs versus µVas cells isolated from channels after 14 days of continual perfusion. GAPDH was used as the housekeeping gene. N=3 independent biological replicates for each condition. Error bars indicate ± 1 SD. Statistical significance was calculated using the student's unpaired t-test: *, $p<0.05$; **, $p<0.01$; n.s., $p>0.05$.

(A)

K (cm/s) (x10^{-7})		
Day 7	BMEC	6.4 ± 3.2
	HUVEC	114 ± 4.1
Day 14	BMEC	5.8 ± 2.2
	HUVEC	109 ± 15.4

(B)

K (cm/s) (x10^{-7})		
µVas	Fluorescein	507 ± 436
	3 kDa dextran	13.9 ± 2.7
	Albumin	0.03 ± 0.05
BMEC	Fluorescein	168 ± 50.8
	3 kDa dextran	102 ± 9.7
	Albumin	0.02 ± 0.001

Figure A. 3.4 Permeability measurements from 3D stop-flow conditions and 2D Transwell controls. (A) Permeability of CC3-derived BMECs and RFP-HUVECs to 3 kDa dextran when cultured on Transwell filters. (B) Permeability values from diffusion of sodium fluorescein, 3 kDa dextran, and albumin across cell monolayers after 14 days under stop-flow conditions. IMR90-4-derived BMECs and µVas were subjected to 10 min of media perfusion per day at 100 µl/min for 14 days. For all experiments, data represent mean ± SD calculated from N=3 independent biological replicates.

(A)

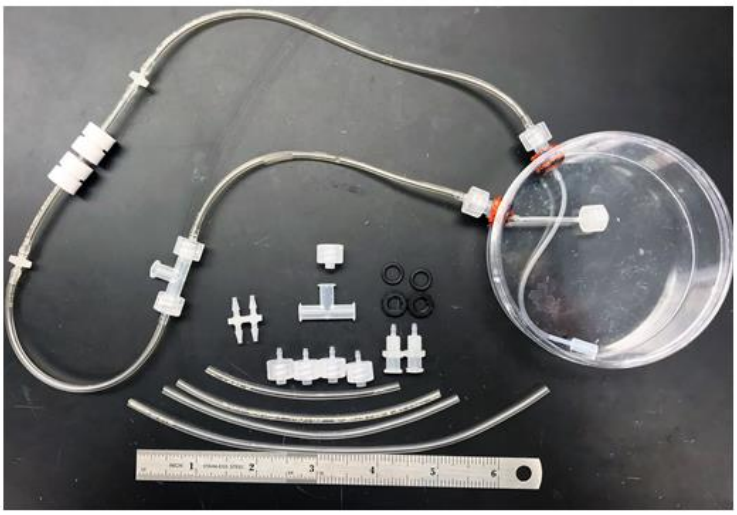

(B)

Materials	Volume
Tygon tubing - 1/16th in. (ID) x 22 in (L)	1.5 ml
Petri dish - 100 mm (D) x 30 mm (H)	40 ml
(4) 1/16th in. polypropylene Male barbed luer	
(2) 1/16th in. polypropylene barb to barb connector	
(2) Polypropylene 28 UNF threaded barb (1/16th in.) bulkhead	
(1) Polypropylene t-junction	
(1) Polypropylene luer cap	
(2) VIKON o-rings	
(2) PVDF bulkead locking nuts	

Figure A. 3.5 Perfusion system assembly components. (A) Fully assembled fluidic culture apparatus used for continual and stop-flow perfusion experiments. (B) List of individual components used to construct perfusion system. The total volume of medium within the perfusion system during an experiment is estimated to be between 40-45 ml.

(A.)

Diffusion Coefficient in 10% Gelatin (μ^2/s)	
Fluorescein (332 Da)	69.3 ± 1
3K Cascade Blue Dextran	22.5 ± 0.6
3K AF 680 Dextran	20.9 ± 0.3
10K Oregon Green Dextran	12.6 ± 0.5
Fluorescein-BSA (66K Da)	4.04 ± 0.3

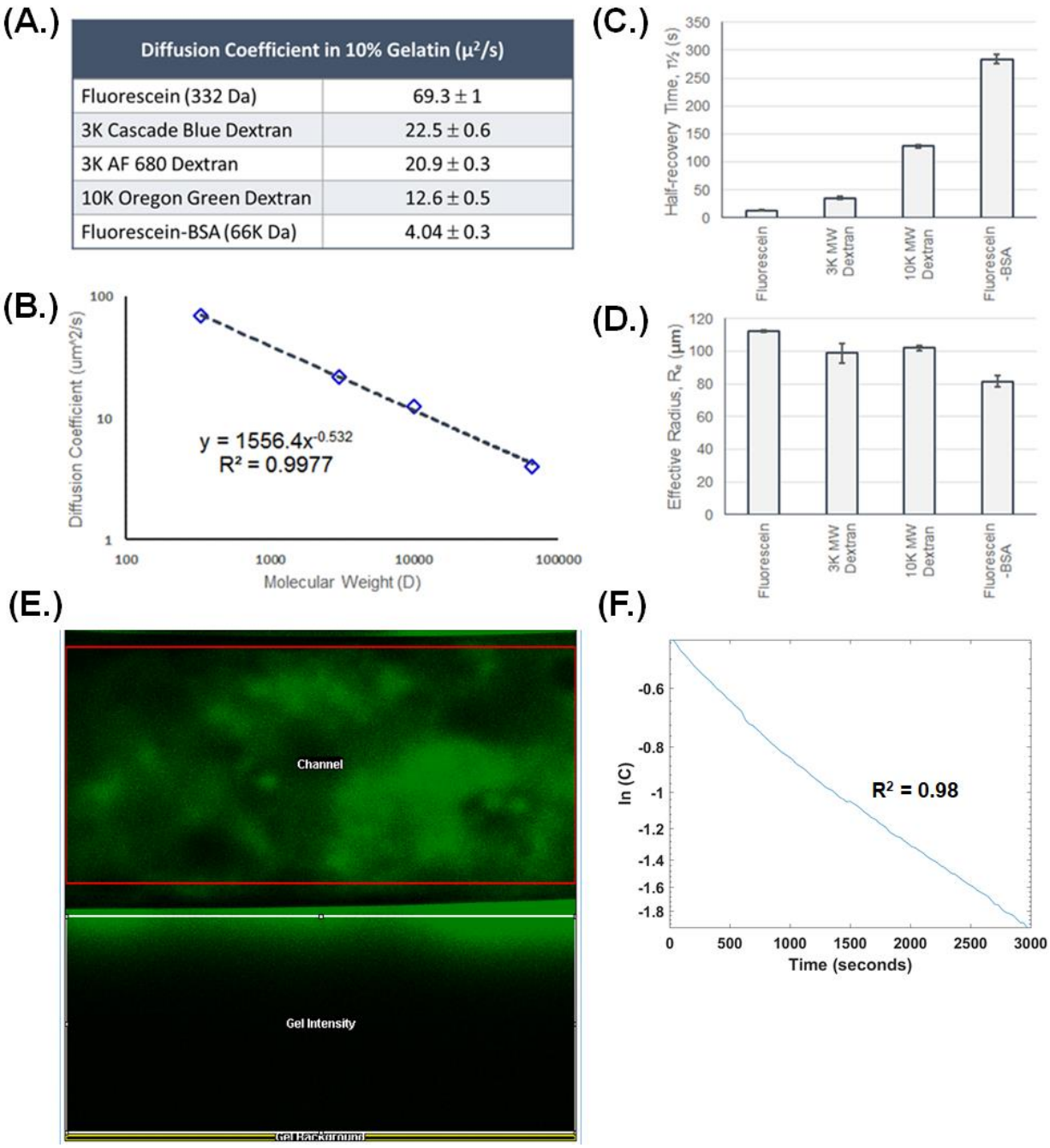

Figure A. 3.6 Measuring diffusion coefficients in gelatin matrix using FRAP analysis. Related to Figure 2 and Experimental Procedures. (A) Calculated diffusion coefficient values based upon N ≥ 3 experiments. (B) Comparison of molecular weight to calculated diffusion coefficient. Slope of the line is -0.53 with an R-squared value of 0.997, which correlates with previous reports [188]. (C) Half-recovery times of fluorescein and dextran FRAP experiments. (D) Effective radius measurements of bleached samples. Error bars indicate ± 1 SD. (E) Screen capture illustrating ROI delineations for image processing in Fiji. (F) Representative plot of Log (C) versus time generated from intensity profiles in MATLAB. The slope of the linear plot corresponds to Lambda (λ) and is used in Equation S4 to calculate the diffusion coefficient.

```
//Analyze confocal timelapse data sets for permeability measurements

//Find Background Intensity of Gelatin
makeRectangle (0,1020, 1024, 10);
	// add roi (x, y, width, height)
macro "Show Statistics" {
if (nSlices>1) run("Clear Results");
		getVoxelSize(w, h, d, unit);
n = getSliceNumber();
for (i=1; i<=nSlices; i++) {
setSlice(i);
getStatistics(area, mean, min, max, std);
row = nResults;
if (nSlices==1)
setResult("Area ("+unit+"^2)", row, area);
setResult("Mean ", row, mean);
setResult("Std ", row, std);
setResult("Min ", row, min);
setResult("Max ", row, max);
	}
setSlice(n);
updateResults();
saveAs("Results","path\\file.csv");

//Find Intensity of Channel
makeRectangle (0,100, 1024, 300);
	//add roi (x,y,w,h)
macro "Show Statistics" {
if (nSlices>1) run("Clear Results");
		getVoxelSize(w, h, d, unit);
n = getSliceNumber();
for (i=1; i<=nSlices; i++) {
setSlice(i);
getStatistics(area, mean, min, max, std);
row = nResults;
if (nSlices==1)
setResult("Area ("+unit+"^2)", row, area);
setResult("Mean ", row, mean);
setResult("Std ", row, std);
setResult("Min ", row, min);
setResult("Max ", row, max);
	}
setSlice(n);
updateResults();
saveAs("Results", "path\\name.csv");
	}
```

```
//Find Intensity of Gelatin near channel
makeRectangle (0,450, 1024, 560);
        // add roi (x, y, w,h)
macro "Show Statistics" {
if (nSlices>1) run("Clear Results");
                getVoxelSize(w, h, d, unit);
n = getSliceNumber();
for (i=1; i<=nSlices; i++) {
setSlice(i);
getStatistics(area, mean, min, max, std);
row = nResults;
if (nSlices==1)
setResult("Area ("+unit+"^2)", row, area);
setResult("Mean ", row, mean);
setResult("Std ", row, std);
setResult("Min ", row, min);
setResult("Max ", row, max);
        }
setSlice(n);
updateResults();
saveAs("Results","path\\filename.csv");
}

//Analyze Time Series
makeLine(0,512,1024,512,1);
        //add line of interest
        //(x1,y1,x2,y2,width)
macro "Stack profile Data" {
if (!(selectionType()==0 || selectionType==5 || selectionType==6))
exit("Line or Rectangle Selection Required");
setBatchMode(true);
        run("Plot Profile");
        Plot.getValues(x, y);
        run("Clear Results");
        for (i=0; i<x.length; i++)
    setResult("x", i, x[i]);
         close();
    n = nSlices;
        for (slice=1; slice<=n; slice++) {
                showProgress(slice, n);
                setSlice(slice);
                profile = getProfile();
                sliceLabel = toString(slice);
                sliceData = split("\n");
                        if (sliceData.length>0) {
```

```
  line0 = sliceData[0];
                                                if (lengthOf(sliceLabel) > 0)
                                                        sliceLabel = sliceLabel+ " ("+ line0 + ")";
          }
                  for (i=0; i<profile.length; i++)
                          setResult(sliceLabel, i, profile[i]);
    }
          setBatchMode(false);
          updateResults;
          saveAs("Results", "path\\filename.csv");
```

Figure A. 3.7 Fiji macro script

```
%% Calculate permeability from confocal imaging datasets

        Dgelatin=20.9 %From FRAP Data 10k=12.6, 3k=20.9
        Distance_microns = 1120 %distance from channel edge to gel edge

        %%Import measurements from fiji macro
        Iedge = xlsread('C:\path\ GelBG.csv',1,'B2:B241');%%Average Intensity at no-flux
region
        Channel_Io = xlsread('C:\pathChannelBG.csv',1,'B2:B241'); %%Intensity within
channel
        Igel=  xlsread('C:\path\GelNearChannelBG.csv','B2:B241');%%Average intensity of
gel

        %% Convert slice/frame number to time interval
        Slice = xlsread('C:\path\Profile.csv','Profile','C1:IH1');
        Time_minute = Slice*.5;
        Time_second = Time_minute*60;

        %%Calculating C for each timepoint
        C_numerator=Iedge-Channel_Io;
        C_denominator = Igel-Channel_Io;
        C=C_numerator./C_denominator;

        %% Graphing logC versus time
        x = Time_second;
        y = C;
        plot=semilogy(x,y);

        %%Fit logC versus time to extract Lambda (slope)
        curvefit = fitlm(x,y,'poly1');
                coeff=curvefit.Coefficients.Estimate;
                Rvalue=curvefit.Rsquared.Ordinary;
                output = xlswrite('C:\path\curvefit.xlsx', coeff,1);

        %Use Lambda to calculate K (permeability) in microns/second
        Lamda = xlsread('C:\path\curvefit.xlsx',1,'A2:A2');
        K=(Dgelatin/Distance_microns)*(Lamda*tan(Lamda));
        K_cm = K*10000; %% conversion to cm/s
                outputValue = {;'K cm/s';'Lambda';'Rsquared'}
                values=[;K_cm; K;Lamda;Rvalue];
                result= table(outputValue, values);
                %Save results in excel file
                writetable(result,'C:\path\Results.xlsx','Sheet',1,'Range','A1:B3')
```

Figure A. 3.8 MATLAB code

Chapter 4

A SIMPLIFIED, FULLY DEFINED DIFFERENTIATION SCHEME FOR PRODUCING BLOOD-BRAIN BARRIER ENDOTHELIAL CELLS FROM HUMAN IPSCS

Adopted from Neal EH, Marinelli NA, Shi Y, McClatchey PM, Balotin KM, Gullett DR, et al. A Simplified, Fully Defined Differentiation Scheme for Producing Blood-Brain Barrier Endothelial Cells from Human iPSCs. Stem Cell Rep. 2019;12:1380–8 *with permission from Elsevier Publishing.*

4.1 Summary

Human induced pluripotent stem cell (iPSC)-derived developmental lineages are key tools for *in vitro* mechanistic interrogations, drug discovery, and disease modeling. iPSCs have previously been differentiated to endothelial cells with blood-brain barrier (BBB) properties, as defined by high transendothelial electrical resistance (TEER), low passive permeability, and active transporter functions. Typical protocols use undefined components, which impart unacceptable variability on the differentiation process. We demonstrate that replacement of serum with fully defined components, from common medium supplements to a simple mixture of insulin, transferrin, and selenium, yields BBB endothelium with TEER in the range of 2000-8000 $\Omega x cm^2$ across multiple iPSC lines, with appropriate marker expression and active transporters. The use of fully defined medium vastly improves the consistency of differentiation, and co-culture of BBB endothelium with iPSC-derived astrocytes produces a robust *in vitro* neurovascular model. This defined differentiation scheme should broadly enable the use of human BBB endothelium for diverse applications.

4.2 Introduction

The blood-brain barrier (BBB) is composed of brain microvascular endothelial cells (BMECs), which strictly maintain central nervous system (CNS) homeostasis by regulating material exchange between the bloodstream and parenchyma [8]. Disruption of the BBB is strongly implicated in many neurodegenerative diseases [93], and its functions are also influenced by peripheral conditions that can reduce its fidelity and result in CNS damage [189]. Conversely, an intact BBB prevents efficient delivery of therapeutics to the CNS. Thus, a better understanding of BBB properties is vital for the treatment of CNS disorders.

In vitro BBB models are often utilized to study mechanisms of neurovascular regulation and dysfunction during disease and also can serve as a tool for high throughput screening of BBB-permeant compounds. Historically, most BBB models have been constructed from primary animal sources, but it is well-recognized that a human model would be preferred owing to general species' differences [51,62]. However, until recently, *in vitro* human BBB models were limited to either primary [64] or immortalized BMECs [190], whereas each source has downsides in terms of yield and barrier fidelity.

In 2012, human pluripotent stem cells (hPSCs) were successfully differentiated to BMECs, as determined by elevated TEER (~850 $\Omega x cm^2$), representative permeability to a cohort of small molecules, and active efflux transporter function [65]. The addition of retinoic acid (RA) during the differentiation process further enhanced passive barrier function (TEER ~3000 $\Omega x cm^2$) [67]. These BMECs have been utilized for mechanistic interrogations [191] and are effective for modeling BBB-specific disease mechanisms [192]. However, limitations still exist in the differentiation process. TEER has been estimated *in vivo* up to 8000 $\Omega x cm^2$ based on radioactive ion permeabilities [193], and although this value may not be the absolute upper limit

in humans, hPSC-derived BMECs in monoculture typically exhibit about half of this TEER threshold [192,194,195]. Moreover, BMEC differentiation generally relies on the use of serum-containing medium, which limits consistency and reliability of the final purified population. Despite advancements in standardization of the differentiation process [111,195], more work is needed to achieve optimum results.

Here, we detail an unexpected improvement to the BBB differentiation procedure when transitioning to serum-free methods. By replacing the serum component of the differentiation medium with fully defined factors, we can consistently achieve TEER maxima of 2000-8000 Ωxcm^2 in BMEC monocultures across multiple induced pluripotent stem cell (iPSC) lines, with expected marker expression and transporter activity. The defined procedure also consistently generated a barrier phenotype in BMECs derived from several disease-specific lines that was equal or better than BMECs derived in serum. Moreover, the exclusion of serum significantly enhanced the responsiveness of BMECs to co-culture with astrocytes, with maximum TEER values reproducibly exceeding 9000-10500 Ωxcm^2. These advances in differentiation technique are expected to have a positive impact towards using iPSC-derived BMECs to model age- and disease-related declines in BBB function.

4.3 Materials and methods

4.3.1 Endothelial cell medium preparation

Basal endothelial medium (human endothelial serum free medium; Thermo Fisher Scientific) was supplemented with 50× diluted B27 (Thermo Fisher Scientific), 200× diluted B27, 100× N2 (Thermo Fisher Scientific), or ITS mixture consisting of 2.14 mg/L insulin (Sigma Aldrich), 10.7 mg/L holo-transferrin (R&D Systems), and 14 μg/L sodium selenite (Fisher

Scientific). These media were further supplemented with 20 ng/mL basic fibroblast growth factor (bFGF; Peprotech) and 10 μM retinoic acid (RA; Sigma Aldrich) for differentiation days 4 to 6 and for subculturing cells onto plates and Transwell filters. bFGF and RA were removed from the medium 24 h after subculturing to induce barrier phenotype.

4.3.2 iPSC maintenance

CC3, CD10, HD70-2, and TSP8-15 iPSCs were maintained in E8 medium [101], prepared as previously described [195], on growth factor reduced Matrigel (Corning). Lines CC3, CD10, and HD70-2 have been described elsewhere [107,108], and line TSP8-15 was derived for this manuscript using previously described methods [196]. iPSCs were passaged upon reaching 60-80% confluence. For passaging, iPSCs were washed once with Versene solution (Thermo Fisher Scientific) and incubated with Versene solution for 5 minutes at 37°C. Cells were then collected in E8 medium and redistributed to Matrigel-coated plates at the desired density.

4.3.3 iPSC differentiation to BMECs

iPSCs were washed once in DPBS (Thermo Fisher Scientific) and incubated with Accutase (Stem Cell Technologies) for 3 min at 37°C. The resultant single cell suspension was collected via centrifugation, resuspended in fresh E8 medium, and density was counted using a Countess II (Thermo Fisher Scientific). Trypan blue was used to measure viability, and cells were seeded according to the measured live cell count. Cells were seeded at a density of 15,800 cells/cm^2 in E8 medium containing 10 μM Y-27632. Differentiation was initiated 24 h after seeding by changing medium to E6 medium [102]. Medium was changed daily for 4 days. Next, cells were given human endothelial serum free medium (hESFM; Thermo Fisher Scientific) supplemented with 20 ng/mL bFGF, 10 μM RA, and either PDS or a serum-free supplement (B27, N2, or ITS). Medium was not changed for 48 h. Following this treatment, cells were washed once with DPBS and incubated

with Accutase for 20 min to 45 min, until a single cell suspension was formed. Cells were collected via centrifugation and plated, also referred to as subculturing, onto substrates coated in a mixture of 400 μg/mL collagen IV (Sigma Aldrich) and 100 μg/mL fibronectin (Sigma Aldrich). Substrates were either tissue culture polystyrene plates (Fisher Scientific) or Transwell filters with 1.1 cm^2 polyethylene terephthalate membranes and 0.4 μm pores (Fisher Scientific). Plates were coated for a minimum of 1 h, up to overnight, and filters were coated for a minimum of 4 h, up to overnight. Cells were replated using a ratio of 1 well of a 6-well plate to 3 wells of a 12-well plate, 3 Transwell filters, or 6 wells of a 24-well plate. Media was then changed to basal endothelial medium with desired supplement but lacking bFGF and RA. 24 h after subculture, TEER was measured using STX2 chopstick electrodes and an EVOM2 voltohmeter (World Precision Instruments) approximately every 24 h, and reported values are corrected for the resistance of an empty Transwell filter. Cells were used for all functional assays 24 h after the removal of bFGF and RA.

4.3.4 iPSC differentiation to astrocytes

CC3 iPSCs were differentiated to astrocytes as previously described [195]. Briefly, CC3 iPSCs were collected and density was determined as described above for BMEC differentiation. Cells were seeded at a density of 2.5×10^5 cells/cm^2 in E8 medium containing 10 μM Y-27632. Differentiation was initiated 24 h after seeding by changing medium to E6 medium supplemented with 10 μM SB431542 (Tocris) and 1 μM dorsomorphin dihydrochloride (Tocris) [102]. Medium was replaced every 24 h for six days, after which cell clumps were manually transferred to a fresh Matrigel-coated plate with E6 medium containing 10 ng/mL ciliary neurotrophic factor (CNTF; Peprotech), 10 ng/mL epidermal growth factor (EGF; Peprotech), and 10 μM Y-27632. Medium was subsequently changed every 72 for 30 days to E6 containing CNTF and EGF but lacking Y-27632. On day 30, cells were collected using Accutase, centrifuged to pellet, and split via a ratio

of 1 well of a 6-well plate to 1 full plate. Medium changes (E6 containing 10 ng/mL CNTF and 10 ng/mL EGF) were performed every 48 h, and cells were passaged upon reaching approximately 80% confluency. Cells were cultured a minimum of two passages prior to being cryopreserved in E6 medium containing 10% DMSO (Sigma-Aldrich) and 10 μM Y-27632. Astrocytes were seeded for co-culture at a ratio of 1 well of a 6-well plate to 9 wells of a 12-well plate and maintained in E6 medium containing 10 ng/mL CNTF and 10 ng/mL EGF until initiation of co-culture. Upon initiation of co-culture, astrocytes were changed to basal endothelial medium containing 200× B27 but lacking bFGF and RA.

4.3.5 TEER measurement

All TEER plots presented are the results of a biological N=1. Each time point is the result of a technical N=9 as BMECs were purified onto triplicate filters for all conditions tested, and each filter was measured in 3 locations per time point. All data are represented as mean ± standard deviation for these collective measurements. All results were confirmed in a minimum of two additional biological replicates (specific numbers of biological replicates are noted in the main text). Following the medium change on day 0 of subculture to remove bFGF and RA, no further medium changes were performed for the duration of the experiments.

4.3.6 Immunocytochemistry

Cells were washed twice with DPBS and incubated with either 4% paraformaldehyde (Sigma Aldrich) for 20 min or 100% ice-cold methanol for 10 min. Cells were then washed three times with DPBS for a minimum of 5 min per wash. Cells fixed in 4% paraformaldehyde were pre-blocked for a minimum of 1 h at room temperature in DPBS with 5% donkey serum (Sigma Aldrich) and 0.3% Triton X-100 (Sigma Aldrich), referred to as PBS-DT. Cells fixed in methanol were pre-blocked for a minimum of 1 h at room temperature in DPBS with 5% donkey serum,

referred to as PBSD. Cells were then incubated with primary antibody (listed in Table A. 4.1) at the desired dilution in PBS-DT or PBSD overnight at 4°C. Cells were rinsed once with DPBS and washed five times with a minimum of 5 min per wash using DPBS with 0.3% Triton X-100 (PBS-T) or DPBS. Secondary antibodies (listed in Table A. 4.2) were diluted in the same buffers used for primary antibodies and incubated with cells for 1-2 h at room temperature. Following this incubation, nuclei were labeled using 4′,6-Diamidino-2-pheny-lindoldihydrochloride (DAPI; Thermo Fisher Scientific) or Hoechst 33342 trihydrochloride trihydrate (Thermo Fisher Scientific) diluted in PBS-T or DPBS for 10 min. DAPI solution was then removed, cells rinsed once with PBS-T or DPBS, and cells were washed four times with PBS-T or DPBS for a minimum of 5 min per wash. Cells were visualized on a Leica DMi8 microscope.

4.3.7 Sodium fluorescein permeability assay

BMECs on Transwell filters were replaced with fresh medium (hESFM plus B27) 1 h prior to the start of the assay. Medium was then aspirated from the apical chamber of the Transwell filter and replaced with 10 μM sodium fluorescein (Sigma Aldrich) diluted in fresh medium. 200 μL of medium was immediately removed from the basolateral chamber of each filter, transferred to a 96-well plate, and replaced with 200 μL of fresh medium. This process was repeated every 30 min for a total of 2 h (5 time points). The process was conducted concurrently on a Transwell filter coated with collagen/fibronectin solution but lacking cells. Fluorescence of the collected samples was measured using a BioTek Synergy H1 multi-mode microplate reader or Tecan Infinite M1000Pro microplate reader. The Pe value was calculated as previously described [197]. The assay was performed for a biological N=3. For each replicate, the flux of sodium fluorescein across cell monolayers was measured using 3 Transwell filters as well as one Transwell filter coated with

collagen IV and fibronectin but not containing cells. Transport across a Transwell filter lacking cells was also measured to correct permeability values for mass transfer resistance due to the filter.

4.3.8 Efflux transporter activity assay: substrate accumulation

iPSCs were subcultured onto 24-well plates and treated with endothelial medium lacking bFGF and RA for 24 h prior to the assay. For inhibitor conditions, BMECs were incubated with 10 μM cyclosporin A (CsA; Fisher Scientific) or 10 μM MK571 (Sigma Aldrich) for 1 h at 37°C. After this incubation, cells were incubated with 10 μM rhodamine 123 (Sigma Aldrich) or 10 μM 2',7'-dichlorodihydrofluorescein diacetate (H_2DCFDA; Thermo Fisher Scientific) with or without their respective inhibitors for 1 h at 37°C. Following this incubation, 3 wells per condition were washed twice with DPBS and lysed using DPBS containing 5% Triton-X. The remaining well of cells for each condition was fixed using 100% ice-cold methanol. The fluorescence of the lysed cells was measured using a BioTek Synergy H1 multi-mode microplate reader or Tecan Infinite M1000Pro microplate reader. Fixed cells were incubated with DAPI for 10 min, and each well of cells was imaged in 6 locations using a Leica DMi8 microscope. Nuclei were counted using Fiji [198] , and fluorescence values were normalized on a per-cell basis to these counts. All conditions were performed using triplicate wells to calculate mean ± standard deviation. Reported trends were confirmed across two additional biological replicates.

4.3.9 Efflux transporter activity assay: directional transport

BMECs on Transwell filters were incubated with 10 μM CsA or 10 μM MK-571 diluted only in the apical chamber for 1 h at 37°C. Next, BMECs were incubated with 10 μM rhodamine 123 or 10 μM H_2DCFDA with or without CsA or MK-571, respectively, for 1 h at 37°C. At the end of the incubation, 200 μL of medium was removed from the basolateral chamber of each filter, and fluorescence was measured using a BioTek Synergy H1 multi-mode microplate reader or a

Tecan Infinite M1000Pro microplate reader. Fluorescence values were normalized to medium collected from the basolateral chamber of BMECs not treated with inhibitor. The assay was performed using triplicate filters, and reported values were calculated as mean ± standard deviation. Reported trends were confirmed across two additional biological replicates.

4.3.10 Quantification of tight junction expression

Raw microscope images were exported in 16-bit TIF format for computational image analysis using a custom MATLAB script (original code included in the Supplemental Information). Briefly, junction and nuclear channels were binarized by comparing the intensity of each individual pixel to the average pixel intensity in the surrounding 10-pixel or 50-pixel neighborhood for junctions and nuclei, respectively. This approach was adapted from algorithms used to identify blood vessels and mitochondria from fluorescence microscope images in previous publications [199,200]. Individual nuclei were detected using a built-in MATLAB function (bwconncomp) for identifying discrete objects in binary images. Finally, the total number of junction-positive pixels was divided by the number of DAPI-positive pixels in the field of view as a confluency-normalized metric of junction density. Secondary confirmation of algorithm results was performed using the MorphoLibJ plugin [201] for Fiji [198] to determine the number of junction-positive pixels per image. The nuclear channel for the image was then binarized and the DAPI-positive pixels determined. Normalized junctional density was calculated as performed in the MATLAB script (Figure A. 4.2), and relative differences in junctional density were confirmed.

4.3.11 Statistical analyses

All data are expressed as mean ± standard deviation. Student's unpaired t-test was used to determine statistical significance for all efflux transport accumulation and directional transport

assays. Statistical significance was verified across all biological replicates, where a minimum of three independent experiments was performed.

4.4 Results and discussion

The confounding influence of serum and serum-derived proteins on hPSC differentiation has been well-documented [202], and the development of fully defined differentiation protocols is thus recognized as an important step for standardizing hPSC research applications. As such, we sought to replace the serum in our BBB differentiation process with more defined components. Our most recent differentiation scheme seeds iPSCs at a defined density, followed by differentiation for four days in fully defined E6 medium [195], then two days in a basal endothelial medium supplemented with platelet-poor plasma-derived serum (PDS), basic fibroblast growth factor (bFGF), and RA. Afterwards, BMECs are purified for phenotypic analyses (Figure 4.1a). A direct comparison of two different lots of PDS showed marked differences in the passive barrier properties of the final BMEC population derived from CC3 iPSCs (Figure 4.1b), a line that has been used previously with good success [195]. Specifically, 44% of BMEC differentiations failed to reach TEER exceeding 1000 Ω×cm2 using a single lot of PDS (N=9 biological replicates; data not shown), while differentiations conducted using a second lot of PDS consistently reached TEER maxima in excess of 2000 Ω×cm2. We decided, therefore, to replace PDS with B27, a common serum alternative in neural cultures [203], tested at either 50× (the manufacturer's recommendation) or 200× dilution (Figure 4.1a). Surprisingly, while a pre-qualified batch of PDS could produce BMECs with the expected maximum TEER of ~4000 Ωxcm2, B27 supplementations produced maximum TEER above 8000 Ωxcm2 (8734 ± 349 Ωxcm2 in 200× B27) (Figure 4.1c). CC3-derived BMECs (Figure 4.1d) and CD10-derived BMECs (Figure 4.1e),

female and male control lines [107,108], respectively, consistently achieved maximum TEER values in excess of 3000 Ωxcm2 across more than 10 independent CC3 differentiations and in excess of 2000 Ωxcm2 across 4 independent CD10 differentiations.

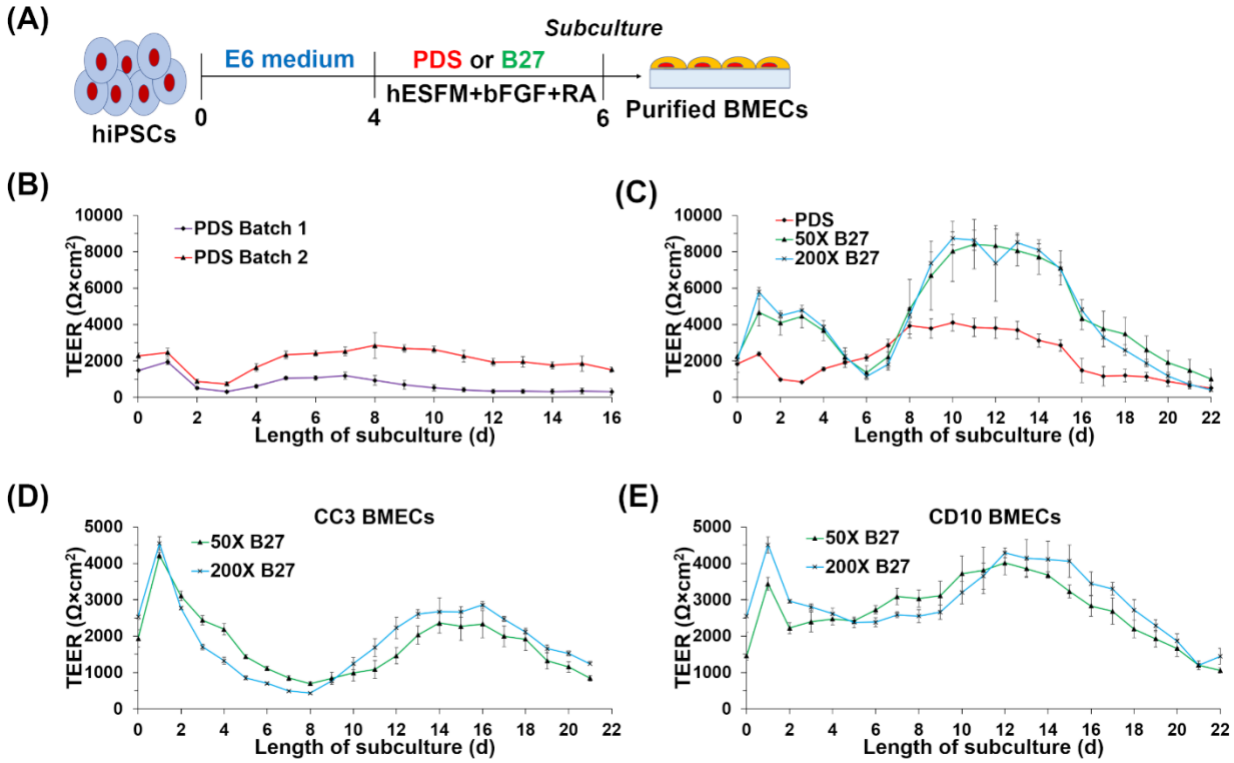

Figure 4.1 Exclusion of serum during the differentiation of iPSCs to BMECs yields robust passive barrier properties. (A) Differentiation scheme, including media variations and timing. (B) iPSCs differentiated concurrently with different batches of serum exhibit varying passive barrier phenotype as assessed by TEER. (C) iPSCs were differentiated concurrently using PDS, 50× diluted B27, or 200× diluted B27. (D-E) CC3 BMECs (panel D) and CD10 BMECs (panel E) produce equivalent TEER profiles at 50× and 200× B27 dilutions. Trends were confirmed across biological N=3.

To follow up on the TEER measurements, we assayed other properties of iPSC-derived BMECs under serum-free conditions. Immediately prior to purification, BMECs expressed occludin, claudin-5, VE-cadherin, GLUT-1 and PECAM-1, indicating acquisition of a BBB phenotype as typically seen in PDS (Figure 4.2a). BMECs were again evaluated 48 h after

purification and expressed occludin, claudin-5, VE-cadherin, and GLUT-1 (Figure 4.2b). Paracellular permeability was assessed using sodium fluorescein, and all replicates had effective permeabilities less than 2.5×10^{-7} cm/s, similar to BMECs differentiated in PDS [195] (Figure 4.2c). Collectively, these results indicate that replacement of serum with B27 during differentiation produces BMECs with robust passive barrier properties, with the added benefit of eliminating reliance on an undefined material with substantial lot-to-lot variability. BMECs were next evaluated for efflux activity of P-glycoprotein and multidrug resistance protein (MRP) transporters. P-glycoprotein activity was assessed by measuring fluorescence accumulation in purified BMECs incubated either with rhodamine-123, a fluorescent P-glycoprotein substrate, or rhodamine-123 containing cyclosporin A, a P-glycoprotein inhibitor. BMECs incubated with inhibitor showed a significant increase in fluorescence accumulation, indicating active P-glycoprotein function (Figure 4.2d). Similarly, purified BMECs were incubated with H_2DCFDA with or without MK-571, an inhibitor of the MRP family, and showed increased fluorescence accumulation compared to control cells, indicating MRP activity (Figure 4.2d). Directionality of P-glycoprotein and MRP transport was assessed by measuring the transport of fluorescent substrate across the monolayer of purified BMECs cultured on Transwell filters. Increased apical to basolateral substrate transport (mimicking blood to brain) was observed upon BMEC treatment with cyclosporin A and MK-571, indicating expected P-glycoprotein and MRP polarization (Figure 4.2e). Last, we co-cultured BMECs with astrocytes, an important constituent of the neurovascular unit previously reported to improve BBB functionality [204], and re-evaluated TEER. Interestingly, BMECs co-cultured with astrocytes reach higher TEER by day 11 of subculture than BMECs in monoculture, exceeding 9000 Ωxcm^2 in biological replicates (Figure

4.2f). These results indicate BMEC responsiveness to astrocytic cues, and the overall dataset validates the BMEC phenotype in serum-free conditions.

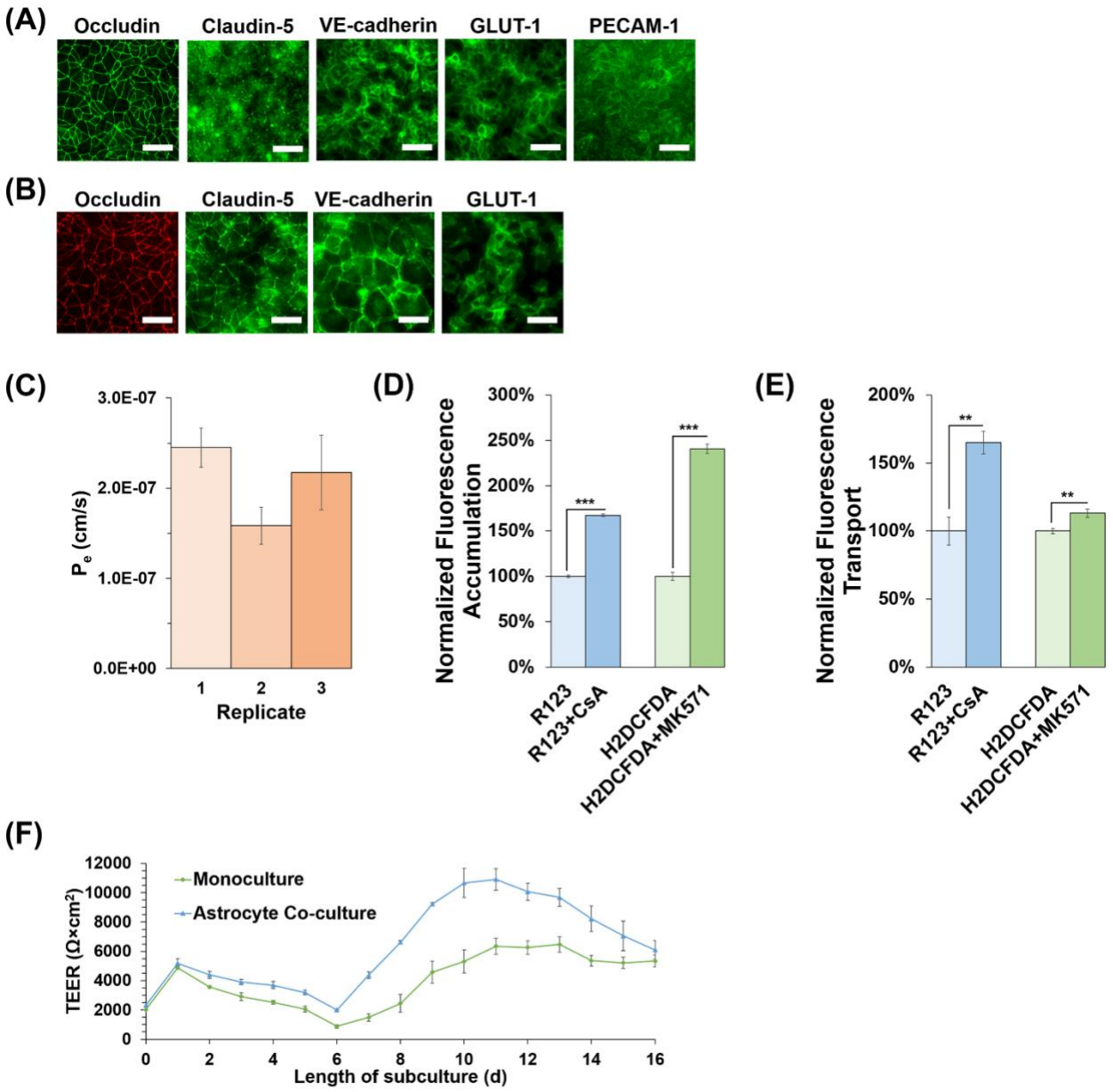

Figure 4.2 Further evaluation of passive and active barrier functions of BMECs differentiated under serum-free conditions. (A) Immunocytochemical detection of occludin, claudin-5, VE-cadherin, GLUT-1, and PECAM-1 on day 6 of differentiation. All scale bars are 50 µm. (B) Immunocytochemical detection of occludin, claudin-5, VE-cadherin, and GLUT1 48 h following purification. All scale bars are 50 µm. (C) Effective permeability of sodium fluorescein for biological N=3. Data are reported as mean ± standard deviation from technical triplicates. (D)

Intracellular fluorescence accumulation was measured in cells incubated with P-glycoprotein and MRP substrates and inhibitors. All values are reported as mean ± standard deviation from technical triplicates. Statistical significance was determined using Student's unpaired t-test (***$p<0.001$). Trends were confirmed across biological N=3. (E) Apical to basolateral flux of rhodamine 123 (R123) and H2DCFDA in the presence or absence of cyclosporin A (CsA) and MK-571, respectively. Data are reported as normalized mean ± standard deviation from technical triplicates. Statistical significance was determined using Student's unpaired t-test (**$p<0.01$). Trends were confirmed across biological N=3. (F) TEER measurements in CC3-derived BMECs co-cultured with CC3-derived astrocytes. Trends were confirmed across biological N=3.

Recently, it was reported that iPSC-derived BMECs from Huntington's Disease (HD) patients exhibit defunct barrier properties that correlate with the severity of the CAG repeat, including an inability to form any physical barrier as measured by TEER and compromised P-glycoprotein activity [205]. Our group had experienced similar unreported difficulties when differentiating patient-derived HD and tuberous sclerosis complex (TSC) iPSCs to BMECs using serum-based methods. Given the striking increase in TEER and improved consistency achieved when differentiating control iPSCs using serum-free medium, we investigated whether this method could rescue the phenotype in disease lines. HD70-2 iPSCs, harboring a 70 CAG repeat [107], and TSP8-15, harboring a nonsense *TSC2* mutation (characterization provided in Figure A. 4.1), were differentiated using either B27 or PDS, and TEER of resultant BMECs from both conditions was assessed (Figure 4.3a and Figure 4.3b, respectively). Notably, for both disease lines, TEER was elevated in BMECs differentiated using B27 rather than PDS across multiple biological replicates (Figure 4.3c).

Given the previous challenges observed in differentiating HD lines to BMECs, we further evaluated the BBB phenotype in HD70-2-derived BMECs. Purified HD70-2-derived BMECs show clear expression of claudin-5, occludin, VE-cadherin, and GLUT-1, as expected for brain endothelium (Figure 4.3d). We subsequently quantified the fidelity of claudin-5 and occludin

expression in HD70-2-derived BMECs and CC3-derived BMECs by normalizing the areal expression of the junction proteins to cell count (Figure 4.3e). Though no differences in occludin localization were observed, HD70-2-derived BMECs expressed significantly less claudin-5 per cell than CC3-derived BMECs. HD70-2-derived BMECs also displayed active P-glycoprotein function as evidenced by a significant increase in fluorescence accumulation in cells treated with inhibitor (Figure 4.3f). Thus, the HD70-2 iPSC line can successfully produce BMECs.

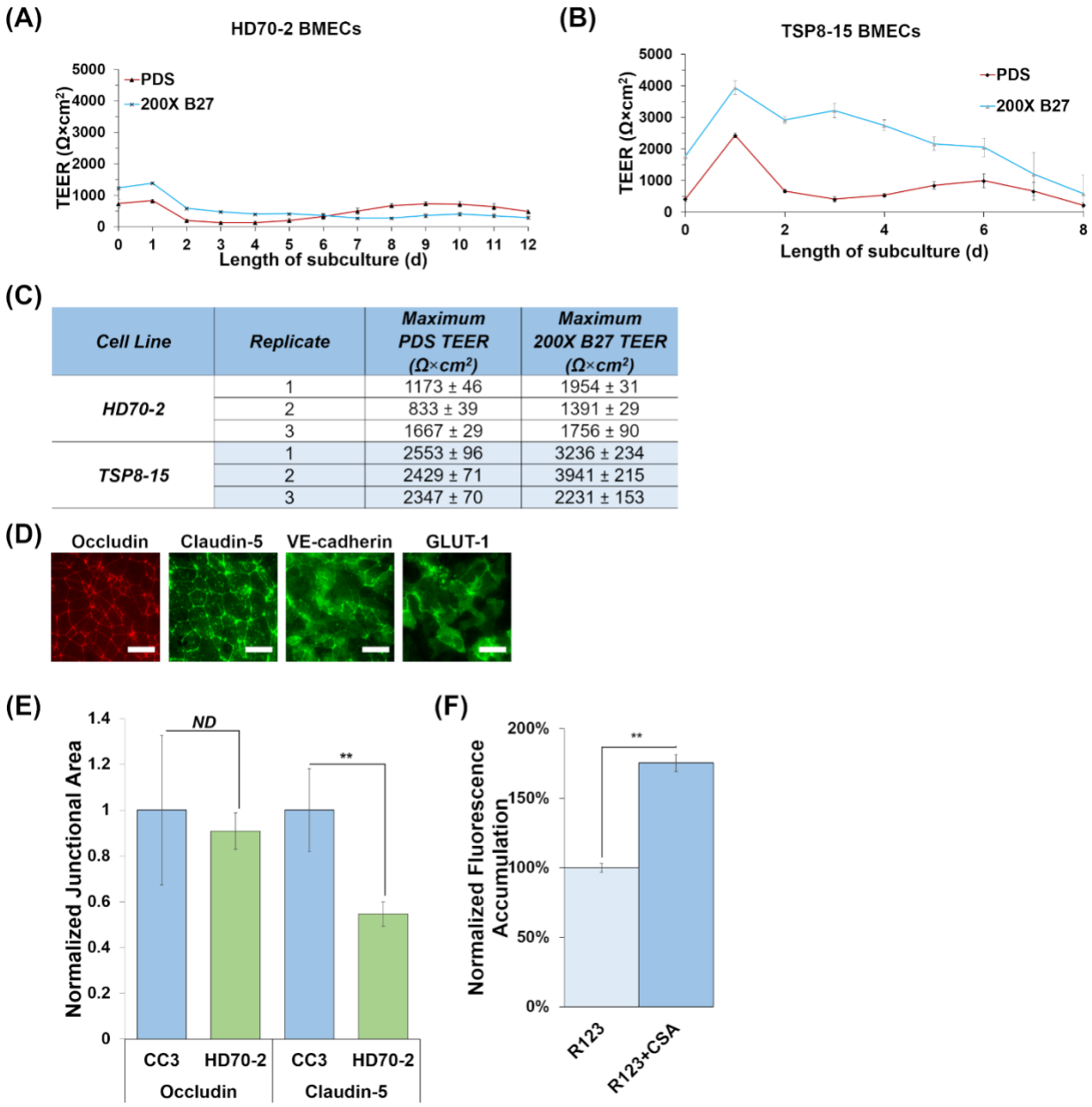

Cell Line	Replicate	Maximum PDS TEER (Ω×cm²)	Maximum 200X B27 TEER (Ω×cm²)
HD70-2	1	1173 ± 46	1954 ± 31
	2	833 ± 39	1391 ± 29
	3	1667 ± 29	1756 ± 90
TSP8-15	1	2553 ± 96	3236 ± 234
	2	2429 ± 71	3941 ± 215
	3	2347 ± 70	2231 ± 153

Figure 4.3 Serum-free differentiation improves BMEC fidelity in iPSC lines harboring known disease mutations. (A) HD70-2 and (B) TSP8-15 iPSCs were differentiated to purified BMECs using either PDS or 200x diluted B27, and TEER was measured approximately every 24 h after purification. (C) Differentiations were replicated for an additional biological N=2 to examine reproducibility. (D) Immunocytochemical detection of occludin, claudin-5, VE-cadherin, and GLUT-1 in purified HD70-2 BMECs. All scale bars are 50 μm. (E) Normalized junctional area for claudin-5 and occludin in HD70-2-derived BMECs and CC3-derived BMECs was calculated across a minimum of 3 fields per marker. Statistical significance was determined using Student's unpaired t-test (**p<0.01). (F) Intracellular fluorescence accumulation was measured in purified HD70-2 BMECs incubated with rhodamine 123 (R123) in the presence or absence of the inhibitor cyclosporin A (CsA). All values are reported as mean ± standard deviation from technical

triplicates. Statistical significance was determined using Student's unpaired t-test (***p<0.001). Trends were confirmed across biological N=3.

To further simplify the differentiation scheme, we sought to identify specific components of B27 that were essential to a successful BMEC differentiation. To this end, iPSCs were differentiated using N2, a chemically defined, serum-free supplement with known component concentrations [206], in place of B27. The resultant BMECs consistently achieved maximum TEER values greater than 2500 Ω×cm2 across seven biological replicates, indicating the presence of an intact endothelial monolayer and suggesting a successful differentiation outcome (Figure 4.4a). We further noted that selenium, insulin, and transferrin were among the conserved components between N2 and B27 and are also core components of E6 medium [102]. We therefore posited that basal endothelium medium supplemented with insulin, transferrin, and selenium (referred to as ITS) might be suitable for BMEC derivation. This hypothesis was supported by the resultant BMEC monolayers differentiated in ITS also achieving maximum TEER values greater than 2500 Ω×cm2 across seven biological replicates (Figure 4.4a). The long-term stability of CC3-derived BMECs was tracked and found to be similar to that of BMECs differentiated using B27 and N2 (Figure 4.4b). The ITS scheme was further tested in CD10-derived BMECs to ensure the method was applicable across iPSC lines, and the long-term TEER stability was similar to CC3-derived BMECs (Figure 4.4c). VE-cadherin, occludin, claudin-5, and GLUT-1 were also uniformly expressed in cells differentiated in ITS (Figure 4.4d). Additionally, cells differentiated in ITS displayed restricted paracellular permeability to sodium fluorescein (Figure 4.4e) and active P-glycoprotein and MRP function (Figure 4.4f), indicating acquisition of the BMEC phenotype. Thus, the undefined, serum-based differentiation procedure used to previously produce BMECs

from iPSCs can ultimately be reduced to three fully defined media additives without compromising passive barrier integrity.

(A)

Cell Line	Supplement	Maximum TEER (Ω×cm²)	
CC3	N2	4379 ± 469	4310 ± 202
		3994 ± 243	3505 ± 114
		4056 ± 43	3133 ± 97
		2714 ± 78	
	ITS	5145 ± 173	2597 ± 108
		3354 ± 122	2671 ± 285
		3869 ± 164	3177 ± 127
		3985 ± 769	

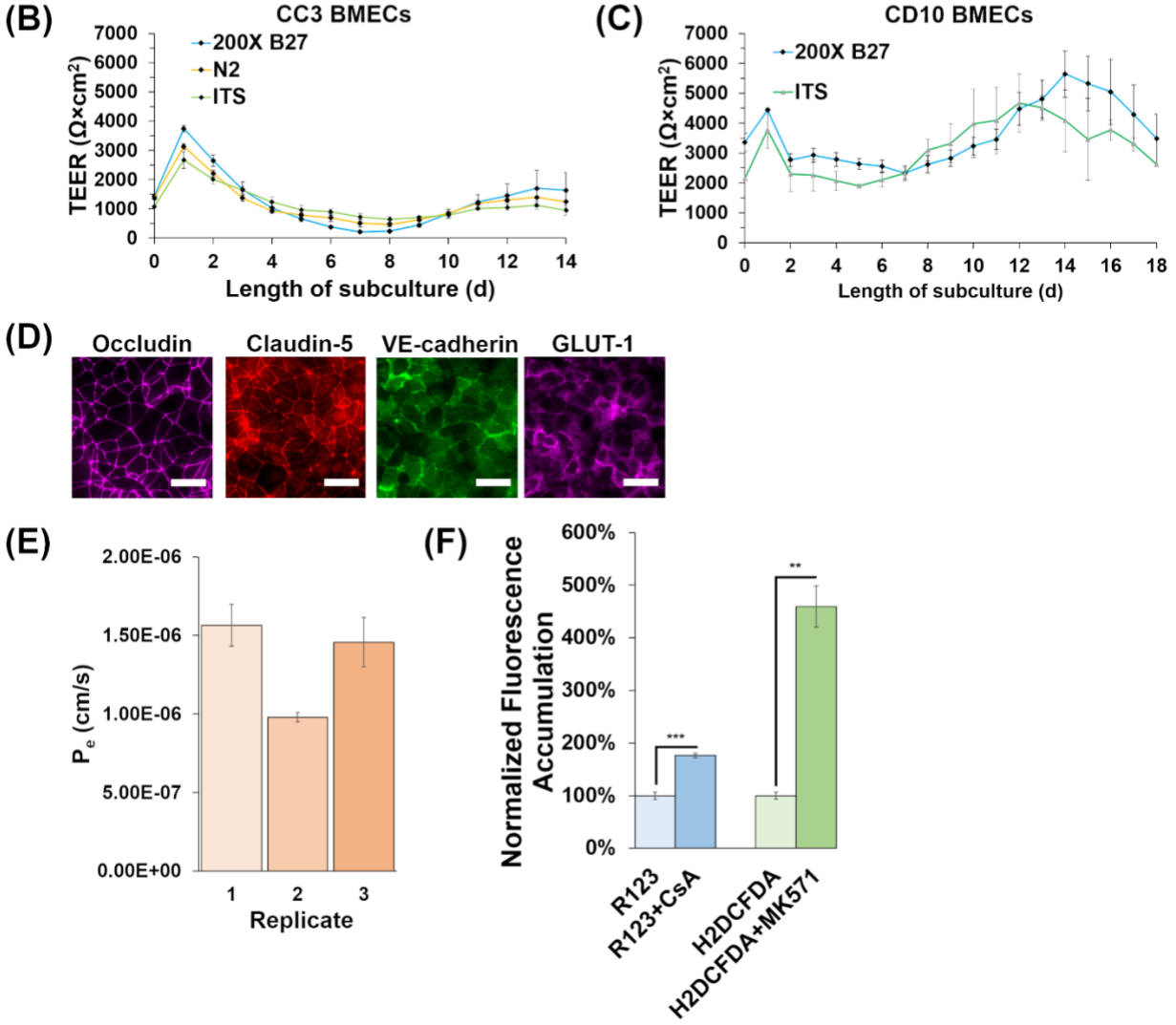

Figure 4.4 Fully defined differentiation medium produces BMECs. (A) iPSCs were differentiated to BMECs using either 1× N2 supplement or a custom cocktail of insulin, transferrin, and selenium (ITS). TEER was measured approximately every 24 h hour after purification. Biological N=7 per condition. (B) The long-term stability of CC3-derived BMECs and (C) CD10-derived BMECs differentiated using 200× diluted B27, 1× N2 (CC3 only), or ITS was tracked via TEER measurements. Biological N=3 per condition per line. (D) Immunocytochemical detection of occludin, claudin-5, VE-cadherin, and GLUT-1 in purified CC3 BMECs differentiated in ITS.

Scale bars are 50 μm. (E) Effective permeability of sodium fluorescein across biological N=3 for CC3-derived BMECs differentiated using ITS. Data are reported as mean ± standard deviation from technical triplicates. (F) Intracellular fluorescence accumulation was measured in CC3-derived BMECs differentiated using ITS incubated with P-glycoprotein and MRP substrates and inhibitors. All values are reported as mean ± standard deviation from technical triplicates. Statistical significance was determined using Student's unpaired t-test (**p<0.01, ***p<0.001). Trends were confirmed across biological N=3.

The variability of differentiation outcomes resulting from batch-to-batch changes in serum composition and quality constitutes a significant hurdle in the use of iPSCs for research and prospective regenerative medicine applications. In this study, we sought to address this issue in the context of BMEC differentiation through the replacement of serum with more defined supplements. This advancement ultimately mitigates procedural variability, thereby providing researchers with more reliable and robust iPSC-derived BMECs to interrogate neurovascular function.

The present study was motivated by our initial observations that different lots of PDS (the serum component in our differentiation medium) produced BMECs of dramatically different quality and in some cases resulted in completely failed differentiations. Qian et al. recently published a fully defined differentiation procedure in which iPSCs were differentiated to BMECs as a homogenous population through a mesoderm intermediate [184], whereas all previous BMEC differentiation procedures have relied on a co-differentiation approach in which the resultant BMECs must be purified from the mixed neural/endothelial cultures. Despite these differences in approach, we suspected that the use of fully defined components may translate to the co-differentiation system used by the majority of researchers. Indeed, in our first experiments, BMECs differentiated using B27 yielded maximum TEER in excess of 8000 $\Omega \times cm^2$ in monoculture. We note that this female iPSC line (CC3) did not always produce BMECs with

TEER up to *in vivo* levels under these defined conditions, nor did the male control line CD10. Indeed, TEER often fell within a range of 2000-5000 Ω×cm^2. We attribute a significant portion of this variability to differences in user skill, noting that subtle differences in culture techniques during iPSC maintenance and differentiation can result in noticeably different TEER profiles and maxima. Additionally, we have observed that BMEC performance, particularly at later timepoints in subculture, appears to be influenced by conditioning of the medium by the BMECs. We speculate that metabolic differences between iPSC lines and passages may influence this conditioning and thereby contribute to the observed TEER variability. Regardless, both iPSC lines consistently produced BMECs with maximum TEER above 2000 Ω×cm^2, with no differentiations failing to reach TEER above 1000 Ω×cm^2 across a total of 14 independent biological replicates and multiple users. Such maximum values are in line with values achieved using previously established methods [67,111], with the benefit of utmost reproducibility. Additionally, co-culture with astrocytes elevated TEER further, exceeding 9000 Ωxcm^2 across multiple biological replicates. For reference, we previously showed that BMECs differentiated with serum and co-cultured with astrocytes in serum-containing medium exhibited maximum TEER of ~5000 Ωxcm^2 [195]. To our knowledge, this TEER value was previously unattainable using serum-based procedures. We suspect two possibilities for this enhanced response to astrocyte co-culture. First, the removal of serum during differentiation may alter BMEC properties and make the cells more responsive to soluble cues from astrocytes. Second, given that serum was previously present during co-culture, its absence may yield healthier astrocytes, which then communicate more effectively with BMECs. We intend to follow up on this outcome, but regardless, our results indicate that serum-free system may have substantial utility for assessing mechanisms of neurovascular crosstalk.

Following rigorous assessments of TEER, BMECs differentiated using B27 were evaluated for other characteristic BBB properties. The effective permeability of sodium fluorescein across the monolayer was on the order of 10^{-7} cm/s across three biological replicates, in line with previously published data by our group and others [111,195]. BMECs differentiated using B27 were shown to have active P-glycoprotein and MRPs as evidenced by increases in fluorescent substrate accumulation and expected P-glycoprotein polarization. The BMECs also expressed expected BBB markers, including tight junction proteins and GLUT-1. These results further suggest that the substitution of serum with B27 in the differentiation procedure ultimately results in BMECs of equal fidelity to previously reported methods.

Next, we evaluated the performance of BMECs differentiated from two iPSC lines harboring mutations implicated in neurological/neurodegenerative disease. BBB dysfunction is associated with multiple neurodegenerative diseases and is increasingly being recognized as a potential therapeutic target in the treatment of such diseases [93,207]. Human iPSCs therefore present an unprecedented opportunity to model neurovascular function in health and disease, and to assess drug treatments *in vitro*. However, iPSC lines with disease-causing mutations are often more difficult to handle and differentiate, as mutations can impart features such as genomic instability [107]. These difficulties confound interpretation of experimental results as it is often unclear whether observed outcomes are a true feature of the disease in question or rather due to other factors, such as sensitivity to *in vitro* culture conditions unrelated to the disease phenotype. To address this issue, we differentiated iPSCs from patients with HD and TSC using both serum-based and B27-based procedures. For both sets of iPSCs, we routinely observed higher maximum TEER in BMECs differentiated using B27 as compared to those using serum in three independent biological replicates. Furthermore, HD iPSC-derived BMECs differentiated in B27 were found to

express key molecular markers of BBB phenotype, though claudin-5 expression had lower fidelity in HD iPSC-derived BMECs as compared to control BMECs, and possessed active P-glycoprotein. These results contrast with a previous report where BMECs differentiated from an HD iPSC line with a similar CAG repeat could not form any appreciable barrier and had lower efflux activity relative to control BMECs [205]. Our findings certainly do not invalidate either the previous observations or the proposed mechanism behind the barrier defects, especially since the HD lines in each study were not identical, but they do again caution that a failure to produce the appropriate BBB phenotype in a given cell line may not always reflect the disease being modeled. More broadly, the ability to create high-fidelity BMECs from disease lines should open new opportunities to investigate neurodegenerative diseases from a holistic neurovascular perspective.

Last, despite the advantages of B27 as a serum-free supplement, we were concerned that its composition is proprietary. BBB function can be influenced by different components that regulate diverse signaling pathways [208]; therefore, if the goal of an experiment is to dynamically investigate the influence of any one particular component on BBB function in real-time, it is desirable to precisely control the composition of the medium. We thus evaluated a chemically defined supplement (N2), as well as a defined mixture of insulin, transferrin, and selenium. Regardless of the supplement composition, resultant BMECs achieved passive barrier properties well above that which is considered to be a functional barrier (TEER above 500-1000 $\Omega x cm^2$) [209]. BMECs also displayed active p-glycoprotein and MRP function. We further note that, although we used Matrigel as the substrate for differentiation, it could be replaced with a fully defined substrate to further standardize this procedure. Overall, the use of fully defined medium represents a robust, reproducible, and cost-effective approach to investigating BBB physiology *in*

vitro in both healthy and diseased states, thereby facilitating broader adoption of iPSC-derived BMEC models across the greater research community.

4.5 Conclusion

In this study, we have described a serum-free differentiation protocol to produced brain microvascular endothelial cells from human induced pluripotent stem cells. The exclusion from serum in this process greatly reduced the variability in differentiation outcomes as compared to previous protocols which relied on serum use. Furthermore, BMECs produced using this improved protocol retained expression of canonical BMEC markers, exhibited physiologically relevant transendothelial electrical resistance values, and responded strongly to inductive cues from inductive cues from astrocytes. This protocol could be further simplified to a fully defined media system in which BMECs were cultured in basal medium supplemented with insulin, transferrin, and selenium. Overall, these advancements should enable broader adoption of the iPSC-based model.

4.6 Appendix

Table A. 4.1 Primary antibodies used in immunocytochemistry experiments

Target	Antibody Species	Vendor	Clone or product number	Dilution
Claudin-5	Rabbit	Abcam	ab15106	1:50
Claudin-5	Mouse	Thermo Fisher Scientific	4C3C2	1:50
Occludin	Mouse	Thermo Fisher Scientific	OC-3F10	1:100
VE-cadherin	Goat	R&D Systems	AF938	1:100
GLUT-1	Mouse	Thermo Fisher Scientific	SPM498	1:50
PECAM-1	Rabbit	Thermo Fisher Scientific	RB-10333-P	1:25

Table A. 4.2 Secondary antibodies used in immunocytochemistry experiments

Species Reactivity	Host	Conjugate	Vendor	Dilution
Rabbit	Donkey	Alexa Fluor 488	Thermo Fisher Scientific	1:200
Mouse	Donkey	Alexa Fluor 488	Thermo Fisher Scientific	1:200
Mouse	Donkey	Alexa Fluor 555	Thermo Fisher Scientific	1:200
Goat	Donkey	Alexa Fluor 488	Thermo Fisher Scientific	1:200
Rabbit	Donkey	Alexa Fluor 546	Thermo Fisher Scientific	1:200
Mouse	Donkey	Alexa Fluor 647	Thermo Fisher Scientific	1:200

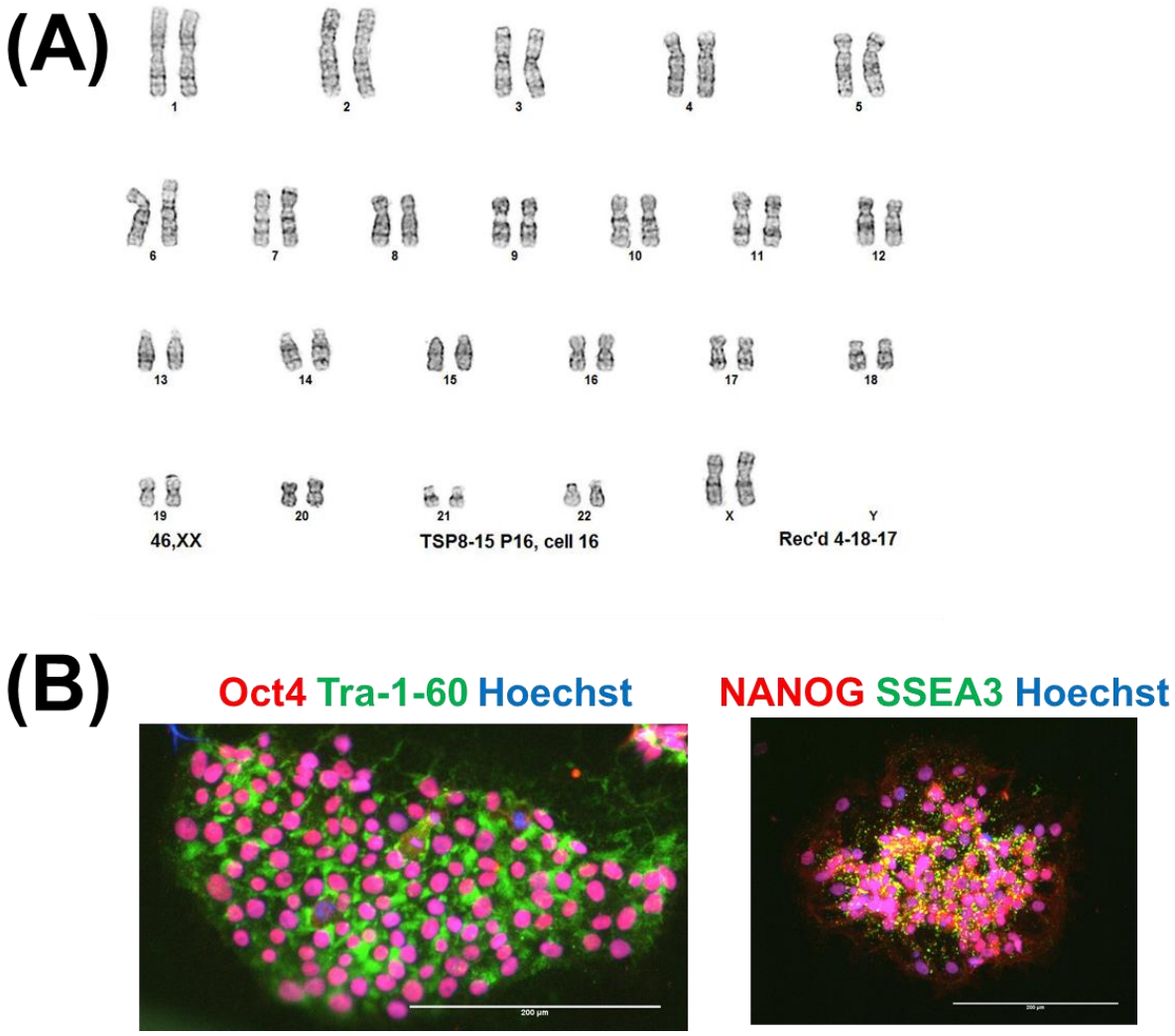

Figure A. 4.1 TSP8-15 iPSC characterization

```
clear
directory=uigetdir;
files=dir(directory);
sm=ones(3)/9;
s=ones(10)/100;
ss=ones(50)/2500;
export={'Image','Number of Nuclei','Junction Area (normalized to DAPI)','Mean Contiguous Junction
Length (pixels)','Mean Junction Width (pixels)'};
for o=1:length(files)
   if length(files(o).name)>4
      if strcmp(files(o).name(end-3:end),'.tif')
         raw=imread([directory,'/',files(o).name]);
         raw=double(raw)/255;
         junct=raw(:,:,1)+raw(:,:,2);
         nuc=raw(:,:,3);
         nuc=nuc-prctile(nuc(:),1);
         nuc=nuc/prctile(nuc(:),99);
         js=conv2(junct,sm,'same');
         jss=conv2(junct,s,'same');
         jp=js-jss;
         jp(1:5,:)=0;
         jp(:,1:5)=0;
         jp(end-5:end,:)=0;
         jp(:,end-5:end)=0;
         jp(jp<0)=0;
         jp=jp/prctile(jp(:),99.5);
         ns=conv2(nuc,sm,'same');
         nss=conv2(nuc,ss,'same');
         jc=jp>0.15;
         jc=bwareaopen(jc,20);
         np=ns-nss;
         nc=np>0.15;
         nc=bwareaopen(nc,50);
         temp=double(jc);
         temp(:,:,2)=0;
         temp(:,:,3)=double(nc)-double(jc);
         showproc=[raw;temp];
         imshow(showproc), title(files(o).name), pause(0.1)
         imwrite(showproc,[directory,'/',files(o).name(1:end-4),'.png'])
         export{end+1,1}=files(o).name;
         nuclei=bwconncomp(nc);
         export{end,2}=nuclei.NumObjects;
         export{end,3}=sum(jc(:))/sum(nc(:));
         junctions=bwconncomp(jc);
         je=edge(jc);
         me=sum(je(:))/junctions.NumObjects;
         ma=sum(jc(:))/junctions.NumObjects;
         mean_length=(me+sqrt(me^2-16*ma))/4;
         mean_width=ma/mean_length
```

```
  export{end,4}=mean_length;
          export{end,5}=mean_width;
        end
    end
end
xlswrite([directory,'/','matlab export'],export);
save([directory,'/','raw data'])
```

Figure A. 4.2 MATLAB script for junction quantification

Chapter 5

INFLUENCE OF BASAL MEDIA COMPOSITION ON BARRIER FIDELITY IN IPSC-DERIVED BLOOD-BRAIN BARRIER ENDOTHELIAL CELLS

5.1 Summary

We recently described a serum-free protocol for differentiating human induced pluripotent stem cells (iPSCs) to blood-brain barrier (BBB) endothelial cells. Here, we follow up on this work by exploring the influence of various basal media on the differentiation process and BBB properties in the purified endothelial cells. iPSCs were differentiated to BBB endothelial cells under serum-free conditions with varying basal media compositions. Immunocytochemistry was used to validate endothelial identity. BBB functional assays, including transendothelial electrical resistance (TEER), sodium fluorescein permeability, and efflux transporter activity and polarization, were performed using a conventional Transwell setup. RNA sequencing and pathway analysis was used to infer how media composition influences cellular transcriptional profile. Phospho-proteomic analysis was used to determine downstream pathway activation. Differentiation of iPSCs using two basal media with publicly available compositions – DMEM/F12 (DMEM medium) and Neurobasal Medium (NB medium) successfully yield VE-cadherin+ endothelial cells with canonical BBB expression markers. Strikingly, NB medium produced BBB endothelial cells with TEER values routinely exceeding 7,000 Ωxcm2 in monoculture, whereas BBB endothelial cells differentiated in DMEM medium routinely formed barriers of markedly lower fidelity (~2,000 Ωxcm2). This effect was highly dynamic and could be reversed by switching to the other basal medium. No significant differences in sodium fluorescein permeability were observed in either medium. Differences in efflux transporter activity were evident. RNA sequencing revealed modest changes in transcriptional activity, but

in combination with phosphor-proteomic analysis, suggested pathway activation that may explain in part differences in BMEC behavior as a result of basal media composition. We provide robust evidence that basal media composition can strongly influence the barrier phenotype in iPSC-derived BBB endothelial cells. The ability to fully define the components of the medium should greatly expand studies revolving around the influence of extracellular cues on BBB function.

5.2 Introduction

The differentiation of human induced pluripotent stem cells (iPSCs) to endothelial cells with blood-brain barrier (BBB) properties has greatly extended capabilities in *in vitro* neurovascular modeling and understanding the role of the human BBB in disease. As first described in 2012 [210], iPSC-derived brain microvascular endothelial cells (BMECs) express canonical endothelial and BBB markers, form a passive barrier as measured by transendothelial electrical resistance (TEER), express a cohort of active efflux transport proteins, and exhibit representative permeability to well-characterized small molecules that correlates well with *in vivo* uptake in rodents. Retinoic acid (RA) treatment was subsequently shown to upregulate VE-cadherin expression, as well as significantly increase TEER and multidrug resistance protein (MRP) activity [211]. Since these initial studies and others that validated the BBB phenotype [204,212–217], iPSC-derived BMECs have been incorporated into increasingly complex neurovascular models ranging from 2D Transwell setups to 3D microfluidic chips that incorporate neurons, astrocytes, and pericytes from either primary or iPSC sources [214,218–222]. Such models have also proven useful for analyzing diseases that afflict the neurovascular unit [223–225].

Despite their considerable utility, one persistent limitation of iPSC-derived BMECs is that the majority of differentiation protocols utilized undefined components such as serum. The use of undefined components in any iPSC differentiation workflow can be a major source of variability. As such, we recently described a series of improvements to the canonical iPSC-to-BMEC differentiation procedure that removed all undefined components in the cell culture media [226,227]. Overall, these changes vastly improved the consistency of differentiation and certain properties in the BMECs (for example, responsiveness to co-culture with astrocytes). However, one problem still remained: the basal medium used in the later stages of differentiation and after purification of the BMECs (human endothelial serum-free medium, or hESFM) has a proprietary composition. Thus, despite the removal of serum from the differentiation procedure, exquisite control over the extracellular milieu exposed to the BMECs remains limited. Given that recent studies have highlighted the dynamic responsiveness of BMECs to blood-born cues *in vivo* [33,228,229], we reasoned that it would be beneficial to further define how media cues influence iPSC-derived BMEC function *in vitro*.

To this end, we examined replacement of hESFM with either Neurobasal Medium (NB) or Dulbecco's Modified Eagle Medium/Nutrient Mixture F12 (DMEM/F12, referred to hereafter as DMEM). In contrast to hESFM, the full compositions of NB and DMEM are publicly available through their manufacturer. Both media contain amino acids, vitamins, nutrients, and inorganic salts at varying compositions, thus providing a useful testbed for assessing how such differences might influence the BBB phenotype *in vitro*. Here, we show that BMECs exhibit markedly different passive and active barrier properties depending on the composition of basal media. However, RNA sequencing and pathway analysis did not reveal overt differences in transcriptional identity as a result of basal media choice, suggesting that phenotypic differences may be the results

of post-transcriptional regulation events. Overall, our results demonstrate the plasticity and responsiveness of iPSC-derived BMECs to their extracellular environment. Moving forward, the use of basal media with defined composition should ultimately enable studies into how specific biological factors explicitly regulate distinct BBB properties.

5.3 Materials and methods

5.3.1 iPSC maintenance

iPSCs were maintained as previously described [226,227]. CC3 [108] and CD10 [107] iPSCs were maintained in E8 medium [101], prepared as previously detailed [226], on tissue culture plates coated with growth-factor reduced Matrigel (Corning). iPSCs were passaged with Versene (Thermo Fisher Scientific) upon reaching 60-80% confluency.

5.3.2 iPSC differentiation to BMECs

iPSCs were differentiated to BMECs as previously described, with minor modifications [227]. iPSCs were washed once with PBS (Thermo Fisher Scientific), dissociated with Accutase (Gibco) for 3 minutes, and collected by centrifugation. iPSCs were then resuspended in E8 medium containing 10 μM Y27632 (Tocris) and seeded onto Matrigel-coated 6-well plates at a density of 15,800 cells/cm2. The following day, the cells were switched to E6 medium [102] to initiate differentiation. Media was changed every day for 4 days. On day 4, the cells were switched to EC medium, which consisted of a basal medium supplemented with 200× B27 (Thermo Fisher Scientific), 10 μM all-trans retinoic acid (RA; Sigma-Aldrich), and 20 ng/mL basic fibroblast growth factor (bFGF; PeproTech). The basal medium was either neurobasal medium (NB; Thermo Fisher Scientific #21103049) or DMEM/F12 with Glutamax (DMEM; Thermo Fisher Scientific

#10565018). Cells were then left to incubate for 48 hours in EC medium without a media exchange. On day 6, resultant BMECs were purified and assayed as described below.

5.3.3 Purification of iPSC-derived BMECs

On day 6 of differentiation, iPSC-derived BMECs were purified similar to previous descriptions [210,211,226,227]. Briefly, cells were washed once with DPBS, incubated with Accutase until a single cell suspension was achieved (approximately 20-45 min), and collected via centrifugation. Cells were resuspended in EC medium and plated onto Transwell filters (Fisher Scientific) or cell culture plates (Corning) coated with 400 μg/mL collagen IV (Sigma-Aldrich) and 100 μg/mL fibronectin (Sigma-Aldrich). In all experiments, BMECs were purified using the same basal medium as during differentiation (e.g. if cells were differentiated in EC medium made from DMEM, they were subsequently subcultured into EC medium made from DMEM). Media was changed approximately 24 h after subculture to EC medium lacking bFGF and RA. In certain experiments, BMECs were changed to different basal media containing 200× B27 at specified time points. With the exception of these noted experiments, medium was not changed again after the removal of bFGF and RA for the duration of culture.

5.3.4 TEER measurements

After purification of BMECs onto Transwell filters (Fisher Scientific), TEER was measured approximately every 24 hours using a World Precision Instruments EVOM2 voltohmmeter with STX2 chopstick electrodes.

5.3.5 Fluorescein permeability measurements

Three Transwell filters plated with BMECs and one Transwell filter coated with collagen IV and fibronectin but containing no cells were used for each basal medium condition tested. All

permeability assays were conducted 24 hours after removal of bFGF and RA from EC medium, referred to as day 1 of subculture. One hour prior to commencement of the assay, BMECs on Transwells received a full medium change in both apical and basolateral compartments. At the start of the assay, medium was fully aspirated from the apical portion of all Transwell filters and replaced with EC medium containing 10 μM sodium fluorescein (Sigma-Aldrich). 200 μL of medium was immediately removed from the basolateral chamber of each filter, transferred to a 96-well plate, and replaced with 200 μL of fresh medium containing no fluorescein. This process was repeated every 30 minutes for a total of five time points with cells incubated at 37°C between medium removal and replacements. At the conclusion of the assay, the fluorescence of the collected samples was measured using a Tecan Infinite M1000Pro microplate reader, and effective permeability (Pe) values were calculated as previously described [197].

5.3.6 Efflux transporter assay – substrate accumulation

BMECs were purified onto 24-well cell culture plates and treated with EC medium lacking bFGF and RA for 24 hours prior to measuring transporter activity. For each efflux transporter studied, BMECs were incubated with fluorescent transporter substrate with or without transporter inhibitors. For inhibitor conditions, BMECs were treated with 10 μM cyclosporin A (CsA; Sigma-Aldrich), a P-glycoprotein inhibitor, or 10 μM MK571 (Sigma-Aldrich), an MRP1 inhibitor for 1 hour at 37°C. After 1 hour, medium was aspirated from all wells and replaced with medium containing 10 μM rhodamine 123 (R123; Thermo Fisher Scientific), a P-glycoprotein substrate) or 10 μM 2',7'-dichlorodihydrofluorescein diacetate (H2DCFDA; Thermo Fisher Scientific), an MRP family substrate, with or without their respective inhibitors. Following a 1 hour incubation at 37°C, BMECs were washed three times with PBS. Three wells of BMECs per condition were lysed in PBS containing 5% Triton X-100 (Sigma-Aldrich), and one well per condition was fixed

in ice cold 100% methanol. The fluorescence of the collected cell lysates was measured using a Tecan Infinite M1000Pro microplate reader. Cells fixed in methanol were incubated with DAPI for 10 minutes and subsequently imaged at 6 locations per condition using a Leica DMi8 microscope. Nuclei at each location were counted using Fiji [198] and used to determine cell density per well of each condition. Measured fluorescence values were subsequently normalized on a per cell basis using these counts.

5.3.7 Immunocytochemistry

Cells were washed twice with PBS before fixation in 4% paraformaldehyde (PFA; Thermo Fisher Scientific) for 20 minutes or ice-cold 100% methanol for 10 minutes. Following fixation, cells were washed with PBS three times for five minutes per wash. Cells fixed in 4% PFA were blocked in PBS containing 5% donkey serum (Sigma-Aldrich) and 0.3% Triton X-100 (Sigma-Aldrich), collectively referred to as PBS-DT, for a minimum of 1 hour. Cells fixed in methanol were blocked in PBS with 5% donkey serum but lacking 0.3% Triton X-100, referred to as PBSD, for a minimum of 1 hour prior to primary antibody addition. Primary antibodies were diluted in either PBS-DT or PBSD, depending on the buffer used to block the cells, to the appropriate dilution (Table A. 5.1), and incubated overnight at 4°C.

Following overnight incubation, cells were rinsed once with DPBS and washed for an additional five times, 5 minutes per wash. Secondary antibodies (Table A. 5.2) were diluted 1:200 into PBS-DT or PBSD and incubated for 1-2 hours at room temperature. Finally, cells were rinsed once and washed four times, 5 minutes per wash, and imaged using a Leica DMi8 microscope.

5.3.8 RNA sequencing and pathway analysis

On day 1 of subculture, BMECs that had been plated on 6-well cell culture plates coated with collagen IV and fibronectin were washed once with PBS and collected via scraping and

centrifugation. Resultant cell pellets were resuspended in 500 μL of TRIzol (Thermo Fisher Scientific) and stored at -80°C. After collection of 3 biological replicates per media condition, RNA from each sample was isolated using a Direct-zol Miniprep kit (Zymo Research), following the manufacturer's instructions with inclusion of a DNase treatment step. Isolated RNA samples were submitted to the Vanderbilt Technologies for Advanced Genomics (VANTAGE) facility for sequencing using an Illumina NovaSeq6000.

Raw sequencing reads were obtained for 9 paired-end samples (3 biological replicates for the 3 conditions identified as CD3254, RA and DMSO) and run through a bulk RNA-Seq pipeline governed by the Snakemake (5.2.4) workflow management system [230]. Quality control was monitored with FastQC v0.11.8 before and after quality and adapter trimming, as performed by Trim Galore v0.5.0. Trimmed paired-end sequences were then aligned to the human genome (GRC38) with STAR 2.60c, utilizing Gencode genomic feature annotations (v26). Once quantitated, the feature counts were used for downstream analysis. The average mapped reads count was 41M reads (85% of total reads).

Gene counts and sample metadata were used for differential gene expression using DESeq2 [231], between the condition groups: DMEM vs NB. For each testing pair, we analyzed differential gene expression results quantitatively and visually. For the up- and down-regulated groups of top genes, we also performed functional gene enrichment analysis for Gene Ontology and KEGG pathways.

5.3.9 Phospho-proteome analysis

The relative phosphorylation levels of various kinases were measured using a Proteome Profiler Array human phosphor-kinase array kit (R&D Systems) according to the manufacturer's instructions. Briefly, on day 1 of subculture, BMECs subcultured onto 6-well cell culture plates

were washed once with DPBS, incubated with Accutase, and collected via centrifugation at 1000 rpm for 4 minutes. Cells were resuspended in 1 mL of DPBS, and cell density was determined using a Countess II. Cells were again centrifuged at 1000 rpm for 4 minutes and resuspended in Lysis Buffer 6 at a concentration of 10_7 cells/mL. The resultant cell suspensions were incubated on ice for 30 minutes, followed by centrifugation at 14,000×g for 5 minutes. Supernatants were transferred to clean microfuge tubes, and protein content was determined using a Pierce BCA protein assay kit (Thermo Fisher Scientific). Lysates were stored at -80°C until the day of the assay. On the day of the assay, all kit components were prepared as directed by the manufacturer's instructions, and 400 μg of protein per condition was diluted in Array Buffer 1 for incubation with kit membranes. Chemiluminescence for all membranes was detected using a Li-Cor Biosciences Fc imaging system at exposure times of 30 seconds, 2 minutes, and 10 minutes. Data collected from the 2 minute exposure were selected for presentation as this time maximized signal intensity while minimizing background signal.

5.4 Results and discussion

As described in the methods, CC3 iPSCs were differentiated for 4 days in E6 medium and 2 days in EC medium (Figure 5.1A), where the basal media that previously consisted of hESFM was replaced with either NB or DMEM. The standard additives to EC medium (RA, B27 supplement, bFGF) were unchanged from our previous protocol [227]. Following purification, BMECs were maintained in whichever media had been previously used during differentiation. As judged by immunocytochemistry, no overt differences in marker expression were observed (Figure 5.1B). Notably, BMECs differentiated in NB or DMEM both displayed a VE-cadherin+ endothelial signature with robust expression of tight junctions. However, TEER measurements

revealed significant differences in passive barrier function. Whereas BMECs differentiated and subcultured in NB exhibited TEER in line with maximum values previously observed in hESFM (7000-8000 Ωxcm$_2$), BMECs differentiated and subcultured in DMEM consistently formed lower fidelity barriers. BMECs differentiated and subcultured in a 50:50 mixture of NB:DMEM exhibited maximum TEER of ~2000 Ωxcm$_2$, highlighting that the observations were a direct result of basal media composition (Figure 5.1C). These relative differences were confirmed in BMECs derived from CD10 iPSCs. Despite these dramatic differences in TEER between the differentiation condition, sodium fluorescein permeability was not significantly different between BMECs in either DMEM or NB medium (Figure 5.1D), but this result was unsurprising given that *in vitro* permeability differences are not observed in Transwell assays when TEER exceeds 500-1000 Ωxcm$_2$ [209].

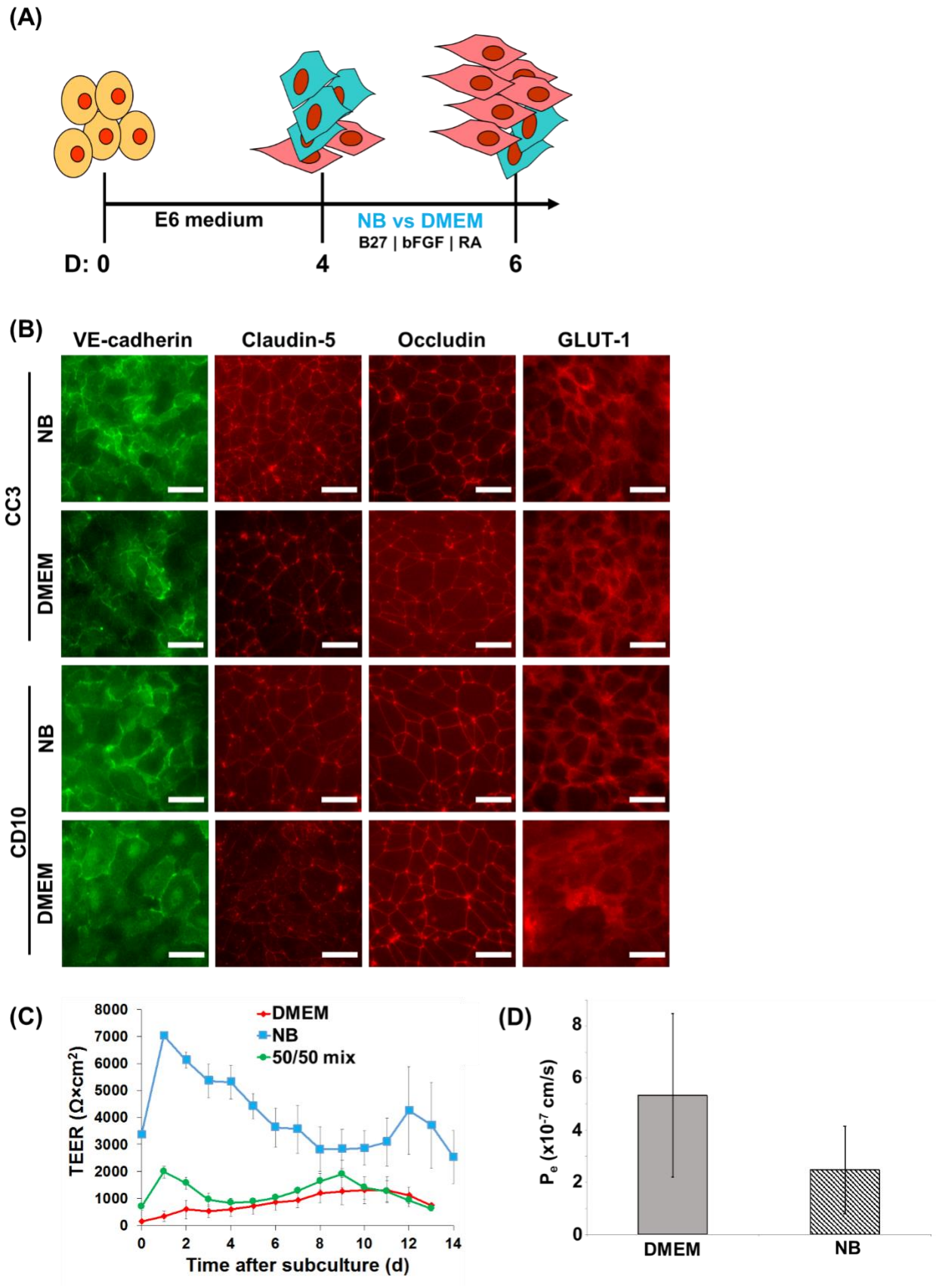
(A)
E6 medium
NB vs DMEM
B27 | bFGF | RA
D: 0
4
6
(B)
VE-cadherin
Claudin-5
Occludin
GLUT-1
CC3
NB
DMEM
CD10
NB
DMEM
(C)
DMEM
NB
50/50 mix
TEER (Ω×cm²)
Time after subculture (d)
(D)
Pe (x10⁻⁷ cm/s)
DMEM
NB

Figure 5.1 Differentiation of iPSCs to BMECs in NB and DMEM basal media. (A) Differentiation scheme to produce BMECs using either neurobasal (NB) or DMEM/F12 with Glutamax (DMEM) basal media with appropriate supplements. BMECs were purified on day 6 for further analyses. (B) Purified BMECs differentiated from CC3 and CD10 iPSCs both DMEM and NB basal media exhibit robust expression of canonical BBB endothelium markers, namely VE-cadherin, claudin-5, occludin, and GLUT-1. Scale bars are 50 μm. (C) CC3 BMECs differentiated using DMEM, NB, or a 50:50 mixture of DMEM and NB display strikingly different TEER as a result of media composition. (D) Despite differences in TEER, permeability to sodium fluorescein was unchanged between conditions. Permeability for all basal medium conditions was measured for a biological N=3, and for each biological replicate, flux was measured across triplicate Transwell filters containing cells. Permeability values for cells on Transwells were corrected for mass transfer resistance due to the filter using the measured permeability across the included empty filter. All permeability values reported herein are therefore effective permeability values.

To clarify whether these results were simply suboptimal differentiations (e.g. if differentiation in DMEM produces worse BMECs because a critical factor is missing from the medium), we characterized the dynamic responsiveness of BMECs to media composition. We first differentiated and subcultured BMECs in DMEM medium, then switched to NB medium after 1 day (Figure 5.2A) or 7 days (Figure 5.2B). In both cases, the switch to NB medium yielded a statistically significant increase in TEER, showcasing that diminished passive barrier function in DMEM was reversible and not the result of an intrinsic defect acquired during the differentiation process. Similarly, differentiation and subculture in NB medium, followed by a switch to DMEM medium, also yielded a statistically significant decrease in TEER, though the effect was less pronounced (Figure 5.2C). Overall, our data suggest that basal media can impart a significant influence on passive barrier function.

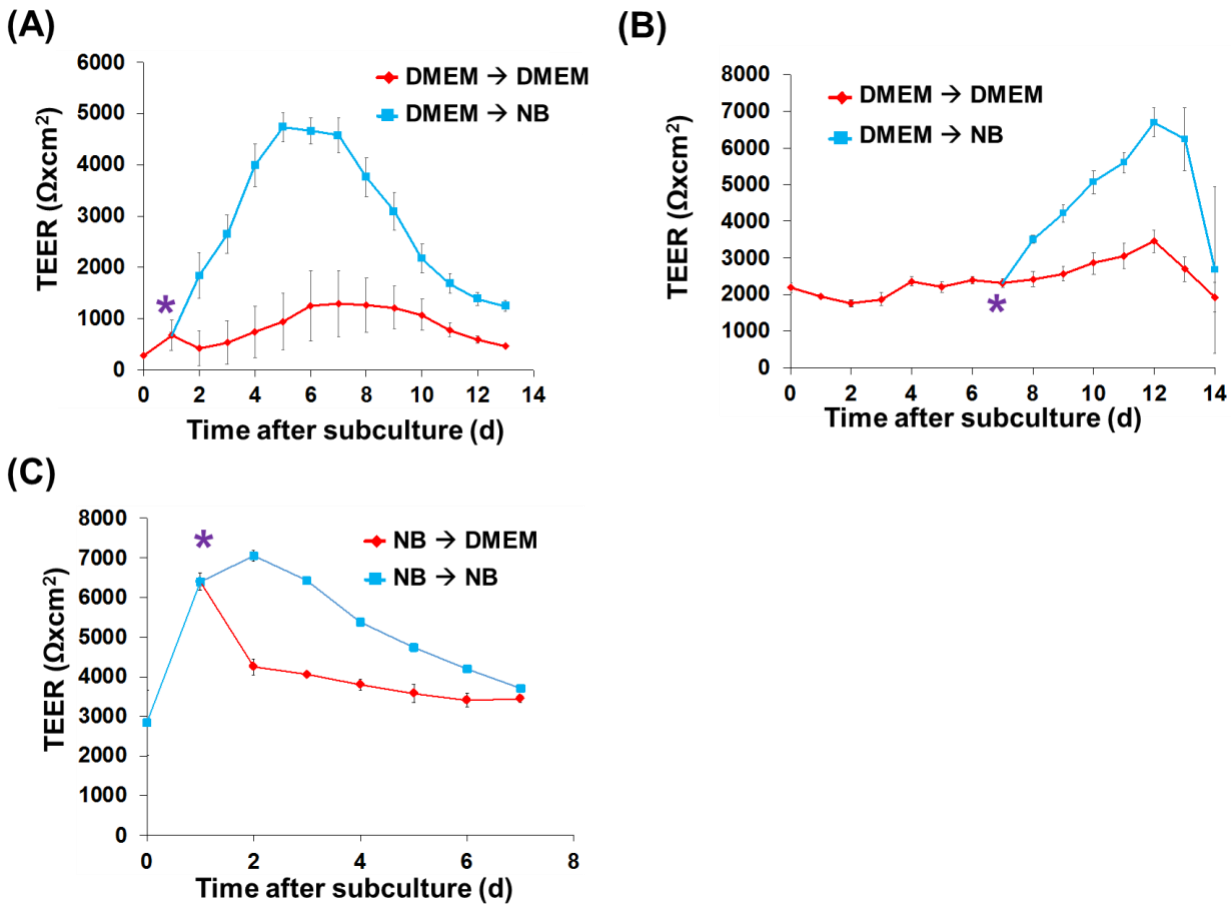

Figure 5.2 iPSC-derived BMECs maintain capacity for dynamic response to media composition changes throughout culture. CC3 BMECs differentiated in DMEM were switched to EC medium containing either DMEM or NB on (A) day 1 or (B) day 7 of subculture; cells switched to NB on either day exhibited a strong increase in TEER. (C) In contrast, cells differentiated in NB and switched to DMEM on day 1 of subculture display a dramatic decrease in TEER as compared to TEER of BMECs given fresh NB on day 1.

We next assessed how media composition influenced efflux activity in iPSC-derived BMECs cultured in either well-plates (for accumulation assays) or Transwell filters (for polarization assays). We utilized pairings of rhodamine 123 (a p-glycoprotein substrate) with cyclosporin A (CsA, a p-glycoprotein inhibitor) and 2',7'-dichlorodihydrofluorescein diacetate (H_2DCFDA, an MRP substrate) with MK-571 (an inhibitor of MRP1). In the accumulation assays, both p-glycoprotein and MRP1 were shown to be active regardless of media composition. No

difference in p-glycoprotein activity was observed between BMECs differentiated in either DMEM or NB medium (Figure 5.3A). However, activity of MRP1 was significantly higher in BMECs differentiated in DMEM relative to NB medium (Figure 5.3B).

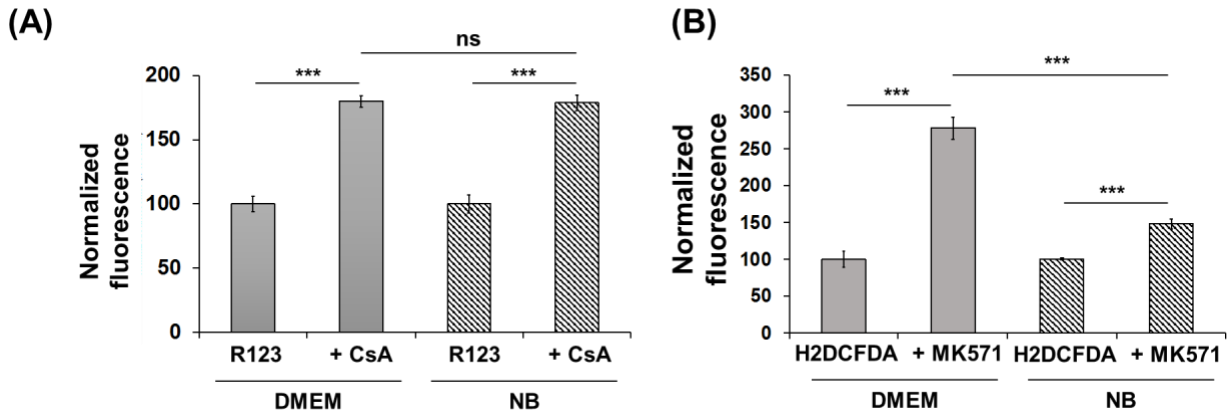

Figure 5.3 BMECs differentiated using NB and DMEM display active efflux transporter activity. CC3 BMECs differentiated using DMEM and NB exhibited active (A) P-glycoprotein activity and (B) MRP efflux activity. Accumulation was measured for each transporter for a biological N=3, and substrate accumulation was normalized in each replicate to the accumulation in cells lacking inhibitor. All values are reported as mean ± standard deviation, and statistical significance was determined using Student's unpaired t-test. ***$p<0.001$

Given the rather striking differences in performance between BMECs differentiated using NB and DMEM, we next employed RNA sequencing to identify differentially regulated genes and/or signaling pathways to gain insight into potential mechanisms of these phenotypic differences. RNA was collected from three independent differentiations of CC3 BMECs in either DMEM or NB, sequenced, and analyzed for differential expression using DESeq2 [231]. Our analysis identified 19,086 genes with a nonzero total read counts within these samples, and differential expression was found to cluster strongly with basal media condition (Figure 5.4A). Using an adjusted $p<0.1$, we identified 3,153 genes as being upregulated (17%) and 2,436 genes as being downregulated (13%) under DMEM conditions as compared to neurobasal conditions. Of

these upregulated genes, 1070 genes were upregulated at least 2-fold under DMEM conditions, and 105 genes were at least 5-fold upregulated under DMEM conditions. 756 genes were downregulated a minimum of 2-fold under DMEM conditions, and 40 genes were downregulated a minimum of 5-fold under DMEM conditions (Figure 5.4B). Though we identified a large cohort of these differentially expressed genes, we were initially surprised by the lack of differential expression of tight junction proteins as might be expected by the large differences in TEER observed between the two conditions. Despite a relatively large number of differentially expressed genes, pathway analysis revealed only a single KEGG pathway downregulated in DMEM BMECs (q<0.1), while 12 KEGG pathways were upregulated in DMEM BMECs (q<0.1) (Figure 5.4C).

Given that differences in basal medium did not seem to strongly alter the transcriptomic profile of iPSC-derived BMECs, we hypothesized that differences in BBB properties may instead be the result of changes in kinase activity altering pathway activities via phosphorylation events. We determined the relative phosphorylation levels of multiple proteins using a commercially available phospho-kinase kit. In general, BMECs differentiated in NB possessed a larger number of phosphorylated proteins than BMECs differentiated in DMEM (Figure A. 5.1). We focused on differences in ERK1/2, CREB, FAK, c-Jun, and HSP60, as these proteins were phosphorylated in both conditions (Figure 5.4D). The starkest contrast was observed in ERK1/2 phosphorylation, which was markedly less phosphorylated in BMECs differentiated in DMEM compared to NB, and FAK phosphorylation, which was notably more phosphorylated in BMECs differentiated in DMEM compared to NB (Figure 5.4E). Collectively, our results suggest that changes in basal media composition can have a dramatic effect on cell performance and influence signaling pathway activation with only modest alteration of the transcriptional identity of the cells.

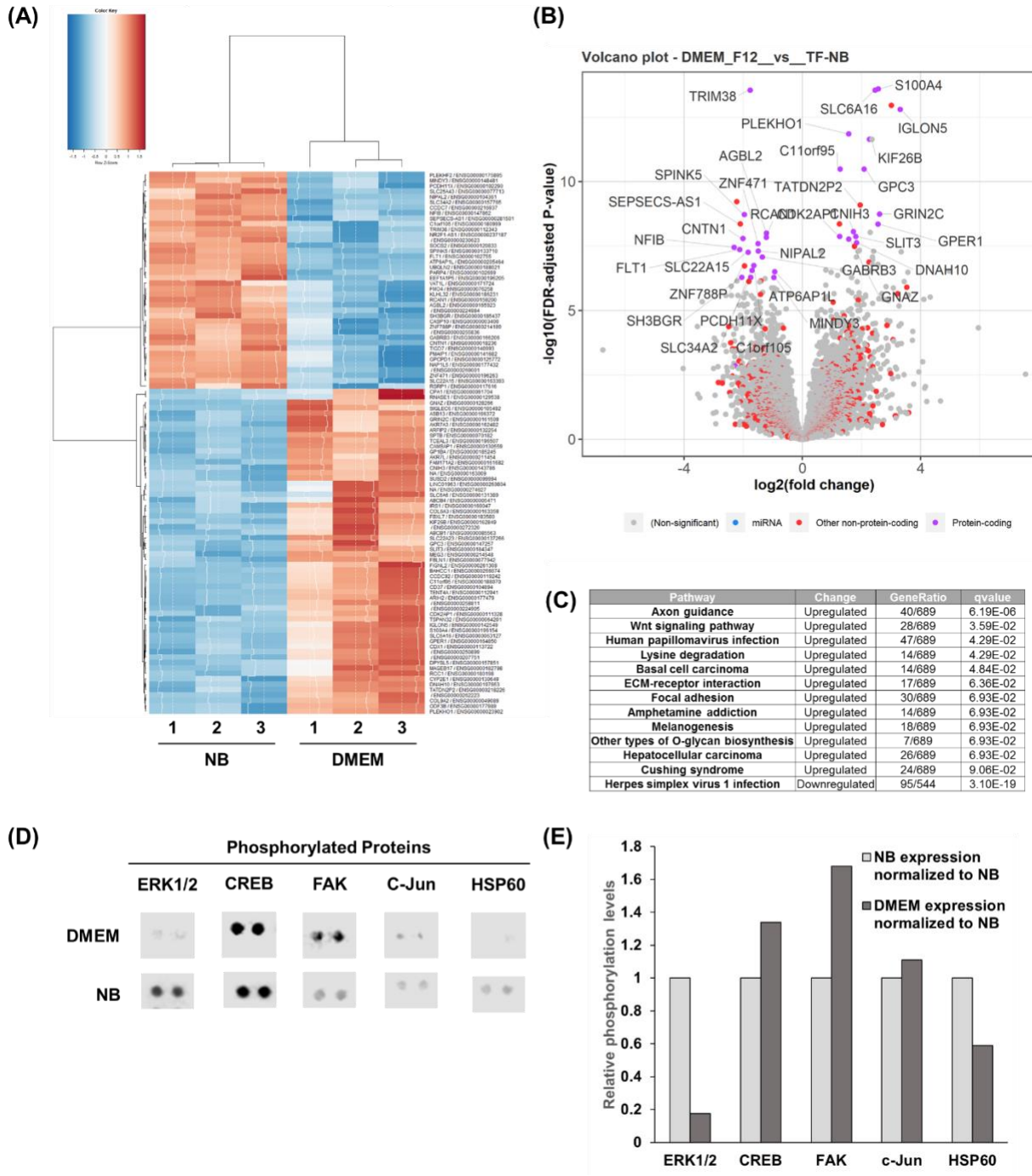

Pathway	Change	GeneRatio	qvalue
Axon guidance	Upregulated	40/689	6.19E-06
Wnt signaling pathway	Upregulated	28/689	3.59E-02
Human papillomavirus infection	Upregulated	47/689	4.29E-02
Lysine degradation	Upregulated	14/689	4.29E-02
Basal cell carcinoma	Upregulated	14/689	4.84E-02
ECM-receptor interaction	Upregulated	17/689	6.36E-02
Focal adhesion	Upregulated	30/689	6.93E-02
Amphetamine addiction	Upregulated	14/689	6.93E-02
Melanogenesis	Upregulated	18/689	6.93E-02
Other types of O-glycan biosynthesis	Upregulated	7/689	6.93E-02
Hepatocellular carcinoma	Upregulated	26/689	6.93E-02
Cushing syndrome	Upregulated	24/689	9.06E-02
Herpes simplex virus 1 infection	Downregulated	95/544	3.10E-19

Figure 5.4 RNA sequencing, pathway, and phospho-proteomic analysis of BMECs provides insight into basis of functional differences. (A) CC3 BMECs differentiate using DMEM and NB underwent RNA sequencing analysis and were found to cluster strongly based on basal media composition across biological N=3 per media condition. (B) Subsequent analysis identified differentially regulated genes under each media composition. (C) Despite the plethora of differentially expressed genes, a small number of pathways were found to be differentially regulated. (D) Phospho-proteomic analysis identified multiple kinase substrates phosphorylated to

varying degrees under the different media conditions. (E) These differences in phosphorylation level were quantified to assess relative levels of pathway activation.

In this study, we explored how basal media composition influences BBB properties in iPSC-derived BMECs. We determined that basal media has a profound influence on both the passive and active BBB phenotype. RNA sequencing revealed many differentially expressed genes, although changes to signaling pathways were minimal. Phosphoproteome analysis was used to confirm activation status in specific cases. Our results benchmark BMEC performance in different media and will serve as a resource in this area moving forward.

These findings have utmost importance for a variety of *in vitro* applications ranging from drug screening to disease modeling. For example, in drug screening applications, although TEER was above the minimal threshold necessary to prevent paracellular leakage, substantial differences were observed in efflux transporter expression and activity. Notably, *ABCB1* was found to be significantly upregulated in BMECs in DMEM as compared to NB (log_2 fold change of 3.45), but this change in transcript expression did not result in a functional change in P-glycoprotein activity, as measured by substrate accumulation, between conditions. *ABCC4* was the only member of the *ABCC* family found to be differentially regulated (log_2 fold change of -1.15) between the two basal media compositions. Despite this modest change in expression for one MRP family member, MRP activity was significantly higher in BMECs in DMEM. Thus, permeability differences could vary widely depending on media composition, without any direct relevance to pathology at the BBB *in vivo*. Similarly, BBB responses to negative stimuli (inflammation, oxidative stress, etc.) could be altered by BMEC status in different media. Increased FAK activity is associated with integrin engagement, growth factor response, and cell survival; in BMECs in DMEM, elevated FAK

activity could be responsible for reduced baseline TEER and these BMECs would perhaps be more responsive to conditions that yield paracellular barrier disruption.

We initially believed that the differences in BMEC properties between the basal media conditions might be the result of changes in the metabolic pathways within the cells. Surprisingly, though, pathway analyses did not identify differences in metabolic state but rather differences in endothelial behavior. Upregulated pathways in DMEM BMECs include axon guidance, Wnt signaling, ECM-receptor interactions, and focal adhesions. Perhaps most surprising of this cohort is the identification of axon guidance. However, identification of this pathway may actually be expected given the increased understanding of the interplay between developing vasculature and neural cells [232], and it has previously been identified using molecular profiling of mouse retinal microvascular cells [233]. Canonical Wnt signaling has well documented roles in CNS angiogenesis [24] as well as development and maintenance of blood-brain barrier properties [8]. In nonpathological conditions, levels of canonical Wnt signaling are lower in mature BBB endothelium compared to developing BBB endothelium [234]. However, the pathway has been shown to become re-activated in experimental autoimmune encephalitis and in multiple sclerosis, likely in an effort for endothelial cells to stabilize and/or restore barrier function [235]. Though outside the scope of the present study, the ability to study this phenomenon *in vitro* through alterations in media composition could prove to be an invaluable tool to study the pathophysiology of such diseases. Finally, the behavior of iPSC-derived BMECs has previously been shown to be strongly dependent upon matrix composition [236,237]. The results of the present study indicate that media composition also strongly influences *in vitro* behavior as well as interaction with extracellular matrices. Future study of the interplay between media composition, extracellular

matrix composition, and endothelial behavior will enable the development of more *in vivo*-like BBB models.

5.5 Conclusion

We have demonstrated that basal media composition can influence both passive and active barrier properties in iPSC-derived BMECs. Moving forward, the ability to explicitly control media composition should enable new research avenues into how any additive (nutrients, metabolites, hormones, etc.) influences the BBB phenotype. This advancement could also improve drug transport predictions by mimicking differential concentrations of soluble cues in health and disease.

5.6 Appendix

Table A. 5.1 Primary antibodies used in immunocytochemistry experiments.

Target	Antibody Species	Vendor	Clone or product number	Dilution
Claudin-5	Mouse	Thermo Fisher Scientific	4C3C2	1:50
Occludin	Mouse	Thermo Fisher Scientific	OC-3F10	1:100
VE-cadherin	Goat	R&D Systems	AF938	1:100
GLUT-1	Mouse	Thermo Fisher Scientific	SPM498	1:50

Table A. 5.2 Secondary antibodies used in immunocytochemistry experiments.

Species Reactivity	Host	Conjugate	Vendor	Dilution
Mouse	Donkey	Alexa Fluor 555	Thermo Fisher Scientific	1:200
Goat	Donkey	Alexa Fluor 488	Thermo Fisher Scientific	1:200

Figure A. 5.1 Complete phospho-proteome array for CC3 BMECs differentiated using DMEM and NB. Coordinates for substrates may be found in manufacturer's instructions.

Chapter 6

ROLE OF SCAFFOLDING PROTEIN IQGAP2 IN BLOOD-BRAIN BARRIER ENDOTHELIAL CELLS

6.1 Summary

Previous studies have identified retinoic acid as well as other nuclear retinoid receptor agonists as potent mediators of human induced pluripotent stem cell (iPSC)-derived brain microvascular endothelial cell (BMEC) maturity. Here, we use RNA sequencing to explore the transcriptional identities of iPSC-derived BMECs of varying maturity in an effort to identify potential contributors to the restrictive blood-brain barrier (BBB) phenotype. We identify *IQGAP2* as being significantly upregulated in mature BBB endothelium and validate its expression *in vivo*. This work highlights the potential predictive power of iPSC-derived BMEC *in vitro* models for understanding mechanisms of in vivo BBB regulation and dysfunction.

6.2 Introduction

Brain microvascular endothelial cells (BMECs), which line brain capillaries and form the blood-brain barrier (BBB), coordinate the exchange of molecules and signals between the blood stream and central nervous system (CNS) with exquisite precision and specificity [8]. This regulation is the result of BMEC expression of a host of molecular transporters [93], tight junction proteins [238], efflux transporters [239], and suppressed rates of nonspecific pinocytosis and transcytosis [6]. Dysfunction of these transport systems is increasingly associated with many neurodegenerative diseases, including Alzheimer's disease [4], Parkinson's disease [240], and multiple sclerosis [241], as well as in normal aging processes [41]. Unfortunately, the increased recognition of the vascular contribution to neurodegenerative diseases has not resulted in an

increased understanding of the molecular and mechanistic underpinnings which impart the specialized nature of the BBB. Indeed, little is known about the BBB-specific proteins and molecular mechanisms responsible for this phenotype as the proteins often used to characterize BBB function may be found in other endothelial beds in the body [242]. This lack of insight hinders effective therapeutic intervention at the BBB and thus represents a significant global health concern.

In part, the identification of BBB-specific proteins has been impeded by a lack of adequately representative models. Traditional animal models, such as mouse [52], pig [56,57], and cow [55], suffer from a lack of species homology [62], while primary [64] and immortalized [243] human BMEC sources fail to recapitulate key in vivo characteristics in a scalable manner. BMECs produced from induced pluripotent stem cell (iPSC) sources overcome many of these challenges by providing a fully human system which more closely recapitulates in vivo behavior [65,67,111,192,195,204,205,244]. The addition of retinoic acid (RA) to the model was found to significantly increase transendothelial electrical resistance (TEER) as well as VE-cadherin expression, suggesting that RA-mediated signaling events serve a prominent role in maturation of the BBB [67,245]. Recent work by Stebbins, et al., identified activation of nuclear retinoid X receptor (RXR) isoform α, known to bind to DNA response elements and in turn regulate gene transcription, by small molecular agonist CD3254 sufficient to induce increased TEER in BMECs similar to that induced by the addition of RA [191]. Though the aforementioned studies did not identify genes responsible for mediating these improvements in BMEC phenotypes, the collective works suggest that the maturity and fidelity of iPSC-derived BMECs may be modulated through small molecule treatment, thereby providing an ideal platform with which to interrogate human-specific mechanisms of BBB function.

To this end, we used RNA sequencing to assess the transcriptional identities of BMECs differentiated using CD3254 and RA. Through these studies, we identified IQGAP2 as a potential novel contributor to the human BBB phenotype. IQGAP2 is one of three members of the evolutionarily conserved scaffolding protein IQGAP family [246]. As molecular scaffolds, these proteins coordinate a vast array of cellular processes [246], including cytoskeletal architecture [247] and intracellular signaling [248–250]. Each protein contains a calponin homology domain (CHD), a poly proline protein-protein domain (WW), IQ domain consisting of calmodulin binding IQ motifs, and the Ras GTPase-activating protein (GAP)-related domain [247,248]. IQGAP2 expression was originally believed to be liver-specific but has since been identified in other tissues [251], including the kidneys [252] and testis [253], both organs in which barrier function in critical to proper physiological function. Moreover, its expression has not previously been conclusively shown in human brain capillaries [254], nor has its expression been shown in databases of RNA sequencing data [32,255]. Here, we demonstrate the ability of iPSC-derived BMECs to identify novel contributors to the blood-brain barrier phenotype with *in vivo* relevance. This predictive power stands to provide unprecedented insight into blood-brain barrier function in health and disease and to help identify much needed therapeutics.

6.3 Materials and methods

6.3.1 Maintenance of iPSCs

CC3 [108] and CD12 [107] iPSCs were maintained in E8 medium [101], prepared as previously described [195], on growth factor reduced Matrigel (Corning). iPSCs were passaged upon reaching 60-80% confluence using Versene (Gibco). iPSCs were not used for experiments after passage 40.

6.3.2 Differentiation of iPSCs to BMECs

iPSCs were differentiated to BMECs as previously described [195,244]. Briefly, iPSCs were seeded onto Matrigel-coated tissue culture plates at a density of 15,800 cells/cm2 in E8 medium containing 10 μM Y27632 (Tocris). Approximately 24 h later, differentiation was initiated via a full media change to E6 medium [102]. Cells were cultured in E6 medium for 4 days with media changes once daily. On the fourth day of differentiation, cells were switched to human endothelial serum free medium (hESFM; Gibco) with platelet poor plasma derived serum (PDS; Alfa Aesar) or 200× B27 (Gibco), collectively referred to as EC medium, supplemented with 20 ng/mL basic fibroblast growth factor (bFGF; Peprotech), and 10 μM all-trans retinoic acid (RA; Sigma-Aldrich). Media was not changed for 48 h. After this two-day incubation, cells were washed 1x with DPBS (Gibco), incubated with Accutase until a single cell suspension was obtained (~25-45 min), and collected via centrifugation. Cells were resuspended in EC medium containing 20 ng/mL bFGF and 10 μM RA and plated onto tissue culture plates or Transwell filters coated with collagen IV (400 μg/mL; Sigma-Aldrich) and fibronectin (100 μg/mL; Sigma-Aldrich). Media was changed 24 h later to fresh EC medium (containing no bFGF or RA) to induce barrier. Transendothelial electrical resistance (TEER) was measured approximately every 24 h using an EVOM2 with STX2 chopstick electrodes (World Precision Instruments).

6.3.3 RNA isolation and sequencing

CC3 BMECs were differentiated as described above with minor modifications [244]. On day 4 of differentiation, cells were switched to hESFM with 200× B27, 20 ng/mL bFGF, and either 10 μM RA, 10 μM CD3254 (Tocris), or an equal volume of DMSO (Sigma-Aldrich). Cells were subsequently purified in the same media they were given on day 4 onto Transwell filters and 6-well cell culture plates coated in collagen IV and fibronectin. 24 h after the removal of bFGF and

RA, CD3254, or DMSO from the media, BMECs purified onto 6-well plates were washed once with DPBS, collected using a cell scraper (Fisher) in an addition 1mL of DPBS, and pelleted via centrifugation. Cell pellets were resuspended in 500 μL of TRIzol (Life Technologies) and stored at -80°C until the day of isolation.

On the day of isolation, RNA from all RA, DMSO, and CD3254 samples was isolated according to manufacturer's instructions using a Direct-zol Miniprep kit (Zymo Research) with DNase I treatment. All samples were isolated at the same time to prevent batch effects. Isolated samples were submitted to the Vanderbilt Technologies for Advanced Genomics (VANTAGE) facility for sequencing using an Illumina NovaSeq6000.

Raw sequencing reads were obtained for 9 paired-end samples (3 biological replicates for the 3 conditions identified as CD3254, RA and DMSO) and run through a bulk RNA-Seq pipeline governed by the Snakemake (5.2.4) workflow management system [230]. Quality control was monitored with FastQC v0.11.8 before and after quality and adapter trimming, as performed by Trim Galore v0.5.0. Trimmed paired-end sequences were then aligned to the human genome (GRC38) with STAR 2.60c, utilizing Gencode genomic feature annotations (v26). Once quantitated, the feature counts were used for downstream analysis. The average mapped reads count was 41M reads (85% of total reads).

Gene counts and sample metadata were used for differential gene expression using DESeq2 [231], between the condition groups: CD3254 vs DMSO and RA vs DMSO. For each testing pair, we analyzed differential gene expression results quantitatively and visually. For the up- and down-regulated groups of top genes, we also performed functional gene enrichment analysis for Gene Ontology and KEGG pathways.

6.3.4 Quantitative polymerase chain reaction

BMECs differentiated using DMSO, CD3254, and RA as described above were purified onto collagen IV and fibronectin coated plates. BMECs were washed once with DPBS and incubated with Accutase until detached. Cells were collected via centrifugation and resuspended in 500 µL of TRIzol. RNA from samples was isolated using a RNeasy Mini kit (Qiagen), according to manufacturer's instructions. Sample concentrations were measured using a Qubit Fluorometer (Thermo Fisher Scientific) and Qubit RNA BR assay kit (Thermo Fisher Scientific). cDNA was generated from samples using a cDNA High Capacity Reverse Transcription Kit (Applied Sciences) without RNase inhibitor according to manufacturer's instructions. PCR reaction mixtures were prepared using TaqMan gene expression assays for IQGAP2 and GAPDH (Thermo Fisher Scientific), TaqMan gene expression master mix, and 15 ng of cDNA per 20 µL reaction. Changes in fluorescence for all samples were measured using a BioRad CFX96 thermocycler.

6.3.5 Protein extraction and western blot

Protein was isolated from samples on day 1 of subculture for BMECs and upon reaching confluence for all other cell types. Fresh RIPA buffer (Sigma-Aldrich) with 1% v/v protease inhibitor cocktail (Sigma-Aldrich) and 1% v/v phosphatase cocktail inhibitor 3 (Sigma-Aldrich) was prepared on the day of isolation. On this day, BMECs were washed once with DPBS, collected using a cell scraper (Fisher Scientific), and pelleted via centrifugation. Cell pellets were resuspended in prepared RIPA buffer, incubated on ice for 30 min, and centrifuged for 15 min at 12,000×g at 4°C. Cleared supernatants were transferred to clean microcentrifuge tubes and stored at -20°C. Protein from all other cell types was collected in a similar manner with the exception that cells were collected using Accutase or TrypLE (Gibco) rather than cell scraping.

Protein concentration for all samples was determined using a Pierce BCA protein assay. Samples were prepared by diluting 20 µg of protein in 1× Laemmli buffer (Bio-Rad) and ultrapure water (Gibco) to a final volume of 20 µL. Samples were then heated at 95°C for 5 min, placed on ice for an additional 5 min, and centrifuged briefly. After, samples were loaded into 4-20% Criterion TGX midi protein gels (Bio-Rad), along with Precision Plus Protein Dual Color Standard (Bio-Rad), and run at 80V until all samples fully entered the gel. Voltage was subsequently increased to 160V until the desired degree of protein separation was achieved. Protein gels were transferred onto iBlot 2 nitrocellulose membranes (Thermo Fisher Scientific) using an iBlot 2 gel transfer device (Thermo Fisher Scientific). Membranes were blocked for a minimum of 30 min at room temperature (RT) in Intercept (TBS) blocking buffer (Li-Cor Biosciences) on an orbital shaker. Membranes were incubated with desired primary antibodies (Table A. 6.1) diluted in blocking buffer with 0.05% Tween-20 (Sigma-Aldrich) overnight at 4°C on an orbital shaker.

Following primary antibody incubation, blots were rinsed once and washed 3 times, 5 min per wash, with tris buffered saline (TBS; Corning) with 0.05% Tween-20 (collectively TBS-T). Blots were incubated with appropriate secondary antibodies (Table A. 6.2) diluted in TBS-T for 1-2 h at RT on an orbital shaker. Blots were washed as described above and imaged using a Li-Cor Odyssey CLx Imager. The intensity of resultant bands was quantified using Image Studio Lite software.

6.3.6 Development of IQGAP2 antibody

A peptide corresponding to amino acid residues 1460-1474 of human IQGAP2 was synthesized with an amino terminal Cys RSIKLDGKGEPKGAK and conjugated to maleimide-activated KLH, maleimide-activated BSA, and SulfoLink resin using manufacturer protocols (ThermoFisher). The peptide-KLH conjugate was used to immunize rabbits (Cocalico

Biologicals). Rabbit antisera was tested for the presence of antibodies recognizing the IQGAP2 peptide by dot blot analysis using the peptide-BSA conjugate. The rabbit antibodies were affinity-purified from the antisera using the peptide-SulfoLink resin. Briefly, 5 ml of rabbit sera was diluted 1:1 with PBS and passed over a 2 ml peptide-SulfoLink column. After extensive washing with PBS, bound antibodies were eluted with 8.5 ml 0.1 M Glycine pH 2.2 and collected in a tube containing 1.5 ml of 1 M Tris pH 8. The affinity-purified antibodies were used at a 1:200 dilution for Western analysis.

6.3.7 Caco2 maintenance

Caco2 cells (ATCC) were cultured in 6-well cell culture plates coated with 0.1% gelatin (Sigma-Aldrich). Plates were coated with 0.1% gelatin for a minimum of 30 min at 37°C prior to use. Caco2s were maintained in DMEM containing glucose, sodium pyruvate, and L-glutamine (Corning) with 1× MEM non-essential amino acids (Sigma-Aldrich), 1× antibiotic/antimycotic (Gibco), and 10% heat inactivated fetal bovine serum (Gibco). Cells were passaged upon 80-100% confluence using TrypLE Express (Gibco).

6.3.8 HUVEC maintenance

Human umbilical vein endothelial cells (HUVECs) were cultured on 0.1% gelatin-coated 6-well plates in EBM-2 media (Lonza) with full growth bullet kit (Lonza). HUVECs were passaged upon reaching confluence using TrypLE Express.

6.3.9 Immunohistochemistry

Human brain cortex, lung, and liver tissue sections were acquired from the Cooperative Human Tissue Network and Dr. Matthew Schrag at Vanderbilt University Medical Center. Flash frozen tissue was submitted to the Vanderbilt Translational Pathology Shared Resource for

embedding in optical cutting temperature (OCT) and cryosectioning. For staining, sections were thawed and washed once with DPBS for 5 min at RT. Sections were subsequently fixed in 4% paraformaldehyde (Thermo Fisher Scientific) for 10 min at RT. Following fixation, tissues were rinsed once with DPBS and washed 3 times with DPBS, 5 min per wash. Sections were blocked in DPBS containing 5% donkey serum (Sigma-Aldrich) and 0.3% Triton X-100 (Sigma-Aldrich), collectively referred to as PBS-DT, for a minimum of 1 h at RT and incubated with primary antibodies (Table A. 6.1) diluted in PBS-DT overnight at 4°C. The following day, samples were rinsed once with DPBS and washed 3 times with DPBS, 5 min per wash. Samples were incubated with appropriate secondary antibodies (Table A. 6.2) diluted in PBS-DT for 1-2 h at RT. Nuclei were subsequently labeled using 4′,6-Diamidino-2-pheny-lindoldihydrochloride (DAPI; Thermo Fisher Scientific). Samples were washed with DPBS as before, and samples were mounted using ProLong Gold Antifade Mountant (Thermo Fisher Scientific). Sections were imaged using a Leica DMi8 microscope or Olympus FV-1000 inverted confocal microscope.

6.3.10 Fluorescence in-situ hybridization

Transcripts were detected using an RNAscope assay (Advanced Cell Diagnostics) with probes against IQGAP2 according to manufacturer's instructions, with minor modifications. Briefly, fresh frozen tissue sections were thawed and incubated with ~3 drops of RNAscope Protease IV for 30 min at RT. During this incubation, 1X wash buffer was prepared by diluting 10 mL of 50X wash buffer in 490 mL ultrapure water. Following incubation, samples were washed once with DPBS, and ~3 drops of IQGAP2 probe was added to the sample. The probe was incubated for 2 h at 40°C in a humidified tray. Samples were then washed 5 times with 1X wash buffer for 2 min per wash at RT. 3 drops of Amp 1-FL were added per sample, incubated for 30 min at 40°C, and washed 5 times with 1X wash buffer for 2 min per wash at RT. Next, samples

were incubated with 3 drops of Amp 2-FL for 15 min at 40°C, followed by 5 washes for 2 min in 1X wash buffer at RT. 3 drops of Amp 3-FL were incubated with samples for 30 min at 40°C, followed by 5 washes as before. Finally, 3 drops of Amp 4-FL were added and incubated for 15 min at 40°C followed by thorough washes with 1X wash buffer. Samples were counterstained with DyLight 488 labeled Lycopersicon esculentum (tomato) lectin (1:100 in 1X wash buffer; Vector Laboratories) to label vasculature for 30 min at RT. Samples were washed again with 1X wash buffer five times, mounted in VECTASHIELD antifade mounting medium with DAPI (Vector Laboratories), and imaged using a Leica DMi8 microscope.

6.3.11 Immunocytochemistry

Cells were rinsed twice with DPBS and incubated with 4% paraformaldehyde or 100% methanol (Fisher Scientific) for 20 min or 10 min, respectively. Following fixation, cells were washed 3 times with DPBS, 5 min per wash. Fixed cells were blocked using PBS-DT if fixed using paraformaldehyde or DPBS with 5% donkey serum (PBSD) if fixed using methanol for a minimum of 1 h at RT. Cells were incubated with desired primary antibodies (Table A. 6.1) diluted in PBS-DT or PBSD overnight at 4°C. The next day, cells were rinse once with DPBS or DPBS with 0.3% Triton X-100 (PBS-T) and washed 5 times with DPBS, 5 min per wash. Secondary antibodies (Table A. 6.2) diluted in PBS-DT or PBSD were incubated with cells for 1-2 h at RT. Nuclei were labeled using a 10 min incubation with 4′,6-Diamidino-2-pheny-lindoldihydrochloride (DAPI; Thermo Fisher Scientific) or Hoechst 33342 trihydrochloride trihydrate (Thermo Fisher Scientific). Cells were subsequently rinsed once with DPBS or PBS-T, washed 4 times with DPBS or PBS-T, 5 min per wash, and imaged using a Leica DMi8 microscope.

6.4 Results and discussion

Previous work has shown that activation of nuclear retinoic acid receptors in iPSC-derived BMECs by all-trans retinoic acid (RA) sufficient to elevate transendothelial electrical resistance (TEER) and VE-cadherin expression [67]. This effect was found to be the result of an increase in the maturation of iPSC-derived BMECs, and the effect could be recapitulated, in part, by treatment of differentiating cells with retinoid X receptor alpha (RXRα) agonist CD3254 [191]. However, no genes have yet to be implicated in imparting this BBB phenotype, and identification of such genes and related signaling pathways could provide valuable insight into potential routes to restoring BBB dysfunction. To this end, we differentiated CC3 iPSCs to BMECs as previously described [244], with minor modifications, and analyzed the transcriptomes of the resultant purified cells. Specifically, BMECs were treated with DMSO (vehicle control), RA, or CD3254 during the differentiation to produce BMECs of varying maturity (Figure 6.1A). Principle component analysis of the transcriptomes found 78% variance within the first component, indicating that retinoic acid signaling was the primary driver of differences in transcriptional landscapes (Figure 6.1B).

Despite its utility in achieving a more mature BMEC phenotype, RA signaling is known to be involved in a wide range of signaling cascades in development [256], many of which are likely not involved in producing the specialized BMEC phenotype. This logic may be extended to the effects of treatment with CD3254, despite its targeted activation of a single receptor. We therefore reasoned that genes upregulated under both RA treatment (Figure 6.1C) and CD3254 treatment (Figure 6.1D) bore the highest likelihood for contributing to the specialized BMEC phenotype. IQGAP2 was found to be highly upregulated under both RA treatment ($p=1.7\times10\text{-}79$, log2(fold

change)=6.33) and CD3254 treatment (p=7.51×10-31, log2(fold change)=4.04) conditions and was selected for further interrogation.

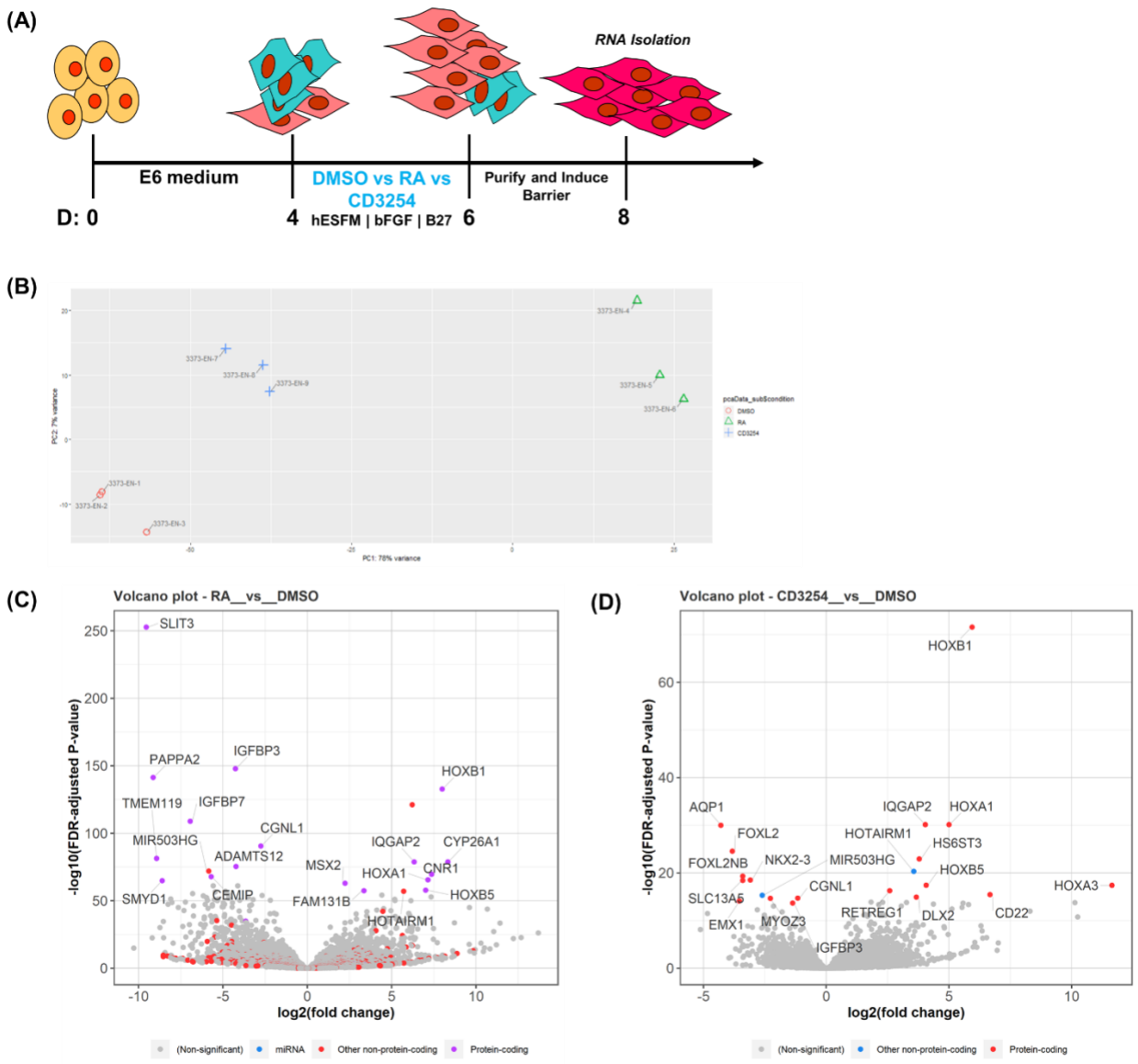

Figure 6.1 RNA sequencing of iPSC-derived BMECs of varying fidelity. (A) iPSCs were differentiated in E6 medium for 4 days before expansion in endothelial medium containing DMSO, RA, or CD3254. Resultant cells were subsequently purified, and barrier formation was induced by the removal of bFGF from the medium. RNA was subsequently extracted from these cells and submitted for sequencing. (B) Principal component analysis indicates that the DMSO/RA/CD3254 treatments were the primary driver of transcriptional differences between the cell populations. (C) Volcano plot highlighting differentially expressed genes in RA versus DMSO conditions. (D) Volcano plot highlighting differentially expressed genes in CD3254 versus DMSO conditions.

We next worked to verify the results of our RNA sequencing experiments using quantitative polymerase chain reaction. We repeated the differentiation conditions used in our RNA sequencing experiments in CD12 iPSCs, a male control iPSC line, differentiated using PDS (Figure 6.2A). Transcript expression levels were measured and found to follow expression trends found in RNA sequencing (Figure 6.2B). Though encouraged by these results, we recognized that post-transcriptional regulation events might prevent differences in transcript expression from resulting in differences in protein expression. We assessed the level of IQGAP2 expression in iPSC-derived BMECs in DMSO, RA, and CD3254 differentiation conditions, as well in Caco2 epithelial cells and HUVECs. IQGAP2 protein expression levels were found to align with transcript expression trends (Figure 6.2C). IQGAP2 expression in HUVECs was strikingly less than IQGAP2 expression in Caco2 cells, indicating that IQGAP2 expression is not endothelial-specific. Finally, as IQGAP family proteins are scaffolding proteins and are capable of performing multiple functions within cells, we assessed cellular localization via immunocytochemistry to provide potential insight into its function. IQGAP2 was found to localize to cell-cell borders in Caco2 cells as well as in CC3 BMECs differentiated using RA. In contrast, IQGAP2 expression was found to be perinuclear in HUVECs with no expression evident in cell-cell contacts (Figure 6.2D).

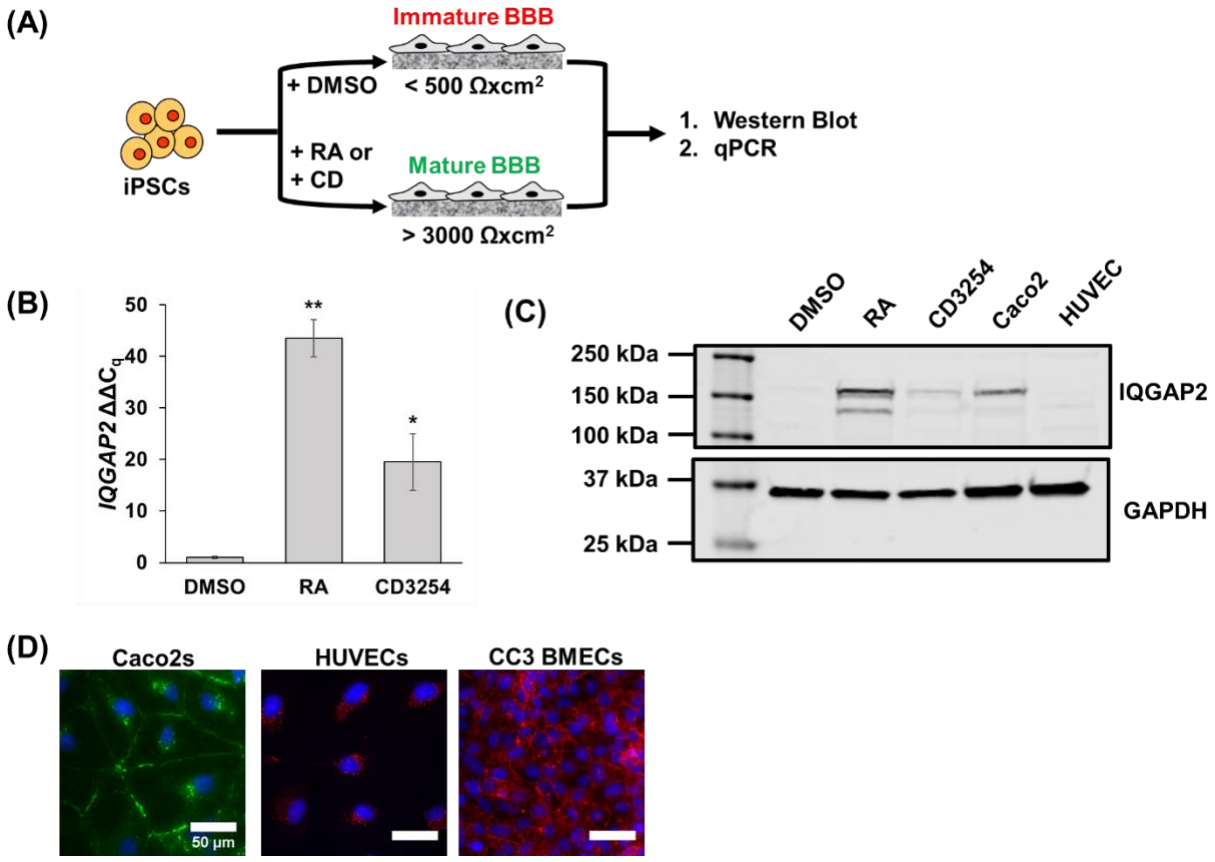

Figure 6.2 Characterization of IQGAP2 expression *in vitro*. (A) iPSCs were differentiated to immature or mature BBB endothelium, and IQGAP2 expression was assessed using qPCR and western blot. (B) qPCR results for *IQGAP2* follow trends found in RNA sequencing data. (C) IQGAP2 expression was assessed in BMECs differentiated using DMSO, RA, and CD3254 as well as in Caco2 and HUVEC controls. (D) Immunocytochemical detection of IQGAP2 in Caco2s, HUVECs, and BMECs. Scale bars are 50 µm.

Though iPSC-derived BMECs closely recapitulate many *in vivo* characteristics of the human BBB, these cells are an *in vitro* model system, and as such, we worked to clarify that IQGAP2 expression patterns were not the result of an *in vitro* artifact. IQGAP2 is not predicted to be expressed in brain endothelial cells by multiple transcriptomic databases [32,255], and available protein expression data is inconclusive [254]. Commercially available IQGAP2 antibodies validated for immunohistochemistry of human tissue are limited, and the high degree of similarity between members of the IQGAP family made antibody specificity a point of concern. Therefore,

we developed a polyclonal antibody against human IQGAP2 specific to known isoforms of this protein. Using this antibody, we detected IQGAP2 expression in brain vasculature in human cortical slices, though its expression pattern was heterogeneous amongst vessels (Figure 3A). We further validated IQGAP2 expression in brain vasculature using fluorescence in situ hybridization and found expression heterogeneity similar to that of the protein expression (Figure 3B). Finally, we wished to validate the specificity of our antibody through staining of human liver tissue where IQGAP2 expression is most widely documented [251]. As expected, abundant IQGAP2 expression was found within this tissue (Figure 3C).

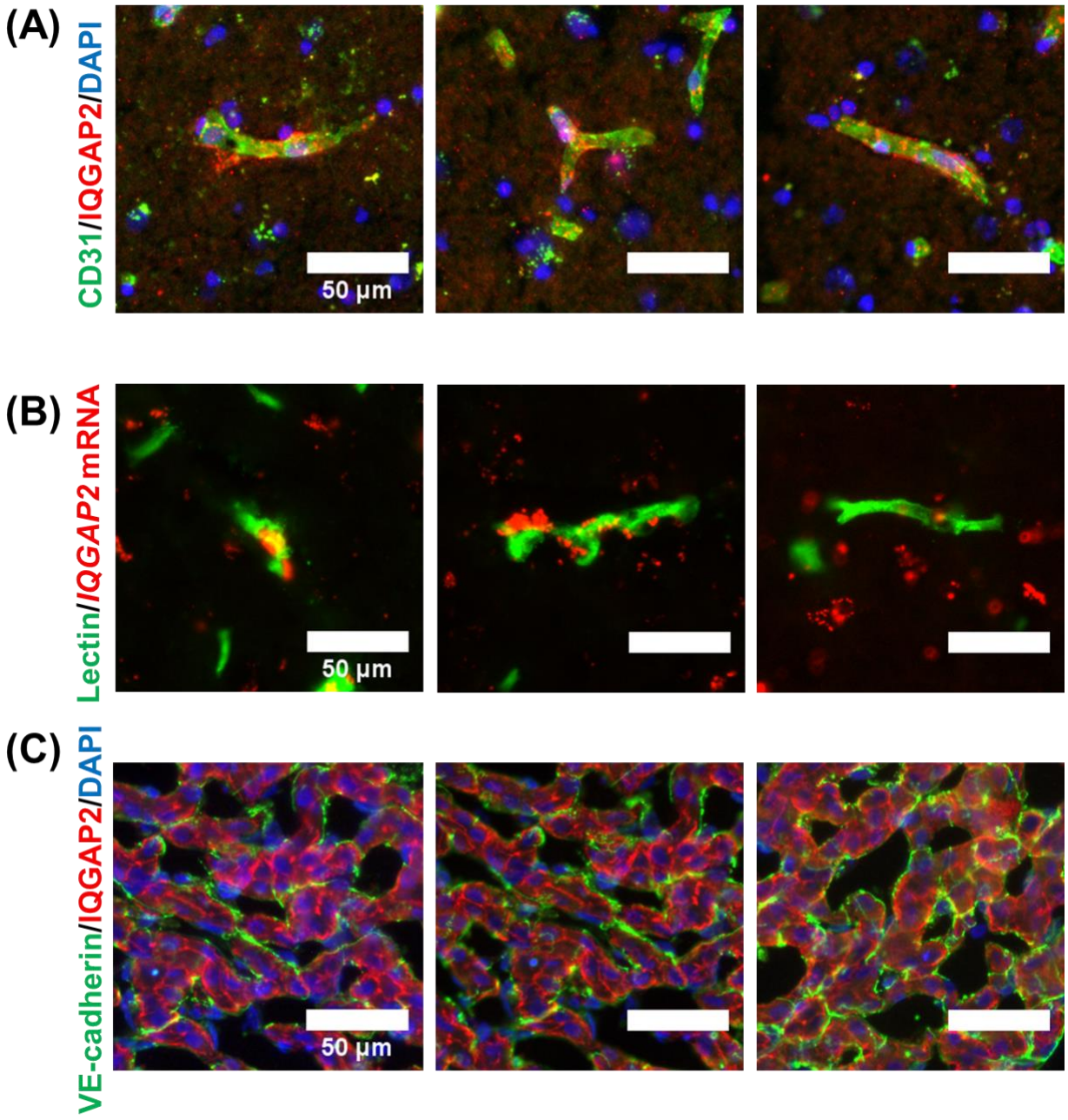

Figure 6.3 *In vivo* detection of IQGAP2 in human tissues. (A) IQGAP2 expression in human brain cortex. (B) *IQGAP2* mRNA transcripts in human brain cortex vasculature. (C) IQGAP2 expression in human liver. Scale bars are all 50 µm.

6.5 Conclusion

Collectively, these results indicate that iPSC-derived BMECs are not only useful for drug screening purposes and targeted interrogation of in vivo findings. Instead, this model possesses predictive power and may be used to as a tool to rapidly uncover mechanisms of BBB maintenance and dysfunction with in vivo relevance in a fully human, highly reproducible environment. Moving forwards, efforts to explore the potential role of IQGAP2 in mediating BBB function may provide insight into the specialized nature of this critical biological interface.

6.6 Appendix

Table A. 6.1 Primary antibodies used in immunocytochemistry and immunohistochemistry experiments.

Target	Antibody Species	Vendor	Clone or product number	Dilution
IQGAP2	mouse	EMD Millipore	BB9	1:1000
IQGAP2	Rabbit	Abcam	ab204225	1:100
IQGAP2	Rabbit	Vanderbilt Antibody Protein Resource	--	1:200
VE-cadherin	Goat	R&D Systems	AF938	1:100
CD31	Mouse	Abcam	JC/70A	1:25

Table A. 6.2 Secondary antibodies used in immunocytochemistry and immunohistochemistry experiments.

Species Reactivity	Host	Conjugate	Vendor	Dilution
Mouse	Donkey	Alexa Fluor 555	Thermo Fisher Scientific	1:200
Mouse	Donkey	Alexa Fluor 488	Thermo Fisher Scientific	1:1000
Goat	Donkey	Alexa Fluor 488	Thermo Fisher Scientific	1:200
Rabbit	Donkey	Alexa Fluor 488	Thermo Fisher Scientific	1:200
Rabbit	Donkey	Alexa Fluor 555	Thermo Fisher Scientific	1:200
--	Lectin	DyLight 488	Vector Laboratories	1:100

Chapter 7

HIGH-THROUGHPUT CRISPR/CAS9 SCREEN TO IDENTIFY MODULATORS OF PARACELLULAR PERMEABILITY

7.1 Summary

The blood-brain barrier is characterized in part by robust expression of tight junction proteins. These tight junctions strictly limit the paracellular passage of materials down to the level of ions. Disruption of this paracellular barrier is associated with many chronic and acute neurodegenerative disorders, such as Alzheimer's disease. Unrestricted extravasation of blood-borne materials leads to vasogenic edema [257], interrupted synaptic transmission, and even cognitive dysfunction [258]. Therefore, therapeutic intervention at this paracellular barrier is a highly promising strategy target in the treatment of such disorders. Here, we present a high throughput CRISPR screen coupled with high content imaging to identify novel regulators of blood-brain barrier paracellular permeability. The results of this screen implicate previously known genes in the maintenance of this barrier as well as genes known to be upregulated in mature endothelium. This screen is the first of its kind to identify modulators of BBB-specific function and represents a new phase in interrogating genomic regulation of the BBB.

7.2 Introduction

The prevalence of neurodegenerative disorders, such as Alzheimer's disease, Parkinson's disease, and stroke, continues to grow in tandem with the growing, aging global population [2,259]. Such diseases are the leading cause of disability worldwide [260], and as such, pose significant personal and economic burdens which are likely to increase in coming years [2]. These disorders have historically been characterized by the dysfunction of neurons and glia [261], both

of which require highly regulated ionic and molecular microenvironments to signal properly and form functional neural networks [6]. The composition of these microenvironments is maintained by the blood-brain barrier (BBB), composed of brain microvascular endothelial cells (BMECs) which line brain capillaries. BMECs control material flux across the BBB into the central nervous system (CNS) parenchyma through their robust expression of a cohort of molecular transporters [20], efflux transporters [262], and tight junction proteins [263] and suppression of nonspecific transcytosis [72]. Dysfunction of the BBB is increasingly associated with many neurodegenerative disorders [13] as well as in natural aging processes [41] and thus is a promising target for therapeutic intervention in the treatment of such diseases.

The paracellular flux of material across the BBB is restricted down to the level of ions by tight junction complexes formed between adjacent BMECs, which more closely resemble epithelial tight junctions than endothelial junctions found in peripheral beds [264,265]. The proteins which form these complexes have been well characterized and include occludin, the first identified tight junction protein [266], as well as several members of the claudin family [265]. The formation of these tight junctions is supported by junctional adhesion molecules (JAMs) and zonula occludens (ZO) proteins, which function as scaffolding proteins and connect tight junctions to the actin cytoskeleton [238]. Since identification of these proteins, significant effort has been placed on understanding their role in maintaining the BBB paracellular barrier. In foundational work by Nitta, et al., claudin-5 deficient mice were found to have the permeability of their BBB altered in a size-specific manner [267]. Specifically, loss of claudin-5 resulted in a loss of restriction against small molecules (<800 Da) but did not permit extravasation of larger molecules such as serum albumin across the barrier. When more significant degeneration of tight junctions occurs, such as is evident in many neurodegenerative diseases, passage of large circulating

molecules, such as thrombin, fibrinogen, and albumin, from the blood stream into the central nervous system parenchyma results in exacerbated BBB disruption, neuronal injury, and neuroinflammation [240]. Therefore, the proteins and pathways which regulate the formation and fidelity of tight junctions are ideal candidates for therapeutic intervention

Unfortunately, many of the molecular constituents and signaling pathways which underpin the highly restrictive nature of the BBB remain poorly understood. Previous attempts to identify genes important to BBB have relied upon transcriptome analyses to identify genes specifically upregulated in neurovasculature [26,32,72,74,242,255,268,269]. These studies provide invaluable insight into previously unknown mechanisms of BBB regulation, but the works relied upon *in vivo* studies followed by tedious isolation and extensive transcriptome analysis. The current and impending burden of neurological disease necessitates the development of high throughput screening methods for BBB functional genomic elements. To this end, we performed a high-throughput CRISPR screen in barrier-forming Caco2 cells to identify modulators of paracellular permeability. Approximately 8400 genes were screened for their potential contribution to the restrict paracellular barrier phenotype and analyzed using high-content imaging of cell-cell junctions. Overall, this study is the first of its kind to identify regulators of BBB-specific functions using CRISPR screening techniques.

7.3 Materials and methods

7.3.1 Preparation of complete growth medium

Complete growth medium was prepared by supplementing DMEM (Corning; 10-013-CV) with 10% heat-inactivated fetal bovine serum (FBS; Thermo Fisher Scientific), 1X penicillin-streptomycin (Gibco) or 1X antibiotic-antimycotic (anti-anti; Thermo Fisher Scientific), and 1X

MEM non-essential amino acid solution (Sigma-Aldrich). FBS was heat-inactivated by heating at 56°C for 30 min followed by rapid cooling on ice.

7.3.2 Preparation of transduction medium

Transduction medium was prepared by supplementing DMEM (Corning; 10-013-CV) with 1X MEM non-essential amino acid solution (Sigma-Aldrich). Transduction medium contained no serum as well as no antibiotics or antimycotics.

7.3.3 Preparation of transfection medium

Transfection medium was prepared similarly to complete growth medium with the omission of anti-anti.

7.3.4 Preparation of 2X anti-anti medium

2X anti-anti medium was prepared similarly to complete growth medium. However, anti-anti was added to the medium to a final concentration of 2X rather than 1X.

7.3.5 Preparation of serum-free barrier formation medium

Neurobasal medium (referred to as HB NB) was prepared by the Vanderbilt Cell Culture Resource Lab according to compositions publicly available through Thermo Fisher Scientific.

7.3.6 Generation of Cas9-expressing Caco2 cells

Approximately 24 h before transduction, Caco2 cells were seeded at a density of 31,600 cells/cm$_2$ onto 24-well cell culture plates coated with 0.1% gelatin (Sigma) in complete growth medium. On the day of transduction, cells were washed once with DPBS (Gibco), incubated with TrypLE Select (Gibco) for 3 min at 37°C, and collected as a single-cell suspension. Density of the collected cells was determined using a Countess II (Thermo Fisher) automated hemocytometer.

Based on the measured density, one well of Caco2s were transduced at a multiplicity of infection (MOI) of 0.3 with Edit-R lentiviral mKate2-tagged, constitutively expressed Cas9 nuclease (Dharmacon) under the hEF1α promoter in transduction medium containing 5 μg/mL polybrene (EMD Millipore). Complete growth medium was added to transduced cells at a 3:1 dilution 5 h after the initiation of transduction, and medium was completely changed 48 h after the initiation of transduction. Medium was changed every 48 h thereafter until selection via fluorescence activated cell sorting (FACS).

7.3.7 Fluorescence activated cell sorting

Transduced Caco2s harboring Cas9 expression were purified via FACS. Briefly, cells were washed once with DPBS, incubated for 3 min at 37°C, and collected via centrifugation. Pelleted cells were resuspended at a density of $5\times10_6$ cells/mL in phenol-red free DMEM medium (Gibco; #21063-029) supplemented with 10 μM Y27632 (Tocris) and 1X penicillin-streptomycin (Gibco). Cells underwent clonal sorting onto 96-well plates coated with 0.1% gelatin and using a 5-laser FACS Aria III (BD Biosciences) with a 100 μm nozzle. Sorted cells were collected in sterile filtered conditioned medium supplemented with 10 μM Y27632, 10 mM HEPES (Gibco), and 1X penicillin-streptomycin. Clones were supplemented with an additional 100 μL of complete growth medium per well approximately 24 h after sorting. Medium was changed to complete growth medium 48 h after sorting and fully changed every 48 h thereafter. Two clones, referred to as C6 and F7, respectively, were selected for further analysis and experimental use.

7.3.8 Cell maintenance

Both Cas9-expressing and non-Cas9-expressing Caco2s were cultured on 0.1% gelatin in complete growth medium. Cells were passaged upon reaching 80-100% confluence using TrypLE (Gibco). For small scale experiments, Cas9-Caco2s were cultured in 6-well cell culture plates

(Corning). For screening experiments, Cas9-Caco2s were cultured in T175 cell culture treated flasks.

7.3.9 Protein isolation and western blotting

Cells were rinsed once with DPBS, incubated with TrypLE Express for 3 min at 37°C, and collected via centrifugation. Pellets were lysed in RIPA buffer (Sigma-Aldrich) containing 1% protease inhibitor cocktail (Sigma-Aldrich) and 1% phosphatase inhibitor cocktail 3 (Sigma-Aldrich) and incubated on ice for 30 min. Samples were then centrifuged for 15 min at 12,000×*g* at 4°C. Cleared supernatants were transferred to clean microcentrifuge tubes and stored at -20°C until used for further analysis.

Protein concentration was measured using a Pierce BCA protein assay (Thermo Fisher Scientific). Using concentrations determined by the BCA assay, 20 μg of protein per sample was diluted in 1× Laemmli buffer (Bio-Rad) and ultrapure water (Gibco) to a total volume of 20 μL. Samples were subsequently heated for 5 min at 95°C, placed on ice for 5 min, and loaded into 4-20% Criterion TGX precast midi protein gels (Bio-Rad). Gels were resolved and transferred to nitrocellulose membranes using an iBlot2 transfer machine (Thermo Fisher Scientific). Membranes were blocked in Intercept blocking buffer (TBS-based; Li-Cor) for a minimum of 30 min at room temperature on an orbital shaker. Blots were incubated with primary antibody overnight at 4°C on an orbital platform. The following morning, blots were washed 3 times, 5 min per wash, with 1× TBS with 0.05% Tween-20 (collectively TBS-T; Sigma-Aldrich). Blots were incubated with secondary antibodies for 1-2 h at room temperature on an orbital shaker, washed as previously described, and imaged using an Odyssey CLx imager (Li-Cor).

7.3.10 Immunocytochemistry

Cells were washed twice with DPBS and fixed using 4% paraformaldehyde (Thermo Fisher Scientific) for a minimum of 10 min at room temperature. Following fixation, cells were washed three times with DPBS, 5 min per wash. Cells were blocked using DPBS containing 5% donkey serum (Sigma-Aldrich) and 0.3% Triton X-100 (Sigma-Aldrich), collectively referred to as PBS-DT, for a minimum of 1 h at room temperature. Cells were incubated with primary antibody (Table A. 7.1) diluted in PBS-DT overnight at 4°C. The following morning, cells were rinsed once and washed five times with DPBS containing 0.3% Triton X-100, referred to as PBS-T, with a minimum of 5 min per wash. Cells were incubated with secondary antibody (Table A. 7.2) for 1-2 h at room temperature. Nuclei were labeled after incubation with secondary antibody using Hoechst 33342 trihydrochloride trihydrate (Thermo Fisher Scientific). Stained cells were rinsed once and washed four times with PBS-T prior to imaging using a Leica DMi8 microscope.

7.3.11 Transfection of synthetic CRISPR reagents

CRISPR RNA (crRNA) and trans-activating RNA (tracrRNA) were resuspended in 10 mM Tris buffer, pH 7.4, all purchased from Dharmacon, were resuspended to create 1 μM and 10 μM working stocks, respectively. For reverse transfection, tracrRNA was further diluted to 333 nM in Opti-MEM reduced serum media (Thermo Fisher Scientific). Dharmafect 1 (Dharmacon) was diluted in Opti-MEM to a concentration of 0.8 μL of Dharmafect 1 per 10 μL of total diluted reagent. crRNA and tracrRNA were mixed such that the concentration of 10 μL of the crRNA:tracrRNA complex was 125 nM upon addition of prepared diluted Dharmafect 1. The crRNA:tracrRNA complex was allowed to incubate with Dharmafect 1 for a minimum of 20 min prior to cell addition.

During this incubation time, cells were washed once with DPBS (Thermo Fisher Scientific) and incubated with TrypLE Express (Thermo Fisher Scientific) for 3 min at 37°C. Cells were collected via centrifugation and resuspended in transfection media to a final concentration of 550,000 cells/mL. 80 μL of this cell suspension was added to each well for reverse transfection, bringing the final concentration of the crRNA:tracrRNA complex to 25 nM. Cells were incubated for 48 h at 37°C and then received a full media change to complete growth medium before use in further assays.

7.3.12 Preparation of synthetic crRNA library

The following Edit-R crRNA libraries were purchased from Dharmacon in 96-well plate format, containing 0.1 nmol of crRNA per well, for use in our arrayed screen: human protein kinase, human GPCR, human phosphatase, human ion channel, human druggable genome, human protease, human transcription factors, and human ubiquitin enzyme. Library plates were centrifuged briefly to collected crRNA at the bottom of each well. crRNA was resuspended in 100 μL of 10 mM Tris pH 7.4 buffer to a final concentration of 10 μM (Dharmacon) using a Multidrop Combi (Thermo Fisher Scientific). Plates were incubated for a minimum of 70 min at room temperature on an orbital shaker to ensure complete resuspension. tracrRNA was resuspended in 10 mM Tris pH 7.4 buffer to a final concentration of 100 μM and also incubated for a minimum of 70 min at room temperature on an orbital shaker to ensure complete resuspension. Screening plates were prepared by transferring 2.5 μL of each well of 10 μM crRNA to flat-bottom, black-walled 96-well μCLEAR cell culture plates (Greiner Bio-One) using a Bravo liquid handler (Agilent Technologies). 7.5 μL of 333 nM tracrRNA, prepared by diluting 100 μM tracrRNA stock in Opti-MEM reduced serum medium (Thermo Fisher Scientific) was then added to each well containing crRNA. 2.5 μL of non-targeting crRNA and *TJP1* crRNA, both at 10 μM

concentrations, were added to 4 wells each in all prepared screening plates, and 7.5 μL of 333 nM tracrRNA was subsequently added to each of these wells. Fully prepared plates were subsequently sealed and stored at -80°C until use.

7.3.13 Transfection of arrayed CRISPR reagents

On the day of seeding for the screen, selected library plates were removed from the -80°C freezer, warmed until reagents frozen within each well were thawed, and were transferred into a biosafety cabinet after spraying with copious amounts of 70% ethanol (Fisher Scientific). Plate seals were removed, and 10 μL of Dharmafect 1 transfection reagent (Dharmacon) diluted in Opti-MEM to a final deliverable concentration of 0.8 μL Dharmafect 1 per well was added to each well using a Multidrop Combi. Prepared plates were incubated for a minimum of 30 min at room temperature, during which time clone F7 Cas9-Caco2s were collected for seeding.

Cas9-Caco2s cultured in T175 flasks were washed once with DPBS and incubated with TrypLE Express for a minimum of 5 min at 37°C before collection via centrifugation. Cell pellets were resuspended in prepared transfection medium, and density of the suspension was determined using a Countess II automated hemocytometer (Thermo Fisher Scientific). The concentration of live cells was adjusted to 550,000 cells/mL using transfection medium, and 80 μL of this cell suspension was delivered to each well of the prepared 96-well plates, bringing the total volume of each well to 100 μL.

7.3.14 Maintenance of transfected cells

Approximately 24 h after reverse transfection, 100 μL of 2X anti-anti medium was delivered to each seeded well using a Multidrop Combi, bringing the effective antibiotic-antimycotic concentration to 1X. Approximately 24 h after the addition of 2X anti-anti medium, cell medium was completely changed for the transfected cells using a BioTek EL406 plate washer

to remove remaining transfection reagents, and all wells received 200 μL of complete growth medium. Culture medium was fully changed 48 h later, and cells were given 200 μL of serum-free barrier formation medium. Cells received half medium changes with this serum-free medium every 48 h for an additional 2 media changes. Cells were subsequently fixed after 6 days of culture in serum-free medium using the methods detailed below.

7.3.15 Immunocytochemistry for arrayed plates

8% formaldehyde was prepared by diluting 37% formaldehyde (Sigma-Aldrich) in DPBS. Using a BioTek EL406 plate washer with peristaltic pump, 100 μL of DPBS was added to each well to be fixed. 200 μL of liquid was then aspirated from each well, bringing the total volume of each well to 100 μL. 100 μL of prepared 8% formaldehyde was added to each well, and plates were fixed for a minimum of 20 min at room temperature on an orbital shaker. Following fixation, liquid was fully aspirate from each well, and 200 μL of DPBS was added to each well. At this point, plates were either used immediately for immunocytochemistry or stored at 4°C for future use.

On the day of staining, DPBS was fully aspirated from all wells using a BioTek EL406 plate washer, and cells were blocked using 50 μL of PBS-DT per well, prepared as described in Section 7.3.10. Cells were blocked for a minimum of 1 h at room temperature before adding 50 μL of Alexa Fluor 488-conjugated ZO-1 antibody (Table A. 7.1) diluted in PBS-DT per well. Cells were incubated with primary antibody overnight at 4°C. The following morning, 50 μL of Hoechst 33342 trihydrochloride trihydrate (Thermo Fisher Scientific) diluted in PBS-T was added to each well to mark nuclei and incubated for a minimum of 10 min at room temperature. 150 μL of PBS-T was subsequently added to each, following full aspiration of all liquid in each well. 100 μL of PBS-T was added to each stained well.

7.3.16 High-content imaging

Stained plates were imaged using an ImageXpress MicroXL automated microscope imager (Molecular Devices). Four images were captured per well for all conditions. Acquired images were exported in tagged image file format (TIFF) for subsequent analysis.

7.3.17 Imaging analysis

Collected images were analyzed using the MATLAB script in Figure A. 4.2. The outputs from this script were averaged across the four images collected per well to generate average results per gene using the MATLAB script in Figure A. 7.1. Averaged well values were subsequently normalized to untreated controls and non-targeting crRNA controls using MATLAB script in Figure A. 7.2. Normalized values for all plates screened were finally compiled into one searchable Excel file using the MATLAB script in Figure A. 7.3.

7.4 Results and discussion

High throughput CRISPR screening to rapidly identify modulators of paracellular permeability will provide insight into potential mechanisms of barrier regulation that would require years to achieve through traditional techniques. The technical constraints of performing a high throughput screen necessitate the use of cells which may be extensively expanded in culture, can withstand the sheer force of a peristaltic pump, and have limited matrix requirements for growth. Furthermore, the chosen cell type must adequately recapitulate the highly restrictive paracellular barrier phenotype we wish to interrogate. Caco2 cells are an intestinal epithelial cell line which have previously been used to model the BBB [270,271]. These cells may be greatly expanded in culture and form extensive tight junctions similar to those present at the BBB [272], making them ideal for use in high throughput screening applications.

To this end, Caco2 cells were transduced with lentivirus containing a vector for mKate2-tagged, constitutively expressed *S. pyogenes cas9*. Caco2s harboring this fluorescent insert, hereafter referred to as Cas9-Caco2s, were clonally selected by mKate2 signal using fluorescence assisted cell sorting (Figure 7.1A) to ensure uniform levels of Cas9 expression and activity in cells used for screening. We verified Cas9 expression levels in our transduced cells via western blots and selected two clones, termed C6 and F7, for further analysis (Figure 7.1B). Following the stress of the genetic manipulation and single cell selection, we verified that our Cas9-Caco2 variants were still capable of forming the tight junctions vital to our screen (Figure 7.1C).

The fidelity of the restrictive barrier formed by tight junctions in both endothelial and epithelial is often functionally evaluated via measurement of transendothelial/epithelial resistance (TEER). We therefore cultured clone C6 and clone F7 Cas9-Caco2s in their normal, serum-containing growth medium on Transwell filters and measured resistance across the monolayer approximately every 24 h. Resistance across the monolayer in both clones failed to exceed 200 $\Omega \times cm^2$, the generally accepted minimum threshold for barrier function, at any point during the 10 day culture span. However, recent work from our group developing serum-free differentiation methods to produce brain microvascular endothelial cells from human induced pluripotent stem cells highlighted the increase in TEER achieved through the use of B27 supplement in place of serum in culture medium. Therefore, after seeding cells onto Transwell filters in their normal growth medium, we cultured clone C6 and F7 Cas9-Caco2s in serum-free medium consisting of basal media prepared in accordance to the publicly available compositions of neurobasal medium [203] and B27 supplement. Both C6 and F7 clones were able to form highly restrictive barriers (TEER > 1,000 $\Omega \times cm^2$) after several days of culture in this serum-free media (Figure 7.1D and

7.1E, respectively). However, clone F7, hereafter referred to as Cas9-Caco2s, displayed superior barrier stability over the length of culture and was selected for use in screening experiments.

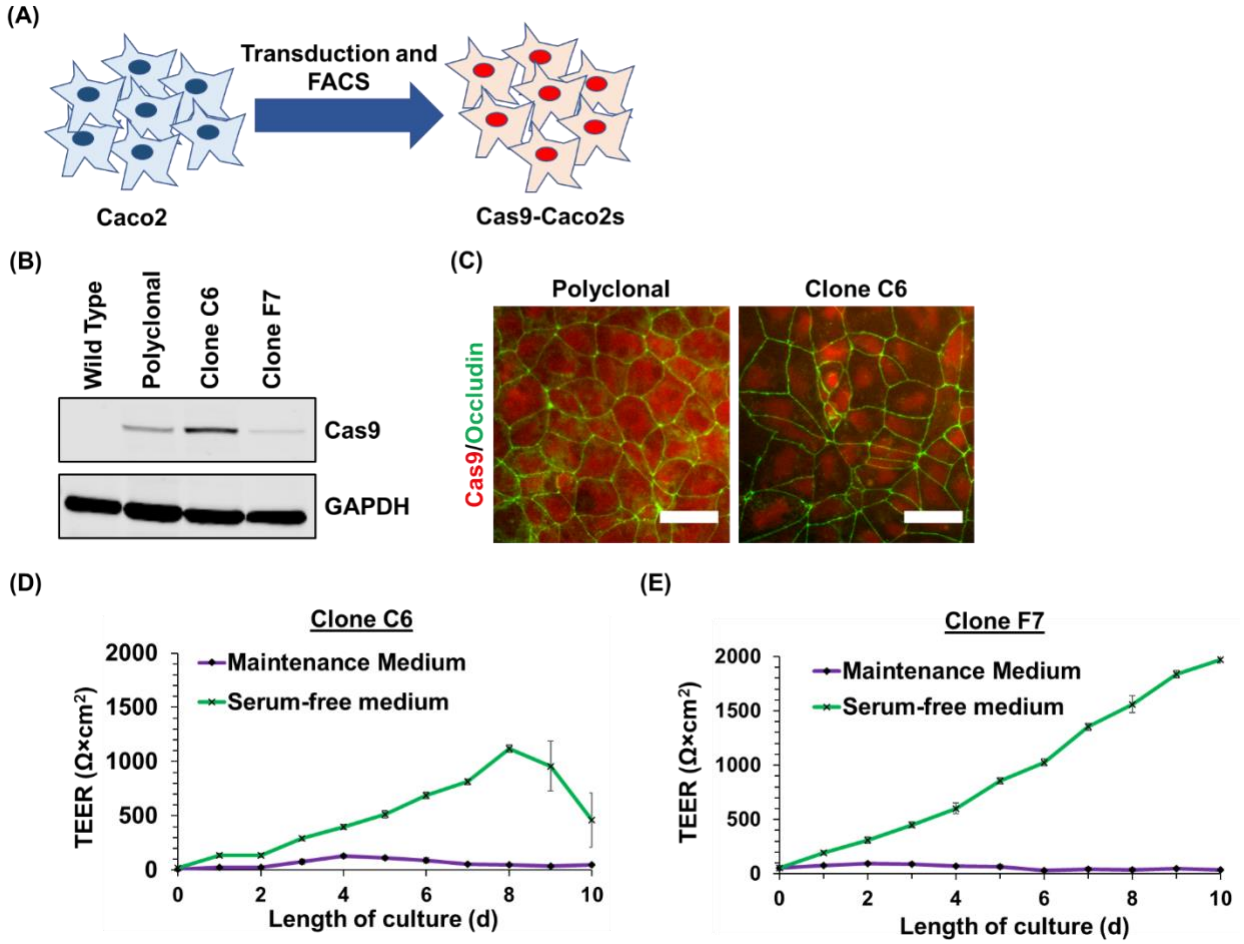

Figure 7.1 Generation of Cas9-expressing Caco2 cells. (A) Unmodified Caco2 epithelial cells were transduced with lentiviral particles encoding a constitutively expressed, mKate2 tagged Cas9 variant. Clones harboring this insertion was selected via FACS. (B) Cas9 expression was measured in selected clones as well as a polyclonal population via western blot. (C) The ability of these modified to form tight junctions following Cas9 insertion and selection was assessed by staining for occludin expression. Scale bars are 50 µm. Clone C6 (D) and Clone F7 (D) Cas9-Caco2s were cultured in maintenance medium and serum-free medium and monitored for barrier formation by TEER measurement.

Following generation of our desired cell line, we next worked to identify transfection conditions which would maximize the degree of gene knockout in our cells without evidence of

cytotoxicity. We selected expression of ZO-1, an adapter protein critical for the formation of tight junctions [238,273], as our marker for paracellular barrier disruption and analyzed its localization via immunocytochemistry. Cas9-Caco2s were transfected using various concentrations Dharmafect 1 lipid transfection reagent and synthetic crRNA complexed to synthetic tracrRNA against *TJP1* and subsequently stained for ZO-1 expression (Figure 7.2A). No cytotoxicity was evident in any of the tested conditions nor was ZO-1 expression significantly altered by exposure to transfection reagent or non-targeting crRNA. The degree of knockout was observed to be proportional to the concentration of transfection reagent used. Images from each condition were analyzed using a MATLAB script previously used to assess junctional fidelity in iPSC-derived BMECs (Figure 7.2B), and the total normalized junctional area (Figure 7.2C), junctional length (Figure 7.2D), and junctional width (Figure 7.2E). From this analysis, we determined that the highest concentration of Dharmafect 1 was necessary to detect significant changes in ZO-1 expression. Furthermore, we determined total junctional area normalized to nuclei count to be the most reliable measure in our analyses for junction loss.

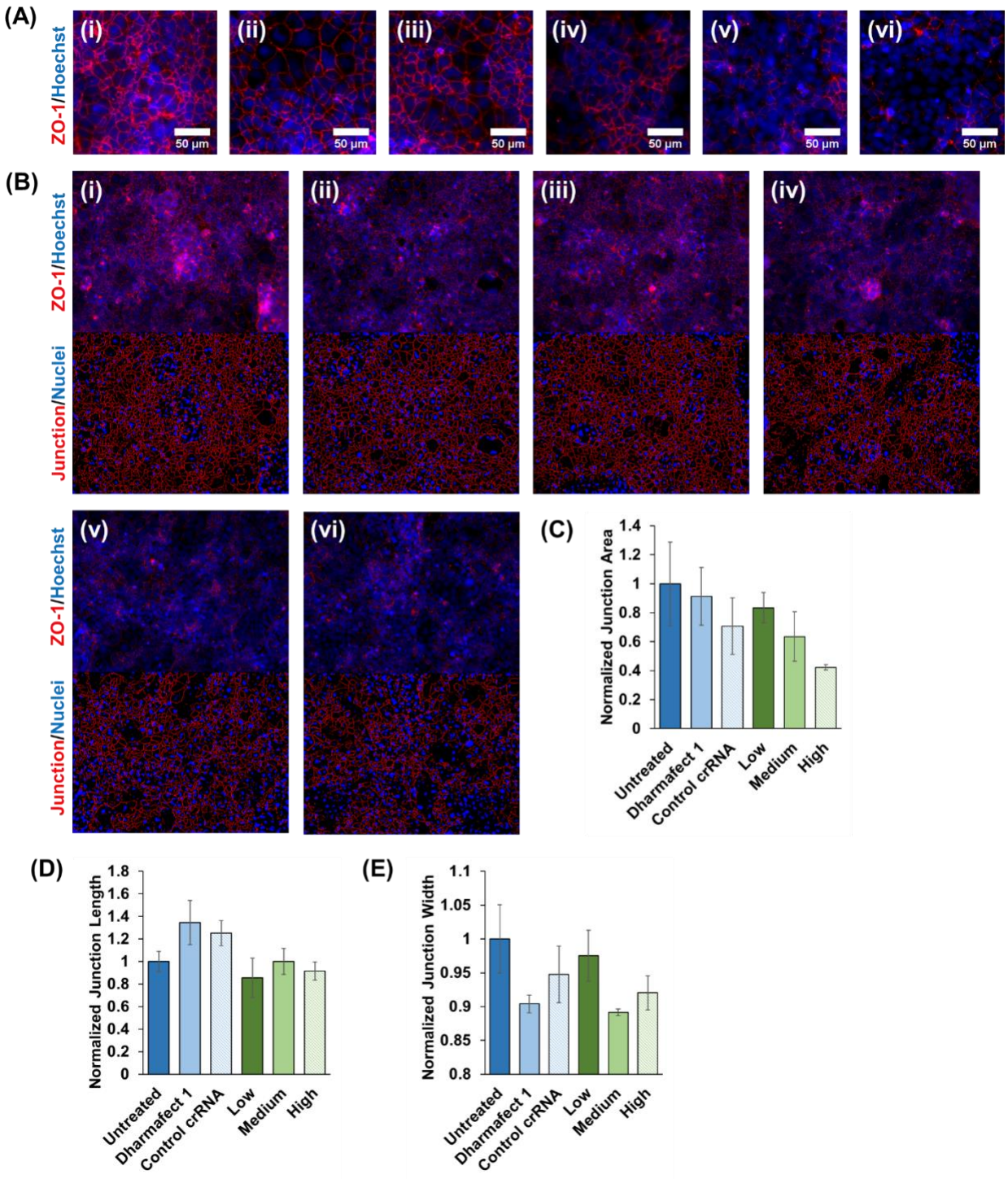

Figure 7.2 Optimization and evaluation of *TJP1* knockout in Cas9-Caco2s. (A) ZO-1 expression was detected via immunocytochemistry in Cas9-Caco2s in untreated (i), Dharmafect 1 only (ii), non-targeting control crRNA (iii), and *TJP1* crRNA delivered via low (iv), medium (v), and high (vi) concentrations of Dharmafect 1 transfection reagent. All scale bars are 50 µm. (B) Degree of junctional disruption was assessed in conditions (i) through (vi) using our custom MATLAB script. This disruption was quantified by (C) junctional area normalized to DAPI, (D) junction

length, and (E) junction width, all of which were normalized to measurements made in untreated control samples.

CRISPR screens may be conducted in either pooled formats or in arrayed formats [274]. Pooled formats commonly use lentiviral vectors to deliver libraries of single guide RNAs (sgRNAs) to cell types of interest. This approach is often advantageous with respect to the cost of reagents and labor required to conduct the screen [275]. However, pooled screens often fail to capture subtle phenotypic changes and changes in behavior in which cell-cell interactions are crucial, such as tight junction formation [276]. We therefore opted to conduct an arrayed CRISPR screen against ~8400 genes in which each well of Cas9-Caco2 cells receives synthetic CRISPR RNA (crRNA) against a single gene. These cells were then cultured in serum-free media to promote barrier formation before fixation and high content imaging (Figure 7.3A). This approach enables unambiguous interpretation of the genotype-to-phenotype connection and allows for detection of nuanced phenotypes such as frayed junctions [67].

Despite the increased specificity of CRISPR-based screens in comparison to screens conducted using RNA interference (RNAi) [92], identification of potential positive hits is still complicated by the potential for off-target effects. Results may also be confounded by cellular adaptations made in response to the particular stresses of screening procedures, potentially masking the effects of targeted genes. We therefore sought initial validation of our screen results by evaluating the effect of knocking out genes previously identified to be essential for tight junction formation. Alterations in ZO-1 expression for wells containing crRNA against *TJP1*, *F11R*, and *RAC1* were assessed as each of these genes is well documented in the literature for their contributions to tight junction formation and regulation under basal conditions [277–281]. All three aforementioned genes exhibited loss of ZO-1 expression, albeit to varying degrees (Figure

7.1B), validating that true positive hits may be extracted from our screening results. We extended these analyses to *RHOA*, previously shown to be necessary for tight junction formation [278,282,283]. Excitingly, knockout of these genes all resulted in detectable alterations in ZO-1 localization (Figure 7.3C), providing further confidence that the results of this screen may provide valuable insight into paracellular barrier regulation.

Finally, we worked to validate that we could extract results with functional relevance in our iPSC-derived *in vitro* blood-brain barrier model. To this end, we compared genes highly upregulated under RA treatment as compared to DMSO treatment, discussed extensively in Section 6.4 of this dissertation, to the results of our junctional analyses. Through these comparisons, we identified *GPR1*, which encodes for G Protein-Coupled Receptor 1 (GPR1), as being high upregulated in mature BBB endothelium ($p_{adjusted}=1.43\times10^{-36}$, log2 fold change=5.49). Loss of *GPR1* in our screen resulted in a 37.6% decrease in ZO-1 junctional area as compared to untreated control cells (Figure 7.3D-E). Though this result does not provide insight into the mechanism by which *GPR1* loss results in a decrease in ZO-1 expression, the results do suggest that the outcomes of our screen may yield hits with blood-brain barrier relevance.

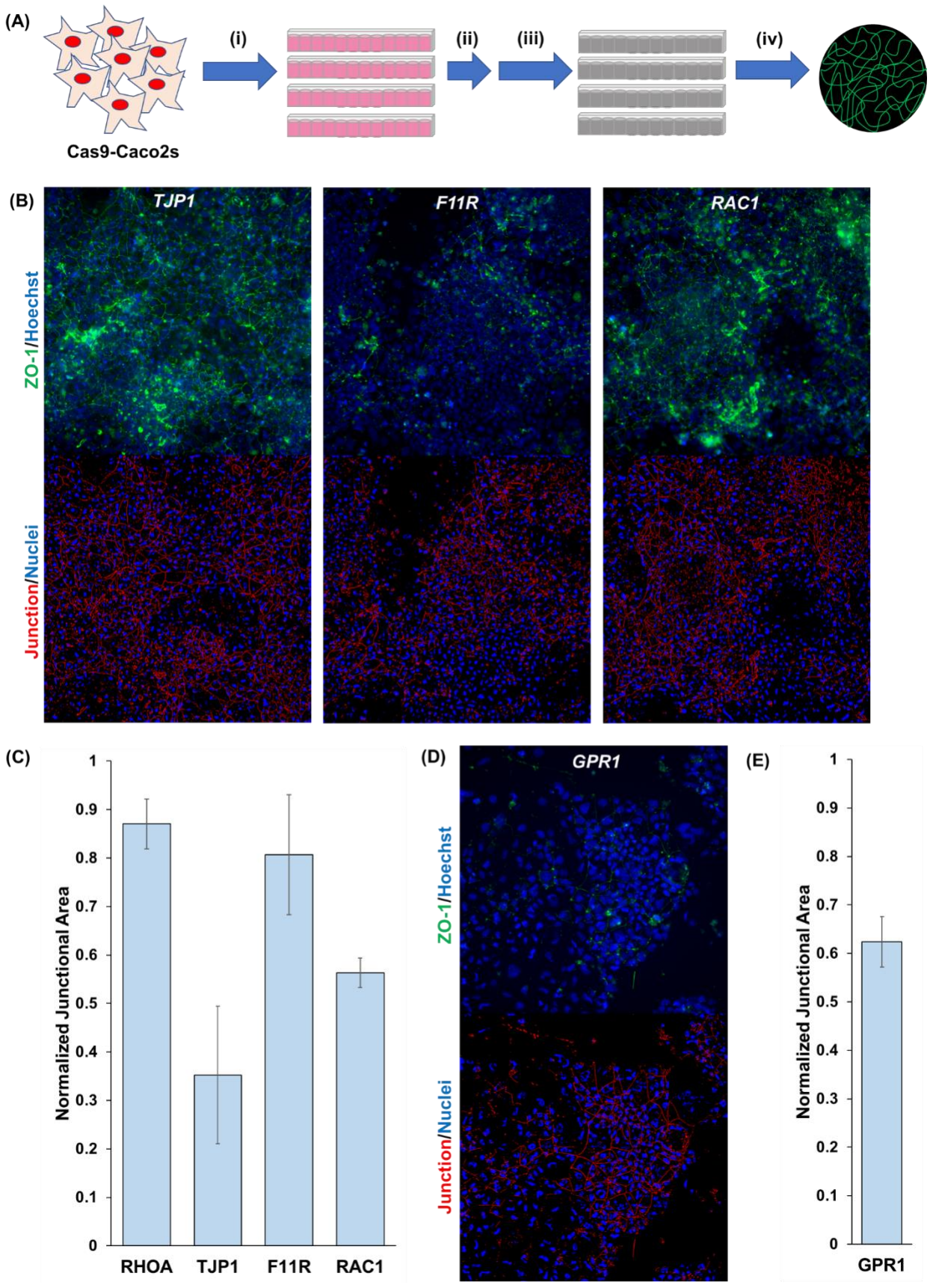
(A)
Cas9-Caco2s
(i)
(ii)
(iii)
(iv)
(B)
TJP1
F11R
RAC1
ZO-1/Hoechst
Junction/Nuclei
(C)
Normalized Junctional Area
1
0.9
0.8
0.7
0.6
0.5
0.4
0.3
0.2
0.1
0
RHOA
TJP1
F11R
RAC1
(D)
GPR1
ZO-1/Hoechst
Junction/Nuclei
(E)
Normalized Junctional Area
GPR1

Figure 7.3 Arrayed CRISPR screen to identify modulators of paracellular permeability. (A) Cas9-Caco2s were (i) seeded onto prepared library plates containing complexed crRNA:tracrRNA and Dharmafect 1 transfection reagent. (ii) Cells were cultured in serum-containing medium for 48 hours before (iii) being switched to serum-free medium for 6 days to enhance barrier formation. (iv) After six days, cells were fixed, stained, and imaged for ZO-1 localization. (B) Screen results for genes previously identified for their contribution for tight junction formation were assessed visually. (C) An extended cohort of genes, including those assessed in (B), were for interrogated for changes in junctional area. (D) Loss of *GPR1*, whose expression was previously identified as being upregulated in mature blood-brain barrier endothelium, was found to result in decreased total junctional area.

7.5 Conclusion

In this chapter, we detail our efforts to identify modulators of blood-brain barrier paracellular permeability through an arrayed, high throughput CRISPR screen coupled with high content imaging. We interrogated the individual contributions of approximately 8400 genes to paracellular barrier function as measured by ZO-1 localization to cell-cell junctions. We validated the ability of our screen to identify genes with relevance to this phenotype by analysis of junctional disruption in wells containing crRNA against genes previously implicated in tight junction formation and regulation, including *TJP1*, *F11R*, *RHOA*, and *RAC1*. Loss of each of these genes resulted in a detectable decrease in ZO-1 expression, suggesting tight junction compromise. The ability of the screen to identify genes with blood-brain barrier relevance was supported by the identification of *GPR1*. This gene was previously identified as being highly upregulated in mature BBB endothelium, and loss of GPR1 resulted in decreased ZO-1 localization in our screen. Future work will seek to validate additional positive hits from this screen in our iPSC-derived blood-brain barrier model.

```
clear
directory=uigetdir;
files=dir(directory);
file_size=size(files);
number_of_files=file_size(1);
for o=3:number_of_files %drops the weird 2 header lines that aren't actually files in files
    full_table=readtable([directory,'\',files(o).name]);
    image_name=full_table(:,1);
    number_nuclei=full_table(:,2);
    junction_area=full_table(:,3);
    junction_length=full_table(:,4);
    junction_width=full_table(:,5);

    %Calculate averages per well
    avg_nuclei=splitapply(@mean,number_nuclei,ceil((1:numel(number_nuclei))'/4));
    avg_area=splitapply(@mean,junction_area,ceil((1:numel(junction_area))'/4));
    avg_length=splitapply(@mean,junction_length,ceil((1:numel(junction_length))'/4));
    avg_width=splitapply(@mean,junction_width,ceil((1:numel(junction_width))'/4));

    %Calculate standard deviations per well
    avg_nuclei_SD=splitapply(@std,number_nuclei,ceil((1:numel(number_nuclei))'/4));
    avg_area_SD=splitapply(@std,junction_area,ceil((1:numel(junction_area))'/4));
    avg_length_SD=splitapply(@std,junction_length,ceil((1:numel(junction_length))'/4));
    avg_width_SD=splitapply(@std,junction_width,ceil((1:numel(junction_width))'/4));

    %Shorten the image names
    condensed_image_name=image_name(1:4:end,:);

    %convert arrays to table for export
    nuclei=array2table(avg_nuclei);
    area=array2table(avg_area);
    length=array2table(avg_length);
    width=array2table(avg_width);
    nuclei_SD=array2table(avg_nuclei_SD);
    area_SD=array2table(avg_area_SD);
    length_SD=array2table(avg_length_SD);
    width_SD=array2table(avg_width_SD);

    %Rename the files and export
    drop_extension=files(o).name(1:end-18);
    text=char(drop_extension);
    filename=[text ' average.xlsx'];
    export= [condensed_image_name nuclei nuclei_SD area area_SD length length_SD width
width_SD];
    writetable(export,[directory,'\',filename]);
end
```

Figure A. 7.1 MATLAB code to average image quantifications for all sites in each well imaged.

```
clear
directory=uigetdir;
files=dir(directory);
file_size=size(files);
number_of_files=file_size(1);
for o=3:number_of_files
   %if length(files(o).name)>4
   %if strcmp(files(o).name(end-3:end),'.xls')
      full_table=readtable([directory,'\',files(o).name]);
      image_name=full_table(:,1);
      number_nuclei=full_table(:,2);
      number_nuclei_SD=full_table(:,3);
      junction_area=full_table(:,4);
      junction_area_SD=full_table(:,5);
      junction_length=full_table(:,6);
      junction_length_SD=full_table(:,7);
      junction_width=full_table(:,8);
      junction_width_SD=full_table(:,9);

      %Untreated controls - averages
      UT_control_names = image_name([1 12 13 24 73 84 85 96],1);
      UT_control_nuclei = number_nuclei([1 12 13 24 73 84 85 96],1);
      UT_control_junction_area = junction_area([1 12 13 24 73 84 85 96],1);
      UT_control_junction_length = junction_length([1 12 13 24 73 84 85 96],1);
      UT_control_junction_width = junction_width([1 12 13 24 73 84 85 96],1);

      %Generate averages of untreated controls
      UT_control_avg_nuclei = mean(table2array(UT_control_nuclei));
      UT_control_avg_junction_area = mean(table2array(UT_control_junction_area));
      UT_control_avg_junction_width = mean(table2array(UT_control_junction_width));
      UT_control_avg_junction_length = mean(table2array(UT_control_junction_length));

      %Generate standard deviations of untreated controls
      UT_control_avg_nuclei_SD = std(table2array(UT_control_nuclei));
      UT_control_avg_junction_area_SD = std(table2array(UT_control_junction_area));
      UT_control_avg_junction_width_SD = std(table2array(UT_control_junction_width));
      UT_control_avg_junction_length_SD = std(table2array(UT_control_junction_length));

      %Non-targeting controls
      NT_control_names = image_name([25 37 60 72],1);
      NT_control_nuclei = number_nuclei([25 37 60 72],1);
      NT_control_junction_area = junction_area([25 37 60 72],1);
      NT_control_junction_length = junction_length([25 37 60 72],1);
      NT_control_junction_width = junction_width([25 37 60 72],1);

      %Generate averages of non-targeting controls
      NT_control_avg_nuclei = mean(table2array(NT_control_nuclei));
      NT_control_avg_junction_area = mean(table2array(NT_control_junction_area));
      NT_control_avg_junction_width = mean(table2array(NT_control_junction_width));
      NT_control_avg_junction_length = mean(table2array(NT_control_junction_length));
```

```
%Generate standard deviations of non-targeting controls
    NT_control_avg_nuclei_SD = std(table2array(NT_control_nuclei));
    NT_control_avg_junction_area_SD = std(table2array(NT_control_junction_area));
    NT_control_avg_junction_width_SD = std(table2array(NT_control_junction_width));
    NT_control_avg_junction_length_SD = std(table2array(NT_control_junction_length));

    %ZO-1 controls
    ZO1_control_names = image_name([49 61 36 48],1);
    ZO1_control_nuclei = number_nuclei([49 61 36 48],1);
    ZO1_control_junction_area = junction_area([49 61 36 48],1);
    ZO1_control_junction_length = junction_length([49 61 36 48],1);
    ZO1_control_junction_width = junction_width([49 61 36 48],1);

    %Generate ZO-1 control averages
    ZO1_control_avg_nuclei = mean(table2array(ZO1_control_nuclei));
    ZO1_control_avg_junction_area = mean(table2array(ZO1_control_junction_area));
    ZO1_control_avg_junction_width = mean(table2array(ZO1_control_junction_width));
    ZO1_control_avg_junction_length = mean(table2array(ZO1_control_junction_length));

    %Generate ZO-1 control standard deviations
    ZO1_control_avg_nuclei_SD = std(table2array(ZO1_control_nuclei));
    ZO1_control_avg_junction_area_SD = std(table2array(ZO1_control_junction_area));
    ZO1_control_avg_junction_width_SD = std(table2array(ZO1_control_junction_width));
    ZO1_control_avg_junction_length_SD = std(table2array(ZO1_control_junction_length));

    %Extracting KO values - pulls the average values I generated in
    %last spread sheet
    target_genes_names = image_name([2:11 14:23 26:35 38:47 50:59 62:71 74:83 86:95],1);
    target_nuclei = number_nuclei([2:11 14:23 26:35 38:47 50:59 62:71 74:83 86:95],1);
    target_junction_area = junction_area([2:11 14:23 26:35 38:47 50:59 62:71 74:83 86:95],1);
    target_junction_length=junction_length([2:11 14:23 26:35 38:47 50:59 62:71 74:83 86:95],1);
    target_junction_width=junction_width([2:11 14:23 26:35 38:47 50:59 62:71 74:83 86:95],1);

    %Extracting KO values - pulls the SD values I generated in
    %last spread sheet
    target_nuclei_SD = number_nuclei_SD([2:11 14:23 26:35 38:47 50:59 62:71 74:83 86:95],1);
    target_junction_area_SD = junction_area_SD([2:11 14:23 26:35 38:47 50:59 62:71 74:83
86:95],1);
    target_junction_length_SD=junction_length_SD([2:11 14:23 26:35 38:47 50:59 62:71 74:83
86:95],1);
    target_junction_width_SD=junction_width_SD([2:11 14:23 26:35 38:47 50:59 62:71 74:83
86:95],1);

    %Normalizing NT controls to UT controls
    NT_to_UT_junction_area = NT_control_avg_junction_area./UT_control_avg_junction_area;
    NT_to_UT_junction_length =
NT_control_avg_junction_length./UT_control_avg_junction_length;
    NT_to_UT_junction_width =
NT_control_avg_junction_width./UT_control_avg_junction_width;
```

```
%Normalizing ZO1 targeting controls to UT controls
    ZO1_to_UT_junction_area = ZO1_control_avg_junction_area./UT_control_avg_junction_area;
    ZO1_to_UT_junction_length =
ZO1_control_avg_junction_length./UT_control_avg_junction_length;
    ZO1_to_UT_junction_width =
ZO1_control_avg_junction_width./UT_control_avg_junction_width;

    %Normalize target gene values to UT values
    target_genes_to_UT_junction_area =
table2array(target_junction_area)./UT_control_avg_junction_area;
    target_genes_to_UT_junction_length =
table2array(target_junction_length)./UT_control_avg_junction_length;
    target_genes_to_UT_junction_width =
table2array(target_junction_width)./UT_control_avg_junction_width;

    %Generate SD for normalizing target gene alues to UT values
    target_genes_to_UT_junction_area_SD =
table2array(target_junction_area_SD)./UT_control_avg_junction_area;
    target_genes_to_UT_junction_length_SD =
table2array(target_junction_length_SD)./UT_control_avg_junction_length;
    target_genes_to_UT_junction_width_SD =
table2array(target_junction_width_SD)./UT_control_avg_junction_width;

    %Normalize target gene values to NT values
    target_genes_to_NT_junction_area =
table2array(target_junction_area)./NT_control_avg_junction_area;
    target_genes_to_NT_junction_length =
table2array(target_junction_length)./NT_control_avg_junction_length;
    target_genes_to_NT_junction_width =
table2array(target_junction_width)./NT_control_avg_junction_width;

    %Normalize target gene values to NT values - standard deviations
    target_genes_to_NT_junction_area_SD =
table2array(target_junction_area_SD)./NT_control_avg_junction_area;
    target_genes_to_NT_junction_length_SD =
table2array(target_junction_length_SD)./NT_control_avg_junction_length;
    target_genes_to_NT_junction_width_SD =
table2array(target_junction_width_SD)./NT_control_avg_junction_width;

    %convert back to array
    target_genes_to_UT_junction_area = array2table(target_genes_to_UT_junction_area);
    target_genes_to_UT_junction_length = array2table(target_genes_to_UT_junction_length);
    target_genes_to_UT_junction_width = array2table(target_genes_to_UT_junction_width);

    target_genes_to_UT_junction_area_SD = array2table(target_genes_to_UT_junction_area_SD);
    target_genes_to_UT_junction_length_SD =
array2table(target_genes_to_UT_junction_length_SD);
    target_genes_to_UT_junction_width_SD =
array2table(target_genes_to_UT_junction_width_SD);
```

```
target_genes_to_NT_junction_area = array2table(target_genes_to_NT_junction_area);
    target_genes_to_NT_junction_length = array2table(target_genes_to_NT_junction_length);
    target_genes_to_NT_junction_width = array2table(target_genes_to_NT_junction_width);

    target_genes_to_NT_junction_area_SD = array2table(target_genes_to_NT_junction_area_SD);
    target_genes_to_NT_junction_length_SD =
array2table(target_genes_to_NT_junction_length_SD);
    target_genes_to_NT_junction_width_SD =
array2table(target_genes_to_NT_junction_width_SD);

    %Compile to table for export
    drop_extension=files(o).name(1:end-5);
    text=char(drop_extension);
    filename=[text ' averaged_to_controls.xlsx'];
    export = [target_genes_names target_nuclei target_genes_to_UT_junction_area
target_genes_to_UT_junction_area_SD target_genes_to_NT_junction_area
target_genes_to_NT_junction_area_SD target_genes_to_UT_junction_length
target_genes_to_UT_junction_length_SD target_genes_to_NT_junction_length
target_genes_to_NT_junction_length_SD target_genes_to_UT_junction_width
target_genes_to_UT_junction_width_SD target_genes_to_NT_junction_width
target_genes_to_NT_junction_width_SD];
    writetable(export,[directory,'\',filename]);
end
```

Figure A. 7.2 MATLAB code to normalize measurements for targeted genes to untreated and non-targeting controls on each plate.

Table A. 7.1 Primary antibodies used for western blot and immunocytochemistry experiments.

Target	Antibody Species	Vendor	Clone or product number	Dilution
Cas9	Mouse	Diagenode	7A9	1:1000
Occludin	Mouse	Thermo Fisher Scientific	OC-3F10	1:100
ZO-1	Mouse	Thermo Fisher Scientific	ZO1-1A12	1:100
ZO-1 (Alexa Fluor 488 conjugated)	Mouse	Thermo Fisher Scientific	MA3-39100-A488	1:1000

Table A. 7.2 Secondary antibodies used for western blot and immunocytochemistry experiments.

Species Reactivity	Host	Conjugate	Vendor	Dilution
Mouse	Donkey	Alexa Fluor 555	Thermo Fisher Scientific	1:200
Mouse	Donkey	Alexa Fluor 488	Thermo Fisher Scientific	1:200
Mouse	Goat	IRDye 800CW	Li-Cor Biosciences	1:15000

```
clear
directory=uigetdir;
files=dir(directory);
file_size=size(files);
number_of_files=file_size(1);
total_export=[];
%export={'Image','Average Number of Nuclei','Target vs. Untreated Junction Area','Target vs. Nontargeted Junction Area','Target vs. Untreated Mean Contiguous Junction Length (pixels)','Target vs. Nontargeted Mean Contiguous Junction Length (pixels)','Target vs. Untreated Mean Junction Width (pixels)', 'Target vs. Nontargeted Mean Junction Width (pixels)'};
for o=3:number_of_files
    ftab=readtable([directory,'/',files(o).name]);
    image_name=ftab(:,1);
    avg_nuclei=ftab(:,2);
    target_UT_area=ftab(:,3);
    target_NT_area=ftab(:,4);
    target_UT_length=ftab(:,5);
    target_NT_length=ftab(:,6);
    target_UT_width=ftab(:,7);
    target_NT_width=ftab(:,8);
    export = [image_name avg_nuclei target_UT_area target_NT_area target_UT_length
target_NT_length target_UT_width target_NT_width];
    total_export = [total_export; export];
end
writetable(total_export,[directory,'\','Master Screen Data Spreadsheet.xlsx']);
```

Figure A. 7.3 MATLAB script to compile all generated spreadsheets into one master spreadsheet.

Chapter 8

CONCLUSIONS AND FUTURE OUTLOOK

8.1 Conclusions

In this dissertation, I have described our efforts towards developing more representative and reproducible models of the human blood-brain barrier (BBB) using human induced pluripotent stem cells (iPSCs). Our initial work implemented the use of fully defined iPSC maintenance medium E8 and fully defined differentiation medium E6 in the differentiation protocol to produce brain microvascular endothelial cells (BMECs) from iPSCs. This change to defined media ultimately shortened the time to produce BMECs by five days compared to previously established protocols. Furthermore, BMECs produced using these defined media retained expression of canonical BBB markers, including VE-cadherin, claudin-5, occludin, and GLUT-1, as well as demonstrated expected activity and polarization of P-glycoprotein and MRP family efflux transporters. The BMECs produced using this method responded strongly to inductive cues provided by co-culture with astrocytes and pericytes, achieving, at the time of publication, the highest transendothelial electrical resistance of such a model in the literature.

Next, we worked to transition our BMECs from a 2-dimensional cell culture system, which lacks physiologically relevant architecture, to a more biomimetic 3-dimensional culture. To this end, we seeded our BMECs in a channel formed by enzymatically cross-linked gelatin channels to create an *in vitro* macrovessel. Cells cultured in this 3D system retained canonical BBB markers as well as active P-glycoprotein. Furthermore, this study highlighted the necessity of perfusion to maintain these characteristics over long periods of culture, suggesting that these cells respond to physiological cues such as shear force. Though this 3D model is unlikely to replace the use of more traditional 2D systems in screening applications, the compatibility of gelatin for

encapsulating and culturing other cell types of the neurovascular unit, including astrocytes, pericytes, and microglia, while providing more physiologically-relevant mechanical cues to the BMECs makes this model an ideal tool to bridge the gap between plate assays and preclinical models in testing therapeutic efficacy of pharmaceuticals.

Though significant strides were made towards a fully defined differentiation system with the use of E6 medium, the expansion and purification of mature endothelial cells in this protocol still required the use of platelet-poor, plasma derived serum (PDS). We next turned our attention to identifying a serum-free media supplement to replace this serum after determining the serum to be a major source of inherent variability in differentiation outcomes. B27, a commonly used serum-free media supplement, was found to produce BMECs with enhanced paracellular barrier properties as compared to those produced using serum-containing methods. BMECs differentiated using B27 retained the expect BBB markers, functional efflux transporter activity, and responded strongly to inductive cues from co-culture with astrocytes. Furthermore, the use of B27 in place of significantly enhanced the reproducibility of differentiations in both control and disease lines. Overall, this serum-free differentiation protocol enables the robust interrogation of BBB physiology in both health and disease, and the increased reproducibility facilitates broader adoption of the model by the research community at large.

The advancement of the BMEC differentiation protocol through the use of fully defined media and serum-free supplements significantly enhances the utility of the model for rigorous mechanistic work. However, these previous studies highlight the responsiveness of iPSC-derived BMECs to the composition of their extracellular environment, and the basal media used to mature and expand the BBB endothelial cells produced using these protocols has a proprietary composition. This unknown composition significantly hinders interpretation of experimental

results in which changes in the extracellular environment are used to elicit changes in cell behavior. We therefore replace this basal media with DMEM/F12 and neurobasal media, both of which have publicly available compositions. Cells differentiated using both media were VE-cadherin+, indicating that this media change did not affect our ability to produce endothelial cells. Furthermore, BMECs produced using both media retained BBB markers. However, BMECs produced using DMEM/F12 continually had significantly lower TEER than those produced using neurobasal media. We utilized RNA sequencing to determine the transcriptional identity of cells producing using both media. Modest changes were observed in the transcriptional landscapes of the sequenced BMECs, and we further identified potential changes in pathway activation by assessing the phospho-proteome of BMECs in each condition. Ultimately, our results highlight the plasticity and responsiveness of our BMECs to extracellular cues, thereby increasing their ability to ultimately produce more representative models of the blood-brain barrier.

The works described above created an ideal platform with which to interrogate the mechanistic underpinnings of the blood-brain barrier. Previous works identified the use of retinoic acid (RA) in the differentiation scheme to produce more mature, high fidelity endothelium. The effects of RA treatment could be somewhat recapitulated by treated cells with CD3254, a small molecular RXRα agonist. We therefore used DMSO, RA, and CD3254 to differentiate BMECs with varying maturity and fidelity and then used RNA sequencing to identify genes potentially responsible for the improvement in barrier phenotype under RA and CD3254 conditions. Through this analysis, we identified *IQGAP2* as being significantly upregulated under both treatment conditions. We validated its expression *in vitro* in our BMECs via immunocytochemistry and western blot. We further validated its expression *in vivo* in human brain cortex via immunohistochemistry and fluorescence in situ hybridization. As IQGAP2 expression was not

predicted to be expressed at the blood-brain barrier by previously published transcriptional datasets, this work highlights the potentially predictive nature of our iPSC-derived model to identify genes *in vitro* with *in vivo* relevance.

Finally, we worked to identify modulators of paracellular permeability at the blood-brain barrier by conducting an arrayed high-throughput CRISPR screen. High content imaging was used to capture alterations in tight junction fidelity in ~8400 genes. Initial results from the screen were validated by measuring junctional disruption in cells receiving crRNA against genes previously identified to be critical for tight junction formation. We cross-validated the ability of the screen to identify genes with blood-brain barrier relevance by comparing hits to our previous RNA sequencing data. *GPR1*, identified as being significantly upregulated in RA-treated endothelium, was found to significantly disrupt junction formation in our screen. Future efforts in this area will focus on validating positive hits both *in vitro* and *in vivo* for their contribution to a robust paracellular barrier.

8.2 Future outlook

The work presented in this dissertation represents exciting steps towards a more representative neurovascular model. Such a model will enable future investigations of BBB development and regulation, interactions between different cell types in the neurovascular unit, and improved screens for brain-penetrating therapeutics. Most excitingly, work presented in this dissertation highlights the potential predictive power of our iPSC-derived BBB model for identifying previously unidentified genes whose protein products have a high probability of contributing to the specialized blood-brain barrier phenotype.

After confirming expression *in vivo*, we have since continued our investigation of IQGAP2 and have expanded our efforts to include its family member IQGAP1. These two family members share a high degree of sequence homology (83%) [247], but previous research on hepatocellular carcinoma suggests that these proteins perform disparate functions [284]. IQGAP1 is expressed ubiquitously throughout the vertebrate body and is typically associated with an oncogenic, invasive phenotype [285,286]. In contrast, IQGAP2 is characterized by its tumor suppressor activity [287]. To date, no evidence exists of direct interactions between these to family members, yet the function of IQGAP1 has been shown to be dependent upon the expression of IQGAP1 [288,289]. We were motivated by these previous findings to investigate the potentially opposing roles of IQGAP1 and IQGAP2 in our *in vitro* system.

We expanded our interrogation of IQGAP2 expression to additional cell types in an effort to ascertain the nature of its expression. Specifically, we measured IQGAP2 expression in human umbilical vein endothelial cells (HUVECs) , non-barrier forming iPSC-derived endothelial cells (non-BBB endothelial cells) [290], Caco2s [271], primary human brain microvascular endothelial cells (hBMECs), immortalized human brain microvascular endothelial cells (hCMEC/D3s) [63], and our iPSC-derived BMECs [147] (Figure 8.1A). These cell types encompass a range of endothelial and epithelial cell types, and within these cell types, barrier forming and non-barrier forming cells. These preliminary studies suggest that IQGAP2 expression is more strongly associated with barrier formation than with endothelial identity. However, because of its role as a scaffold protein, it is unclear if IQGAP2 performs the same functions within this subset of endothelial and epithelial cells.

We next assessed IQGAP1 expression in this same cohort of cell types. As expected, IQGAP1 expression was detected in all cell types used, and interestingly, its expression did not

seem strongly associated with endothelial versus epithelial identity or barrier formation (Figure 8.1B). Further investigation of the relative balance of IQGAP1 and IQGAP2 expression highlighted the potential that the relative balance of these two family members, rather than the absolute expression level of either, may be of critical importance to the blood-brain barrier phenotype (Figure 8.1C), and that this balance may be shifted even within the context of high fidelity barriers (Figure 8.1D).

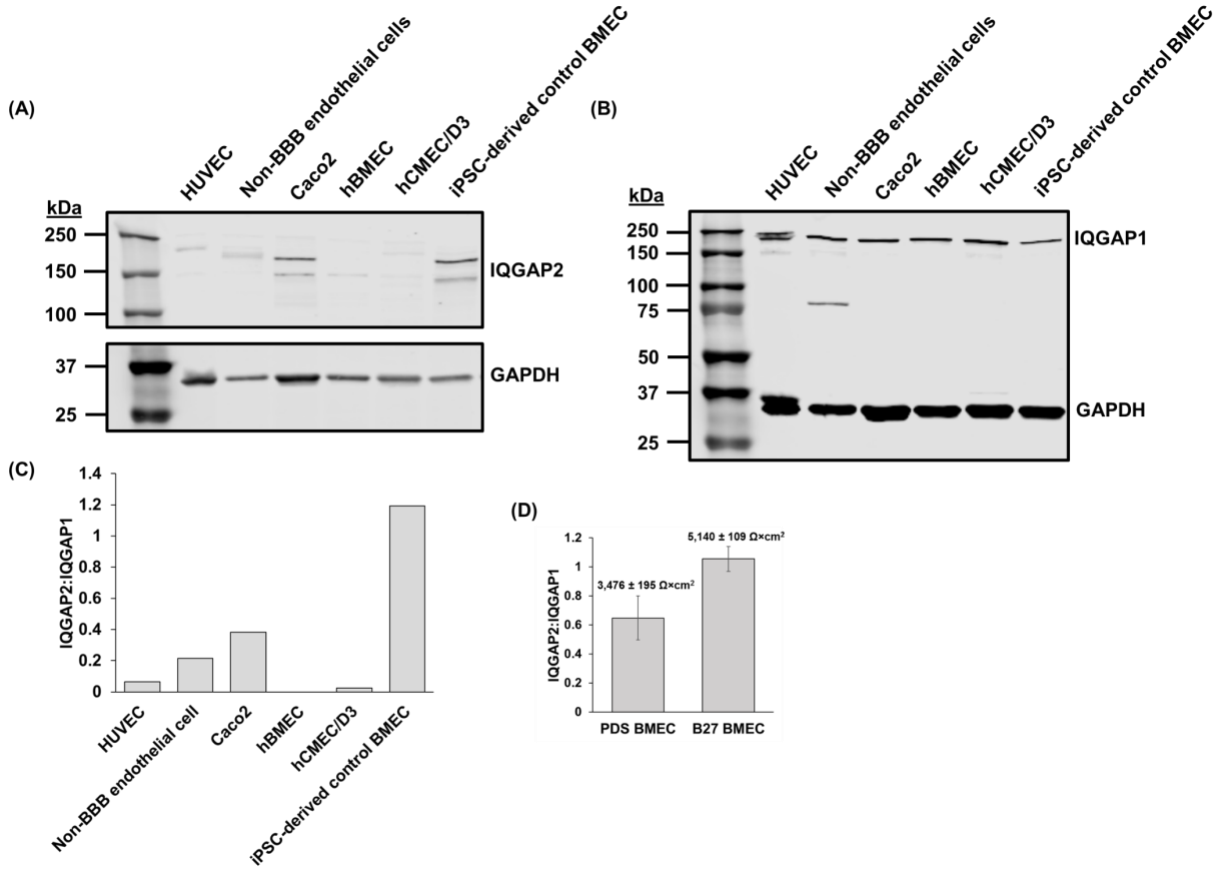

Figure 8.1 Evaluation of IQGAP1 and IQGAP2 expression in multiple cell types.

Despite our extensive, albeit preliminary, investigations of IQGAP1 and IQGAP2 expression, we did not have any insight into the potential functional consequences of IQGAP2

expression. Recently published work implicates IQGAP1 as being necessary for leukocyte transendothelial migration [291]. Based upon this work and previous works suggesting the opposing functions of IQGAP1 and IQGAP2 [289], we hypothesized that IQGAP2 may inhibit immune cell migration across the blood-brain barrier by opposing the leukocyte trafficking functions of IQGAP1. If so, this finding represents one of the first known mediators of immune privilege across the blood-brain barrier.

Preliminary studies to evaluate this hypothesis are currently underway. In conjunction with collaborators at Harvard University, we are currently conducting preliminary *in vivo* investigations of *iqgap2* function in zebrafish. Mosaic *iqgap2* knockouts were generated in *mpeg1*:EGFP zebrafish, in which cells of the macrophage lineage express GFP [292]. When imaged at 3 days post-fertilization, appreciably more GFP^+ cells are found in the midbrain (Figure 8.2A), and quantification of this accumulation showed a nearly two-fold increase in GFP^+ cell infiltration ($p<0.0001$).

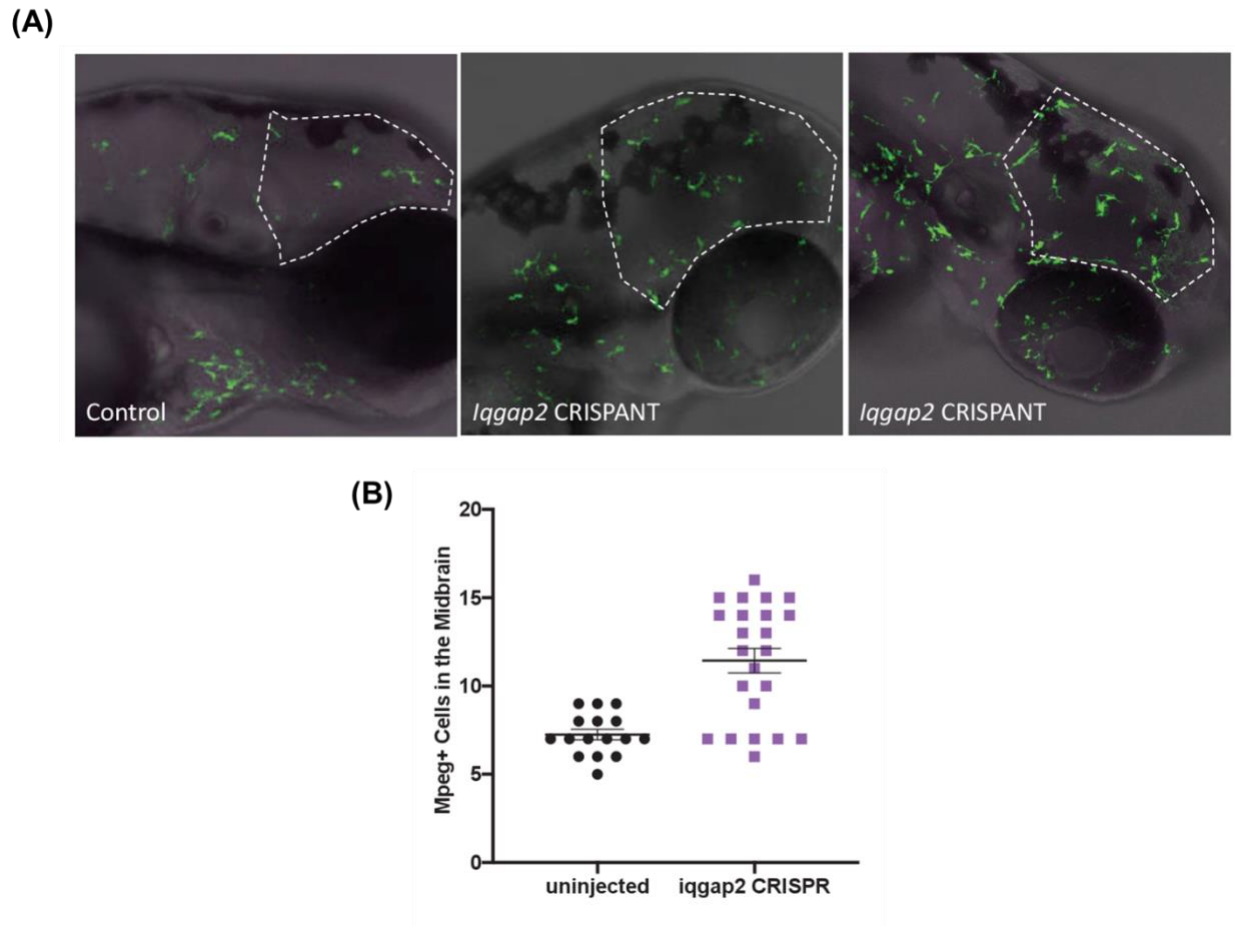

Figure 8.2 Loss of IQGAP2 in zebrafish results in increased immune cell infiltration into the midbrain. Images are courtesy of Natasha O'Brown, Harvard University.

Though extremely exciting, these initial *in vivo* results are highly preliminary. First, because the reporter driving GFP expression labels all cells of the macrophage lineage, it is unclear if the accumulation in the midbrain is the result of peripheral immune cell infiltration or increase microglia activity. Furthermore, the mosaic nature of the knockout precludes the interpretation of if this increase accumulation is the result of changes in endothelial function or changes in some other cell type. Finally, we must address whether loss of the tumor-suppressor function of IQGAP2

in this model has resulted in increased cell proliferation, leading to increased infiltration. Future experiments will aim to clarify the basis of these results in zebrafish, and we will also be investigating if similar phenomena occur in global *Iqgap2* knockout mice. Collectively, these results motivate further investigation of IQGAP2 function at the blood-brain barrier. Moreover, and more importantly, the results of this study suggest that iPSC-derived BMECs are a powerful tool for understanding and interrogating *in vivo* physiology, potentially fundamentally changing investigations into blood-brain barrier function.

Chapter 9

REFERENCES

1. Borlongan CV, Burns J, Tajiri N, Stahl CE, Weinbren NL, Shojo H, et al. Epidemiological Survey-Based Formulae to Approximate Incidence and Prevalence of Neurological Disorders in the United States: a Meta-Analysis. PLOS ONE. 2013;8:e78490.

2. Gooch CL, Pracht E, Borenstein AR. The burden of neurological disease in the United States: A summary report and call to action. Ann Neurol. 2017;81:479–84.

3. Garbuzova-Davis S, Rodrigues MCO, Hernandez-Ontiveros DG, Louis MK, Willing AE, Borlongan CV, et al. Amyotrophic lateral sclerosis: A neurovascular disease. Brain Res. 2011;1398:113–25.

4. Zlokovic BV. Neurovascular pathways to neurodegeneration in Alzheimer's disease and other disorders. Nat Rev Neurosci. 2011;12:723–38.

5. Engelhardt B, Ransohoff RM. Capture, crawl, cross: the T cell code to breach the blood–brain barriers. Trends Immunol. 2012;33:579–89.

6. Abbott NJ, Rönnbäck L, Hansson E. Astrocyte–endothelial interactions at the blood–brain barrier. Nat Rev Neurosci. 2006;7:41–53.

7. Kniesel U, Wolburg H. Tight junctions of the blood–brain barrier. Cell Mol Neurobiol. 2000;20.

8. Obermeier B, Daneman R, Ransohoff RM. Development, maintenance and disruption of the blood-brain barrier. Nat Med. 2013;19:1584–96.

9. Butt AM, Jones HC, Abbott NJ. Electrical resistance across the blood-brain barrier in anaesthetized rats: a developmental study. J Physiol. 1990;429:47–62.

10. Bazzoni G, Dejana E. Endothelial Cell-to-Cell Junctions: Molecular Organization and Role in Vascular Homeostasis. Physiol Rev. 2004;84:869–901.

11. Rubin LL, Hall DE, Porter S, Barbu K, Cannon C, Horner HC, et al. A cell culture model of the blood-brain barrier. J Cell Biol. 1991;115:1725–35.

12. Reese TS, Karnovsky MJ. Fine Structural Localization of a Blood-Brain Barrier to Exogenous Peroxidase. J Cell Biol. 1967;34:207–17.

13. Zhao Z, Nelson AR, Betsholtz C, Zlokovic BV. Establishment and Dysfunction of the Blood-Brain Barrier. Cell. 2015;163:1064–78.

14. Dermietzel R, Krause D, Kremer M, Wang C, Stevenson B. Pattern of glucose transporter (Glut 1) expression in embryonic brains is related to maturation of blood-brain barrier tightness. Dev Dyn Off Publ Am Assoc Anat. 1992;193:152–63.

15. Stenman JM, Rajagopal J, Carroll TJ, Ishibashi M, McMahon J, McMahon AP. Canonical Wnt Signaling Regulates Organ-Specific Assembly and Differentiation of CNS Vasculature. Science. 2008;322:1247–50.

16. Begley DJ. ABC Transporters and the Blood-Brain Barrier. Curr Pharm Des. 2004;10:1295–312.

17. Bendayan R, Lee G, Bendayan M. Functional expression and localization of P-glycoprotein at the blood brain barrier. Microsc Res Tech. 2002;57:365–80.

18. Schinkel AH. P-Glycoprotein, a gatekeeper in the blood–brain barrier. Adv Drug Deliv Rev. 1999;36:179–94.

19. Leslie EM, Deeley RG, Cole SPC. Multidrug resistance proteins: role of P-glycoprotein, MRP1, MRP2, and BCRP (ABCG2) in tissue defense. Toxicol Appl Pharmacol. 2005;204:216–37.

20. Abbott NJ, Patabendige AAK, Dolman DEM, Yusof SR, Begley DJ. Structure and function of the blood–brain barrier. Neurobiol Dis. 2010;37:13–25.

21. Engelhardt B. Development of the blood-brain barrier. Cell Tissue Res. 2003;314:119–29.

22. Raab S, Beck H, Gaumann A, Yüce A, Gerber H-P, Plate K, et al. Impaired brain angiogenesis and neuronal apoptosis induced by conditional homozygous inactivation of vascular endothelial growth factor. Thromb Haemost. 2004;91:595–605.

23. Shalaby F, Rossant J, Yamaguchi TP, Gertsenstein M, Wu XF, Breitman ML, et al. Failure of blood-island formation and vasculogenesis in Flk-1-deficient mice. Nature. 1995;376:62–6.

24. Daneman R, Agalliu D, Zhou L, Kuhnert F, Kuo CJ, Barres BA. Wnt/beta-catenin signaling is required for CNS, but not non-CNS, angiogenesis. Proc Natl Acad Sci U A [Internet]. 2009;106. Available from: http://dx.doi.org/10.1073/pnas.0805165106

25. Tam SJ, Richmond DL, Kaminker JS, Modrusan Z, Martin-McNulty B, Cao TC, et al. Death Receptors DR6 and TROY Regulate Brain Vascular Development. Dev Cell. 2012;22:403–17.

26. Kuhnert F, Mancuso MR, Shamloo A, Wang H-T, Choksi V, Florek M, et al. Essential Regulation of CNS Angiogenesis by the Orphan G Protein–Coupled Receptor GPR124. Science. 2010;330:985.

27. Cho C, Smallwood PM, Nathans J. Reck and Gpr124 Are Essential Receptor Cofactors for Wnt7a/Wnt7b-Specific Signaling in Mammalian CNS Angiogenesis and Blood-Brain Barrier Regulation. Neuron. 2017;95:1056-1073.e5.

28. Alvarez JI, Dodelet-Devillers A, Kebir H, Ifergan I, Fabre PJ, Terouz S, et al. The Hedgehog pathway promotes blood-brain barrier integrity and CNS immune quiescence. Science. 2011;334:1727–31.

29. Armulik A, Genové G, Mäe M, Nisancioglu MH, Wallgard E, Niaudet C, et al. Pericytes regulate the blood–brain barrier. Nature. 2010;468:557.

30. Thurgur H, Pinteaux E. Microglia in the Neurovascular Unit: Blood–Brain Barrier–microglia Interactions After Central Nervous System Disorders. Neuroscience. 2019;405:55–67.

31. Noumbissi ME, Galasso B, Stins MF. Brain vascular heterogeneity: implications for disease pathogenesis and design of in vitro blood–brain barrier models. Fluids Barriers CNS [Internet]. 2018 [cited 2020 Feb 9];15. Available from: https://www.ncbi.nlm.nih.gov/pmc/articles/PMC5911972/

32. Vanlandewijck M, He L, Mäe MA, Andrae J, Ando K, Del Gaudio F, et al. A molecular atlas of cell types and zonation in the brain vasculature. Nature. 2018;554:475–80.

33. Yousef H, Czupalla CJ, Lee D, Chen MB, Burke AN, Zera KA, et al. Aged blood impairs hippocampal neural precursor activity and activates microglia via brain endothelial cell VCAM1. Nat Med. 2019;25:988–1000.

34. Friese MA, Schattling B, Fugger L. Mechanisms of neurodegeneration and axonal dysfunction in multiple sclerosis. Nat Rev Neurol. 2014;10:225–38.

35. Korn A, Golan H, Melamed I, Pascual-Marqui R, Friedman A. Focal cortical dysfunction and blood-brain barrier disruption in patients with Postconcussion syndrome. J Clin Neurophysiol Off Publ Am Electroencephalogr Soc. 2005;22:1–9.

36. Sandoval KE, Witt KA. Blood-brain barrier tight junction permeability and ischemic stroke. Neurobiol Dis. 2008;32:200–19.

37. Strbian D, Durukan A, Pitkonen M, Marinkovic I, Tatlisumak E, Pedrono E, et al. The blood–brain barrier is continuously open for several weeks following transient focal cerebral ischemia. Neuroscience. 2008;153:175–81.

38. Barzó P, Marmarou A, Fatouros P, Corwin F, Dunbar J. Magnetic resonance imaging—monitored acute blood-brain barrier changes in experimental traumatic brain injury. J Neurosurg. 1996;85:1113–21.

39. Drouin-Ouellet J, Sawiak SJ, Cisbani G, Lagacé M, Kuan W-L, Saint-Pierre M, et al. Cerebrovascular and blood-brain barrier impairments in Huntington's disease: Potential implications for its pathophysiology. Ann Neurol. 2015;78:160–77.

40. Rosell A, Cuadrado E, Ortega-Aznar A, Hernández-Guillamon M, Lo EH, Montaner J. MMP-9–Positive Neutrophil Infiltration Is Associated to Blood–Brain Barrier Breakdown and Basal Lamina Type IV Collagen Degradation During Hemorrhagic Transformation After Human Ischemic Stroke. Stroke. 2008;39:1121–6.

41. Montagne A, Barnes SR, Sweeney MD, Halliday MR, Sagare AP, Zhao Z, et al. Blood-Brain Barrier Breakdown in the Aging Human Hippocampus. Neuron. 2015;85:296–302.

42. Muldoon LL, Soussain C, Jahnke K, Johanson C, Siegal T, Smith QR, et al. Chemotherapy Delivery Issues in Central Nervous System Malignancy: A Reality Check. J Clin Oncol. 2007;25:2295–305.

43. Abbott NJ. Blood–brain barrier structure and function and the challenges for CNS drug delivery. J Inherit Metab Dis. 2013;36:437–49.

44. Knowland D, Arac A, Sekiguchi KJ, Hsu M, Lutz SE, Perrino J, et al. Stepwise Recruitment of Transcellular and Paracellular Pathways Underlies Blood-Brain Barrier Breakdown in Stroke. Neuron. 2014;82:603–17.

45. Bartels AL, Willemsen ATM, Kortekaas R, Jong BM de, Vries R de, Klerk O de, et al. Decreased blood–brain barrier P-glycoprotein function in the progression of Parkinson's disease, PSP and MSA. J Neural Transm. 2008;115:1001–9.

46. Vogelgesang S, Cascorbi I, Schroeder E, Pahnke J, Kroemer H, Siegmund W, et al. Deposition of Alzheimer's beta-amyloid is inversely correlated with p-Glycoprotein expression in the brains of elderly non-demented humans. Pharmacogenetics. 2002;12:535–41.

47. Park R, Kook S-Y, Park J-C, Mook-Jung I. Aβ1–42 reduces P-glycoprotein in the blood–brain barrier through RAGE–NF-κB signaling. Cell Death Amp Dis. 2014;5:e1299.

48. Sweeney MD, Ayyadurai S, Zlokovic BV. Pericytes of the neurovascular unit: key functions and signaling pathways. Nat Neurosci. 2016;19:771–83.

49. Naik P, Cucullo L. In Vitro Blood–Brain Barrier Models: Current and Perspective Technologies. J Pharm Sci. 2012;101:1337–54.

50. Pardridge WM. CNS Drug Design Based on Principles of Blood-Brain Barrier Transport. J Neurochem. 1998;70:1781–92.

51. Helms HC, Abbott NJ, Burek M, Cecchelli R, Couraud P-O, Deli MA, et al. In vitro models of the blood–brain barrier: An overview of commonly used brain endothelial cell culture models and guidelines for their use. J Cereb Blood Flow Metab. 2016;36:862–90.

52. Song L, Pachter JS. Culture of murine brain microvascular endothelial cells that maintain expression and cytoskeletal association of tight junction-associated proteins. Vitro Cell Dev Biol - Anim. 2003;39:313–20.

53. Al Ahmad A, Taboada CB, Gassmann M, Ogunshola OO. Astrocytes and pericytes differentially modulate blood–brain barrier characteristics during development and hypoxic insult. J Cereb Blood Flow Metab. 2011;31:693–705.

54. Al Ahmad A, Gassmann M, Ogunshola O o. Maintaining blood–brain barrier integrity: Pericytes perform better than astrocytes during prolonged oxygen deprivation. J Cell Physiol. 2009;218:612–22.

55. Dehouck M-P, Méresse S, Delorme P, Fruchart J-C, Cecchelli R. An Easier, Reproducible, and Mass-Production Method to Study the Blood–Brain Barrier In Vitro. J Neurochem. 1990;54:1798–801.

56. Franke H, Galla H-J, Beuckmann CT. An improved low-permeability in vitro-model of the blood–brain barrier: transport studies on retinoids, sucrose, haloperidol, caffeine and mannitol. Brain Res. 1999;818:65–71.

57. Patabendige A, Skinner RA, Abbott NJ. Establishment of a simplified in vitro porcine blood–brain barrier model with high transendothelial electrical resistance. Brain Res. 2013;1521:1–15.

58. Nakagawa S, Deli MA, Kawaguchi H, Shimizudani T, Shimono T, Kittel A, et al. A new blood-brain barrier model using primary rat brain endothelial cells, pericytes and astrocytes. Neurochem Int. 2009;54:253–63.

59. Nakagawa S, Deli MA, Nakao S, Honda M, Hayashi K, Nakaoke R, et al. Pericytes from Brain Microvessels Strengthen the Barrier Integrity in Primary Cultures of Rat Brain Endothelial Cells. Cell Mol Neurobiol. 2007;27:687–94.

60. Dohgu S, Takata F, Yamauchi A, Nakagawa S, Egawa T, Naito M, et al. Brain pericytes contribute to the induction and up-regulation of blood-brain barrier functions through transforming growth factor-beta production. Brain Res. 2005;1038:208–15.

61. Vandenhaute E, Dehouck L, Boucau M-C, Sevin E, Uzbekov R, Tardivel M, et al. Modelling the neurovascular unit and the blood-brain barrier with the unique function of pericytes. Curr Neurovasc Res. 2011;8:258–69.

62. Syvänen S, Lindhe Ö, Palner M, Kornum BR, Rahman O, Långström B, et al. Species Differences in Blood-Brain Barrier Transport of Three Positron Emission Tomography Radioligands with Emphasis on P-Glycoprotein Transport. Drug Metab Dispos. 2009;37:635–43.

63. Weksler BB, Subileau EA, Perrière N, Charneau P, Holloway K, Leveque M, et al. Blood-brain barrier-specific properties of a human adult brain endothelial cell line. FASEB J. 2005;

64. Bernas MJ, Cardoso FL, Daley SK, Weinand ME, Campos AR, Ferreira AJG, et al. Establishment of primary cultures of human brain microvascular endothelial cells to provide an in vitro cellular model of the blood-brain barrier. Nat Protoc. 2010;5:1265–72.

65. Lippmann ES, Azarin SM, Kay JE, Nessler RA, Wilson HK, Al-Ahmad A, et al. Derivation of blood-brain barrier endothelial cells from human pluripotent stem cells. Nat Biotechnol. 2012;30:783–91.

66. Mizee MR, Wooldrik D, Lakeman KAM, van het Hof B, Drexhage JAR, Geerts D, et al. Retinoic acid induces blood-brain barrier development. J Neurosci Off J Soc Neurosci. 2013;33:1660–71.

67. Lippmann ES, Al-Ahmad A, Azarin SM, Palecek SP, Shusta EV. A retinoic acid-enhanced, multicellular human blood-brain barrier model derived from stem cell sources. Sci Rep. 2014;4:4160.

68. Daneman R, Prat A. The Blood–Brain Barrier. Cold Spring Harb Perspect Biol. 2015;7:a020412.

69. Shusta EV. Blood-Brain Barrier Genomics, Proteomics, and New Transporter Discovery. NeuroRx. 2005;2:151–61.

70. Shusta EV, Boado RJ, Mathern GW, Pardridge WM. Vascular genomics of the human brain. J Cereb Blood Flow Metab Off J Int Soc Cereb Blood Flow Metab. 2002;22:245–52.

71. Huntley MA, Bien-Ly N, Daneman R, Watts RJ. Dissecting gene expression at the blood-brain barrier. Front Neurosci [Internet]. 2014 [cited 2017 Dec 29];8. Available from: https://www.ncbi.nlm.nih.gov/pmc/articles/PMC4222230/

72. Ben-Zvi A, Lacoste B, Kur E, Andreone BJ, Mayshar Y, Yan H, et al. Mfsd2a is critical for the formation and function of the blood–brain barrier. Nature. 2014;509:507.

73. Anderson KD, Pan L, Yang XM, Hughes VC, Walls JR, Dominguez MG, et al. Angiogenic sprouting into neural tissue requires Gpr124, an orphan G protein-coupled receptor. Proc Natl Acad Sci U A [Internet]. 2011;108. Available from: http://dx.doi.org/10.1073/pnas.1019761108

74. Chang J, Mancuso MR, Maier C, Liang X, Yuki K, Yang L, et al. Gpr124 is essential for blood-brain barrier integrity in central nervous system disease. Nat Med. 2017;23:450–60.

75. Cullen M, Elzarrad MK, Seaman S, Zudaire E, Stevens J, Yang MY, et al. GPR124, an orphan G protein-coupled receptor, is required for CNS-specific vascularization and establishment of the blood–brain barrier. Proc Natl Acad Sci U A [Internet]. 2011;108. Available from: http://dx.doi.org/10.1073/pnas.1017192108

76. Andreone BJ, Chow BW, Tata A, Lacoste B, Ben-Zvi A, Bullock K, et al. Blood-Brain Barrier Permeability Is Regulated by Lipid Transport-Dependent Suppression of Caveolae-Mediated Transcytosis. Neuron. 2017;94:581-594.e5.

77. Shalem O, Sanjana NE, Zhang F. High-throughput functional genomics using CRISPR-Cas9. Nat Rev Genet. 2015;16:299–311.

78. Boutros M, Ahringer J. The art and design of genetic screens: RNA interference. Nat Rev Genet. 2008;9:554.

79. Jackson AL, Linsley PS. Recognizing and avoiding siRNA off-target effects for target identification and therapeutic application. Nat Rev Drug Discov. 2010;9:57.

80. Jackson AL, Bartz SR, Schelter J, Kobayashi SV, Burchard J, Mao M, et al. Expression profiling reveals off-target gene regulation by RNAi. Nat Biotechnol. 2003;21:635.

81. Miller JC, Holmes MC, Wang J, Guschin DY, Lee Y-L, Rupniewski I, et al. An improved zinc-finger nuclease architecture for highly specific genome editing. Nat Biotechnol. 2007;25:778.

82. Urnov FD, Miller JC, Lee Y-L, Beausejour CM, Rock JM, Augustus S, et al. Highly efficient endogenous human gene correction using designed zinc-finger nucleases. Nature. 2005;435:646.

83. Mahfouz MM, Li L, Shamimuzzaman M, Wibowo A, Fang X, Zhu J-K. De novo-engineered transcription activator-like effector (TALE) hybrid nuclease with novel DNA binding specificity creates double-strand breaks. Proc Natl Acad Sci. 2011;108:2623–8.

84. Cong L, Ran FA, Cox D, Lin S, Barretto R, Habib N, et al. Multiplex Genome Engineering Using CRISPR/Cas Systems. Science. 2013;339:819–23.

85. Mali P, Yang L, Esvelt KM, Aach J, Guell M, DiCarlo JE, et al. RNA-Guided Human Genome Engineering via Cas9. Science. 2013;339:823–6.

86. Jinek M, East A, Cheng A, Lin S, Ma E, Doudna J. RNA-programmed genome editing in human cells. eLife. 2013;2:e00471.

87. Cho SW, Kim S, Kim JM, Kim J-S. Targeted genome engineering in human cells with the Cas9 RNA-guided endonuclease. Nat Biotechnol. 2013;31:230.

88. Gaj T, Gersbach CA, Barbas CF. ZFN, TALEN, and CRISPR/Cas-based methods for genome engineering. Trends Biotechnol. 2013;31:397–405.

89. Doudna JA, Charpentier E. The new frontier of genome engineering with CRISPR-Cas9. Science. 2014;346:1258096.

90. Barrangou R, Fremaux C, Deveau H, Richards M, Boyaval P, Moineau S, et al. CRISPR provides acquired resistance against viruses in prokaryotes. Science. 2007;315:1709–12.

91. Wang T, Wei JJ, Sabatini DM, Lander ES. Genetic screens in human cells using the CRISPR-Cas9 system. Science. 2014;343:80–4.

92. Shalem O, Sanjana NE, Hartenian E, Shi X, Scott DA, Mikkelsen TS, et al. Genome-Scale CRISPR-Cas9 Knockout Screening in Human Cells. Science. 2014;343:84–7.

93. Zlokovic BV. The Blood-Brain Barrier in Health and Chronic Neurodegenerative Disorders. Neuron. 2008;57:178–201.

94. Olesen SP, Crone C. Electrical resistance of muscle capillary endothelium. Biophys J. 1983;42:31–41.

95. Löscher W, Potschka H. Drug resistance in brain diseases and the role of drug efflux transporters. Nat Rev Neurosci. 2005;6:591–602.

96. Al Ahmad A, Taboada CB, Gassmann M, Ogunshola OO. Astrocytes and pericytes differentially modulate blood–brain barrier characteristics during development and hypoxic insult. J Cereb Blood Flow Metab. 2011;31.

97. Al Ahmad A, Gassmann M, Ogunshola OO. Maintaining blood–brain barrier integrity: pericytes perform better than astrocytes during prolonged oxygen deprivation. J Cell Physiol. 2009;218.

98. Abbott NJ. Prediction of blood–brain barrier permeation in drug discovery from in vivo, in vitro and in silico models. Drug Discov Today Technol. 2004;1:407–16.

99. Reichel A. Addressing Central Nervous System (CNS) Penetration in Drug Discovery: Basics and Implications of the Evolving New Concept. Chem Biodivers. 2009;6:2030–49.

100. Ludwig TE, Levenstein ME, Jones JM, Berggren WT, Mitchen ER, Frane JL, et al. Derivation of human embryonic stem cells in defined conditions. Nat Biotechnol. 2006;24:185–7.

101. Chen G, Gulbranson DR, Hou Z, Bolin JM, Ruotti V, Probasco MD, et al. Chemically defined conditions for human iPSC derivation and culture. Nat Methods. 2011;8:424–9.

102. Lippmann ES, Estevez-Silva MC, Ashton RS. Defined Human Pluripotent Stem Cell Culture Enables Highly Efficient Neuroepithelium Derivation Without Small Molecule Inhibitors. Stem Cells. 2014;32:1032–42.

103. Lian X, Bao X, Zilberter M, Westman M, Fisahn A, Hsiao C, et al. Chemically defined, albumin-free human cardiomyocyte generation. Nat Methods. 2015;12:595–6.

104. Patel R, Alahmad AJ. Growth-factor reduced Matrigel source influences stem cell derived brain microvascular endothelial cell barrier properties. Fluids Barriers CNS. 2016;13:6.

105. Calabria AR, Weidenfeller C, Jones AR, De Vries HE, Shusta EV. Puromycin-purified rat brain microvascular endothelial cell cultures exhibit improved barrier properties in response to glucocorticoid induction. J Neurochem. 2006;97:922–33.

106. Yu J, Vodyanik MA, Smuga-Otto K, Antosiewicz-Bourget J, Frane JL, Tian S, et al. Induced pluripotent stem cell lines derived from human somatic cells. Science. 2007;318.

107. Tidball AM, Neely MD, Chamberlin R, Aboud AA, Kumar KK, Han B, et al. Genomic Instability Associated with p53 Knockdown in the Generation of Huntington's Disease Human Induced Pluripotent Stem Cells. PLOS ONE. 2016;11:e0150372.

108. Kumar KK, Lowe, Jr. EW, Aboud AA, Neely MD, Redha R, Bauer JA, et al. Cellular manganese content is developmentally regulated in human dopaminergic neurons. Sci Rep. 2014;4.

109. Aboud AA, Tidball AM, Kumar KK, Neely MD, Ess KC, Erikson KM, et al. Genetic risk for Parkinson's disease correlates with alterations in neuronal manganese sensitivity between two human subjects. Neurotoxicology. 2012;33:1443–9.

110. Aboud AA, Tidball AM, Kumar KK, Neely MD, Han B, Ess KC, et al. PARK2 patient neuroprogenitors show increased mitochondrial sensitivity to copper. Neurobiol Dis. 2015;73:204–12.

111. Wilson HK, Canfield SG, Hjortness MK, Palecek SP, Shusta EV. Exploring the effects of cell seeding density on the differentiation of human pluripotent stem cells to brain microvascular endothelial cells. Fluids Barriers CNS. 2015;12:13.

112. Carpenter AE, Jones TR, Lamprecht MR, Clarke C, Kang IH, Friman O, et al. CellProfiler: image analysis software for identifying and quantifying cell phenotypes. Genome Biol. 2006;7:R100.

113. Katt ME, Xu ZS, Gerecht S, Searson PC. Human Brain Microvascular Endothelial Cells Derived from the BC1 iPS Cell Line Exhibit a Blood-Brain Barrier Phenotype. PLOS ONE. 2016;11:e0152105.

114. Wang YI, Abaci HE, Shuler ML. Microfluidic blood–brain barrier model provides in vivo-like barrier properties for drug permeability screening. Biotechnol Bioeng. 2017;114:184–94.

115. Chambers SM, Fasano CA, Papapetrou EP, Tomishima M, Sadelain M, Studer L. Highly efficient neural conversion of human ES and iPS cells by dual inhibition of SMAD signaling. Nat Biotechnol. 2009;27:275–80.

116. Pankratz MT, Li X-J, LaVaute TM, Lyons EA, Chen X, Zhang S-C. Directed Neural Differentiation of Human Embryonic Stem Cells via an Obligated Primitive Anterior Stage. STEM CELLS. 2007;25:1511–20.

117. Kawasaki H, Mizuseki K, Nishikawa S, Kaneko S, Kuwana Y, Nakanishi S, et al. Induction of Midbrain Dopaminergic Neurons from ES Cells by Stromal Cell–Derived Inducing Activity. Neuron. 2000;28:31–40.

118. Smith QR, Rapoport SI. Cerebrovascular permeability coefficients to sodium, potassium, and chloride. J Neurochem. 1986;46.

119. Sweeney MD, Sagare AP, Zlokovic BV. Blood-brain barrier breakdown in Alzheimer disease and other neurodegenerative disorders. Nat Rev Neurol. 2018;14:133–50.

120. Prasad S, Sajja RK, Naik P, Cucullo L. Diabetes Mellitus and Blood-Brain Barrier Dysfunction: An Overview. J Pharmacovigil. 2014;2:125.

121. Huh D, Hamilton GA, Ingber DE. From 3D cell culture to organs-on-chips. Trends Cell Biol. 2011;21:745–54.

122. Ravi M, Paramesh V, Kaviya SR, Anuradha E, Solomon FDP. 3D cell culture systems: advantages and applications. J Cell Physiol. 2015;230:16–26.

123. Wikswo JP. The relevance and potential roles of microphysiological systems in biology and medicine. Exp Biol Med Maywood NJ. 2014;239:1061–72.

124. Tibbitt MW, Anseth KS. Hydrogels as extracellular matrix mimics for 3D cell culture. Biotechnol Bioeng. 2009;103:655–63.

125. Cabodi M, Choi NW, Gleghorn JP, Lee CSD, Bonassar LJ, Stroock AD. A microfluidic biomaterial. J Am Chem Soc. 2005;127:13788–9.

126. Golden AP, Tien J. Fabrication of microfluidic hydrogels using molded gelatin as a sacrificial element. Lab Chip. 2007;7:720–5.

127. Zheng Y, Chen J, Craven M, Choi NW, Totorica S, Diaz-Santana A, et al. In vitro microvessels for the study of angiogenesis and thrombosis. Proc Natl Acad Sci U S A. 2012;109:9342–7.

128. Bertassoni LE, Cecconi M, Manoharan V, Nikkhah M, Hjortnaes J, Cristino AL, et al. Hydrogel bioprinted microchannel networks for vascularization of tissue engineering constructs. Lab Chip. 2014;14:2202–11.

129. Kolesky DB, Truby RL, Gladman AS, Busbee TA, Homan KA, Lewis JA. 3D bioprinting of vascularized, heterogeneous cell-laden tissue constructs. Adv Mater Deerfield Beach Fla. 2014;26:3124–30.

130. Miller JS, Stevens KR, Yang MT, Baker BM, Nguyen D-HT, Cohen DM, et al. Rapid casting of patterned vascular networks for perfusable engineered three-dimensional tissues. Nat Mater. 2012;11:768–74.

131. Barry C, Schmitz MT, Propson NE, Hou Z, Zhang J, Nguyen BK, et al. Uniform neural tissue models produced on synthetic hydrogels using standard culture techniques. Exp Biol Med. 2017;1535370217715028.

132. Pellett S, Schwartz MP, Tepp WH, Josephson R, Scherf JM, Pier CL, et al. Human Induced Pluripotent Stem Cell Derived Neuronal Cells Cultured on Chemically-Defined Hydrogels for Sensitive In Vitro Detection of Botulinum Neurotoxin. Sci Rep. 2015;5:14566.

133. Prabhakarpandian B, Shen M-C, Nichols JB, Mills IR, Sidoryk-Wegrzynowicz M, Aschner M, et al. SyM-BBB: a microfluidic blood brain barrier model. Lab Chip. 2013;13:1093–101.

134. Brown JA, Pensabene V, Markov DA, Allwardt V, Neely MD, Shi M, et al. Recreating blood-brain barrier physiology and structure on chip: A novel neurovascular microfluidic bioreactor. Biomicrofluidics. 2015;9:054124.

135. Markov DA, Lu JQ, Samson PC, Wikswo JP, McCawley LJ. Thick-tissue bioreactor as a platform for long-term organotypic culture and drug delivery. Lab Chip. 2012;12:4560–8.

136. Kim S, Lee H, Chung M, Li Jeon N. Engineering of functional, perfusable 3D microvascular networks on a chip. Lab Chip. 2013;13:1489–500.

137. Phan DTT, Wang X, Craver BM, Sobrino A, Zhao D, Chen JC, et al. A vascularized and perfused organ-on-a-chip platform for large-scale drug screening applications. Lab Chip. 2017;17:511–20.

138. Cho H, Seo JH, Wong KHK, Terasaki Y, Park J, Bong K, et al. Three-Dimensional Blood-Brain Barrier Model for *in vitro* Studies of Neurovascular Pathology. Sci Rep. 2015;5:srep15222.

139. Ingram PN, Hind LE, Jiminez-Torres JA, Huttenlocher A, Beebe DJ. An Accessible Organotypic Microvessel Model Using iPSC-Derived Endothelium. Adv Healthc Mater. 2016;10.1002/adhm.201700497.

140. Jiménez-Torres JA, Peery SL, Sung KE, Beebe DJ. LumeNEXT: A Practical Method to Pattern Luminal Structures in ECM Gels. Adv Healthc Mater. 2016;5:198–204.

141. Helms HC, Abbott NJ, Burek M, Cecchelli R, Couraud P-O, Deli MA, et al. In vitro models of the blood-brain barrier: An overview of commonly used brain endothelial cell culture models and guidelines for their use. J Cereb Blood Flow Metab Off J Int Soc Cereb Blood Flow Metab. 2016;36:862–90.

142. Deo AK, Theil F-P, Nicolas J-M. Confounding parameters in preclinical assessment of blood-brain barrier permeation: an overview with emphasis on species differences and effect of disease states. Mol Pharm. 2013;10:1581–95.

143. Weksler BB, Subileau EA, Perrière N, Charneau P, Holloway K, Leveque M, et al. Blood-brain barrier-specific properties of a human adult brain endothelial cell line. FASEB J. 2005;19:1872–4.

144. Lippmann ES, Azarin SM, Kay JE, Nessler RA, Wilson HK, Al-Ahmad A, et al. Derivation of blood-brain barrier endothelial cells from human pluripotent stem cells. Nat Biotechnol. 2012;30:783–91.

145. Lippmann ES, Al-Ahmad A, Azarin SM, Palecek SP, Shusta EV. A retinoic acid-enhanced, multicellular human blood-brain barrier model derived from stem cell sources. Sci Rep. 2014;4:4160.

146. Appelt-Menzel A, Cubukova A, Günther K, Edenhofer F, Piontek J, Krause G, et al. Establishment of a Human Blood-Brain Barrier Co-culture Model Mimicking the Neurovascular Unit Using Induced Pluri- and Multipotent Stem Cells. Stem Cell Rep. 2017;8:894–906.

147. Hollmann EK, Bailey AK, Potharazu AV, Neely MD, Bowman AB, Lippmann ES. Accelerated differentiation of human induced pluripotent stem cells to blood-brain barrier endothelial cells. Fluids Barriers CNS. 2017;14:9.

148. Katt ME, Xu ZS, Gerecht S, Searson PC. Human Brain Microvascular Endothelial Cells Derived from the BC1 iPS Cell Line Exhibit a Blood-Brain Barrier Phenotype. PloS One. 2016;11:e0152105.

149. Wilson HK, Canfield SG, Hjortness MK, Palecek SP, Shusta EV. Exploring the effects of cell seeding density on the differentiation of human pluripotent stem cells to brain microvascular endothelial cells. Fluids Barriers CNS. 2015;12:13.

150. Wang YI, Abaci HE, Shuler ML. Microfluidic blood–brain barrier model provides in vivo-like barrier properties for drug permeability screening. Biotechnol Bioeng. 2017;114:184–94.

151. Yu J, Vodyanik MA, Smuga-Otto K, Antosiewicz-Bourget J, Frane JL, Tian S, et al. Induced Pluripotent Stem Cell Lines Derived from Human Somatic Cells. Science. 2007;318:1917–20.

152. Kumar KK, Lowe EW, Aboud AA, Neely MD, Redha R, Bauer JA, et al. Cellular manganese content is developmentally regulated in human dopaminergic neurons. Sci Rep. 2014;4:6801.

153. Wilson HK, Faubion MG, Hjortness MK, Palecek SP, Shusta EV. Cryopreservation of Brain Endothelial Cells Derived from Human Induced Pluripotent Stem Cells Is Enhanced by Rho-Associated Coiled Coil-Containing Kinase Inhibition. Tissue Eng Part C Methods. 2016;22:1085–94.

154. O'Grady B, Wang J, Faley S, Balikov D, Lippmann E, Bellan LM. A Customizable, Low-Cost Perfusion System for Sustaining Tissue Constructs. SLAS Technol Transl Life Sci Innov. 2018;2472630318775059.

155. Schindelin J, Arganda-Carreras I, Frise E, Kaynig V, Longair M, Pietzsch T, et al. Fiji: an open-source platform for biological-image analysis. Nat Methods. 2012;9:676–82.

156. Axelrod D, Koppel DE, Schlessinger J, Elson E, Webb WW. Mobility measurement by analysis of fluorescence photobleaching recovery kinetics. Biophys J. 1976;16:1055–69.

157. Braeckmans K, Peeters L, Sanders NN, De Smedt SC, Demeester J. Three-dimensional fluorescence recovery after photobleaching with the confocal scanning laser microscope. Biophys J. 2003;85:2240–52.

158. Soumpasis DM. Theoretical analysis of fluorescence photobleaching recovery experiments. Biophys J. 1983;41:95–7.

159. Kang M, Day CA, Kenworthy AK, DiBenedetto E. Simplified equation to extract diffusion coefficients from confocal FRAP data. Traffic Cph Den. 2012;13:1589–600.

160. Schneider CA, Rasband WS, Eliceiri KW. NIH Image to ImageJ: 25 years of image analysis. Nat Methods. 2012;9:671–5.

161. Yeom E, Kang YJ, Lee S-J. Changes in velocity profile according to blood viscosity in a microchannel. Biomicrofluidics [Internet]. 2014;8. Available from: https://www.ncbi.nlm.nih.gov/pmc/articles/PMC4162413/

162. Kim D, Langmead B, Salzberg SL. HISAT: a fast spliced aligner with low memory requirements. Nat Methods. 2015;12:357–60.

163. Karolchik D, Hinrichs AS, Furey TS, Roskin KM, Sugnet CW, Haussler D, et al. The UCSC Table Browser data retrieval tool. Nucleic Acids Res. 2004;32:D493-496.

164. Pertea M, Pertea GM, Antonescu CM, Chang T-C, Mendell JT, Salzberg SL. StringTie enables improved reconstruction of a transcriptome from RNA-seq reads. Nat Biotechnol. 2015;33:290–5.

165. Frazee AC, Pertea G, Jaffe AE, Langmead B, Salzberg SL, Leek JT. Ballgown bridges the gap between transcriptome assembly and expression analysis. Nat Biotechnol. 2015;33:243–6.

166. Bozza A, Coates EE, Incitti T, Ferlin KM, Messina A, Menna E, et al. Neural differentiation of pluripotent cells in 3D alginate-based cultures. Biomaterials. 2014;35:4636–45.

167. Ben-Zvi A, Lacoste B, Kur E, Andreone BJ, Mayshar Y, Yan H, et al. Mfsd2a is critical for the formation and function of the blood-brain barrier. Nature. 2014;509:507–11.

168. Knowland D, Arac A, Sekiguchi KJ, Hsu M, Lutz SE, Perrino J, et al. Stepwise recruitment of transcellular and paracellular pathways underlies blood-brain barrier breakdown in stroke. Neuron. 2014;82:603–17.

169. Daneman R, Prat A. The Blood–Brain Barrier. Cold Spring Harb Perspect Biol. 2015;7:a020412.

170. DeStefano JG, Xu ZS, Williams AJ, Yimam N, Searson PC. Effect of shear stress on iPSC-derived human brain microvascular endothelial cells (dhBMECs). Fluids Barriers CNS. 2017;14:20.

171. Reinitz A, DeStefano J, Ye M, Wong AD, Searson PC. Human brain microvascular endothelial cells resist elongation due to shear stress. Microvasc Res. 2015;99:8–18.

172. Ye M, Sanchez HM, Hultz M, Yang Z, Bogorad M, Wong AD, et al. Brain microvascular endothelial cells resist elongation due to curvature and shear stress. Sci Rep. 2014;4:srep04681.

173. Nitta T, Hata M, Gotoh S, Seo Y, Sasaki H, Hashimoto N, et al. Size-selective loosening of the blood-brain barrier in claudin-5-deficient mice. J Cell Biol. 2003;161:653–60.

174. Kluger MS, Clark PR, Tellides G, Gerke V, Pober JS. Claudin-5 controls intercellular barriers of human dermal microvascular but not human umbilical vein endothelial cells. Arterioscler Thromb Vasc Biol. 2013;33:489–500.

175. Cheng C, Helderman F, Tempel D, Segers D, Hierck B, Poelmann R, et al. Large variations in absolute wall shear stress levels within one species and between species. Atherosclerosis. 2007;195:225–35.

176. Cucullo L, Couraud P-O, Weksler B, Romero I-A, Hossain M, Rapp E, et al. Immortalized human brain endothelial cells and flow-based vascular modeling: a marriage of convenience for rational neurovascular studies. J Cereb Blood Flow Metab Off J Int Soc Cereb Blood Flow Metab. 2008;28:312–28.

177. Garcia-Polite F, Martorell J, Del Rey-Puech P, Melgar-Lesmes P, O'Brien CC, Roquer J, et al. Pulsatility and high shear stress deteriorate barrier phenotype in brain microvascular endothelium. J Cereb Blood Flow Metab Off J Int Soc Cereb Blood Flow Metab. 2017;37:2614–25.

178. Koutsiaris AG, Tachmitzi SV, Batis N. Wall shear stress quantification in the human conjunctival pre-capillary arterioles in vivo. Microvasc Res. 2013;85:34–9.

179. Cordon-Cardo C, O'Brien JP, Casals D, Rittman-Grauer L, Biedler JL, Melamed MR, et al. Multidrug-resistance gene (P-glycoprotein) is expressed by endothelial cells at blood-brain barrier sites. Proc Natl Acad Sci U S A. 1989;86:695–8.

180. Rochfort KD, Collins LE, McLoughlin A, Cummins PM. Shear-dependent attenuation of cellular ROS levels can suppress proinflammatory cytokine injury to human brain microvascular endothelial barrier properties. J Cereb Blood Flow Metab Off J Int Soc Cereb Blood Flow Metab. 2015;35:1648–56.

181. Kutys ML, Chen CS. Forces and mechanotransduction in 3D vascular biology. Curr Opin Cell Biol. 2016;42:73–9.

182. Galie PA, Nguyen D-HT, Choi CK, Cohen DM, Janmey PA, Chen CS. Fluid shear stress threshold regulates angiogenic sprouting. Proc Natl Acad Sci. 2014;111:7968–73.

183. Partyka PP, Godsey GA, Galie JR, Kosciuk MC, Acharya NK, Nagele RG, et al. Mechanical stress regulates transport in a compliant 3D model of the blood-brain barrier. Biomaterials. 2017;115:30–9.

184. Qian T, Maguire SE, Canfield SG, Bao X, Olson WR, Shusta EV, et al. Directed differentiation of human pluripotent stem cells to blood-brain barrier endothelial cells. Sci Adv. 2017;3:e1701679.

185. Zhang Y, Sloan SA, Clarke LE, Caneda C, Plaza CA, Blumenthal PD, et al. Purification and Characterization of Progenitor and Mature Human Astrocytes Reveals Transcriptional and Functional Differences with Mouse. Neuron. 2016;89:37–53.

186. Zhang J, Schwartz MP, Hou Z, Bai Y, Ardalani H, Swanson S, et al. A Genome-wide Analysis of Human Pluripotent Stem Cell-Derived Endothelial Cells in 2D or 3D Culture. Stem Cell Rep. 2017;8:907–18.

187. Lee JB, Wang X, Faley S, Baer B, Balikov DA, Sung H-J, et al. Development of 3D Microvascular Networks Within Gelatin Hydrogels Using Thermoresponsive Sacrificial Microfibers. Adv Healthc Mater. 2016;5:781–5.

188. Arrio-Dupont M, Cribier S, Foucault G, Devaux PF, d'Albis A. Diffusion of fluorescently labeled macromolecules in cultured muscle cells. Biophys J. 1996;70:2327–32.

189. Huber JD, Witt KA, Hom S, Egleton RD, Mark KS, Davis TP. Inflammatory pain alters blood-brain barrier permeability and tight junctional protein expression. Am J Physiol-Heart Circ Physiol. 2001;280:H1241–8.

190. Weksler BB, Subileau EA, Perrière N, Charneau P, Holloway K, Leveque M, et al. Blood-brain barrier-specific properties of a human adult brain endothelial cell line. FASEB J Off Publ Fed Am Soc Exp Biol. 2005;19:1872–4.

191. Stebbins MJ, Lippmann ES, Faubion MG, Daneman R, Palecek SP, Shusta EV. Activation of RARα, RARγ, or RXRα Increases Barrier Tightness in Human Induced Pluripotent Stem Cell-Derived Brain Endothelial Cells. Biotechnol J. 2017;13:1700093.

192. Vatine GD, Al-Ahmad A, Barriga BK, Svendsen S, Salim A, Garcia L, et al. Modeling Psychomotor Retardation using iPSCs from MCT8-Deficient Patients Indicates a Prominent Role for the Blood-Brain Barrier. Cell Stem Cell. 2017;20:831-843.e5.

193. Smith QR, Rapoport SI. Cerebrovascular Permeability Coefficients to Sodium, Potassium, and Chloride. J Neurochem. 1986;46:1732–42.

194. Appelt-Menzel A, Cubukova A, Günther K, Edenhofer F, Piontek J, Krause G, et al. Establishment of a Human Blood-Brain Barrier Co-culture Model Mimicking the Neurovascular Unit Using Induced Pluri- and Multipotent Stem Cells. Stem Cell Rep. 2017;8:894–906.

195. Hollmann EK, Bailey AK, Potharazu AV, Neely MD, Bowman AB, Lippmann ES. Accelerated differentiation of human induced pluripotent stem cells to blood–brain barrier endothelial cells. Fluids Barriers CNS. 2017;14:9.

196. Armstrong LC, Westlake G, Snow JP, Cawthon B, Armour E, Bowman AB, et al. Heterozygous loss of TSC2 alters p53 signaling and human stem cell reprogramming. Hum Mol Genet. 2017;26:4629–41.

197. Stebbins MJ, Wilson HK, Canfield SG, Qian T, Palecek SP, Shusta EV. Differentiation and characterization of human pluripotent stem cell-derived brain microvascular endothelial cells. Methods. 2016;101:93–102.

198. Schindelin J, Arganda-Carreras I, Frise E, Kaynig V, Longair M, Pietzsch T, et al. Fiji: an open-source platform for biological-image analysis. Nat Methods. 2012;9:676–82.

199. McClatchey PM, Keller AC, Bouchard R, Knaub LA, Reusch JEB. Fully automated software for quantitative measurements of mitochondrial morphology. Mitochondrion. 2016;26:58–71.

200. McClatchey PM, Mignemi NA, Xu Z, Williams IM, Reusch JEB, McGuinness OP, et al. Automated quantification of microvascular perfusion. Microcirculation. 2018;25:e12482.

201. Legland D, Arganda-Carreras I, Andrey P. MorphoLibJ: integrated library and plugins for mathematical morphology with ImageJ. Bioinforma Oxf Engl. 2016;32:3532–4.

202. Mannello F, Tonti GA. Concise Review: No Breakthroughs for Human Mesenchymal and Embryonic Stem Cell Culture: Conditioned Medium, Feeder Layer, or Feeder-Free; Medium with Fetal Calf Serum, Human Serum, or Enriched Plasma; Serum-Free, Serum Replacement Nonconditioned Medium, or Ad Hoc Formula? All That Glitters Is Not Gold! STEM CELLS. 2007;25:1603–9.

203. Brewer GJ, Torricelli JR, Evege EK, Price PJ. Optimized survival of hippocampal neurons in B27-supplemented neurobasalTM, a new serum-free medium combination. J Neurosci Res. 1993;35:567–76.

204. Canfield SG, Stebbins MJ, Morales BS, Asai SW, Vatine GD, Svendsen CN, et al. An Isogenic Blood-Brain Barrier Model Comprising Brain Endothelial Cells, Astrocytes and Neurons Derived from Human Induced Pluripotent Stem Cells. J Neurochem. 2017;140:874–88.

205. Lim RG, Quan C, Reyes-Ortiz AM, Lutz SE, Kedaigle AJ, Gipson TA, et al. Huntington's Disease iPSC-Derived Brain Microvascular Endothelial Cells Reveal WNT-Mediated Angiogenic and Blood-Brain Barrier Deficits. Cell Rep. 2017;19:1365–77.

206. Bottenstein J. Cell Culture in the Neurosciences [Internet]. Boston, MA: Springer US; 1985 [cited 2018 Sep 7]. Available from: //www.springer.com/us/book/9781461295006

207. Banks WA. From blood-brain barrier to blood-brain interface: new opportunities for CNS drug delivery. Nat Rev Drug Discov. 2016;15:275–92.

208. Salvador E, Shityakov S, Förster C. Glucocorticoids and endothelial cell barrier function. Cell Tissue Res. 2014;355:597–605.

209. Mantle JL, Min L, Lee KH. Minimum Transendothelial Electrical Resistance Thresholds for the Study of Small and Large Molecule Drug Transport in a Human in Vitro Blood–Brain Barrier Model. Mol Pharm. 2016;13:4191–8.

210. Lippmann ES, Azarin SM, Kay JE, Nessler RA, Wilson HK, Al-Ahmad A, et al. Derivation of blood-brain barrier endothelial cells from human pluripotent stem cells. Nat Biotechnol. 2012;30:783–91.

211. Lippmann ES, Al-Ahmad A, Azarin SM, Palecek SP, Shusta EV. A retinoic acid-enhanced, multicellular human blood-brain barrier model derived from stem cell sources. Sci Rep. 2014;4:4160.

212. Katt ME, Xu ZS, Gerecht S, Searson PC. Human Brain Microvascular Endothelial Cells Derived from the BC1 iPS Cell Line Exhibit a Blood-Brain Barrier Phenotype. PLOS ONE. 2016;11:e0152105.

213. DeStefano JG, Xu ZS, Williams AJ, Yimam N, Searson PC. Effect of shear stress on iPSC-derived human brain microvascular endothelial cells (dhBMECs). Fluids Barriers CNS. 2017;14:20.

214. Vatine GD, Barrile R, Workman MJ, Sances S, Barriga BK, Rahnama M, et al. Human iPSC-Derived Blood-Brain Barrier Chips Enable Disease Modeling and Personalized Medicine Applications. Cell Stem Cell. 2019;24:995-1005.e6.

215. Delsing L, Dönnes P, Sánchez J, Clausen M, Voulgaris D, Falk A, et al. Barrier Properties and Transcriptome Expression in Human iPSC-Derived Models of the Blood–Brain Barrier. STEM CELLS. 2018;36:1816–27.

216. Linville RM, DeStefano JG, Sklar MB, Xu Z, Farrell AM, Bogorad MI, et al. Human iPSC-derived blood-brain barrier microvessels: validation of barrier function and endothelial cell behavior. Biomaterials. 2019;190–191:24–37.

217. Lim RG, Quan C, Reyes-Ortiz AM, Lutz SE, Kedaigle AJ, Gipson TA, et al. Huntington's Disease iPSC-Derived Brain Microvascular Endothelial Cells Reveal WNT-Mediated Angiogenic and Blood-Brain Barrier Deficits. Cell Rep. 2017;19:1365–77.

218. Wang YI, Abaci HE, Shuler ML. Microfluidic blood–brain barrier model provides in vivo-like barrier properties for drug permeability screening. Biotechnol Bioeng. 2016;114:184–94.

219. Canfield SG, Stebbins MJ, Morales BS, Asai SW, Vatine GD, Svendsen CN, et al. An isogenic blood–brain barrier model comprising brain endothelial cells, astrocytes, and neurons derived from human induced pluripotent stem cells. J Neurochem. 2017;140:874–88.

220. Canfield SG, Stebbins MJ, Faubion MG, Gastfriend BD, Palecek SP, Shusta EV. An isogenic neurovascular unit model comprised of human induced pluripotent stem cell-derived brain microvascular endothelial cells, pericytes, astrocytes, and neurons. Fluids Barriers CNS. 2019;16:25.

221. Appelt-Menzel A, Cubukova A, Günther K, Edenhofer F, Piontek J, Krause G, et al. Establishment of a Human Blood-Brain Barrier Co-culture Model Mimicking the Neurovascular Unit Using Induced Pluri- and Multipotent Stem Cells. Stem Cell Rep. 2017;8:894–906.

222. Park T-E, Mustafaoglu N, Herland A, Hasselkus R, Mannix R, FitzGerald EA, et al. Hypoxia-enhanced Blood-Brain Barrier Chip recapitulates human barrier function and shuttling of drugs and antibodies. Nat Commun. 2019;10:1–12.

223. Page S, Munsell A, Al-Ahmad AJ. Cerebral hypoxia/ischemia selectively disrupts tight junctions complexes in stem cell-derived human brain microvascular endothelial cells. Fluids Barriers CNS. 2016;13:16.

224. Lim RG, Quan C, Reyes-Ortiz AM, Lutz SE, Kedaigle AJ, Gipson TA, et al. Huntington's Disease iPSC-Derived Brain Microvascular Endothelial Cells Reveal WNT-Mediated Angiogenic and Blood-Brain Barrier Deficits. Cell Rep. 2017;19:1365–77.

225. Vatine GD, Al-Ahmad A, Barriga BK, Svendsen S, Salim A, Garcia L, et al. Modeling Psychomotor Retardation using iPSCs from MCT8-Deficient Patients Indicates a Prominent Role for the Blood-Brain Barrier. Cell Stem Cell. 2017;20:831–43.

226. Hollmann EK, Bailey AK, Potharazu AV, Neely MD, Bowman AB, Lippmann ES. Accelerated differentiation of human induced pluripotent stem cells to blood–brain barrier endothelial cells. Fluids Barriers CNS. 2017;14:9.

227. Neal EH, Marinelli NA, Shi Y, McClatchey PM, Balotin KM, Gullett DR, et al. A Simplified, Fully Defined Differentiation Scheme for Producing Blood-Brain Barrier Endothelial Cells from Human iPSCs. Stem Cell Rep. 2019;12:1380–8.

228. Katsimpardi L, Litterman NK, Schein PA, Miller CM, Loffredo FS, Wojtkiewicz GR, et al. Vascular and Neurogenic Rejuvenation of the Aging Mouse Brain by Young Systemic Factors. Science. 2014;344:630–4.

229. Lin R, Cai J, Kenyon L, Iozzo R, Rosenwasser R, Iacovitti L. Systemic Factors Trigger Vasculature Cells to Drive Notch Signaling and Neurogenesis in Neural Stem Cells in the Adult Brain. STEM CELLS. 2019;37:395–406.

230. Köster J, Rahmann S. Snakemake-a scalable bioinformatics workflow engine. Bioinforma Oxf Engl. 2018;34:3600.

231. Love MI, Huber W, Anders S. Moderated estimation of fold change and dispersion for RNA-seq data with DESeq2. Genome Biol. 2014;15:550.

232. Paredes I, Himmels P, Almodóvar CR de. Neurovascular Communication during CNS Development. Dev Cell. 2018;45:10–32.

233. Jeong H-W, Hernández-Rodríguez B, Kim J, Kim K-P, Enriquez-Gasca R, Yoon J, et al. Transcriptional regulation of endothelial cell behavior during sprouting angiogenesis. Nat Commun. 2017;8:1–14.

234. Tran Khiem A., Zhang Xianming, Predescu Dan, Huang Xiaojia, Machado Roberto F., Göthert Joachim R., et al. Endothelial β-Catenin Signaling Is Required for Maintaining Adult Blood–Brain Barrier Integrity and Central Nervous System Homeostasis. Circulation. 2016;133:177–86.

235. Lengfeld JE, Lutz SE, Smith JR, Diaconu C, Scott C, Kofman SB, et al. Endothelial Wnt/β-catenin signaling reduces immune cell infiltration in multiple sclerosis. Proc Natl Acad Sci. 2017;114:E1168–77.

236. Al-Ahmad AJ, Patel R, Palecek SP, Shusta EV. Hyaluronan impairs the barrier integrity of brain microvascular endothelial cells through a CD44-dependent pathway. J Cereb Blood Flow Metab Off J Int Soc Cereb Blood Flow Metab. 2019;39:1759–75.

237. Katt ME, Linville RM, Mayo LN, Xu ZS, Searson PC. Functional brain-specific microvessels from iPSC-derived human brain microvascular endothelial cells: the role of matrix composition on monolayer formation. Fluids Barriers CNS. 2018;15:7.

238. Luissint A-C, Artus C, Glacial F, Ganeshamoorthy K, Couraud P-O. Tight junctions at the blood brain barrier: physiological architecture and disease-associated dysregulation. Fluids Barriers CNS. 2012;9:23.

239. Löscher W, Potschka H. Blood-Brain Barrier Active Efflux Transporters: ATP-Binding Cassette Gene Family. NeuroRx. 2005;2:86–98.

240. Sweeney MD, Sagare AP, Zlokovic BV. Blood-brain barrier breakdown in Alzheimer disease and other neurodegenerative disorders. Nat Rev Neurol. 2018;14:133–50.

241. Ortiz GG, Pacheco-Moisés FP, Macías-Islas MÁ, Flores-Alvarado LJ, Mireles-Ramírez MA, González-Renovato ED, et al. Role of the blood-brain barrier in multiple sclerosis. Arch Med Res. 2014;45:687–97.

242. Daneman R, Zhou L, Agalliu D, Cahoy JD, Kaushal A, Barres BA. The Mouse Blood-Brain Barrier Transcriptome: A New Resource for Understanding the Development and Function of Brain Endothelial Cells. PLOS ONE. 2010;5:e13741.

243. Weksler BB, Subileau EA, Perriere N, Charneau P, Holloway K, Leveque M, et al. Blood–brain barrier-specific properties of a human adult brain endothelial cell line. FASEB J. 2005;19.

244. Neal EH, Marinelli NA, Shi Y, McClatchey PM, Balotin KM, Gullett DR, et al. A Simplified, Fully Defined Differentiation Scheme for Producing Blood-Brain Barrier Endothelial Cells from Human iPSCs. Stem Cell Rep. 2019;12:1380–8.

245. Pawlikowski B, Wragge J, Siegenthaler JA. Retinoic acid signaling in vascular development. Genes N Y N 2000. 2019;57:e23287.

246. Hedman AC, Smith JM, Sacks DB. The biology of IQGAP proteins: beyond the cytoskeleton. EMBO Rep. 2015;16:427–46.

247. Briggs MW, Sacks DB. IQGAP proteins are integral components of cytoskeletal regulation. EMBO Rep. 2003;4:571–4.

248. Smith JM, Hedman AC, Sacks DB. IQGAPs choreograph cellular signaling from the membrane to the nucleus. Trends Cell Biol. 2015;25:171–84.

249. Abel AM, Schuldt KM, Rajasekaran K, Hwang D, Riese MJ, Rao S, et al. IQGAP1: insights into the function of a molecular puppeteer. Mol Immunol. 2015;65:336–49.

250. Choi S, Anderson RA. And Akt-ion! IQGAP1 in control of signaling pathways. EMBO J. 2017;36:967–9.

251. Brill S, Li S, Lyman CW, Church DM, Wasmuth JJ, Weissbach L, et al. The Ras GTPase-activating-protein-related human protein IQGAP2 harbors a potential actin binding domain and interacts with calmodulin and Rho family GTPases. Mol Cell Biol. 1996;16:4869–78.

252. Dong F, Li L, Chen X, Allen T, Liu J. Glomerular endothelial cell IQGAP2 and filtration barrier function. Kidney Int. 2016;89:1160–1.

253. Wang H, Huo R, Xu M, Lu L, Xu Z, Li J, et al. Cloning and characterization of a novel transcript variant of IQGAP2 in human testis. DNA Seq J DNA Seq Mapp. 2004;15:319–25.

254. Uhlén M, Fagerberg L, Hallström BM, Lindskog C, Oksvold P, Mardinoglu A, et al. Proteomics. Tissue-based map of the human proteome. Science. 2015;347:1260419.

255. Zhang Y, Chen K, Sloan SA, Bennett ML, Scholze AR, O'Keeffe S, et al. An RNA-Sequencing Transcriptome and Splicing Database of Glia, Neurons, and Vascular Cells of the Cerebral Cortex. J Neurosci. 2014;34:11929–47.

256. Duester G. Retinoic Acid Synthesis and Signaling during Early Organogenesis. Cell. 2008;134:921–31.

257. Michinaga S, Koyama Y. Pathogenesis of Brain Edema and Investigation into Anti-Edema Drugs. Int J Mol Sci. 2015;16:9949–75.

258. Nation DA, Sweeney MD, Montagne A, Sagare AP, D'Orazio LM, Pachicano M, et al. Blood–brain barrier breakdown is an early biomarker of human cognitive dysfunction. Nat Med. 2019;25:270–6.

259. Feigin VL, Nichols E, Alam T, Bannick MS, Beghi E, Blake N, et al. Global, regional, and national burden of neurological disorders, 1990–2016: a systematic analysis for the Global Burden of Disease Study 2016. Lancet Neurol. 2019;18:459–80.

260. Carroll WM. The global burden of neurological disorders. Lancet Neurol. 2019;18:418–9.

261. Castillo X, Castro-Obregón S, Gutiérrez-Becker B, Gutiérrez-Ospina G, Karalis N, Khalil AA, et al. Re-thinking the Etiological Framework of Neurodegeneration. Front Neurosci [Internet]. 2019 [cited 2020 Feb 2];13. Available from: https://www.ncbi.nlm.nih.gov/pmc/articles/PMC6667555/

262. Strazielle N, Ghersi-Egea J-F. Efflux transporters in blood-brain interfaces of the developing brain. Front Neurosci [Internet]. 2015 [cited 2020 Feb 2];9. Available from: https://www.ncbi.nlm.nih.gov/pmc/articles/PMC4318338/

263. Berndt P, Winkler L, Cording J, Breitkreuz-Korff O, Rex A, Dithmer S, et al. Tight junction proteins at the blood–brain barrier: far more than claudin-5. Cell Mol Life Sci. 2019;76:1987–2002.

264. Bouldin TW, Krigman MR. Differential permeability of cerebral capillary and choroid plexus to lanthanum ion. Brain Res. 1975;99:444–8.

265. Tietz S, Engelhardt B. Brain barriers: Crosstalk between complex tight junctions and adherens junctions. J Cell Biol. 2015;209:493–506.

266. Occludin: a novel integral membrane protein localizing at tight junctions. J Cell Biol. 1993;123:1777–88.

267. Nitta T, Hata M, Gotoh S, Seo Y, Sasaki H, Hashimoto N, et al. Size-selective loosening of the blood-brain barrier in claudin-5–deficient mice. J Cell Biol. 2003;161:653–60.

268. Munji RN, Soung AL, Weiner GA, Sohet F, Semple BD, Trivedi A, et al. Profiling the mouse brain endothelial transcriptome in health and disease models reveals a core blood–brain barrier dysfunction module. Nat Neurosci. 2019;22:1892–902.

269. He L, Vanlandewijck M, Mäe MA, Andrae J, Ando K, Gaudio FD, et al. Single-cell RNA sequencing of mouse brain and lung vascular and vessel-associated cell types. Sci Data. 2018;5:1–11.

270. Hellinger É, Veszelka S, Tóth AE, Walter F, Kittel Á, Bakk ML, et al. Comparison of brain capillary endothelial cell-based and epithelial (MDCK-MDR1, Caco-2, and VB-Caco-2) cell-based surrogate blood–brain barrier penetration models. Eur J Pharm Biopharm. 2012;82:340–51.

271. Fogh J, Wright WC, Loveless JD. Absence of HeLa cell contamination in 169 cell lines derived from human tumors. J Natl Cancer Inst. 1977;58:209–14.

272. Seki T, Harada S, Hosoya O, Morimoto K, Juni K. Evaluation of the establishment of a tight junction in Caco-2 cell monolayers using a pore permeation model involving two different sizes. Biol Pharm Bull. 2008;31:163–6.

273. Fanning AS, Jameson BJ, Jesaitis LA, Anderson JM. The Tight Junction Protein ZO-1 Establishes a Link between the Transmembrane Protein Occludin and the Actin Cytoskeleton. J Biol Chem. 1998;273:29745–53.

274. Shalem O, Sanjana NE, Zhang F. High-throughput functional genomics using CRISPR–Cas9. Nat Rev Genet. 2015;16:299.

275. Kim HS, Lee K, Kim S-J, Cho S, Shin HJ, Kim C, et al. Arrayed CRISPR screen with image-based assay reliably uncovers host genes required for coxsackievirus infection. Genome Res. 2018;28:859–68.

276. Agrotis A, Ketteler R. A new age in functional genomics using CRISPR/Cas9 in arrayed library screening. Front Genet [Internet]. 2015 [cited 2020 Feb 7];6. Available from: http://www.frontiersin.org/articles/10.3389/fgene.2015.00300/full

277. Mertens AEE, Rygiel TP, Olivo C, van der Kammen R, Collard JG. The Rac activator Tiam1 controls tight junction biogenesis in keratinocytes through binding to and activation of the Par polarity complex. J Cell Biol. 2005;170:1029–37.

278. Zihni C, Balda MS, Matter K. Signalling at tight junctions during epithelial differentiation and microbial pathogenesis. J Cell Sci. 2014;127:3401–13.

279. Yamada S, Nelson WJ. Localized zones of Rho and Rac activities drive initiation and expansion of epithelial cell–cell adhesion. J Cell Biol. 2007;178:517–27.

280. Ebnet K. JAM-A and aPKC. Tissue Barriers. 2013;1:e22993.

281. Van Itallie CM, Fanning AS, Bridges A, Anderson JM. ZO-1 stabilizes the tight junction solute barrier through coupling to the perijunctional cytoskeleton. Mol Biol Cell. 2009;20:3930–40.

282. Zihni C, Terry SJ. RhoGTPase signalling at epithelial tight junctions: Bridging the GAP between polarity and cancer. Int J Biochem Cell Biol. 2015;64:120–5.

283. González-Mariscal L, Raya-Sandino A, González-González L, Hernández-Guzmán C. Relationship between G proteins coupled receptors and tight junctions. Tissue Barriers [Internet]. 2018 [cited 2020 Feb 7];6. Available from: https://www.ncbi.nlm.nih.gov/pmc/articles/PMC5823551/

284. Schmidt VA, Chiariello CS, Capilla E, Miller F, Bahou WF. Development of Hepatocellular Carcinoma in Iqgap2-Deficient Mice Is IQGAP1 Dependent. Mol Cell Biol. 2008;28:1489–502.

285. Chen F, Zhu H-H, Zhou L-F, Wu S-S, Wang J, Chen Z. IQGAP1 is overexpressed in hepatocellular carcinoma and promotes cell proliferation by Akt activation. Exp Mol Med. 2010;42:477–83.

286. Swiech L, Blazejczyk M, Urbanska M, Pietruszka P, Dortland BR, Malik AR, et al. CLIP-170 and IQGAP1 cooperatively regulate dendrite morphology. J Neurosci Off J Soc Neurosci. 2011;31:4555–68.

287. White CD, Brown MD, Sacks DB. IQGAPs in Cancer: A Family of Scaffold Proteins Underlying Tumorigenesis. FEBS Lett. 2009;583:1817–24.

288. Xia F-D, Wang Z-L, Chen H-X, Huang Y, Li J-D, Wang Z-M, et al. Differential expression of IQGAP1/2 in Hepatocellular carcinoma and its relationship with clinical outcomes. Asian Pac J Cancer Prev APJCP. 2014;15:4951–6.

289. White CD, Khurana H, Gnatenko DV, Li Z, Odze RD, Sacks DB, et al. IQGAP1 and IQGAP2 are reciprocally altered in hepatocellular carcinoma. BMC Gastroenterol. 2010;10:125.

290. Bao X, Lian X, Palecek SP. Directed endothelial progenitor differentiation from human pluripotent stem cells via Wnt activation under defined conditions. Methods Mol Biol Clifton NJ. 2016;1481:183–96.

291. Nakhaei-Nejad M, Zhang Q-X, Murray AG. Endothelial IQGAP1 regulates efficient lymphocyte transendothelial migration. Eur J Immunol. 2010;40:204–13.

292. Ellett F, Pase L, Hayman JW, Andrianopoulos A, Lieschke GJ. mpeg1 promoter transgenes direct macrophage-lineage expression in zebrafish. Blood. 2011;117:e49–56.